Modelling and Control of Unmanned Ground Vehicles

Thanh Hung Tran

A thesis submitted in fulfilment of the requirements

for the degree of Doctor of Philosophy

ARC Centre of Excellence for Autonomous Systems

Faculty of Engineering

University of Technology, Sydney, Australia

September 2007

CERTIFICATE OF AUTHORSHIP/ORIGINALITY

I certify that the work in this thesis has not previously been submitted for a degree nor has it been submitted as part of the requirements for a degree except as fully acknowledged within the text.

I also certify that the thesis has been written by me. Any help that I have received in my research work and in the preparation of the thesis itself has been acknowledged. In addition, I certify that all information sources and literature used are indicated in the thesis.

Thanh Hung Tran

Abstract

The thesis focuses on issues of vehicle modelling incorporating wheel-terrain interaction and low-level control design taking into account uncertainties and input time delay. Addressing these issues is of significant importance in achieving persistent autonomy for outdoor UGVs, especially when navigating on unprepared terrains.

The test-bed vehicle used for this research is retrofitted from an all-terrain 20-hp, 0.5-tonne vehicle. Its driveline system consists of an internal combustion engine, continuous variable transmission (CVT), gearbox, differential, chains, and eight wheels. The vehicle is driven in the skid-steering mode, which is popular for many off-road land-vehicle platforms.

In this thesis, a comprehensive approach is proposed for modelling the driveline. The approach considers the difference in speed between two outputs of the differential and the turning mechanism of the vehicle. It describes dynamics of all components in the vehicle driveline in an integrated manner with the vehicle motion. Given a pattern of the throttle position, left and right braking efforts as the inputs, the dynamic behaviour of the wheels and other components of the UGV can be predicted.

For controlling the vehicle at the low level, PID controllers are firstly used for all actuators. As many components of the vehicle exhibit nonlinearities and time delay, the large overshoots encountered in the outputs can lead to undesirable vehicle behaviours. To alleviate the problem, a novel control approach is proposed for suppression of overshoots resulting from PID control. Sliding mode control (SMC) is employed, for this, with time delay compensated by using an output predictor. As a result, the proposed approach can improve significantly system robustness and reduce substantially step response overshoot. Notably, the design is generic in that it can be applied for many dynamic processes.

Knowledge of the interaction between the UGV and the terrain plays an important role in increasing its autonomy and securing the safety for off-road locomotion. In this regard, vehicle kinematic equations are combined with the theory of terramechanics for dynamic modelling of the interaction between the vehicle wheels and a variety of terrain types. Also, a fast algorithm is developed to enable online implementation. The novel interaction model takes into account the relationship between normal stresses, shear stresses, and shear displacement of the terrain that is in contact with the wheels in deriving the three-dimensional reaction forces.

Finally, all modelling and control algorithms are integrated into a unique simulator for emulating the vehicle mobility characteristics. In particular, the wheel's slip and rolling resistance can also be derived to provide useful information for closed-loop control when the UGV is navigating in an unknown environment. The simulator, as a tool for analysing the vehicle mobility, is helpful for further research on relevant topics such as traction control, safe and effective locomotion.

Acknowledgements

First of all, I would like to thank my principal supervisor, Quang Ha, for his advice and support during my stay here in the University of Technology Sydney (UTS). My special thanks go to my co-supervisor, Steve Scheding, leader of the ARGO project at the ARC Centre of Excellence for Autonomous Systems (CAS). Thanks also go to team member Richard Grover, Alex Green, and Sisir Karumanchi, for helping me in conducting field tests and other experiments. Without their help, I would not be able to finish my work.

I would like to thank Professor Ken Waldron. His document on the derivation of the UGV ground interaction model is very helpful for my work on the vehicle terrain interaction analysis. Thanks also go to Ngai Kwok for his advice and help during the period of my study.

I would like to take this opportunity to thank Hung Nguyen, Associate Dean of UTS Faculty of Engineering, and Gamini Dissanayake, Director of the UTS node of CAS, for their support during my study. My special thanks also go to Mr. Luong Van Son, former Dean of the College of Information & Communication Technology, Can Tho University, and to the Vietnamese Ministry of Education and Training (MOET), for supporting my candidature. Without their support, I would not be able to go to Sydney to study.

I want to thank all my friends here in Sydney and my colleagues in Can Tho University. Their encouragement and friendship make my PhD student life more enjoyable.

Finally, I owe my greatest debt to my parents for giving birth to me, to my grandparents who raised and taught me, and to my wife and my little daughter who have given me love and support throughout my time in Sydney.

Contents

List of Figures

List of Tables

List of Symbols

Symbols	Nomenclature	Unit
α_i , β_i	Angles of shear stress on the i^{th} wheel in standard spherical coordinates	rad
χ	Ground slope angle	rad
δ	Damping ratio	-
δ_1	Lower limit of damping ratio	-
δ_2	Higher limit of damping ratio	-
$\hat{\delta}$	Approximation of damping ratio	-
ε	Error threshold in search algorithm	%
ϕ	Terrain internal friction angle	rad
γ_i	Angle between slip velocity on the i^{th} wheel and its tangential component	rad
η	SMC parameter	-
φ_i	Elevation angle of shear stress in new spherical coordinates	rad
λ	SMC parameter	-
θ	Angle of wheel contact with terrain	rad
θ_1	Wheel entry angle at first contact point	rad
θ_{1_i}	The i^{th} wheel entry angle	rad
θ_2	Wheel exit angle at last contact point	rad
θ_{2_i}	The i^{th} wheel exit angle	rad
θ_b	Brake actuator position	%
θ_{c1_i} , θ_{c2_i}	Intersection points between shear stress under the i^{th} wheel and its linearisation	rad
θ_e	Engine throttle position	%
θ_i	The i^{th} wheel contact angle	rad
θ_m	Maximum stress point	rad

Symbols	Nomenclature	Unit
θ_{m_i}	Maximum stress point on the i^{th} wheel	rad
$\theta_{x1_i}, \theta_{x2_i}$	Intersection points between the normal stress distribution under the i^{th} wheel and its linearisation	rad
θ_M	Motor position (throttle control)	%
ρ	Azimuth angle between vehicle frame and earth coordinates	rad
σ	Normal stress under a wheel	kPa
σ_1	Normal stress in front region	kPa
σ_{1_i}	Normal stress in front region under the i^{th} wheel	kPa
$\hat{\sigma}_{1_i}$	Linear approximation of normal stress in front region under the i^{th} wheel	kPa
σ_{1X_i}	Longitudinal component of normal stress in front region under the i^{th} wheel	kPa
σ_{1Z_i}	Vertical component of normal stress in front region under the i^{th} wheel	kPa
$\hat{\sigma}_{1X_i}$	Linear approximation of the longitudinal component of normal stress in front region under the i^{th} wheel	kPa
$\hat{\sigma}_{1Z_i}$	Linear approximation of the vertical component of normal stress in front region under the i^{th} wheel	kPa
σ_2	Normal stress in rear region	kPa
σ_{2_i}	Normal stress in rear region under the i^{th} wheel	kPa
$\hat{\sigma}_{2_i}$	Linear approximation of normal stress in rear region under the i^{th} wheel	kPa
σ_{2X_i}	Longitudinal component of normal stress in rear region under the i^{th} wheel	kPa

Symbols	Nomenclature	Unit
σ_{2Z_i}	Vertical component of normal stress in rear region under the i^{th} wheel	kPa
$\hat{\sigma}_{2X_i}$	Linear approximation of longitudinal component of normal stress in rear region under the i^{th} wheel	kPa
$\hat{\sigma}_{2Z_i}$	Linear approximation of vertical component of normal stress in rear region under the i^{th} wheel	kPa
σ_i	Normal stress under the i^{th} wheel	kPa
σ_{X_i}	Longitudinal component of normal stress under the i^{th} wheel	kPa
σ_{Y_i}	Lateral component of normal stress under the i^{th} wheel	kPa
σ_{Z_i}	Vertical component of normal stress under the i^{th} wheel	kPa
τ	Shear stress	kPa
τ_1	Shear stress in front region	kPa
τ_{1_i}	Shear stress in front region on the i^{th} wheel	kPa
$\hat{\tau}_{1_i}$	Linear approximation of shear stress in front region on the i^{th} wheel	kPa
τ_{1t_i}	Tangential component of shear stress in front region on the i^{th} wheel	kPa
$\hat{\tau}_{1t_i}$	Linear approximation of tangential shear stress in front region on the i^{th} wheel	kPa
τ_{1X_i}	Longitudinal component of shear stress in front region on the i^{th} wheel	kPa
τ_{1Y_i}	Lateral component of shear stress in front region on the i^{th} wheel	kPa
τ_{1Z_i}	Vertical component of shear stress in front region on the i^{th} wheel	kPa

Symbols	Nomenclature	Unit
$\hat{\tau}_{1X_i}$	Linear approximation of longitudinal component of shear stress in front region on the i^{th} wheel	kPa
$\hat{\tau}_{1Y_i}$	Linear approximation of lateral component shear stress in front region on the i^{th} wheel	kPa
$\hat{\tau}_{1Z_i}$	Linear approximation of vertical component shear stress in front region on the i^{th} wheel	kPa
τ_2	Shear stress in rear region	kPa
τ_{2_i}	Shear stress in rear region on the i^{th} wheel	kPa
$\hat{\tau}_{2_i}$	Linear approximation of shear stress in rear region on the i^{th} wheel	kPa
τ_{2t_i}	Tangential component of shear stress in rear region on the i^{th} wheel	kPa
$\hat{\tau}_{2t_i}$	Linear approximation of tangential shear stress in rear region on the i^{th} wheel	kPa
τ_{2X_i}	Longitudinal component of shear stress in rear region on the i^{th} wheel	kPa
τ_{2Y_i}	Lateral component of shear stress in rear region on the i^{th} wheel	kPa
τ_{2Z_i}	Vertical component of shear stress in rear region on the i^{th} wheel	kPa
$\hat{\tau}_{2X_i}$	Linear approximation of longitudinal component of shear stress in rear region on the i^{th} wheel	kPa
$\hat{\tau}_{2Y_i}$	Linear approximation of lateral component shear stress in rear region on the i^{th} wheel	kPa
$\hat{\tau}_{2Z_i}$	Linear approximation of vertical component of shear stress in rear region on the i^{th} wheel	kPa

Symbols	Nomenclature	Unit
τ_e	Engine time constant	s
τ_i	Shear stress on the i^{th} wheel	kPa
τ_m	Motor time constant	s
τ_{t_i}	Tangential component of the shear stress on the i^{th} wheel	kPa
τ_{X_i}	Longitudinal component of shear stress on the i^{th} wheel	kPa
τ_{Y_i}	Lateral component of shear stress on the i^{th} wheel	kPa
τ_{Z_i}	Vertical component of shear stress on the i^{th} wheel	kPa
ω_e	Engine rotational speed	RPM
ω_c	CVT output speed	RPM
ω_d	Rotational speed of differential's case	RPM
ω_{dL}	Differential's output speed on left side	RPM
ω_{dR}	Differential's output speed on right side	RPM
ω_G	Gearbox output speed	RPM
ω_n	Natural frequency	rad/s
ω_{n1}	Lower limit of natural frequency	rad/s
ω_{n2}	Higher limit of natural frequency	rad/s
$\hat{\omega}_n$	Approximation of natural frequency	rad/s
ω_i	Speed of the i^{th} wheel	rad/s
ω_w	Wheel rotational speed	rad/s
ω_{wL}, ω_L	Left wheel rotational speed	rad/s
ω_{wR}, ω_R	Right wheel rotational speed	rad/s
Ω	Vehicle turning rate	rad/s
a	Longitudinal distance between successive wheel axles	m

Symbols	Nomenclature	Unit
a_X	Vehicle acceleration along longitudinal direction	m/s
a_Y	Vehicle acceleration along lateral direction	m/s
b	Wheel width	m
b_e	Engine damping coefficient	Nms
b_d	Differential damping coefficient	Nms
b_w	Wheel damping coefficient	Nms
$b_{D,in}$	Damping coefficient inside differential	Nms
b_G	Gearbox damping coefficient	Nms
c	Terrain cohesion parameter	kPa
c_{r1}, c_{r2}	Wheel friction cofficients	$m.s^{-2}$, s^{-1}
d	Distance between the vehicle centroid and the centre of mass	m
dA_i	Area increment around a contact point	m^2
dF_{X_i}	Total force increment along longitudinal direction acting on a very small contact area around a contact point	N
dF_{Y_i}	Total force increment along lateral direction acting on a very small contact area around a contact point	N
dF_{Z_i}	Total force increment along vertical direction acting on a very small contact area around a contact point	N
e	Control error	
e_{emf}	Motor back electromotive force	V
e_o	PID error	
f	Nonlinear function	-
$\hat{f}$	Approximation of nonlinear function	-
g	Gravitational acceleration	m/s^2

Symbols	Nomenclature	Unit
h	Height of the centre of mass above the ground	m
i	Vehicle wheel slip	%
i_{CVT}	CVT belt slip	%
j	Shear displacement	m
j_i	Shear displacement at a contact point on the i^{th} wheel	m
j_{X_i}	Shear displacement at a contact point on the i^{th} wheel along longitudinal direction	m
j_{Y_i}	Shear displacement at a contact point on the i^{th} wheel along lateral direction	m
j_{Z_i}	Shear displacement at a contact point on the i^{th} wheel along vertical direction	m
k	SMC parameter / time step	-
$k_{1_i}, k_{2_i}, c_{1_i}, c_{2_i}$	Linearisation parameters for normal stress on the i^{th} wheel	kPa/rad, kPa/rad, kPa, kPa
$k_{1X_i}, k_{2X_i}, c_{1X_i}, c_{2X_i}$	Linearisation parameters for longitudinal component of normal stress on the i^{th} wheel	kPa/rad, kPa/rad, kPa, kPa
$k_{1Z_i}, k_{2Z_i}, c_{1Z_i}, c_{2Z_i}$	Linearisation parameters for lateral component of normal stress on the i^{th} wheel	kPa/rad, kPa/rad, kPa, kPa
$k_{3_i}, k_{4_i}, c_{3_i}, c_{4_i}$	Linearisation parameters for shear stress on the i^{th} wheel	kPa/rad, kPa/rad, kPa, kPa
$k_{3t_i}, k_{4t_i}, c_{3t_i}, c_{4t_i}$	Linearisation parameters for tangential component of shear stress on the i^{th} wheel	kPa/rad, kPa/rad, kPa, kPa
$k_{3X_i}, k_{4X_i}, c_{3X_i}, c_{4X_i}$	Linearisation parameters for longitudinal component of shear stress on the i^{th} wheel	kPa/rad, kPa/rad, kPa, kPa
$k_{3Y_i}, k_{4Y_i}, c_{3Y_i}, c_{4Y_i}$	Linearisation parameters for lateral component of shear stress on the i^{th} wheel a	kPa/rad, kPa/rad, kPa, kPa
$k_{3Z_i}, k_{4Z_i}, c_{3Z_i}, c_{4Z_i}$	Linearisation parameters for vertical component of shear stress on the i^{th} wheel	kPa/rad, kPa/rad, kPa, kPa

Symbols	Nomenclature	Unit
k_c , k_ϕ	Pressure-sinkage moduli parameters of a terrain	kN/m^{n+1}, kN/m^{n+2}
m	Vehicle's mass	kg
m_w	Wheel's mass	kg
n	Sinkage exponent parameter of terrain	-
r	Wheel radius	m
t_d	Time delay	s
t_P	Peak time	s
u	SMC output, PID input	%
u_{eq}	Equivalent control output	%
u_R	Robust control output	%
x	Speed difference between the differential's case and its outputs	RPM
(x_i, y_i)	Cartesian coordinates of a contact point on the i^{th} wheel frame	m
$\mathbf{x}(t)$	State variable vector	
y	Process output	%
y_d	Desired output (Reference or set-point)	%
z	Wheel sinkage	m
z_i	Sinkage of the i^{th} wheel	m
A, **B**	System matrices in state space form	
B	Half of the vehicle track	m
B_m	Motor damping ratio	Nms
D	Boundary of disturbance	
F	Boundary of nonlinear function's approximation error	-
F_R	Wheel rolling resistance	N
$F_{t,w}$	Traction force at wheels	N
F_{X_i}	Total reaction force acting on the i^{th} wheel along longitudinal direction	N

Symbols	Nomenclature	Unit
$\hat{F}_{X_i}$	Estimate of total reaction force acting on the i^{th} wheel along longitudinal direction	N
F_{Y_i}	Total reaction force acting on the i^{th} wheel along lateral direction	N
$\hat{F}_{Y_i}$	Estimate of total reaction force acting on the i^{th} wheel along lateral direction	N
F_{Z_i}	Total reaction force acting on the i^{th} wheel along vertical direction	N
$\hat{F}_{Z_i}$	Estimate of total reaction force acting on the i^{th} wheel along vertical direction	N
I	Motor armature current	A
I_Z	Vehicle moment of inertia around Z axis	$kg.m^2$
J_e	Engine moment of inertia	$kg.m^2$
J_m	Motor rotor's moment of inertia	$kg.m^2s^{-2}$
J_w	Wheel moment of inertia	$kg.m^2$
K	Shear deformation modulus	m
K_1	CVT gear ratio	-
K_2	Gearbox gear ratio	-
K_3	Chain system gear ratio	-
K_a	Amplifier' voltage to current gain	AV^{-1}
K_e	Engine gain	N.m
$K_{em}=K_t$	Motor electromotive force constant	$N.m.A^{-1}$
K_i	Actuator's current to force gain	NA^{-1}
K_m	Motor gain	-
K_D	Derivative gain (D)	-
K_I	Integral gain (I)	-
K_G	Motor gear ratio	-
K_P	Proportional gain (P)	-
L_m	Motor electric inductance	H
M_P	Percentage of overshoot	%

Symbols	Nomenclature	Unit
M_R	Moment of turning resistance	N.m
M_X	Rolling moment around X axis	N.m
M_Y	Rolling moment around Y axis	N.m
M_Z	Turning moment around Z axis	N.m
$\hat{M}_Z$	Estimate of turning moment	N.m
(N, E)	Position of the vehicle in earth coordinates	m, m
R_m	Motor electric resistance	Ω
T	Traction torque	N.m
T_{bL}	Left brake torque	N.m
T_{bR}	Right brake torque	N.m
T_c	Load on CVT	N.m
T_d	Load on differential's case	N.m
T_{dL}	Load on differntial's left output	N.m
T_{dR}	Load on differential's right output	N.m
T_e	Engine generated torque	N.m
T_{ec}	Load on engine	N.m
$T_{fric,e}$	Engine friction torque	N.m
$T_{fric,D}$	Differential friction torque	N.m
$T_{fric,G}$	Gearbox friction torque	N.m
T_i	Traction torque developed on the i^{th} wheel	N.m
$\hat{T}_i$	Estimate of traction torque developed on the i^{th} wheel	N.m
T_m	Motor torque	N.m
T_{sL}	Total load torque on the left sun gear (differential)	N.m
T_{sR}	Total load torque on the right sun gear (differential)	N.m
T_w	Total load torque on all wheels	N.m
T_{wL}	Load torque from left wheels	N.m
T_{wR}	Load torque from right wheels	N.m

Symbols	Nomenclature	Unit
T_G	Load torque on gearbox	N.m
V	PID output (Process input, or Voltage)	V
$\mathbf{V}$	Vehicle velocity vector	m/s
V_{jX_i}	Longitudinal component of slip velocity of a contact point on the i^{th} wheel	m/s
V_{jY_i}	Lateral component of slip velocity of a contact point on the i^{th} wheel	m/s
V_{jZ_i}	Vertical component of slip velocity of a contact point on the i^{th} wheel	m/s
V_{t_i}	Tangential component of slip velocity of a contact point on the i^{th} wheel	m/s
V_L	Lyapunov function	-
V_E	Vehicle velocity along east direction	m/s
V_N	Vehicle velocity along north direction	m/s
V_X	Vehicle longitudinal velocity	m/s
V_Y	Vehicle lateral velocity	m/s
S	Sliding surface	-
S_{X_i}	Wheel slip ratio along longitudinal direction	%
S_{Y_i}	Wheel slip ratio along lateral direction	%
(X_i, Y_i, Z_i)	Cartesian coordinates of a contact point on the vehicle frame	m
W	Vehicle weight	N
W_i	Vertical load on the i^{th} wheel	N

Abbreviations

ALV	Autonomous Land Vehicle
CCD	Charge-Coupled Device
CVT	Continuous Variable Transmission
DARPA	Defense Advanced Research Projects Agency
FLIR	Forward Looking InfraRed
HMMWV	High-Mobility, Multipurpose, Wheeled Vehicle
LADAR	Light Detection And Ranging
MIMO	Multiple-Input Multiple-Output
MVEM	Mean Value Engine Model
SSV	Semiautonomous Surrogate Vehicle
SI	Spark Ignition
SMC	Sliding Mode Controller
PID	Proportional – Integral – Derivative
UGV	Unmanned Ground Vehicle

Chapter 1

Introduction

Unmanned ground vehicles (UGVs) have many potential applications, both in military and civilian areas, such as reconnaissance, surveillance, target acquisition, search and rescue, and exploration. Knowledge of UGV behaviours under control commands on different terrain types plays an important role on improving their safety, reliability and autonomy. In this thesis, the complex processes involved in a UGV driveline and its interaction with terrain are thoroughly analysed and a robust low-level control scheme is developed for driving the autonomous vehicle. An overview of the research is given in this chapter.

In Section 1.1, a brief history of UGV developments is provided. Sections 1.2 and 1.3 introduce the research areas in the context of UGVs and the focus of this thesis. Section 1.4 summarizes the main contributions of the research, herein. Publications reporting the findings of this work are listed in Section 1.5. Finally, the structure of the thesis is given in the last section.

1.1 Unmanned Ground Vehicles

A UGV is defined as "any piece of mechanized equipment that moves across the surface of the ground and serves as a means of carrying or transporting something, but explicitly does not carry a human being" (Gage, 1995). In the robotic community, a

UGV is usually considered as an automated motion platform or just a mobile robot. It can be classified as tele-operated or autonomous depending on whether it requires human intervention or not (Wikipedia, 2007). A UGV is sometimes called an autonomous land vehicle (ALV).

Over the years, many efforts have been made in UGV development. Shakey, built at Stanford Research Institute from 1966 to 1972, can be considered as the first major development in the UGV field (Nilsson, 1969). Equipped with a TV camera, an ultrasonic range finder, and bump sensors on a three-wheeled platform, it had a restricted capability in environment perception. Controlled by an off-board SDS-940 mainframe computer, it could execute some form of automatic navigation and simple object rearranging tasks in a laboratory environment. Notwithstanding its accomplished capability, Shakey was not an autonomous robot as desired. Details about Shakey can be found in (Nilsson, 1984; Wilber, 1972).

Another attempt, the Stanford Cart, was made at Standford University AI Lab from 1973 to 1981 (Moravec, 1980; Moravec, 1983). It used a complex stereo camera which could take pictures from 9 different positions to perceive the environment. An off-board KL-10 mainframe computer was used to extract features and correlation information between pictures. This combined with information of the angles between the camera's positions could be used to rebuild a 3D model of the environment. With suitable navigation and obstacle avoidance schemes, the Cart could move to a goal position without hitting obstacles in an indoor environment. However, it travelled extremely slowly, taking up to fifteen minutes to move only one meter.

An early development for outdoor applications was made under the Autonomous Land Vehicle program from 1985 to 1988, sponsored by the US Defense Advanced Research Projects Agency (DARPA). The vehicle, known as the DARPA ALV (Lowrie *et al.*, 1985), was based on an eight-wheel all-terrain platform equipped with a colour video camera and a 64x256 pixel laser scanner (Everett, 1995). The model of outdoor environment obtained from video data and range information enabled the vehicle to follow a road at an average speed of 14.5km/h and move at a maximum 3 km/h in an off-road area while avoiding small obstacles (Douglass, 1998).

Following the success of the DARPA ALV, efforts were concentrated in the DARPA DEMO I, II, and III programs from 1990 to 2001 (Shoemaker and Bomstein, 1998). DEMO I (1991) used high-mobility, multipurpose, wheeled vehicle (HMMWV) platforms, equipped with all actuators and sensors, to demonstrate mobility in on-road and off-road environments, primary in teleoperated mode. In DEMO II (1996), three semiautonomous surrogate vehicles (SSVs), automated from HMMWVs and outfitted with FLIR, LADAR, and CCD camera sensors, were incorporated in reconnaissance, surveillance, and target acquisition tasks (Spofford *et al.*, 1997). The DEMO III program (1998-2001) focused on advanced technologies for small, survival UGVs (Kurtz, 1998). Equipped with CCD/FLIR stereo vision and LADAR sensors for daylight/night obstacle detection (Matthies *et al.*, 1998), the vehicles could navigate autonomously to target destinations, set by operators, at maximum speeds of 32 kph during day time and 16 kph at night on rough terrain.

1.2 Research areas in autonomous UGV development

It is pointed out in (Durrant-Whyte, 2001) that technologies required for a general autonomous UGV can be divided up into five areas: mobility, localisation, navigation, planing, and communication. The relationship between them is depicted in Figure 1.1.

Mobility deals with the vehicle mechanism design, the motion control technique, and the interaction between the vehicle and terrain. It is concerned with the kinematics and dynamics of the vehicle platform and the control algorithms for the vehicle as well as all actuators outfitted on the vehicle to obtain the desired motion on a certain terrain.

Localisation is related to estimation of the vehicle position and attitude in a fixed frame: for example, an earth-fixed coordinates system. It is concerned with robust algorithms for more accurate estimation to deal with sensor uncertainties. Taking information from internal and external sensors as inputs, its outputs affect both navigation and mobility processes.

Navigation handles information obtained from environment sensors to build up a map of the environment. The representation of the environment is then used to control the

vehicle in small area around the current vehicle position in order to follow a trajectory defined in a planning process. It also manages obstacle detection and avoidance.

Mission and path **planning** makes use of all known information from prior maps, mission goals, sensory and control structures to generate trajectories, or way points and other actions for the vehicle to execute. However, due to the incomplete knowledge of the world in outdoor missions, the vehicle must use the environment information gathered along the local path to update or rebuild the trajectory.

Communication allows the vehicle to be connected with human operators and other vehicles or systems. Whether the vehicle is fully autonomous or not, it requires a communication link to co-operate with other vehicles or the base station in many missions.

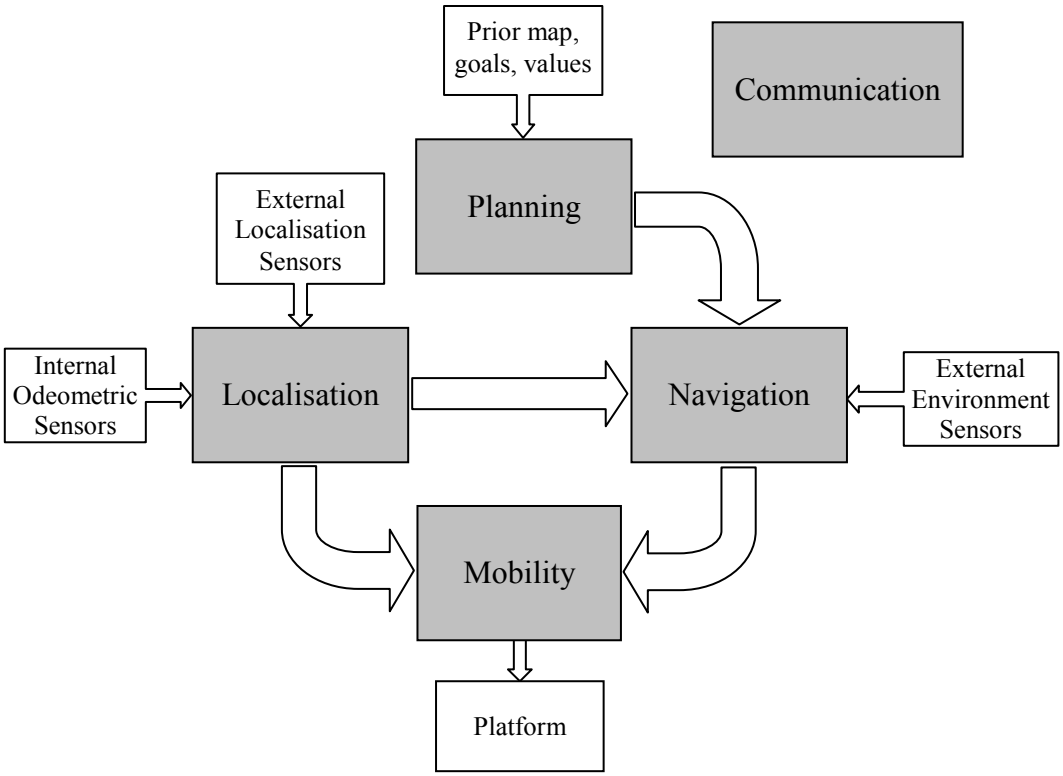

Figure 1.1 Relationship between elements of an autonomous UGV (Durrant-Whyte, 2001)

1.3 Thesis objectives

This research is part of a larger project conducted at the ARC Centre for Autonomous System at The University of Sydney. The project aims to develop an UGV by augmenting the autonomous capability for an existing 8x8 skid-steering vehicle with equipped actuators and sensors to achieve full autonomy of persistent navigation over unknown, unprepared terrain.

This thesis focuses on mobility issues of the vehicle. Particularly, it develops a model of the vehicle driveline system in which the behaviours of each component can be obtained from the vehicle dynamic performance. In addition, low-level robust controllers for actuators are designed. Kinematics and dynamics of the vehicle are combined with the terramechanics theory to build up a model for the interaction between the vehicle and terrain. For online implementation of the terrain interaction model, a fast algorithm is developed. Finally, all models and control algorithms are integrated into a unique simulator which enables designers to test all issues related to the vehicle mobility.

The driveline of the vehicle consists of a combustion engine, transmission, gearbox, differential, chains, and eight wheels involved in a skid-steering configuration which is more similar to a track than a normal car. Knowledge of the behaviour of these components in straight-line running as well as in turning plays an important role in controlling the vehicle. It is desired to have a model of the vehicle that can be used to predict the responses of each component in the driveline, especially the wheels, with a certain pattern of throttle and braking forces at the inputs for skid steering. That model is useful for the development of control algorithms.

For this vehicle, important variables needed to be controlled at the low level include the engine throttle, left and right braking forces, linear velocity and turning rate of the vehicle. The systems are very complicated to be controlled as they exhibit time delays, nonlinearities, and uncertainties; however, to comply with navigation constraints the controller must satisfy strict requirements. Firstly, the controller must not produce overshoots because the variables are correlated, overshoots in one controlled variable can result in adverse responses of the others. On the other hand, a fast rise time is

always an essential requirement for the control systems for these variables. In addition, it is desired that the control design should be general enough to be applied for any mobile platform without much modification. Lastly, robustness to uncertainties is required to overcome disturbance, nonlinearities, and model errors.

Knowledge of the interaction between the UGV and terrain plays an important role in achieving full autonomy and safety for off-road locomotion. Terrain has strong effects on traction development, motion resistance and moment turning resistance. The response of the vehicle is therefore also determined by the type of the ground on which the vehicle is running. To understand this relationship, a comprehensive dynamic model for the interaction between the wheels and terrain is required. Given the terrain parameters, the vehicle configuration, and the current state of the vehicle, the model should be able to predict the next states as well as other important outputs for safe and effective control.

1.4 Main contributions of the thesis

The main contributions of this thesis are summarized as follows:

- Driveline modelling development for the skid-steering vehicle. This approach takes into account the difference in speeds between two outputs of the differential, and the turning mechanism of the vehicle. It describes dynamically the motion of all components of the vehicle driveline in a decomposed manner from the motion of the vehicle. Given a pattern of the throttle position, left and right braking efforts at the input of the model, behaviour of wheels and other components can be obtained. The approach is general enough to be applied for other skid-steering vehicles.

- The development of a robust non-overshoot sliding mode control (SMC) and proportional-integral-derivative control (PID) scheme taking into account a delayed input. This combines the advantages of SMC and PID controllers to achieve high control performance at the low level. In particular, the PID controller is used to obtain a model-free feature which is not available for SMC.

Meanwhile, desirable robustness and system order reduction of SMC are exploited to treat nonlinearity and overshoot, which remain major problems found with PID control. As a result, the proposed approach can yield no or extremely small overshoot. It is interesting to note that the approach can be applied for many processes without prior model knowledge.

- Analysis and modelling development for vehicle-terrain interaction incorporating wheel slips and reaction forces in three dimensions. This approach describes comprehensively the relationship between the reaction forces, the vehicle kinetics and terrain properties. The novel model extends current knowledge in the field of vehicle-terrain interaction applied for multi-wheel skid-steering vehicles.

- Fast algorithm for terrain interaction analysis. This approach is attractive in terms of computational efficiency and accuracy when comparing with the current method. It enables designers to implement the vehicle-terrain interaction analysis for online applications.

- Development of a simulator for the whole vehicle, incorporating the driveline model, terrain interaction, and motion controllers. It is also useful for further research on areas related to mobility such as traction control, safe and effective locomotion.

1.5 List of publications

1.5.1 Journal articles

Tran, T. H., Scheding , S., and Ha, Q. P., and Waldron, K. "A new model for vehicle-terrain interaction of skid-steering wheeled UGV", *IEEE Transactions on Automation Science and Engineering* (submitted).

Tran, T. H., Ha, Q. P., and Nguyen, H. T. (2007) "Robust non-overshoot time responses using cascade sliding mode-PID control." *Journal of Advanced Computational Intelligence and Intelligent Informatics*, **11**(10), 1224-1231.

Ha, Q. P., Tran, T. H., and Dissanayake, G. (2005). "A wavelet-and neural network-based voice interface system for wheelchair control." *International Journal of Intelligent Systems Technologies and Applications*, **1**(1/2), 49-65.

1.5.2 Peer reviewed conference papers

Tran, T. H., Kwok, N. M., Scheding, S., and Q. P. Ha. (2007) "Dynamic modelling of wheel-terrain interaction of a UGV." *Proc. of the IEEE Conference on Automation Science and Engineering*, Scottsdale, Arizona, USA, 369-374, September 22-25, 2007 (Best student paper award).

Tran, T. H., Kwok, N. M., Nguyen, M. T., Ha, Q. P., and Fang, G. (2006) "Sliding mode-PID controller for robust low-level control of a UGV." *Proc. of the IEEE Conference on Automation Science and Engineering*, Shanghai, China, 684-689, October 7-10, 2006.

Tran, T. H., Ha, Q. P., and Nguyen, H. T. (2005) "Cascade sliding mode-PID controller for non-overshoot time responses." *Proc. of the 6th International Conference on Intelligent Technologies*, Phuket, Thailand, 27-33, December 14-16, 2005.

Ha, Q. P., Tran, T. H., Scheding, S., Dissanayake, G., and Durrant-Whyte, H. F. (2005) "Control issues of an autonomous vehicle." *Proc. of the 22th IAARC/CIB/IEEE/IFAC/IFR International Symposium on Automation and Robotics in Construction*, Italy, (CD-ROM), September 11-14, 2005.

Tran, T. H., Ha, Q. P., Grover, R., and Scheding, S. (2004) "Modelling of an autonomous amphibious vehicle." *Proc. of the 2004 Australian Conference on Robotics and Automation*, Canberra, Australia, (CD-ROM), December 6-8, 2004.

Tran, T. H., Ha, Q. P., and Dissanayake, G. (2004) "New wavelet-based pitch detection method for human-robot voice interface." *Proc. of the 2004 IEEE/RSJ International Conference on Intelligent Robots and Systems*, Sendai, Japan, 527-532, September 28 - October 2, 2004.

Ha, Q. P., Tran, T. H., and Trinh, H. (2004) "Observer-based output feedback variable structure control with application to a two-link manipulator." *Proc. of the 3rd IFAC Symposium on Mechatronic Systems*, Sydney, Australia, (CD-ROM), September 6-8.

1.6 Structure of the thesis

The rest of this thesis is organised as follows.

Chapter 2 reviews research publications related to the work covered in this thesis. It focuses on three areas of mobility: driveline modelling, low-level robust controllers, and vehicle-terrain interaction. Each area is covered with a review of the current literature, remaining problems, and the proposed approaches for solving the problems.

Modelling of the vehicle driveline is described in Chapter 3. Based on basic motion of a vehicle, e.g. car or truck, a new model for the driveline of a skid-steering wheeled vehicle is developed. It takes into account the differential mechanics combined with basic dynamics of other components. Simulation results are provided and a problem in computation for the model is pointed out. A simplified model is introduced to alleviate the solution complexity. Simulation results and comparison with experiments are provided.

Chapter 4 deals with the development of robust low-level controllers for solving the overshoot problem associated with PID control. A robust control algorithm is developed for nonlinear systems with and without time delay. Simulation results are provided as samples of throttle and braking control which are impaired by nonlinearity and time delay.

The vehicle-terrain interaction problem is analysed in Chapter 5. Theoretical development for the interaction is comprehensively elaborated from mathematical analysis of slip velocities, shear displacements, and shear stresses in three dimensions. Kinetics and dynamics of the vehicle are combined with reaction forces on all wheels derived from shear stresses to obtain the vehicle acceleration, velocity and position. Wheel sinkage, rolling resistance, and moment turning resistance can then be computed. A novel model for the interaction between the skid-steering wheeled vehicle and terrain

is proposed as a sample application of the terrain interaction analysis. The model can be used to predict the vehicle behaviour on various terrain types. Simulation results and a comparison with experiments are given.

A fast algorithm for online implementation of the terrain interaction model is described in Chapter 6. Based on an idea of using linear approximation of shear and normal stresses to avoid integral computation (with a certain error), a new algorithm is developed. A smallest error criterion is applied for linear approximations of stresses to minimize the difference in results between the modified model and the original benchmark. The proposed algorithm is compared with other method, in term of accuracy, and with the original, in term of computational efficiency.

In Chapter 7, the vehicle driveline model is incorporated with the terrain interaction analysis to estimate the vehicle trajectory and other variables on a certain terrain type under a pattern of throttle and braking forces. The approach proposed in Chapter 4 is employed to control the vehicle velocity and turning rate. Simulation results are provided.

Finally, Chapter 8 provides a summary and conclusion of the thesis.

Chapter 2

Literature survey and proposed approaches

As introduced in Chapter 1, this thesis focuses on motion control and dynamic issues of an UGV. The vehicle driveline is modelled and incorporated with terrain interaction analysis to predict behaviours of the vehicle on different terrain types under the developed robust low-level control. In this chapter, an overview of the relevant literature and the proposed approaches are presented.

Work related to driveline modelling is reviewed in the first section, followed by the proposed approach for the vehicle driveline modelling. Then UGV control techniques, problems and the proposed approach are introduced in Section 2.2. Issues related to vehicle-terrain interaction are examined in Section 2.3. The last section addresses fast algorithms required for vehicle-terrain interaction modelling.

2.1 Driveline modelling

The driveline is the power transmission system of a vehicle. It transfers the power from the engine to the wheels. Many cars and trucks have the same basic configuration of driveline, which consist of engine, clutch or torque converter, gearbox, propeller shaft, differential, drive shaft, and wheels, as shown typically in Figure 2.1. Models of these

components have been developed. Some recent works on driveline modelling of normal vehicles can be found in (Fredriksson, 2006; Grotjahn *et al.*, 2006; Lu and Hedrick, 2005; Lucente *et al.*, 2005). However, in the context of driveline modelling for skid-steering vehicles has not attracted much research.

2.1.1 Engine

There are many approaches in the modelling of a spark ignition (SI) engine. The simplest way is to consider it as a torque producer. Torque generated from a combustion engine is modelled either as a function of throttle position (Zanasi *et al.*, 2001) or a function of the amount of fuel injected into the engine (Hendricks and Sorenson, 1990; Kiencke and Nielsen, 2000). This torque, after overcoming the internal friction and external load, is then applied to an inertia moment, representing the flywheel (Figure 2.2). Speed at the engine shaft is obtained from the Newton's second law. This approach is often used for driveline modelling and control purpose as it does not require many experiments on the engine.

Crossley and Cook (1991) look into the details of an engine's operation and model it as a series of five components, based on the ideal gas law and experiments. In the throttle body, the mass flow rate of air taken to the manifold is described as an empirical function of the throttle position and manifold pressure. From the ideal gas law, the manifold pressure is modelled by a differential equation of the amount of air into and out of the manifold, manifold volume and temperature. The mass flow rate of air at the output of the manifold (cylinder input) is expressed as an empirical function of the manifold pressure and the engine speed. For a four-stroke engine, the effect of the compression stroke is accounted for by a delay of 180^0 in the engine shaft rotation after the end of intake stroke. Again, torque produced by the engine is obtained by an empirical function of the mass of intake air, air to fuel ratio, spark advance, and the engine speed. Finally, the engine acceleration is obtained from the Newton's second law, similarly to the previous method. Although this approach can model some physical phenomena inside the engine, it relies too much on empirical experiments and can be only applied for a certain engine.

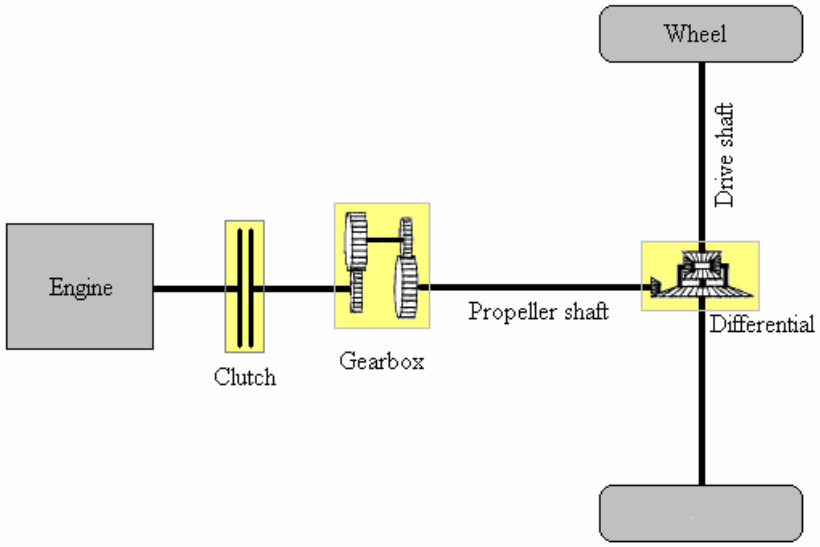

Figure 2.1 Basic driveline configuration

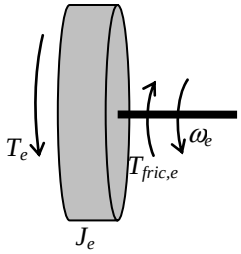

Figure 2.2 Simple engine model. T_e: generated torque, $T_{fric,e}$: load torque, J_e: engine inertia moment, ω_e: engine rotational speed

Another engine model, known as mean value engine model (MVEM), was developed by Hendricks and Sorenson (1990) and later refined in (Hendricks, 1997). In these works, the model consists of three main elements: fuelling dynamics, crank shaft dynamics, and manifold air dynamics. The fuel film flow model describes the details of fuel injection by differential equations. The crank shaft speed is still calculated from Newton's second law; however, the engine torque is obtained from combustion energy of the fuel with a certain value of efficiency applied. The manifold air pressure is still derived from the ideal gas law, but the air mass flow rates into and out of the manifold are completely different from those in (Crossley and Cook, 1991). The manifold air dynamics in (Hendricks, 1997) seems independent of the other components, while the air mass flow rate going out of the manifold is used to calculate the injected fuel in

(Deur *et al.*, 2003). Although these MVEMs are claimed to be more general than Crossley and Cook's model, they still require a lot of experimental verification.

2.1.2 Clutch

The clutch enables connecting or disconnecting the engine power to or from other components. Friction-based clutches are widely used, although there are many other types. For this type, the simplest model assumes it as stiff without power losses (in engaged mode) (Kiencke and Nielsen, 2000). When the transmitted torque is larger than the static friction torque of the clutch, it enters a slip mode and is modelled by kinematic friction (Balluchi *et al.*, 2005). For a wet clutch, additional viscous friction is taken into account (Deur *et al.*, 2005).

2.1.3 Gearbox

The gearbox in a mechanical system plays the role of an ideal transformer in electric circuits. It multiplies the transmitted torque at low gear ratios or increases speed at higher gear ratios depending on which is needed. Ignoring backlash, the relationship between speed and torque at the input and output of a gearbox can be derived from the gear ratio and the amount of torque required to overcome internal friction as well as gear acceleration (Kiencke and Nielsen, 2000).

2.1.4 Propeller shaft and drive shaft

The propeller shaft and drive shafts transfer rotation respectively from gearbox to differential, and from differential to wheels. If they are short and hard enough, they can be considered as stiff. It means that speed and torque at the output and input are the same. Otherwise, they are modelled as damped torsional flexibilities with stiffness and damping coefficients (Kiencke and Nielsen, 2000).

2.1.5 Differential

The differential, while transferring equal torque to each drive wheel, enables the left and right wheels to run at different speeds in turning to avoid slipping. However, in an Ackermann-steering configuration found in most cars and trucks, the differential has a

passive role in turning because the turning rate is mainly determined by the steering wheel angle. Therefore, the mechanism for that purpose is normally not considered in the modelling of a vehicle differential and it is described as the same way as a gearbox (Kiencke and Nielsen, 2000).

2.1.6 Wheels and vehicle

Ignoring the difference in rotational speeds, all drive wheels can be combined and modelled as one wheel. Newton's second law, both in the form of rotational and linear motions, is used to describe the wheel dynamics (Kiencke and Nielsen, 2000). The torque supplied from the vehicle differential through the drive shaft, after overcoming internal and external friction torques, provides the wheel acceleration. The external friction torque provides the force required for the vehicle to accelerate and overcome rolling resistance, air drag, and gravitational force.

2.1.7 Proposed approach for driveline modelling

In the driveline used for this project, only the engine, gearbox, and wheels are similar to those of cars and can be modelled by using the above approaches. Other components are sufficiently different to require a new and thorough development for modelling of all components involved in the UGV motion.

Figure 3.2 shows the driveline configuration used for the UGV under investigation in this thesis. Instead of a normal clutch, this driveline uses a Continuous Variable Transmission (CVT). It is a V-belt CVT which can change driver or driven clutch radius depending on acceleration or load. The mechanics of this component are complicated and will not be analysed in details in this thesis. Instead, it is modelled by a variable gear ratio which is simplified as a linear function of engine speed and load, based on experiment.

Different from that of a car, the differential used in this vehicle plays an active role in turning via left and right brakes in the skid-steering mode. Therefore, the mechanics which enables the differential's outputs to rotate at different speeds has to be taken into account. The difference in speed depends on the loading differences between the

outputs. In a steady turning scenario, the loading difference will balance the internal friction of the differential. Assuming this friction is mainly due to viscosity, the difference in speed can be obtained. Two outputs of the differential are connected to the wheels by the chain system. Ignoring backlash and assuming the chains are stiff, they can be modelled as a constant gear ratio.

In driveline models used for cars and trucks, torque is normally transferred from engine through other components to wheels (Deur *et al.*, 2005; Kiencke and Nielsen, 2000; Zanasi *et al.*, 2001). At each component, the net torque after overcoming loads on the component is used to calculate the speed. However, the method is not applicable for this UGV driveline because of the CVT component. It requires both the input speed and the load on output to determine the CVT gear ratio and its output speed. Therefore, a different approach is proposed, as shown in Figure 2.3. The engine speed is transferred through CVT, gearbox, differential, and chains to the wheels. Total loads at each wheel sides, consisting of rolling resistance, gravitational force, and the load required for the vehicle acceleration, are referred to the outputs of the differential. At the differential, they are combined with braking forces to derive the difference in speed. Total load at the differential is then transferred back to the CVT through the gearbox. At the CVT, this load is used to update the CVT gear ratio. The feedback load from CVT input decides the engine speed.

2.2 Vehicle control

In the first stage of the development, the original vehicle driveline is equipped with actuators and sensors which require suitable controllers. At the low level, the throttle position and brake efforts need be controlled. The motion controllers to be developed have to be able to track the vehicle velocity and turning rate references, as shown in Figure 2.4. Numerous techniques have been proposed for control design, including traditional PID control (see, Ioannou and Xu, 1994; Yanakiev and Kanellakopoulos, 1996; Kuang *et al.*, 1999; Deur *et al.*, 2002; Deur *et al.*, 2004; Tanelli *et al.*, 2006) and modern sliding mode control (Maciuca and Hedrick, 1995; Yokoyama *et al.*, 1998; Rossi *et al.*, 2000). At a higher level, pure pursuit controllers are usually applied for

vehicle path following control (Murphy, 1992; Kelly, 1994; Murphy, 1994; Durrant-Whyte, 2001; Hogg *et al.*, 2002). This issue is, however, beyond of the scope of this thesis.

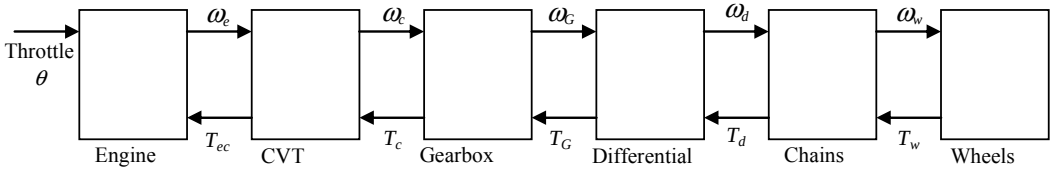

Figure 2.3 Driveline modelling diagram

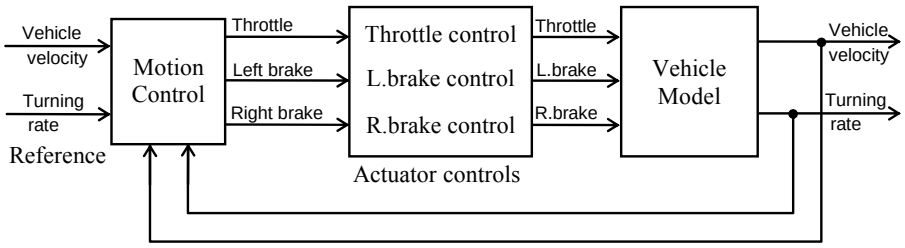

Figure 2.4 UGV control requirements

2.2.1 PID controller

To date, the classical PID control is still popular in industry because it is a general-purpose controller and does not require complex design procedures (Wang *et al.*, 1999). In this project, the PID control scheme is the first deployed for all controlled variables. However, there are many components of the vehicle that exhibit nonlinearities and time delays which lead to high overshoots in the responses when using conventional PID control.

In control engineering it is well known that the performance of PID control system can be improved by properly tuning their parameters. Many methods for tuning PID controllers are available, ranging from manual to auto-tuning. Most tuning methods focus on obtaining reasonable responses conforming to such performance criteria as stability, rise-time, and settling-time. However, there has been less attention paid to the reduction of overshoots, especially for time-delay systems.

Figure 2.5 shows a typical PID control system. Based on knowledge of characterizing effects for each control parameter, engineers can adjust the proportional (K_P), integral (K_I), and derivative (K_D) gains until a desired response is obtained. However, this manual method is time-consuming and not always yields a desired response because changing one parameter may affect the performance designated by other two parameters. To speed up the tuning process, a number of auto-tuning methods have been proposed (see, for example, Aström and Hagglund, 1995; Besharati Rad *et al.*, 1997; Shen, 2001; Visioli, 2001; Cominos and Munro, 2002; Karimi *et al.*, 2003; Gaing, 2004; Tan *et al.*, 2007). Among them, the pioneer Ziegler-Nichols approach has been the most popular (Ziegler and Nichols, 1942).

Ziegler and Nichols proposed two methods for auto-tuning of PID controllers. In the first one, controller parameters are calculated from an open-loop response of the process to a step input (called the process reaction curve). In the second one, both K_I and K_D are set to zero while K_P is increased gradually until the system oscillates. The period of the oscillation (called the ultimate period) and the K_P value (called the ultimate gain) are used to calculate the desired controller parameters. The Ziegler-Nichols rules help to speed up the tuning process. However, they are not practical in many situations where experiments with open-loop or instable closed-loop systems can damage the plant itself (Cominos and Munro, 2002). To avoid this problem, many techniques such as relay feedback (Yu, 1999), approximate system identification (Hang *et al.*, 1984), and cross-correlation (Hang and Sin, 1991) have been developed to estimate the ultimate gain and ultimate period in Ziegler-Nichols rules.

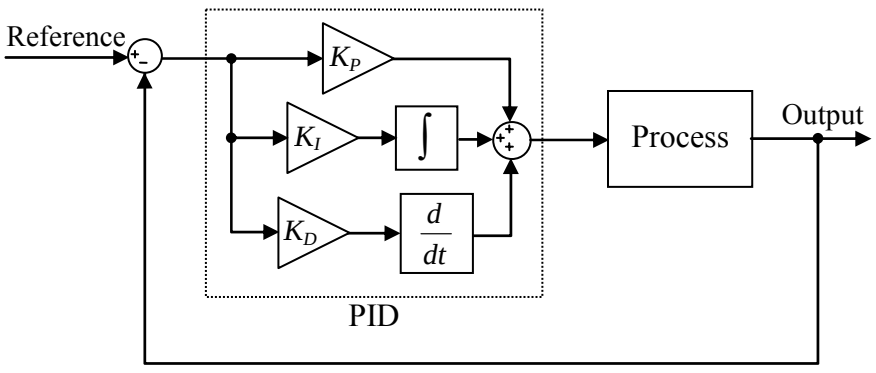

Figure 2.5 PID controller configuration

It is well known that the control performance obtained by the Ziegler-Nichols tuning methods are acceptable at best and the controller parameters need to be fine-tuned to provide the desired response (Franklin *et al.*, 2002). This is because they are based on a quarter amplitude-damping criteria to obtain reasonable responses in order to compromise between settling time and stability (Aström and Hagglund, 2004). The quarter decay corresponds to a damping ratio of 0.21 and leads to an overshoot of around 50%, as shown in Figure 2.6. Hang *et al*. (1991) proposed a method to reduce the overshoot from Ziegler-Nichols tuning rules. Using the set-point weighting, this method can reduce the overshoot to 10% or 20%, depending on the type of application. However, this still appears inadequate for the UGV motion, which appears to be subject to nonlinear uncertainties and input time-delay.

For integral processes with time delay such as actuator position control and braking control system, Zhang *et al*. used H_∞ performance criterion to optimize PID controller parameters (Zhang *et al.*, 1999). Therein, an extra parameter is introduced to adjust responses of PID controllers, and can result in a reduction of overshoot from 58% to 22%. As a trade-off, the settling-time is, however, increased subsequently from 6 to 20 time delay periods.

When single-loop PID control systems cannot satisfy the control requirements, cascade PID control systems are often used, especially in electric drive control (Cho *et al.*, 2002; Kaya, 2001; Kaya and Atherton, 2005; Lee and Oh, 2002). In general, a cascade control system has several nested control loops, as shown in Figure 2.7. The design procedure begins with the inner-loop to derive a suitable controller K_2, then the inner- loop is replaced equivalently by its corresponding closed-loop transfer function and the procedure continues with the design of controller K_1 for outer-loop taking into account this equivalent transfer function of the inner-loop. Cascade control has many advantages compared with single-loop control (Tan *et al.*, 2005), especially with complex processes. In (Zhuang and Atherton, 1994), both optimization and auto-tuning methods are used for tuning cascade control systems. The results show that a cascade control system gives better responses with shorter settling time and smaller overshoot compared with its single-loop control option.

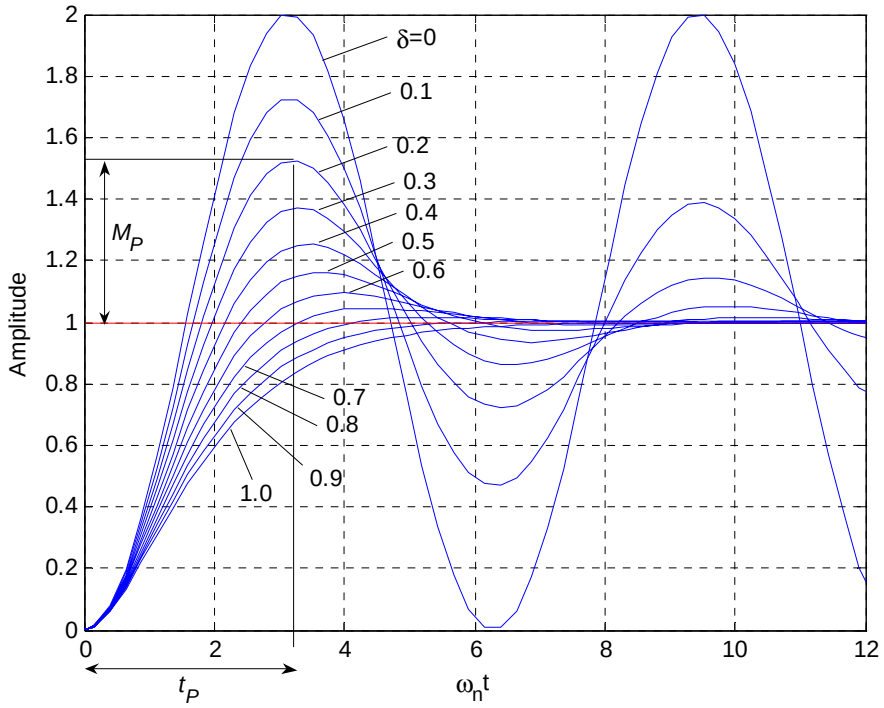

Figure 2.6 Step responses of second-order systems with different values of damping ratio (δ)

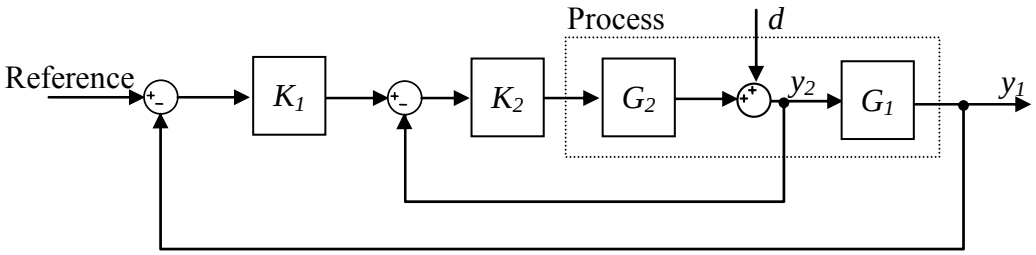

Figure 2.7 Cascade control system

2.2.2 Sliding Mode Controller

The idea of variable structure control with sliding modes was first introduced in the Soviet Union in the early 1960's and appeared worldwide after the mid 1970's. Since then, the idea has attracted many researchers around the world and several developments have been made for nonlinear systems, MIMO systems, discrete-time, large scale and infinite-dimensional systems (Hung *et al.*, 1993). In the past two decades, applications of sliding mode control have been widely found in the literature

for controlling motors (Utkin, 1993), robots, automobiles, aircraft, spacecraft (Hung *et al.*, 1993), and underwater vehicles (Yoerger and Slotine, 1987).

The basic idea of sliding mode control is to force the system trajectory towards a sliding surface (in the reaching mode) and keep it on this surface (in the sliding mode) by a switching rule. Figure 2.8 presents a typical schematic diagram for a n^{th} order control system. The sliding surface (S) is designed so that once the system trajectory is on the surface desired features such as stability and tracking performance are achieved (Hung *et al.*, 1993).

A sliding mode controller (SMC) has many desirable features. First of all, the order of the system is reduced during the sliding mode. Desired control performances are therefore easier to obtain as compared to the original system. In addition, the robustness property of SMC can effectively deal with nonlinearity, modelling and disturbance uncertainties (Slotine and Li, 1991).

In order to design a SMC it is required, however, to have a priori knowledge of the system. At least, an approximate model of the system and the bounds of the approximation must be known to enable the design process. In addition, the effort to keep the system trajectory on the sliding surface can result in undesirable chattering. Lastly, SMC is sensitive to time-delay.

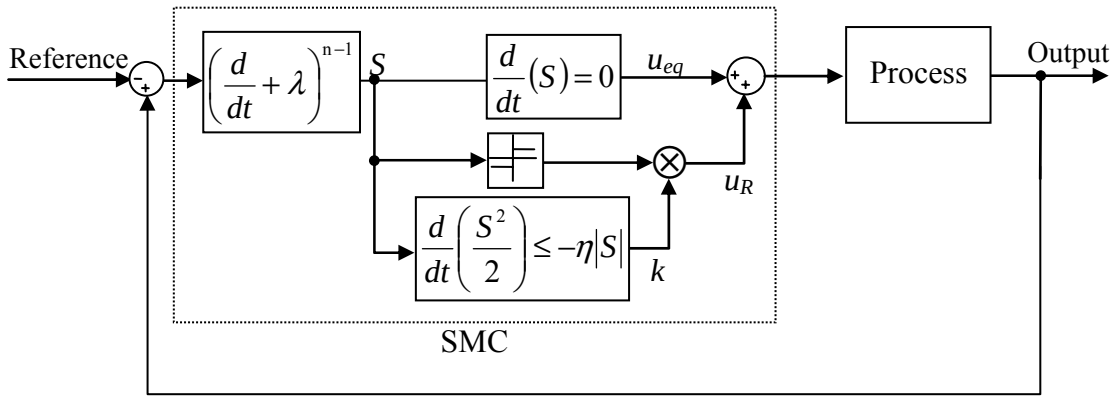

Figure 2.8 Schematic diagram of sliding mode controller for an nth order system

2.2.3 Methods for time-delay system treatment

The presence of time-delay in a system can make the control performance vulnerable and deviated from the desired features. Many methods for time-delay treatment can be found in the literature (Richard, 2003). Two major approaches are described in the following.

The first approach is, broadly, to truncate a delay of an infinite order to a finite one. It includes Taylor series expansion (Camacho *et al.*, 1999), Padé approximation (Wang and Hu, 1999), Fourier-Laguerre series representation (Partington, 1991), and Kautz approximation (Makila and Partington, 1999). However, it is difficult to choose the right order for the approximation. In some cases, the approximation error can lead the system to unstable states (Richard, 2003).

The other broad approach is based on prediction techniques. In general, a new variable is introduced to transform the delay system to a non-delay one. Techniques include, for example, Artstein model reduction (Artstein, 1982) for input-delay systems, and other developments for state-delay systems (Fiagbedzi and Pearson, 1986). Despite difficulties in computation, these techniques are widely used to compensate for the effects of time-delay (Richard, 2003).

2.2.4 Proposed controller

In this thesis, the PID and Sliding Mode Control strategies are combined in a cascade control configuration in which PID controller is incorporated in the inner loop coupled with SMC at the outer loop, as shown in Figure 2.9. The proposed controller is based on the following remarks:

- Closed-loop response of the system with a PID control loop exhibits a large overshoot, which may be considered equivalently as that of a second order function. Therefore, although the system may be unknown, the PID closed-loop system can be modelled by a second-order transfer function. Effects of nonlinearity can then be accounted for by changing coefficients of the second-order function.

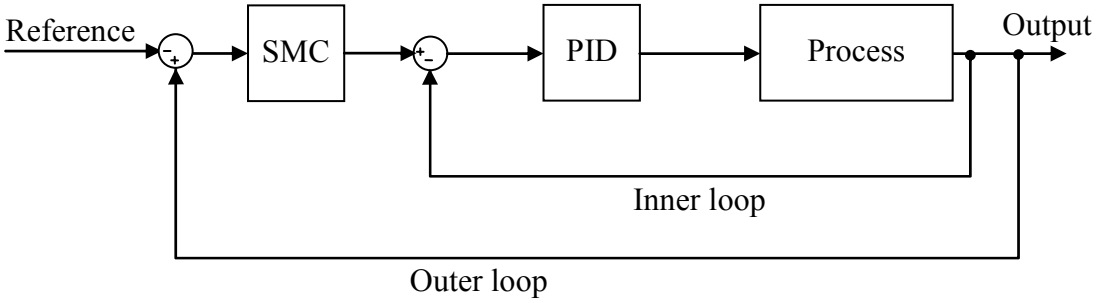

Figure 2.9 Configuration of SMC-PID controller

- SMC by its nature can reduce the equivalent second-order closed-loop system to a first-order one. This means that overshoot can be eliminated, in principle.

- Robustness of SMC can be achieved by its well-recognised ability to overcome modelling errors, nonlinearity, external disturbances and other uncertainties.

The proposed design procedure contains three steps. In the first step, the desired settling time and steady-state error of the output are obtained by tuning the parameters of a PID controller while overshoot is not considered. Based on the closed-loop response obtained, a second-order model with input time delay is derived to represent equivalently the system dynamics. Using this approximate model, a SMC is designed to shape the input to the PID-controlled system to achieve the system robustness and to suppress overshoots in its responses. An output predictor in (Young-Hoon and Jun-Ho, 2000) is employed to estimate the system output for implementation of the equivalent control, taking the effect of time delay into account.

2.3 Vehicle-terrain interaction

Knowledge of the vehicle-terrain interaction is desirable for predicting behaviours of the vehicle navigating on different terrains, as well as for safe and effective motion control. In the context of vehicle-terrain interaction, the behaviour of tracked vehicles is quite well understood; see, for example, (Wong and Chiang, 2001) for a comprehensive theory for skid-steering mechanics. For skid-steering wheeled vehicles, however, it seems there is less work available in the literature for a comprehensive analysis of the complicated processes involved. In (Weiss, 1971), the mechanics of skid-steering for

wheeled vehicles in steady manoeuvres are analysed. He used lateral forces to calculate vertical loads acting on each row of wheels and then assumed that these loads are distributed equally to all wheels in the row. Consequently, the shear stress developed at each wheel is derived from the load on that wheel. Creedy (1985) later extended Weiss's idea by considering the difference of vertical loads on the wheels in a row due to their positions and torque transitions. However, in both works, the shear stress acting on each wheel is assumed to obey Coulomb's friction law. This implies that the shear stress can change immediately from zero to its maximum value when the wheel begins its motion on the ground. In contrast, experiments have shown that the shear stress follows an exponential function of the shear displacement between the wheel and the ground and only attains its maximum value after a certain shear displacement has occurred in the ground. This remark is illustrated in Figure 2.10, after (Wong, 2001). In addition, the requirement for constant velocities is not always true for operations of an unmanned ground vehicle in practice.

In this thesis, the vehicle-terrain interaction will be thoroughly analysed, based on the theory of terramechanics (Bekker, 1956; Wong, 2001), and kinetic equations of the skid-steering wheeled vehicle. In general, the analytical relationship between shear stress, shear displacement, and vertical load is used to derive reaction forces. The load on each wheel is determined depending on the position of each wheel of the vehicle. The shear displacement is obtained by taking integrals of the slip velocity of the considered point of each wheel which is in contact with the ground. The shear displacement is then used to derive the magnitude and direction of the shear stress acting at the contact point. The shear stress over the contact zone is further integrated to obtain the reaction forces, i.e. the forces on each wheel reacted by the ground. The vehicle performance during contact with different terrain types can then be predicted by making use of the vehicle kinetics.

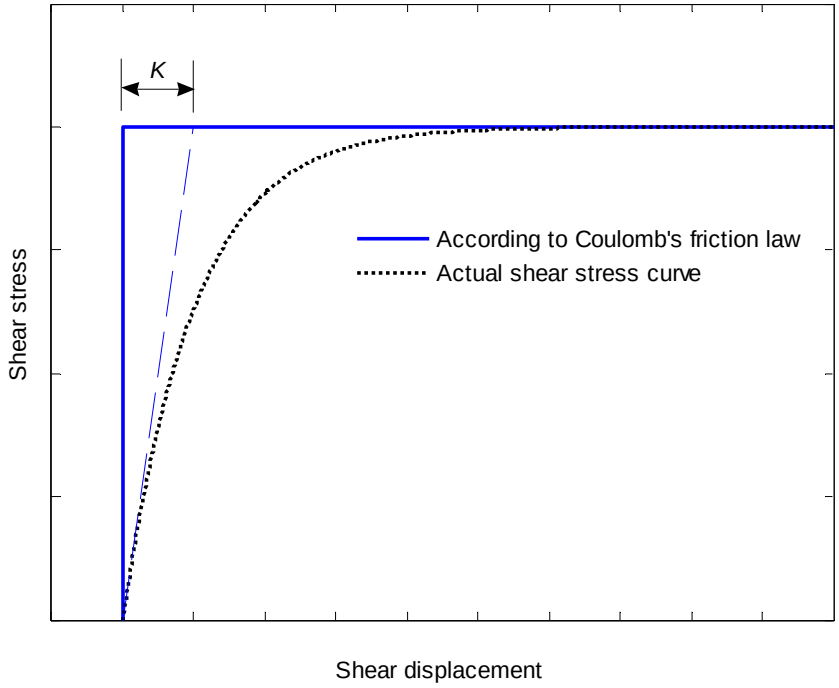

Figure 2.10 Shear stress-shear displacement relationship (Wong, 2001)

2.4 Fast algorithm for terrain interaction analysis

In the above approach, computation of the integrals appearing in the terrain interaction analysis is time-consuming. This makes the approach not suitable for online applications. Therefore, a fast algorithm is desired for the terrain interaction analysis. In (Shibly *et al.*, 2005), a linearisation of the normal stress and shear stress is used to avoid integration. Normal stress is approximated by lines through the start and the end points of each stress curve, as shown in Figure 2.11 (a) and (c). This leads to a large error in the linearisation; and therefore, results in inaccurate analysis. In this thesis, Shibly's method is modified to improve the accuracy of the approximation. A stress curve is also approximated by a line going through the maximum stress point (start point) on the curve. However, the other intersection point between the stress and its linearisation is deliberately chosen so that the largest effect of the stress on the vehicle behaviour will remain the same. This advantage is illustrated in Figure 2.11 (b) and (d). The proposed method ensures that the error of the approximation is always minimized.

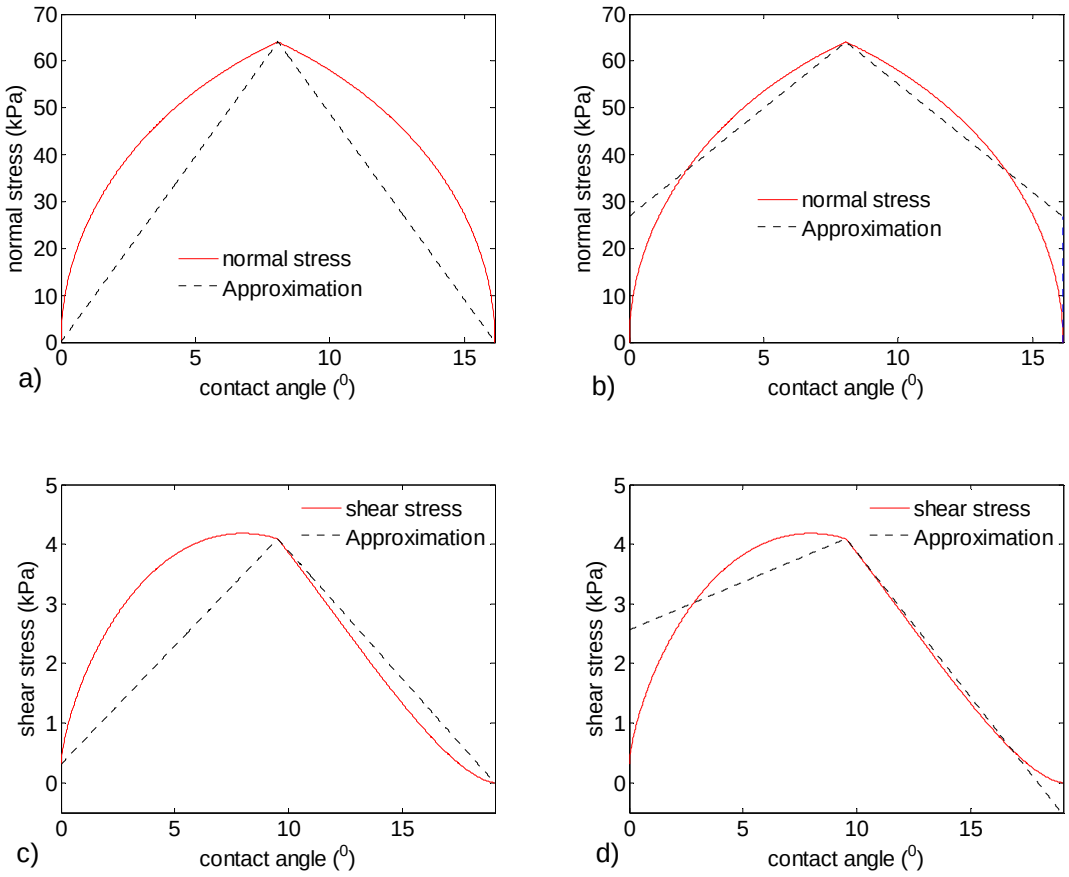

Figure 2.11 Stress approximation used in the present work: a), c) Shibly's method; b), d) modified method

2.5 Conclusion

This chapter has reviewed the relevant literature related to mobility control and analysis for UGVs. It has focused on driveline modelling, low-level robust control technique, and terrain interaction analysis. The details of these approaches will be presented in the following chapters.

Chapter 3

Vehicle driveline and modelling

In this chapter, all components in the vehicle driveline are analysed and modelled for the control design and for the development of a vehicle simulator. An introduction to the vehicle platform is given in Section 3.1. The model is developed in Section 3.2. Simulation is conducted in the next section. A simplified model is described in Section 3.4 and verified by experiment data. Finally, a conclusion is drawn in the last section.

3.1 Introduction

The UGV used as a demonstrator for outdoor autonomy and as a testbed in this thesis is retrofitted from the ARGO Conquest 8x8, a 20hp, 3m x 1.45m x 1.1m, 0.5 tonne vehicle. It can achieve 30km/h on land and 3km/h on water. Figure 3.1 shows a photo of the ARGO developed at CAS, Sydney. Equipped with eight drive wheels in a skid-steering configuration, this platform is very suitable for all-terrain mobility which is a desirable feature of the UGV.

Figure 3.2 shows the driveline of this vehicle. The power transmission system includes a spark ignition (SI) engine, continuous variable transmission (CVT), gearbox, differential, and a chain system. In the figure, notations T, ω, and K represent the torques, rotational speeds, and gear ratios at respective components.

The vehicle has eight 22x10.0 inch wheels, connected together by the chain system and driven by the left and right outputs of the differential. Two brake discs are attached to the outputs of the differential and can be operated separately. The differential and the brake system decide the turning of the vehicle in skid-steering.

This driveline of the vehicle is equipped with rotary encoders to allow for measurement of the engine speed, gearbox input speed, and left and right wheel speeds. The engine throttle, left brake and right brake can be controlled separately by suitable actuators. Inputs to these actuators are deliberately set from 0 to 100% of their rated capacities.

The vehicle represents a highly nonlinear and dynamically coupled complex system. For control purposes, it is therefore essential to find a simplified and useful model for the vehicle, which is the objective of this chapter. Some parts of the modelling have to use data collected from trial tests. The model is tested on Matlab/Simulink and the simulation results are also compared with data obtained from characterising experiments.

Figure 3.1 The vehicle platform

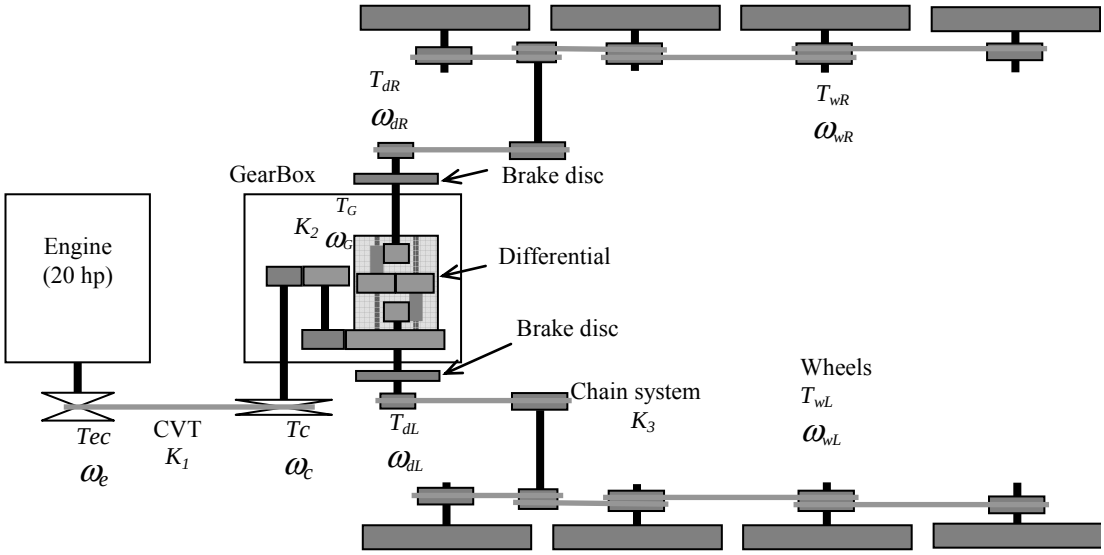

Figure 3.2 Driveline of the vehicle

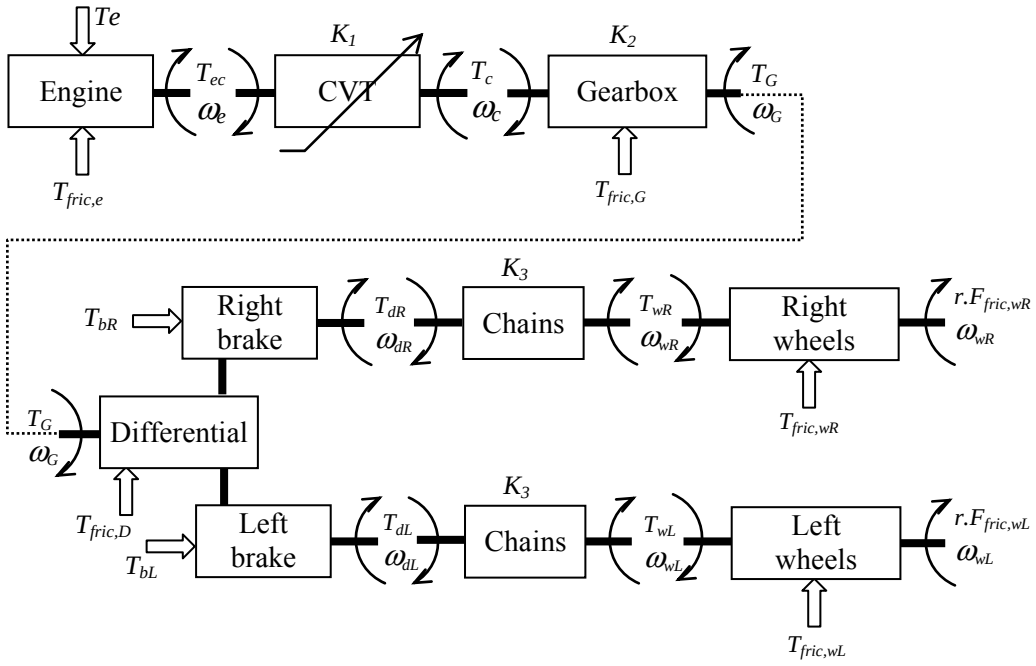

Figure 3.3 Subsystems of the driveline

3.2 Modelling of the vehicle driveline

The driveline of the vehicle consists of the engine, CVT, gearbox, differential (within the gearbox), chains, and eight wheels. Figure 3.3 shows the subsystems of the driveline with their distributed torques and speeds. It is noted that the models of the engine, CVT, gearbox, and chains are independent of the braking subsystem. To derive the wheel speeds, the model of the differential-wheel system should, however, take into account the applied braking torques.

3.2.1 Engine

This vehicle uses Kawasaki FD620D, a 620 cc, 20 H.P, V-twin 4 cycle SI engine. Figure 3.4 shows a photograph of the engine and its performance characteristics. The engine can be modelled by combining dynamics of its components including throttle body, intake manifold, mass flow rate, compression and torque generation (Crossley and Cook, 1991; Hendricks and Sorenson, 1990). For control purposes, it is not necessary to look into details of the engine dynamics. Indeed, experiments show that the generating torque, T_e, of a combustion engine can be modelled as a first-order transfer function (Zanasi *et al.*, 2001),

$$T_e = \frac{K_e}{\tau_e s + 1}\theta_e, \tag{3.1}$$

where θ_e is the throttle position, K_e and τ_e are respectively the engine gain and time constant.

The engine motion equation is then

$$J_e\dot{\omega}_e = T_e - T_{fric,e} - T_{ec}, \tag{3.2}$$

where J_e is its moment of inertia, including flywheel, crankshaft, and CVT driver clutch; $T_{fric,e}$ is the torque due to friction inside the engine; and T_{ec} is the load torque from the CVT acting on the engine.

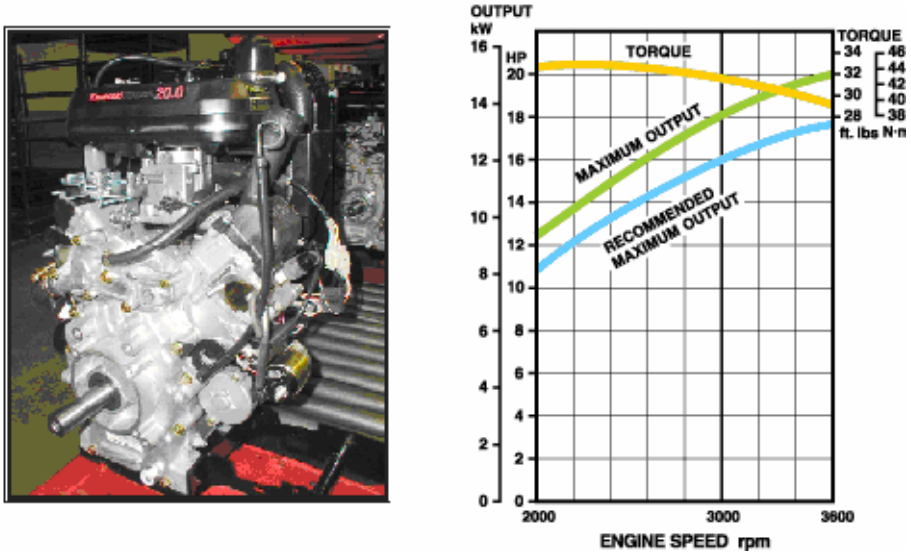

Figure 3.4 Kawasaki FD620D engine and performance curves (Source: (Kawasaki, 2004))

3.2.2 Continuous variable transmission

The vehicle uses an automatic torque converter known as a continuous variable transmission (CVT). It consists of a driver clutch located on the engine output shaft, a driven clutch located on the input shaft of the gearbox, and a drive belt. Figure 3.5 shows details of the CVT with its main components described in Table 3.1. Both clutches comprise of a fixed face and a movable face. In acceleration, the driver clutch movable face travels towards the fixed face as the weights in the clutch are pushed outwards due to the centrifugal force. As the driver clutch faces get narrower, they grip the drive belt and move it towards the top of the driver clutch. At the same time, the driven clutch plates spread apart as the belt rides down between the faces. The tension in this clutch is also regulated by a spring. As the engine comes under load, the spring loaded cam on the driven clutch forces the clutch plates together.

The driver clutch can therefore be considered as a pulley whose radius is increased when accelerated, resulting in an increase of the output speed. Similarly, when the engine is under load, the driven clutch increases its radius and more torque can be transmitted to the wheels. At the engine idle speed, the centrifugal force is not enough to overcome the spring load between driver clutch faces and the clutch is completely disengaged. It is only engaged after the engine reaches a certain speed, in the manner of

a conventional centrifugal clutch. Assuming that no slip occurs between the belt and clutch when it is engaged, the CVT can be modelled as a variable gear ratio, which depends on the engine speed and load torque (Setlur *et al.*, 2003),

$$K_1 = f(\omega_e, T_c), \tag{3.3}$$

where *f*() is a function to be estimated from experiments.

The torque and speed at the output of the CVT are thus given by:

$$\begin{aligned} T_c &= T_{ec} / K_1, \\ \omega_c &= \omega_e K_1. \end{aligned} \tag{3.4}$$

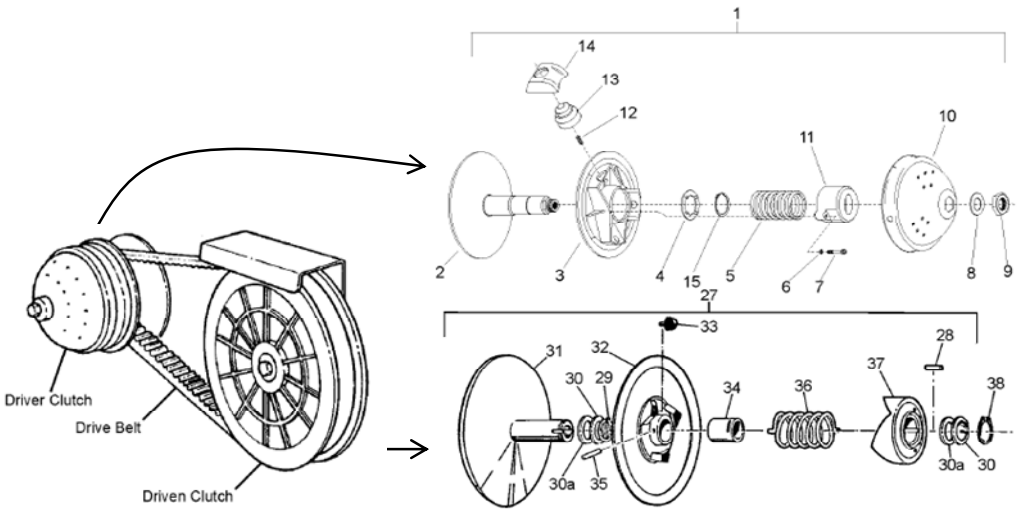

Figure 3.5 CVT and its components (Source: (Ontario Drive & Gear, 2007))

TABLE 3.1

CVT'S MAIN COMPONENTS

Driver clutch		Driven clutch	
Reference	*Description*	*Reference*	*Description*
2	Fixed face	31	Fixed face
3	Movable face	32	Movable face
5	Spring	36	Spring
13	Weight	37	Cam

3.2.3 Gearbox

The gearbox has four positions, namely Reverse - for backing up the vehicle; Neutral - for starting the engine or idling; Low - for use when extra pulling power or very low speed is required on rough terrain; and High - for general use at normal operating speeds. The output of gearbox engages directly to the case gear of the differential. Therefore, the differential's case can be considered as the output of the gearbox when calculating the gearbox ratio, K_2.

$$K_2 = \begin{cases} -0.1295, & \text{Reverse} \\ 0, & \text{Neutral} \\ 0.1295, & \text{Low} \\ 0.2655, & \text{High} \end{cases} \tag{3.5}$$

where the numerical values for K_2 are derived from the number of teeth of each gear in the gearbox.

The torque and speed at the output of the gearbox are

$$\begin{aligned} T_G &= \left(T_c - T_{fric,G}\right)/K_2, \\ \omega_G &= \omega_c K_2, \end{aligned} \tag{3.6}$$

where $T_{fric,G}$ is the friction torque in the gearbox.

3.2.4 Chains

Ignoring backlash, the chain system can be simplified as a gear ratio K_3, calculated from the number of teeth of each sprocket in the chain system, giving

$$K_3 = 0.2483\,. \tag{3.7}$$

The wheel torques and speeds depend on the braking torques applied on the left and right wheels.

3.2.5 Differential - wheels

Figure 3.6 shows the structure of the differential. It is a planetary gear system consisting of two sun gears, six planet gears and a case. The left sun gear engages with three left planet gears, which, in turn, engage in right planet gears. The right sun gear engages with the right planet gears. All the planet gears are carried by the case. The case spins at speed ω_d (or ω_G because the case is considered as the output of gearbox). If the load torques on the left and right sun gears are equal, the two outputs of the differential will have the same speed as the case. Otherwise, they are different.

The differential distributes the torque from the gearbox to the left and right wheels. The two driving shafts of the differential are attached to the left and right brake discs. The torque difference enables the vehicle to turn. It is necessary to consider the differential in two cases when the vehicle is straightly running and when the vehicle is turning.

During straight-line running, the torque from the gearbox is distributed equally for the left and right wheels. Total loads on the left and right outputs of the differential the same. The differential is in a balance mode in which there is no relative motion between the case and two sun gears. All wheels have the same speed and therefore are modelled as one wheel. One can derive

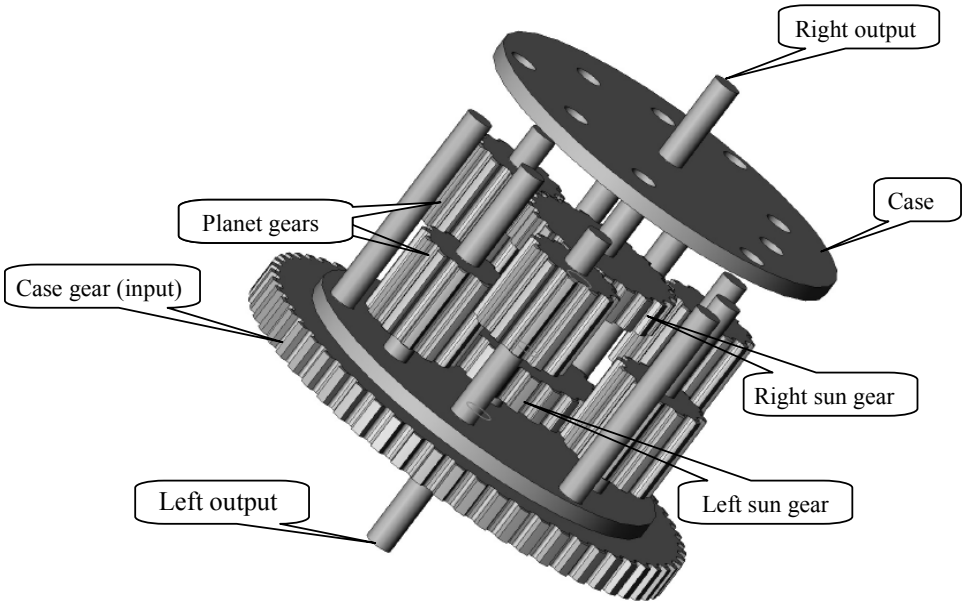

Figure 3.6 Differential configuration

$$\begin{aligned} T_{dL} &= T_{dR}, \\ T_{dL} + T_{dR} &= T_d = T_G - T_{fric,D}, \\ \omega_{dR} &= \omega_{dL} = \omega_d = \omega_G, \end{aligned} \tag{3.8}$$

where $T_{fric,D}$ is the differential friction load.

The wheel torque and speed, obtained after the chain system, are as follows

$$\begin{aligned} T_w &= T_d / K_3, \\ \omega_w &= \omega_d K_3. \end{aligned} \tag{3.9}$$

Now let us assume that the vehicle with mass m and longitudinal velocity V_X (at the centre of mass) is travelling on a flat terrain of a slope angle, χ, as shown in Figure 3.7. The force equation can be derived from the Newton's second law in the longitudinal direction as:

$$F_{t,w} = m\dot{V}_X + F_{wind} + F_R + mg\sin(\chi), \tag{3.10}$$

where $F_{t,w}$ is the traction force at the wheel, F_{wind} is the air drag force, F_R is the rolling resistance, and g is the gravitational acceleration.

The air drag force, F_{wind}, can be ignored as the vehicle runs at low speed.

The rolling resistance is determined by,

$$F_R = m(c_{r1} + c_{r2}V_X), \tag{3.11}$$

in which c_{r1}, and c_{r2} are friction coefficients depending on the tyres and road conditions (Kiencke and Nielsen, 2000).

The total load torque acting on the wheel shaft includes the torque required for traction, the torque due to internal friction, and the torque for wheel acceleration,

$$T_w = J_w\dot{\omega}_w + T_{fric,w} + rF_{t,w}, \tag{3.12}$$

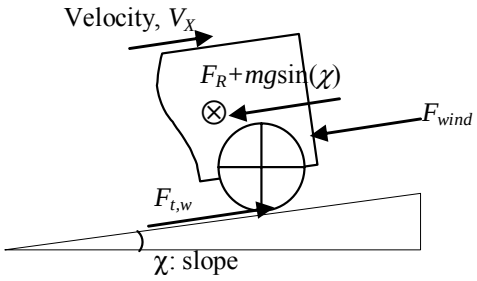

Figure 3.7 Longitudinal forces acting on the vehicle during straight-line running

where J_w is the wheel moment of inertia and $T_{fric,w}$ is the wheel internal friction load.

Substituting equations (3.10-3.11) into (3.12) gives

$$T_w = J_w\dot{\omega}_w + T_{fric,w} + mr\dot{V}_X + mr\left(c_{r1} + c_{r2}V_X\right) + mgr\sin(\chi). \tag{3.13}$$

Assume that no slip occurs between the wheels and the ground. In that case,

$$V_X = r\omega_w, \tag{3.14}$$

and equation (3.13) becomes,

$$T_w = \left(J_w + m.r^2\right)\dot{\omega}_w + T_{fric,w} + mr\left(c_{r1} + c_{r2}r\omega_w\right) + mgr\sin(\chi). \tag{3.15}$$

From equations (3.1-3.15) above, a block diagram for simulation is suggested in Figure 3.8, where the engine speed is transferred through CVT, gearbox, differential and chains to the wheels and the load torques from the wheels are referred backward to the engine shaft. Note that friction torques of the engine, gearbox, differential and wheels are modelled in this simulation as due to viscosity.

$$\begin{aligned} T_{fric,e} &= b_e\omega_e, \\ T_{fric,G} &= b_G\omega_C, \\ T_{fric,d} &= b_d\omega_G, \\ T_{fric,w} &= b_w\omega_w, \end{aligned} \tag{3.16}$$

where b_e, b_G, b_d and b_w are corresponding damping coefficients.

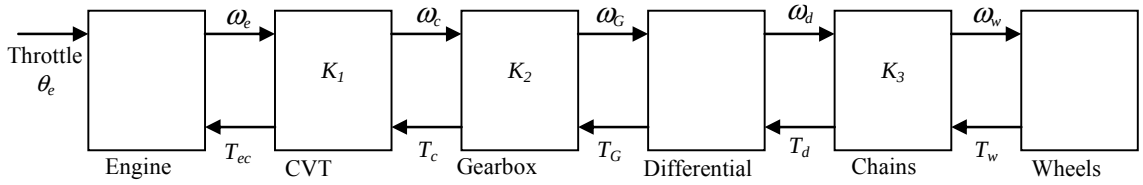

Figure 3.8 Simulation block diagram- during straight-line running

During turning, total loads on the outputs of the differential do not balance due to the braking effort or the load on the wheels. The left and right wheel speeds are different. The difference takes place at the outputs of the differential, chains and wheels.

It is assumed that longitudinal forces acting on the vehicle are distributed equally to the left wheels and right wheels. Applying equations (3.10), (3.12), and (3.13) to the left wheels and right wheels gives

$$\begin{aligned} T_{wL} &= \frac{1}{2}\left(J_w + mr^2\right)\dot{\omega}_{wL} + T_{fric,wL} + \frac{1}{2}mr\left(c_{r1} + c_{r2}r\omega_{wL}\right) + \frac{1}{2}mgr\sin(\chi), \\ T_{wR} &= \frac{1}{2}\left(J_w + mr^2\right)\dot{\omega}_{wR} + T_{fric,wR} + \frac{1}{2}mr\left(c_{r1} + c_{r2}r\omega_{wR}\right) + \frac{1}{2}mgr\sin(\chi), \end{aligned} \tag{3.17}$$

where $T_{fric,wL}$ and $T_{fric,wR}$ are respectively internal friction at the left and right wheel.

Torques and speeds for the chains in this case are,

$$\begin{aligned} T_{dL} &= T_{wL}K_3, \\ T_{dR} &= T_{wR}K_3, \\ \omega_{wL} &= \omega_{dL}K_3, \\ \omega_{wR} &= \omega_{dR}K_3. \end{aligned} \tag{3.18}$$

For the differential, let us first define the speed difference, $x = \omega_d - \omega_{dR} = \omega_G - \omega_{dR}$. The speeds at the left and right differential outputs are respectively

$$\begin{aligned} \omega_{dL} &= \omega_G + x, \\ \omega_{dR} &= \omega_G - x. \end{aligned} \tag{3.19}$$

When brake torques T_{bL} and T_{bR} are applied, the total load torques on the left and right sun gears are

$$\begin{aligned} T_{sL} &= T_{dL} + T_{bL}, \\ T_{sR} &= T_{dR} + T_{bR}. \end{aligned} \tag{3.20}$$

The total load on the case is

$$T_d = T_{sR} + T_{sL}. \tag{3.21}$$

The relative motion between the gears inside the differential causes a friction loss, which can be modelled as viscous damping. In steady state, this loss basically balances with the difference between the left and right load torques of the sun gears

$$T_{sR} - T_{sL} = b_{D,in} x. \tag{3.22}$$

Hence, one can approximate the speed difference as

$$x = \frac{T_{sR} - T_{sL}}{b_{D,in}}, \tag{3.23}$$

where $b_{D,in}$ represents viscosity inside the differential's case.

The simulation of the driveline during straight-line running is now based on the set of equations (3.1-3.7) and (3.17-3.23), according to the block diagram shown in Figure 3.9. Note that this model can be reduced to the previous one when total loads on the differential outputs are the same.

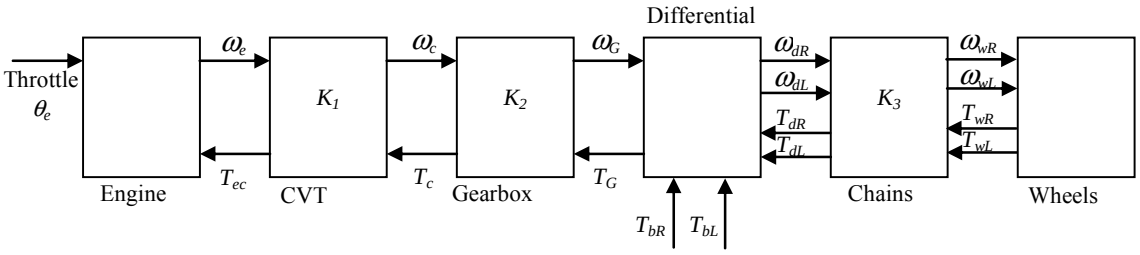

Figure 3.9 Simulation block diagram- during turning

3.3 Validation and simulation

3.3.1 Validation

In the above driveline model, the CVT is very complex to be modelled mathematically. Therefore, an experiment-based approach is used to derive the CVT ratio, K_1. Based on the data acquired from the input (engine speed) and output (gearbox speed) of the CVT when the vehicle runs about 15 minutes in a field test (Figure 3.10), a distribution of CVT ratio with engine speed is obtained (Figure 3.11). From this distribution, it is shown that the CVT ratio increases with engine speed and affected by the load from the gearbox. These relationships are shown in Figure 3.12 and Figure 3.13 with the total brake (left and right) and with estimated load, respectively. The load is estimated from the wheel speed and the brake data with the help of gearbox, differential, chain, and wheel models.

From Figures (3.11-3.13), it is suggested that the CVT ratio can be modelled by decoupling the effects of the engine speed and the load, as follows,

$$K_1 = f(\omega_e, T_c) = g(\omega_e).h(T_c), \tag{3.24}$$

where functions $g(\omega_e)$ and $h(T_c)$ describe the relationships with the engine speed and the load on the CVT.

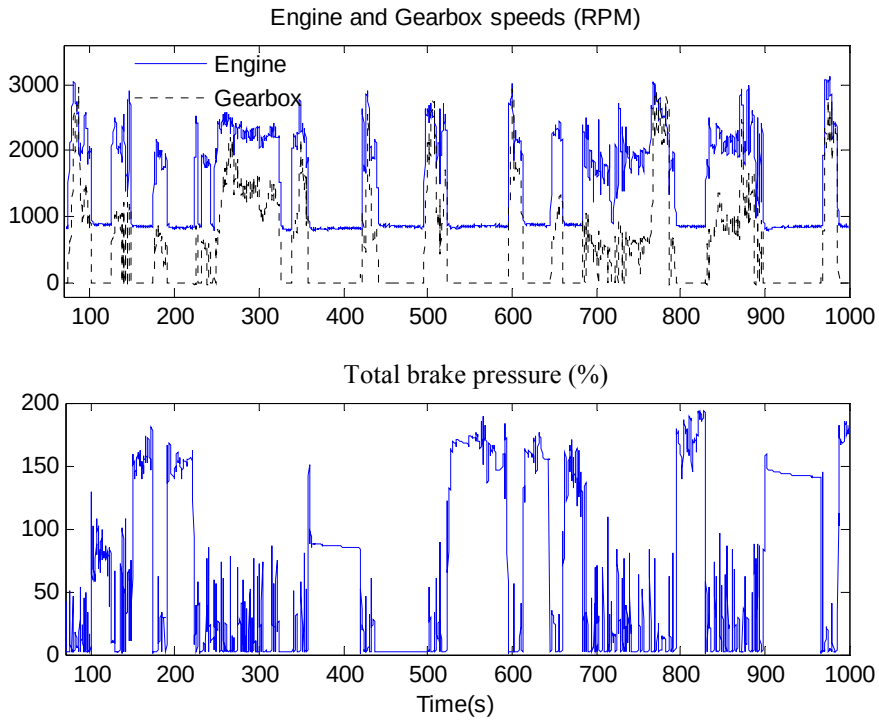

Figure 3.10 Experimental data collected from a field test

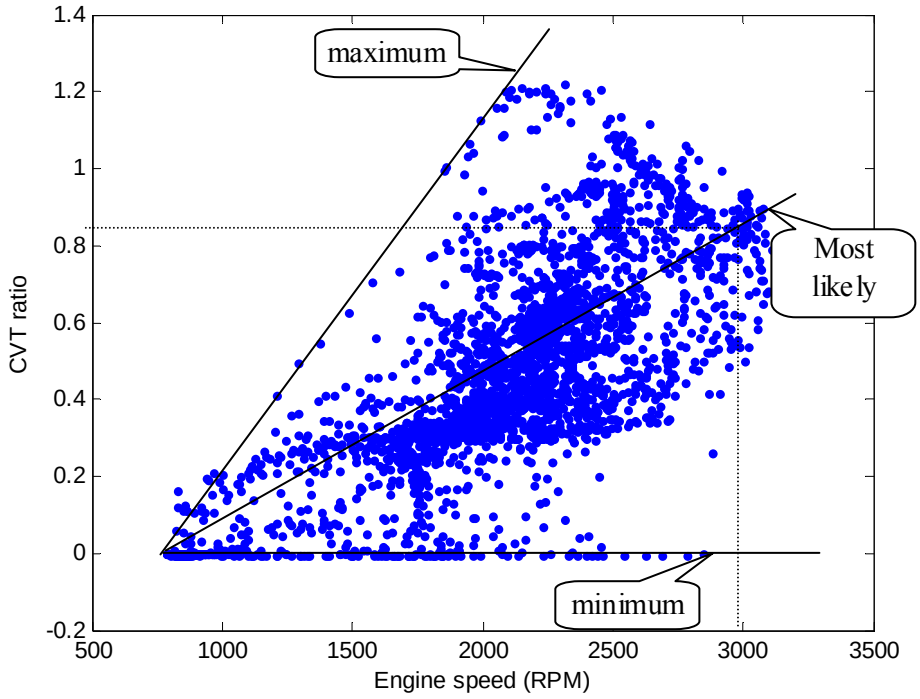

Figure 3.11 Distribution of the CVT ratio with the engine speed

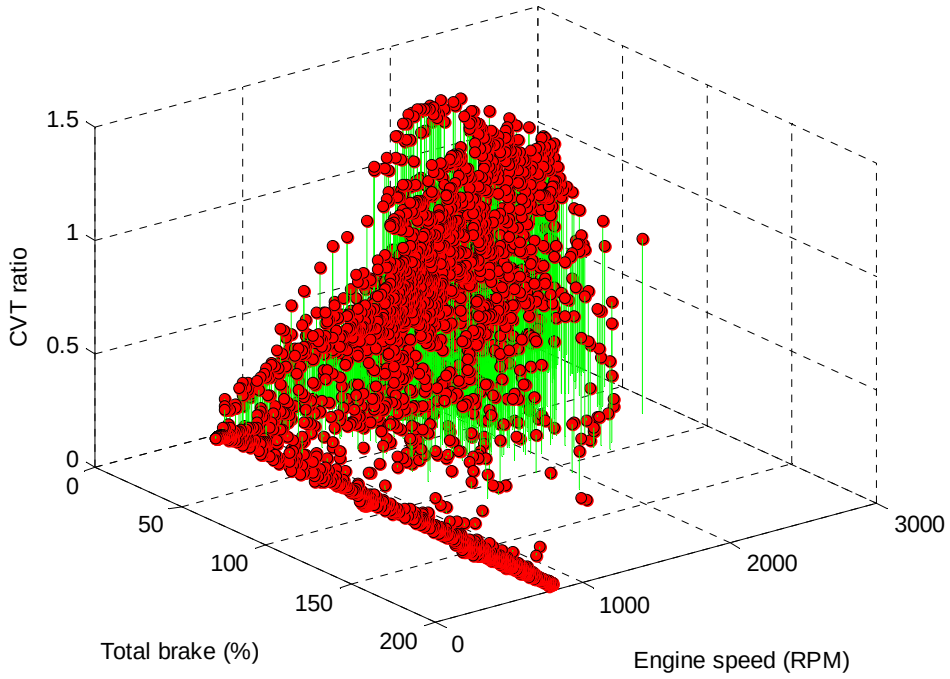

Figure 3.12 Distribution of the CVT ratio with the engine speed and total brake

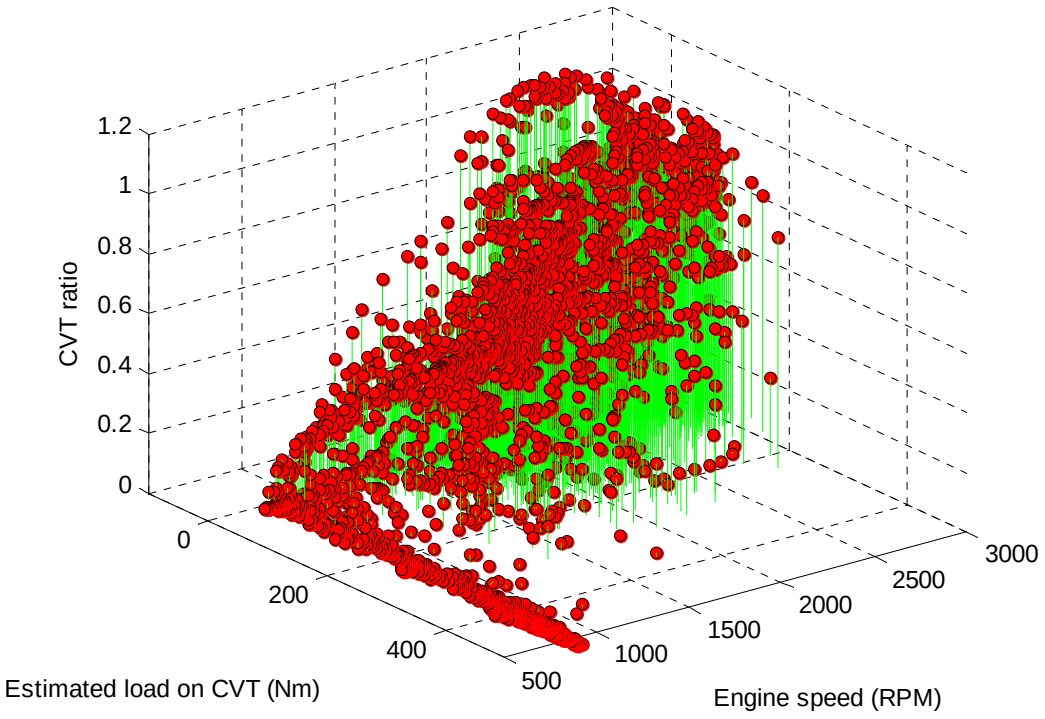

Figure 3.13 Distribution of the CVT ratio with the engine speed and estimated load

These relationships can be nonlinear and include belt slip and mechanical backlash. For simplicity, however, here they are approximated by following linear functions, chosen from the most populous areas in Figures 3.11 and 3.13,

$$g(\omega_e)=\begin{cases} 1/2500\,(\omega_e-850), & \text{if } \omega_e \geq 850\,\text{rpm} \\ 0, & \text{if } \omega_e \leq 850\,\text{rpm} \end{cases} \tag{3.25}$$

$$h(T_c)=\begin{cases} 1/500\,(500-T_c), & \text{if } T_c \leq 500\text{Nm} \\ 0, & \text{if } T_c \geq 500\text{Nm}\,. \end{cases} \tag{3.26}$$

The CVT ratio, described by equations (3.24-3.26), is drawn in Figure 3.14.

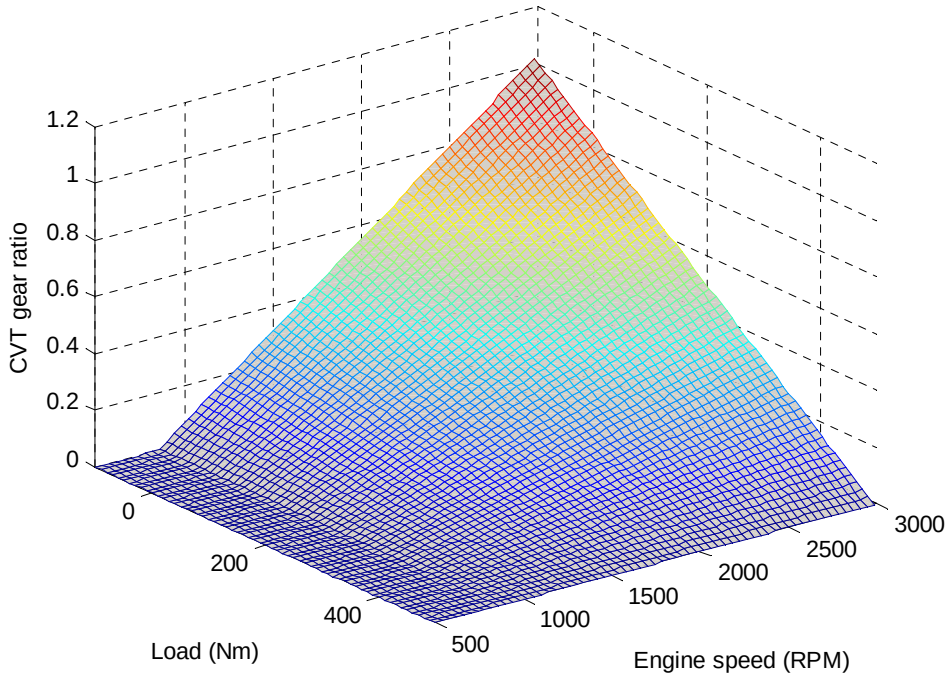

Figure 3.14 Linear approximation of the CTV ratio

Other numerical values for parameters used in the driveline simulation are listed in Table 3.2. The engine gain and damping coefficient are estimated from linearisation of the engine torque curve. The engine time constant is obtainted on average from experiment data. Engine moment of inertia and other damping coefficients are empirically chosen. Rolling resistance coefficients of a typical field road as given in

(Wong, 2001) are used here. Other parameters are provided in the vehicle datasheet, including weight of the vehicle and of each wheel, wheel radius, and gear ratios.

TABLE 3.2

PARAMETERS USED IN SIMULATION

Driveline component	**Nomenclature**	**Symbol and value**
Engine	Engine gain	$K_e = 0.5$ Nm
	Time constant	$\tau_e = 0.3$ s
	Moment of inertia	$J_e = 0.07$ kgm^2
	Damping coefficient	$b_e = 0.0026$ Nms
Gearbox	Damping coefficient	$b_G = 0.0955$ Nms
	Gearbox gear ratio	$K_2 = \begin{cases} -0.1295, & \text{Reverse} \\ 0, & \text{Neutral} \\ 0.1295, & \text{Low} \\ 0.2655, & \text{High.} \end{cases}$
Differential	Damping coefficient	$b_d = 0.00955$ Nms
	Damping coefficient inside	$b_{D,in} = 2.3873$ Nms
Chain	Chain gear ratio	$K_3 = 0.2483$
Wheel-body	Vehicle weight	$m = 490$ kg
	Wheel radius and weight	$r = 0.25$ m, $m_w = 6.6$kg
	Damping coefficient	$b_w = 0.04$ Nms
	Rolling resistance	$c_{r1} = 0.1$ m.s^{-2}
	Rolling resistance	$c_{r2} = 0.08$ s^{-1}

3.3.2 Simulation

In this section simulation results are shown for some interesting cases: step response of the throttle input, and turning the vehicle with step inputs of left and right brake. These signals are references to the actuator control systems for throttle and brakes. Here the throttle and brake control systems are modelled by first-order functions respectively without, and with, a time delay, estimated from responses of closed-loop systems in the next chapter.

$$G_{throttle} = \frac{\text{Throttle position}}{\text{Throttle setpoint}} = \frac{1}{0.07s+1},$$
$$G_{brake} = \frac{\text{Brake pressure}}{\text{Presure setpoint}} = \frac{e^{-0.2s}}{0.25s+1}. \tag{3.26}$$

Figure 3.15 presents the engine and gearbox speeds when running the simulated vehicle with 100% throttle position for 10 seconds (from t=5 to t=15s), turning right by applying 20% braking torque to the right brake for 10 seconds (from t=15 to t=20s), then turning left (from t=25 to t=30s) by applying 30% braking torque to the left brake according to the pattern shown in Figure 3.16. Responses of the engine and gearbox are similar to those of first-order functions. It can be seen that the gearbox speed is more load sensitive than the engine speed, as expected in automotive engineering. The transients of the engine speed and gearbox speed to a step response of the throttle exhibit a time delay of approximately 0.3 sec due to the engine time constant, and a time constant of 0.4 sec due to the CVT speed threshold, respectively.

The braking pattern and resulting left and right wheel speeds are shown in Figure 3.16. During periods of turning, the inner wheel speed is reduced while the outer wheel speed is slightly increased. The difference between the left and right speeds enables the turning of the vehicle. Responses of wheel speed to throttle and braking patterns are also similar to first-order functions. The dynamic torque distribution of the right/left wheels, gearbox and engine over the period of 35 sec is depicted in Figure 3.17. It is noticed that the load on wheels increases significantly on acceleration. On the other hand, when one row of wheels slows down its motion, load on the wheels fall to negative.

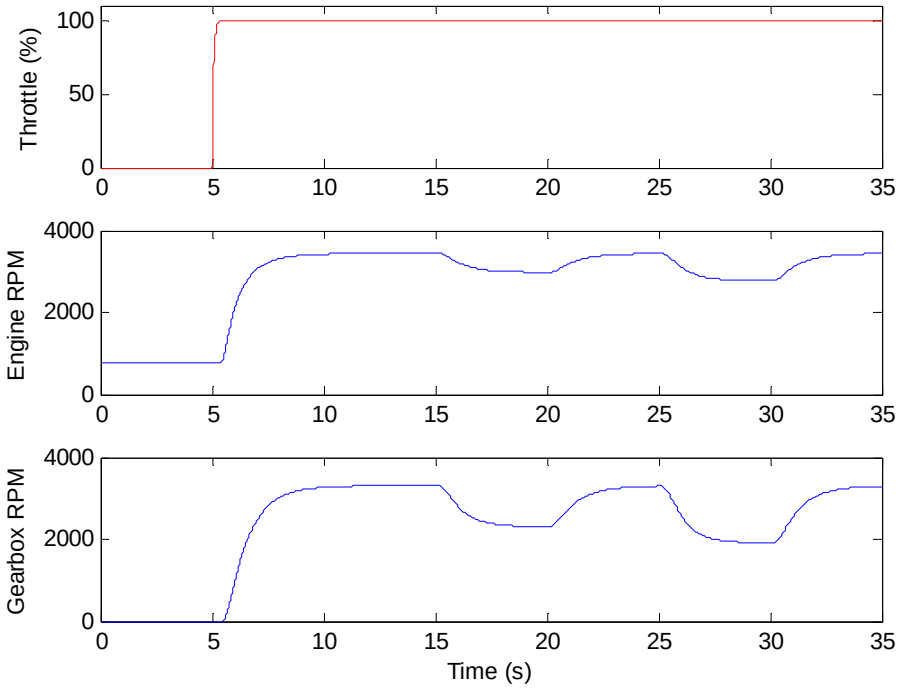

Figure 3.15 Responses to throttle step input

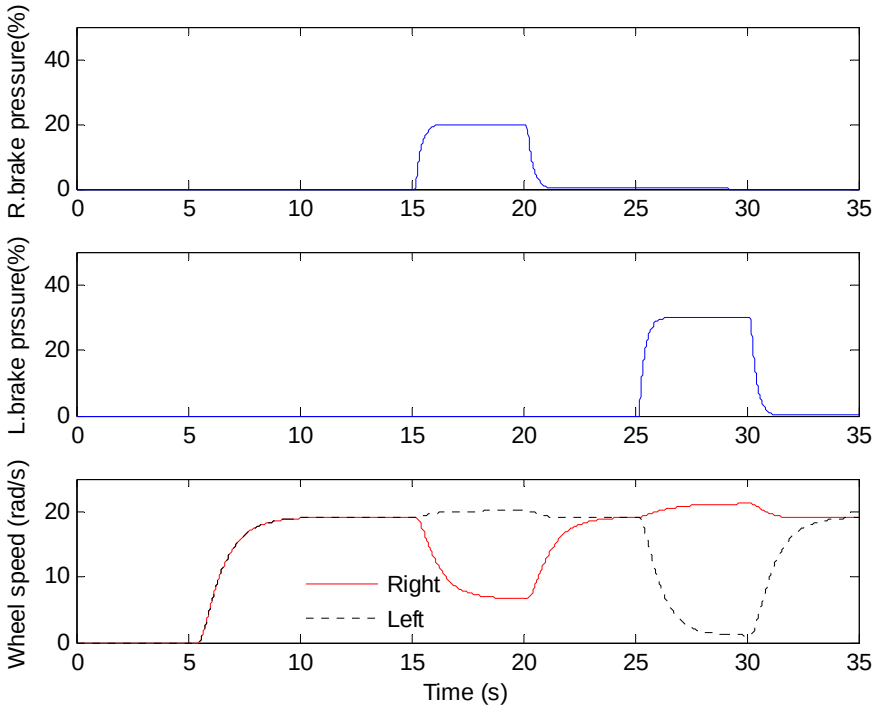

Figure 3.16 Braking pattern and wheel speeds

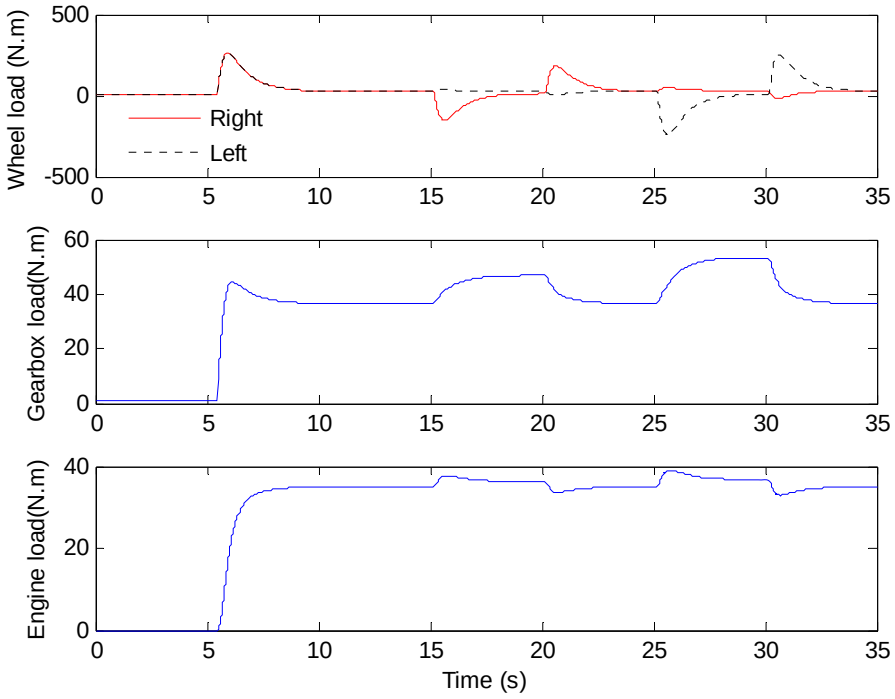

Figure 3.17 Load distribution on components of the driveline

3.4 Simplified model

There are many dynamic loops in the original model. This requires a lot of computation and sometimes it can not find solutions. The problem occurs more often when the model is tested with experimental data or more loops are added for vehicle motion control. In this section, a simplified model is developed to avoid the encountered numerical problem. The simplified model is then compared with the original model and verified with real data from experiment.

3.4.1 Simplified model development

Let us first consider the model in the case of straight-line running. From equations (3.15) and (3.16), total load acting on the wheel shafts is

$$T_w = \left(J_w + m.r^2\right)\dot{\omega}_w + \left(b_w + mr^2 c_{r2}\right)\omega_w + mrc_{r1} + mgr\sin(\chi). \qquad (3.27)$$

Substitution of (3.8), (3.9) and (3.16) into (3.27) give the load on the differential outputs and the gearbox:

$$T_d = \left(J_w + m.r^2\right)K_3^2\dot{\omega}_d + \left(b_w K_3^2 + mr^2 c_{r2} K_3^2\right)\omega_d + \left(mrc_{r1} + mgr\sin(\chi)\right)K_3, \quad (3.28)$$

$$T_G = \left(J_w + m.r^2\right)K_3^2\dot{\omega}_d + \left(b_w K_3^2 + b_d + mr^2 c_{r2} K_3^2\right)\omega_d + \left(mrc_{r1} + mgr\sin(\chi)\right)K_3. \quad (3.29)$$

The total load referred to the CVT output is then obtained from (3.6), (3.16), and (3.29) as

$$\begin{aligned} T_c = {} & \left(J_w + m.r^2\right)K_3^2K_2^2\dot{\omega}_c + \\ & + \left(b_w K_3^2K_2^2 + b_d K_2^2 + b_G + mr^2 c_{r2} K_3^2K_2^2\right)\omega_c + \left(mrc_{r1} + mgr\sin(\chi)\right)K_3K_2. \end{aligned} \quad (3.30)$$

The equation (3.30) suggests that when the vehicle is running straight, the gearbox, differential, chain, and wheels can be combined together and described by a single equation. Other components, namely the engine and the CVT, are still modelled by equations (3.1-3.4). The wheel speed is derived from (3.6), (3.8), and (3.9) as

$$\omega_w = \omega_c K_3 K_2. \quad (3.31)$$

In the case of turning, total loads acting on left and right wheel shafts are calculated from (3.16) and (3.17).

$$\begin{aligned} T_{wL} &= \frac{1}{2}\left(J_w + mr^2\right)\dot{\omega}_{wL} + \left(\frac{1}{2}b_w + \frac{1}{2}mr^2 c_{r2}\right)\omega_{wL} + \frac{1}{2}mrc_{r1} + \frac{1}{2}mgr\sin(\chi), \\ T_{wR} &= \frac{1}{2}\left(J_w + mr^2\right)\dot{\omega}_{wR} + \left(\frac{1}{2}b_w + \frac{1}{2}mr^2 c_{r2}\right)\omega_{wR} + \frac{1}{2}mrc_{r1} + \frac{1}{2}mgr\sin(\chi). \end{aligned} \quad (3.32)$$

These loads are then referred back to the left and right outputs of the differential as

$$\begin{aligned} T_{dL} &= \frac{1}{2}\left(J_w + mr^2\right)K_3^2\dot{\omega}_{dL} + \left(\frac{1}{2}b_w K_3^2 + \frac{1}{2}mr^2 c_{r2} K_3^2\right)\omega_{dL} + \left(\frac{1}{2}mrc_{r1} + \frac{1}{2}mgr\sin(\chi)\right)K_3, \\ T_{dR} &= \frac{1}{2}\left(J_w + mr^2\right)K_3^2\dot{\omega}_{dR} + \left(\frac{1}{2}b_w K_3^2 + \frac{1}{2}mr^2 c_{r2} K_3^2\right)\omega_{dR} + \left(\frac{1}{2}mrc_{r1} + \frac{1}{2}mgr\sin(\chi)\right)K_3. \end{aligned} \quad (3.33)$$

Combined with the brake forces required for turning, the total load acting on the differential is

$$T_d = \frac{1}{2}\left(J_w + mr^2\right)K_3^2\left(\dot{\omega}_{dL} + \dot{\omega}_{dR}\right) + \left(\frac{1}{2}b_w K_3^2 + \frac{1}{2}mr^2 c_{r2} K_3^2\right)\left(\omega_{dL} + \omega_{dR}\right) + \\ + \left(mrc_{r1} + mgr\sin(\chi)\right)K_3 + T_{bL} + T_{bR}. \tag{3.34}$$

From (3.19), $\omega_{dL} + \omega_{dR} = 2\omega_G = 2\omega_d$, equation (3.34) becomes

$$T_d = \left(J_w + mr^2\right)K_3^2\dot{\omega}_d + \left(b_w K_3^2 + mr^2 c_{r2} K_3^2\right)\omega_d + \\ + \left(mrc_{r1} + mgr\sin(\chi)\right)K_3 + T_{bL} + T_{bR}. \tag{3.35}$$

Following the same approach, the total load on the CVT is obtained as

$$T_c = \left(J_w + mr^2\right)K_3^2K_2^2\dot{\omega}_c + \left(b_w K_3^2 K_2^2 + b_d K_2^2 + b_G + mr^2 c_{r2} K_3^2 K_2^2\right)\omega_c + \\ + \left(mrc_{r1} + mgr\sin(\chi)\right)K_3K_2 + \left(T_{bL} + T_{bR}\right)K_2. \tag{3.36}$$

During turning, the speed difference is determined from (3.23) and (3.20) as

$$x = \frac{\left(T_{dR} - T_{dL}\right) + \left(T_{bR} - T_{bL}\right)}{b_{D,in}}. \tag{3.37}$$

Substitution of (3.33) and (3.19) into (3.37) gives,

$$\left(J_w + mr^2\right)K_3^2\dot{x} + \left(\left(b_w K_3^2 + mr^2 c_{r2} K_3^2\right) + b_{D,in}\right)x = \left(T_{bR} - T_{bL}\right). \tag{3.38}$$

Equation (3.38) indicates that the speed difference can be calculated by a first-order function of the brake forces,

$$x = \frac{\left(T_{bR} - T_{bL}\right)}{\left(J_w + mr^2\right)K_3^2 s + \left(\left(b_w K_3^2 + mr^2 c_{r2} K_3^2\right) + b_{D,in}\right)}, \tag{3.39a}$$

with a time constant derived from (3.39a) as

$$\tau_x = \frac{\left(J_w + mr^2\right)K_3^2}{\left(\left(b_w K_3^2 + mr^2 c_{r2} K_3^2\right) + b_{D,in}\right)}. \tag{3.39b}$$

When turning, the inner wheels can be locked if the brake force is large enough. To take into account this case, the speed difference is limited to

$$-|\omega_c|K_2 \le x \le |\omega_c|K_2 . \tag{3.40}$$

The wheel speeds are determined from (3.6), (3.18), and (3.19) as

$$\begin{aligned} \omega_{wL} &= \omega_c K_2 K_3 + xK_3 , \\ \omega_{wR} &= \omega_c K_2 K_3 - xK_3 . \end{aligned} \tag{3.41}$$

From the above equations, it is suggested that the driveline model can be simplified to cover adequately dynamics of the engine, CVT, and a combined component presented for the gearbox, differential, chain, and wheels. The combined component is described by equations (3.36), (3.39a-3.41) while the engine and CVT are not changed. It is noted that when brake forces are zero, the model is the same one in case of straight-line running.

3.4.2 Comparison with original model and experimental data

For comparison purposes, the same patterns of throttle and brake forces are applied for the both models: original and modified. Simulation results are given in Figures 3.18 and 3.19 for responses of the engine, gearbox, and wheels. It can be seen that responses of the simplified model are exactly the same as those of the original model. Therefore, the simplified model can be used as an alternative to the original model. By combining the gearbox, differential, chain, and wheels together, algebraic loops inside these components are avoided. As a result, solutions can be found faster and easier. The problem encountered in the original model is solved.

A set of experiment data collected on a field trial is used to verify the model. The data cover records of throttle, brake, engine speed, gearbox speed, and wheel speeds. The engine and gearbox rotations are measured in RPM by Hall Effect sensors while the wheel speeds are gauged in rad/s by rotational encoders. The throttle data are reference for input of the throttle actuator control while brake data include the hydraulic pressure inside the brake cylinder. Assuming the brake force is proportional to the hydraulic pressure, the brake pressure data are input to the driveline model through a proportional gain. Meanwhile, the throttle is connected to the model through the transfer function presented for the throttle control system (3.36). The ground is assumed to be flat (χ=0).

Responses of the model to the real input data are compared with the experimental output data in Figure 3.20 for engine, gearbox speeds, and Figure 3.21 for left and right wheel speeds. In general, it can be seen that the engine, gearbox, and wheel speeds are close to the experimental data in a steady state with corresponding 2.7%, 3.6%, and 5.6% of RMS errors, calculated in the 603s-608s interval. Some noise spikes are observed in the wheel encoder data; perhaps because of the rough terrain encountered or wheel slip during the trial.

During acceleration, however, the gearbox and wheels respond slower than those measured in practice while the engine runs faster. This is probably because slip occurs between the CVT belt and clutches in acceleration while it is ignored in the model. The responses of the engine and gearbox to brake inputs are very similar to those observed on the real system. During turning, the wheel speeds follow closely the experimental data, however, at a slower rate. This can be explained by the wheel slip. In the model, it is assumed that no slip occurs between the wheels and the ground. For a skid-steering vehicle, however, in order to turn the vehicle the wheels have to slip on the ground.

The wheel slip can be taken into account by replacing equation (3.14) with

$$V_X = (1-i) r \omega_w , \tag{3.42}$$

where i is the average wheel slip ratio, defined in (Wong, 2001) as:

$$i = 1 - \frac{V_X}{r\omega_w}. \tag{3.43}$$

It is easy to adjust the model in the case of a wheel slip by modifying equations (3.36) and (3.39a) as follows:

$$\begin{aligned} T_c = {} & \left(J_w + (1-i)mr^2\right)K_3^2 K_2^2 \dot{\omega}_c + \left(b_w K_3^2 K_2^2 + b_d K_2^2 + b_G + (1-i)mr^2 c_{r2} K_3^2 K_2^2\right)\omega_c + \\ & + \left(mrc_{r1} + mgr\sin(\chi)\right)K_3 K_2 + \left(T_{bL} + T_{bR}\right)K_2 , \end{aligned} \tag{3.44}$$

$$x = \frac{\left(T_{bR} - T_{bL}\right)}{\left(J_w + (1-i)mr^2\right)K_3^2 s + \left(\left(b_w K_3^2 + (1-i)mr^2 c_{r2} K_3^2\right) + b_{D,in}\right)}. \tag{3.45}$$

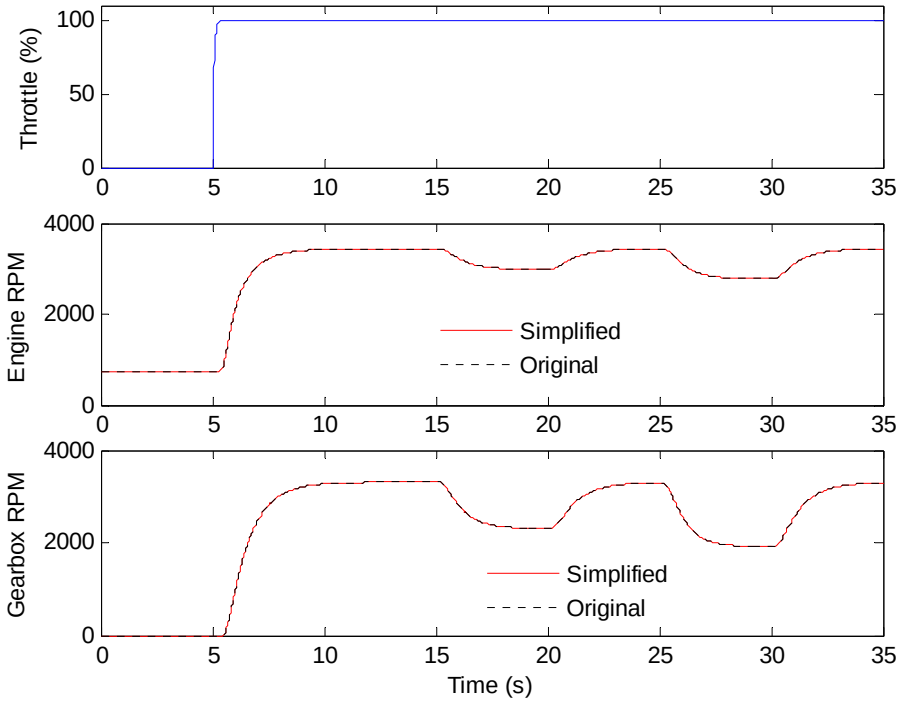

Figure 3.18 Simplified model vs. original model: engine and gearbox responses

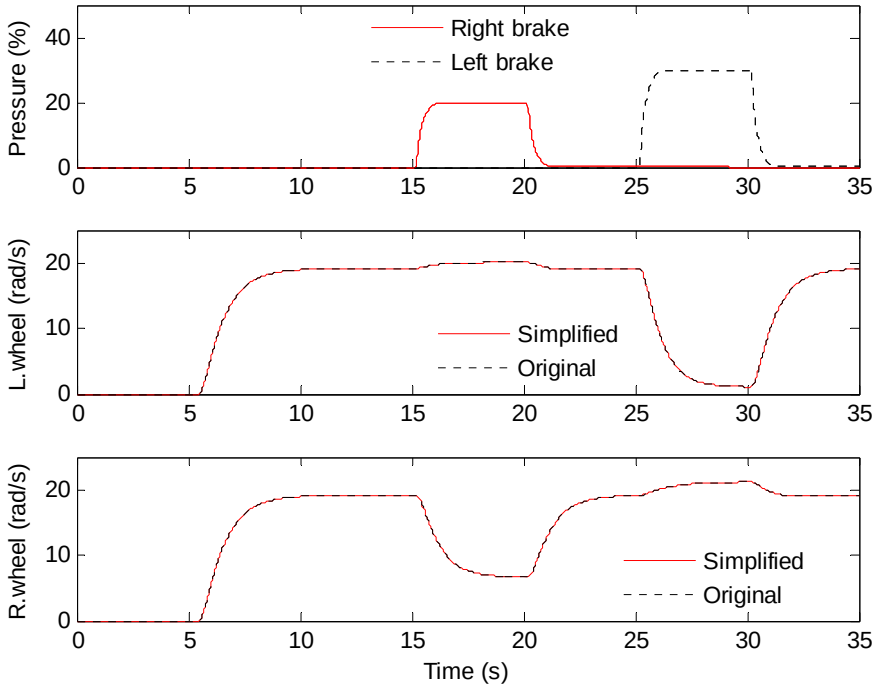

Figure 3.19 Simplified model vs. original model: wheel responses

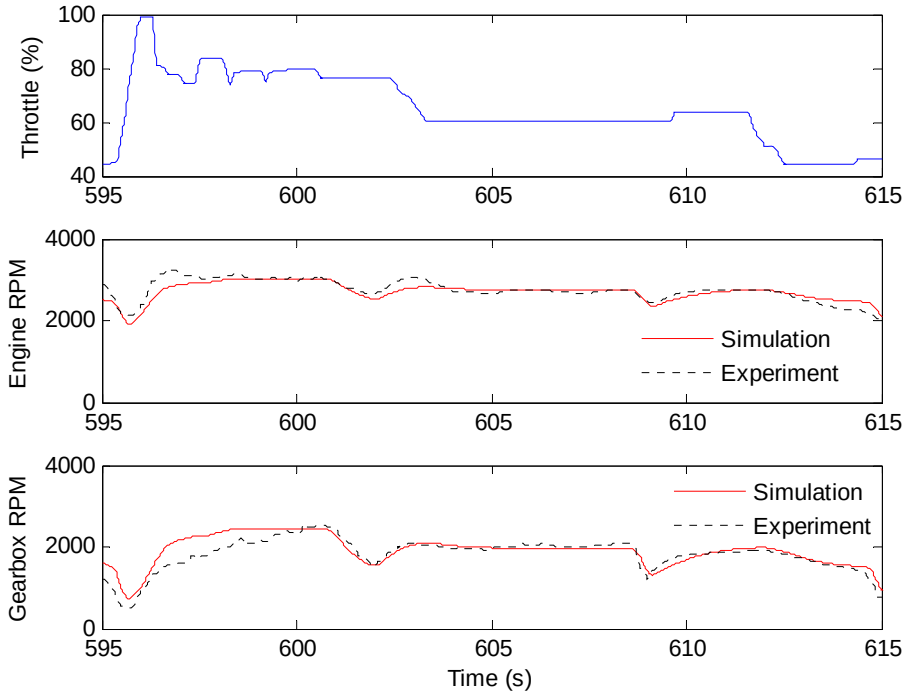

Figure 3.20 Simulation vs. experiment: engine and gearbox responses

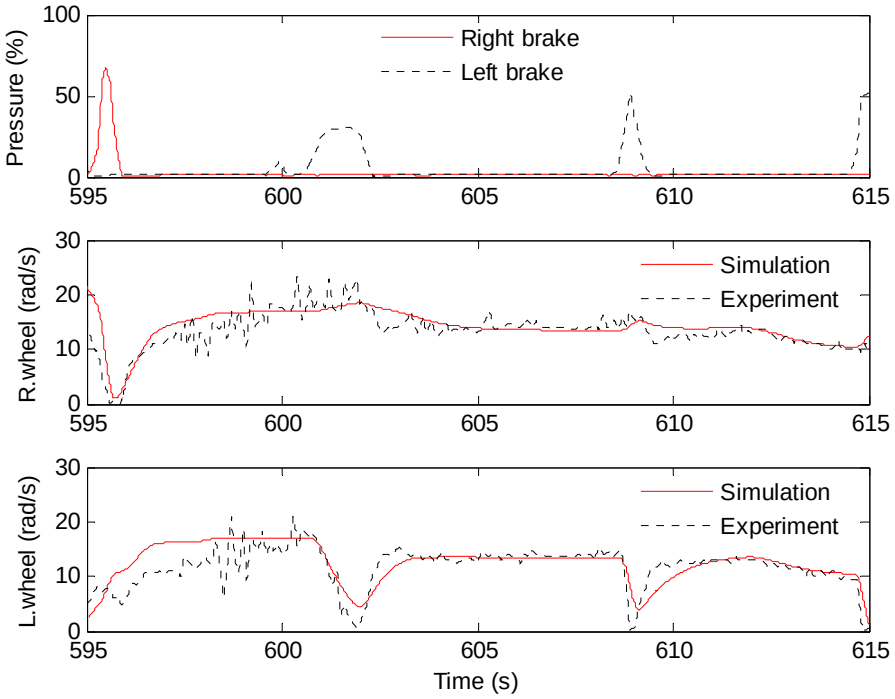

Figure 3.21 Simulation vs. experiment: wheel responses

Simulation results with wheel slip are shown in Figures 3.22 and 3.23. It can be seen that, with a slip ratio of 60%, the responses of wheels in turning are closer to the experiment than in case of no slip (see Figure 3.22). However, the difference between the gearbox speed and that of the experiment during acceleration is larger (see Figure 3.23).

Similarly, by defining the CVT belt slip ratio as

$$i_{CVT} = 1 - \frac{\omega_c}{K_1 \omega_e}, \tag{3.46}$$

and modifying equation (3.4) with

$$\begin{aligned} T_{ec} &= (1 - i_{CVT}) T_c K_1 , \\ \omega_c &= (1 - i_{CVT}) \omega_e K_1 , \end{aligned} \tag{3.47}$$

the CVT's slip can be also taken into account. However, modelling of the CVT belt slip is more complicated and not considered in this thesis.

The other mismatches between trial tests and simulation results are perhaps due to the linearisation of the engine torque production and the CVT gear ratio. In addition, the model did not consider the weight and backlash of the gears in gearbox, differential, brake discs, and chains. More importantly, complicated interaction between the vehicle and terrain was not taken into account. This will be addressed in Chapter 5.

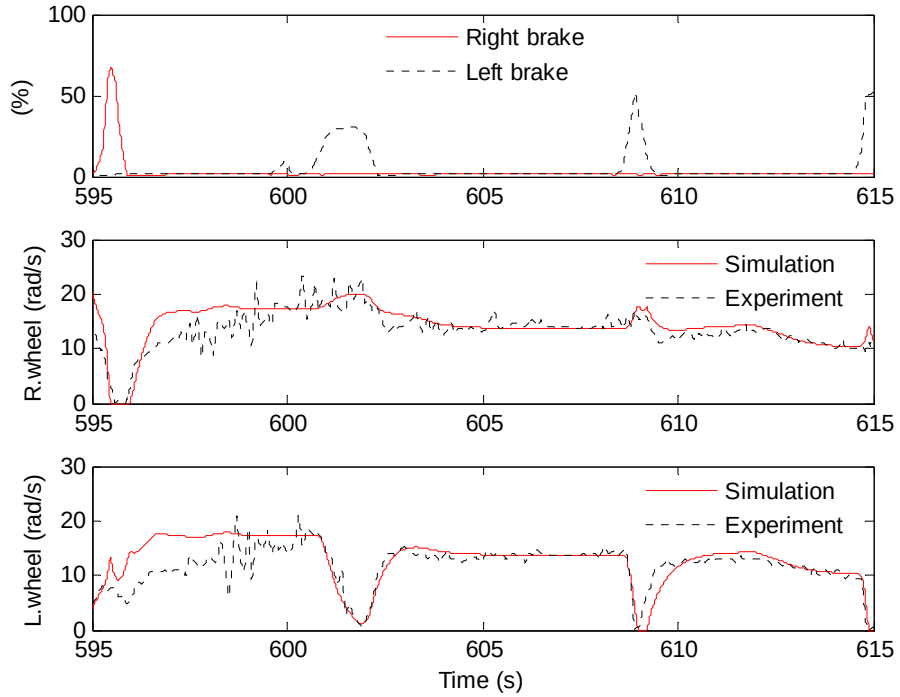

Figure 3.22 Simulation vs. experiment: wheel responses with 60% slip

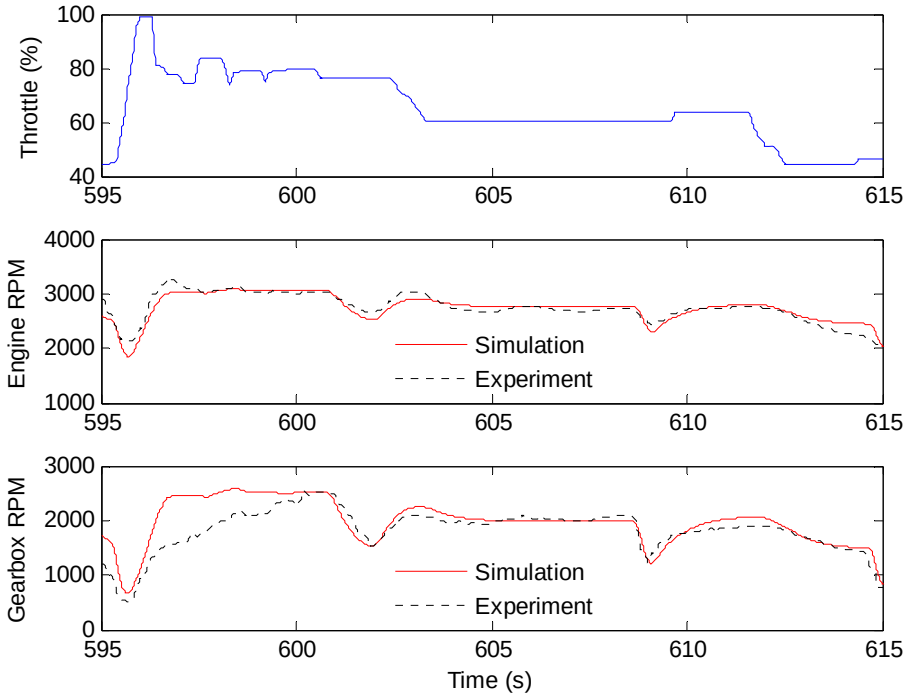

Figure 3.23 Simulation vs. experiment: engine and gearbox responses at 60% slip

3.5 Conclusion

In this chapter, the vehicle's driveline, including the engine, CVT, gearbox, differential, chains and wheels have been analysed and modelled. An original model was first developed and simulation results were provided. A simplified model was proposed to improve computational efficiency. Simulation showed that there was no significant difference in the results between these models. In comparison with field tests, effects due to slips in wheel-ground contact and CVT belt-clutch contact were observed. The model was then modified to take into account these slips. Simulation results with a constant wheel slip showed a close agreement with experiment data. The dynamics of wheel slip will be analysed in Chapter 5 while the CVT slip is still considered as an open problem.

Chapter 4

Robust low-level control design

In Chapter 3, the responses of the throttle and brake control systems were assumed to be first-order functions. This may be not true in practice, however. In this chapter the limitations encountered by the default PID control scheme for the UGV are considered and solution for them is reached.

The control requirements for the vehicle and the disadvantages with PID controller design are to be introduced in the first section. In Section 4.2, the proposed control approach is described for linear and nonlinear systems with and without time delay. Simulation results for a wide range of systems are given in Section 4.3. A conclusion is drawn in the last section.

4.1 Introduction

As mentioned in Chapter 1 and Chapter 2, the vehicle is equipped with a set of actuators and therefore requires suitable controllers. The engine throttle is actuated by a servo motor. It needs a controller to manipulate the throttle position and therefore the engine speed. Similarly, linear actuators attached to the inputs of the left and right brakes need to be controlled to supply appropriately brake forces for turning and stopping the vehicle. At a higher level, the vehicle velocity and turning rate must also be controlled because they are very important for further developments of the UGV. PID controllers

were initially implemented for all control requirements. In this section, the problem of the brake control system is described.

The vehicle uses two separate hydraulic brake systems, one for the left and the other for the right wheels. These systems are identical and consist of pistons and cylinders, pipes, brake discs, pads and calipers, as shown in Figure 4.1. Two linear actuators are used to control the brake pistons instead of using brake levers as in the original vehicle. The actuator consists of a DC motor combined with gears and ball screw systems for transferring rotation to linear motion, as shown in Figure 4.2. An amplifier is used to convert the voltage signal from the brake controller to the supplying current for the actuator. Position and pressure transducers are used to measure the actuator positions and the hydraulic pressures inside the brake calipers.

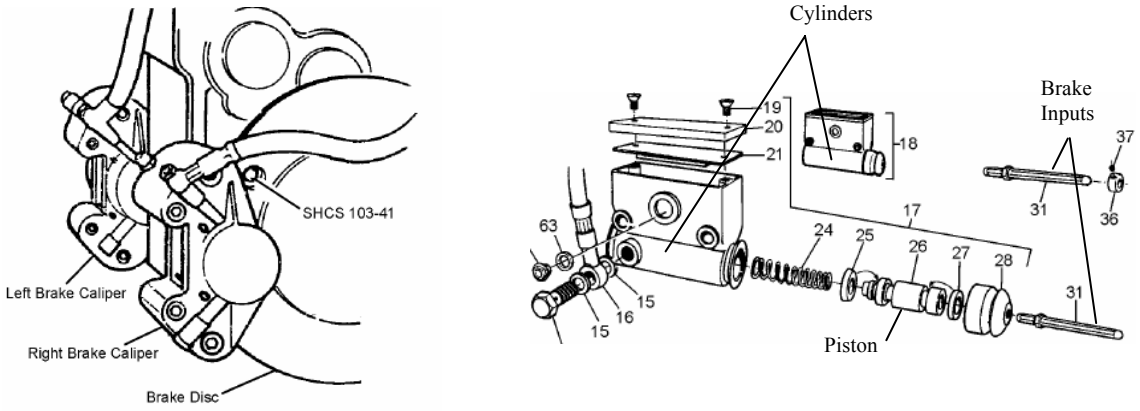

Figure 4.1 Hydraulic brake systems (Source: (Ontario Drive & Gear, 2007))

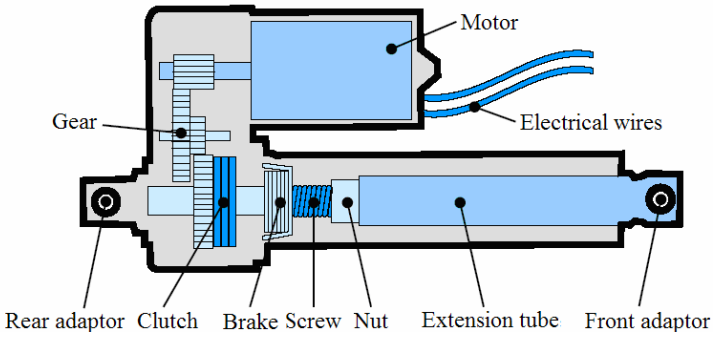

Figure 4.2 Configuration of linear actuator (Source: (Thomson, 2007))

Assuming that the brake forces are proportional to the pressures inside the calipers, PID controllers were first implemented to control the brake pressures. The controllers were manually tunned according to the desired response specifications in rise- and settling-time. Some responses of the brake control systems are shown in Figure 4.3. Here the position is scaled to the movable range of the actuator while the pressure is normalised between its minimum and maximum values. Note that the pressure rises sharply from the minimum to the maximum values over just a short range of the position as the caliper contacts the disk. From Figure 4.3, it can be seen that there exists a time delay between the pressure set-point signal and the pressure responses. In addition, the relationship between the piston position and brake pressure is highly nonlinear. Due to the effects of the time-delay and nonlinearity, the pressure responses exhibit large overshoots. Despite much effort in tuning the PID controllers, overshoots could not be eliminated. An overshoot in brake pressure in turn results in an overshoot in the brake force which can lock the wheels during turning. It is therefore very difficult to control the vehicle's turning at a desired angular speed. The same problem may take place in an interconnected system with many PID-based controllers.

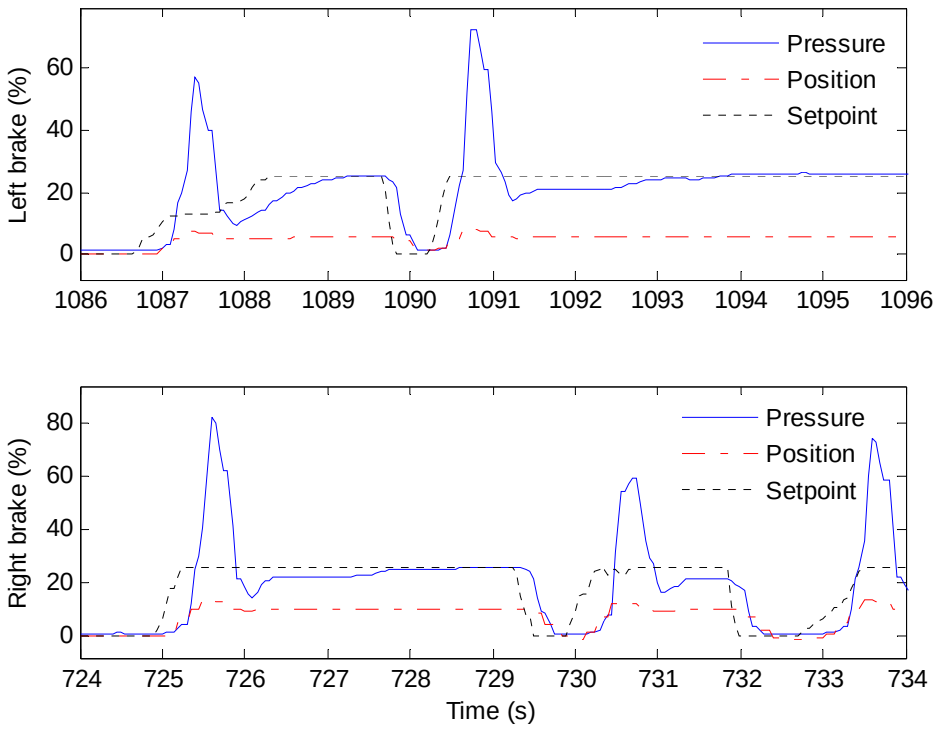

Figure 4.3 Responses of PID brake pressure controllers

In the next sections, robust control algorithms are proposed to suppress overshoot in the system brake responses under PID control. This idea is based on two observations. First, the responses of the PID controller with large overshoots are similar to those seen in second-order systems. The whole system, including PID in closed-loop control, can then be modelled equivalently by a second-order transfer function. Second, sliding mode control, a well-known robust control technique, can reduce the equivalent dynamics of a second-order to a first-order system, which is free of overshoot. It is therefore proposed in this thesis to use the cascade control principle coupled with a sliding mode controller (SMC) as the outer loop to eliminate the overshoot of the PID-controlled inner loop. It is expected that not only overshoot will be alleviated but also that such prominent properties of SMC such as robustness to external disturbances, uncertainties and nonlinearities can be retained.

4.2 Control development

The proposed controller is first designed for the case without time-delay and then extended for input time-delay systems. Let us first consider the PID controller and its closed-loop model.

4.2.1 PID controller and closed-loop model

Figure 4.4 shows a simple PID controller in a closed-loop feedback system. The output of the controller, V, is a function of the difference between the input and the current process output, i.e. of the error, $e_0 = u - y$,

$$V = K_P e_0 + K_I \int e_0 dt + K_D \frac{de_0}{dt}, \tag{4.1}$$

where u is the reference input to the system.

The response of a PID control system is determined by its parameters, namely the proportional gain (K_P) to reduce the rise time the steady-state error, the integral gain (K_I) to eliminate the steady-state error while degrading the transient response, and the derivative gain (K_D) to improve the stability of the system.

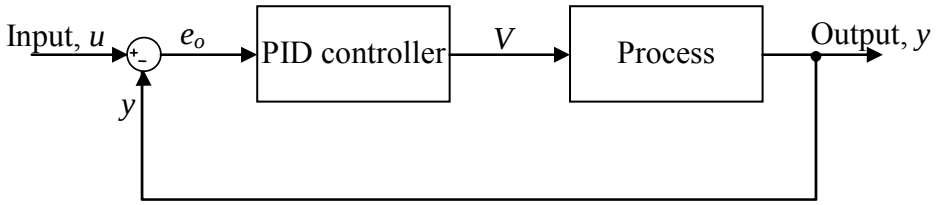

Figure 4.4 PID control loop

To obtain a desired response, PID parameters need to be tuned properly. By using manual tuning or auto-tuning methods, the desired settling time and steady-state error can be achieved. There is, however, a trade-off between the rise time and overshoot. As mentioned in Chapter 2, overshoot with a PID controller is unavoidable without sacrificing fast rise time, especially for nonlinear and time-delay systems.

To utilise sliding mode control, knowledge of the process to be controlled must be obtained prior to the design process. In practice, the process may be unknown. As the system under PID control exhibits large overshoot in its step response, however, the whole system can be modelled equivalently by a time-delayed second-order transfer function

$$G(s)=\frac{\omega_n^2}{s^2+2\delta\omega_n s+\omega_n^2}e^{-t_d s}, \tag{4.2}$$

where δ is the damping ratio, ω_n is the natural frequency and t_d is the time delay. The time delay can be measured directly from the response. The equivalent natural frequency and damping ratio can be calculated from the percentage of overshoot and peak time, as follows (Franklin *et al.*, 2002):

$$\omega_n=\frac{\pi}{t_P\sqrt{1-\delta^2}}, \tag{4.3}$$

$$\delta=-\frac{\ln(M_P)}{\sqrt{\pi^2+\ln^2(M_P)}}, \tag{4.4}$$

where M_p and t_p are the percentage of overshoot and peak time, respectively.

It is noted that for a non-delay system, the model is reduced to

$$G(s) = \frac{\omega_n^2}{s^2 + 2\delta\omega_n s + \omega_n^2}. \tag{4.5}$$

Due to the effects of nonlinearities and uncertainties, the overshoot and peak time can vary and lead to the changes of the calculated equivalent natural frequency and damping ratio. For many engineering applications, the time-delay does not vary much and may be practically considered as constant.

Although PID controllers have been widely adopted in industry their performance can always be improved by combining them with more advanced control techniques. For this, a robust controller such as the SMC is proposed as detailed in the following.

4.2.2 Sliding mode – PID controller

Assuming that zero steady state error can be obtained by a PID controller, the relationship between the input and output of the inner PID – controlled loop derived from (4.5) can be described in the form of

$$\ddot{y} = f + \omega_n^2 u, \tag{4.6}$$

where f is obtained as

$$f = -2\delta\omega_n \dot{y} - \omega_n^2 y. \tag{4.7}$$

As mentioned in Section 4.2.1, for nonlinear dynamics, the modelling parameters in (4.6) and (4.7) can vary so that the function f is unknown. However, if the ranges of variation of these parameters are known, for example,

$$\begin{aligned} &\omega_{n1} \le \omega_n \le \omega_{n2}, \\ &\delta_1 \le \delta \le \delta_2, \end{aligned} \tag{4.8}$$

the nonlinear function can be approximated by

$$\hat{f} = -2\hat{\delta}\hat{\omega}_n \dot{y} - \hat{\omega}_n^2 y, \tag{4.9}$$

where $\hat{\omega}_n$ and $\hat{\delta}$ are nominal values of the natural frequency and the damping ratio which, in the frequency domain, can be chosen as the geometric mean of their boundaries (Slotine and Li, 1991), conveniently

$$\begin{aligned} \hat{\omega}_n &= \sqrt{\omega_{n1}\omega_{n2}}\,, \\ \hat{\delta} &= \sqrt{\delta_1\delta_2}\,. \end{aligned} \tag{4.10}$$

The error of this approximation is bounded by a known function,

$$\left|\hat{f} - f\right| \le F\,, \tag{4.11}$$

where

$$F = \left|2\left(\delta_2\omega_{n2} - \hat{\delta}\hat{\omega}_n\right)\dot{y} + \left(\omega_{n2}^2 - \hat{\omega}_n^2\right)y\right|. \tag{4.12}$$

Let the control error be defined as

$$e = y - y_d\,, \tag{4.13}$$

where y_d is the desired output (or reference).

In order to force the second-order system in (4.6) to first-order one, the sliding surface is defined as

$$S = \left(\frac{d}{dt} + \lambda\right) e = \dot{e} + \lambda e, \tag{4.14}$$

where λ is a positive constant to be determined.

The output of the SMC has the form

$$u = u_{eq} + u_R\,, \tag{4.15}$$

where u_{eq} is the equivalent control for the system (4.6) without uncertainties and u_R is the robust control added to overcome the uncertainties of the system.

The equivalent control is chosen so that when the system trajectory is off the sliding surface, it will force the system error dynamics to the sliding surface. This condition can be obtained by solving the equation

$$\dot{S} = 0 \,. \tag{4.16}$$

Differentiating *S* from (4.17) gives

$$\dot{S} = \ddot{e} + \lambda \dot{e} = \ddot{y} - \ddot{y}_d + \lambda \dot{e}. \tag{4.17}$$

Substitution of (4.14) into (4.17) yields

$$\dot{S} = f + \hat{\omega}_n^2 u - \ddot{y}_d + \lambda \dot{e}. \tag{4.18}$$

Then the equivalent control is derived from (4.16) as

$$u_{eq} = \frac{1}{\hat{\omega}_n^2}\left(- \hat{f} + \ddot{y}_d - \lambda \dot{e}\right). \tag{4.19}$$

It is noted that the equivalent control in (4.19) will only drive the system trajectory to the sliding surface if the system parameters are known. To take into account the effects of nonlinearities, modelling error and other uncertainties, the robust control is introduced as

$$u_R = -k.sign(S), \tag{4.20}$$

where the gain *k* must be large enough to counteract the effects of uncertainties.

To ensure system stability under uncertainties, let us define a Lyapunov function

$$V_L = \frac{1}{2} S^2 \,. \tag{4.21}$$

The coefficient *k* shall be chosen to satisfy the following condition:

$$\dot{V}_L \le -\eta |S|, \tag{4.22}$$

where η is a strictly positive constant.

From (4.18) and (4.21), one has

$$\dot{V}_L = S\dot{S} = S\left(f + \omega_n^2 u - \ddot{y}_d + \lambda\dot{e}\right). \tag{4.23}$$

Substitution of (4.15), (4.19) and (4.20) into (4.23) gives,

$$\begin{aligned}\dot{V}_L &= S\left[f + \frac{\omega_n^2}{\hat{\omega}_n^2}\left(-\hat{f} + \ddot{y}_d - \lambda\dot{e}\right) - \omega_n^2 k.sign(S) - \ddot{y}_d + \lambda\dot{e} \right] \\ &= \left[\left(f - \hat{f}\right) + \left(\frac{\omega_n^2}{\hat{\omega}_n^2} - 1 \right)\left(-\hat{f} + \ddot{y}_d - \lambda\dot{e}\right) \right] S - \omega_n^2 k.|S|.\end{aligned} \tag{4.24}$$

If k is chosen as

$$k \geq \frac{1}{\omega_{n1}^2}(F + \eta) + \left|1 - \frac{\hat{\omega}_n^2}{\omega_{n1}^2}\right| |u_{eq}|, \tag{4.25}$$

then condition (4.22) is satisfied which means that the system is stable.

The total control output of the SMC now becomes

$$u = \frac{1}{\hat{\omega}_n^2}\left(-\hat{f} + \ddot{y}_d - \lambda\dot{e}\right) - k.sign(S). \tag{4.26}$$

This output is used as a reference input for the PID controller in the cascade configuration, as shown in Figure 4.5.

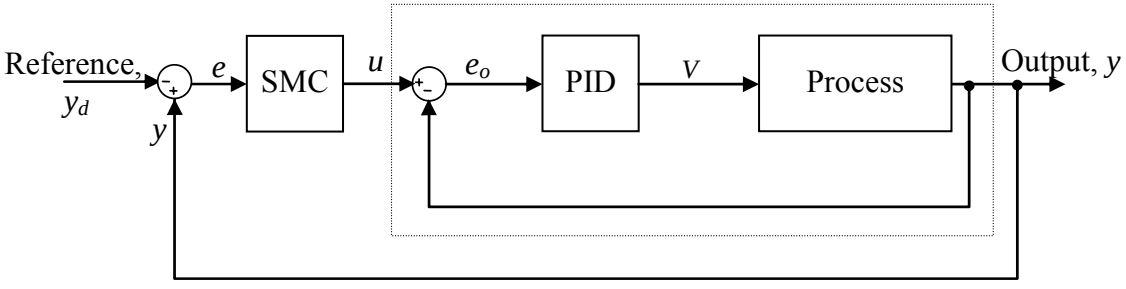

Figure 4.5 Cascade Sliding Mode – PID controller for non-delay systems

If the system is subject to an external disturbance, the model becomes

$$\ddot{y} = f + \omega_n^2 u + d\,, \tag{4.27}$$

where d represents the disturbance and is bounded by D.

Following the same design approach as above, the control law is obtained as

$$u = \frac{1}{\hat{\omega}_n^2}\left(-\hat{f} + \ddot{y}_d - \lambda\dot{e}\right) - k.sign(S), \tag{4.28}$$

where k is chosen to satisfy

$$k \geq \frac{1}{\omega_{n1}^2}(F + D + \eta) + \left(1 - \frac{\hat{\omega}_n^2}{\omega_{n1}^2}\right)\left|u_{eq}\right|. \tag{4.29}$$

It is noticed that the disturbance boundary is included in the robust control component to compensate for the effect of the disturbance. This ensures that the condition (4.22) is satisfied. If the system is linear and its modelling parameters are estimated correctly, condition (4.29) can be reduced to

$$k \geq \frac{1}{\omega_n^2}(D + \eta). \tag{4.30}$$

4.2.3 Sliding mode – PID controller for input-delay case

In this section, the above control approach is extended to account for time-delay. The full design process which includes parts of the previous section is described here in the interest of simplicity.

By cascading a SMC with the PID-controlled system as shown in Figure 4.6, the time-delay system (4.2) becomes a plant described by

$$\ddot{y}(t) + 2\delta\omega_n\dot{y}(t) + \omega_n^2 y(t) = \omega_n^2 u(t - t_d), \tag{4.31}$$

where y is the output and u is the input. Equation (4.31) can be transformed to

$$\ddot{y}(t+t_d) = f(t+t_d) + \omega_n^2 u(t), \tag{4.32}$$

where

$$f(t+t_d) = -2\delta\omega_n \dot{y}(t+t_d) - \omega_n^2 y(t+t_d). \tag{4.33}$$

As discussed in Section 4.2.1, due to nonlinearities the modelling parameters can vary within the ranges (4.8) and can be approximated by (4.10).

In that case, the function $f(t+t_d)$ (4.33) is approximated by

$$\hat{f}(t+t_d) = -2\hat{\delta}\hat{\omega}_n \dot{y}(t+t_d) - \hat{\omega}_n^2 y(t+t_d). \tag{4.34}$$

The approximation error is bounded by

$$\left|\hat{f} - f\right| \le F, \tag{4.35}$$

where F is now

$$F = \left|2\left(\delta_2\omega_{n2} - \hat{\delta}\hat{\omega}_n\right)\dot{y}(t+t_d) + \left(\omega_{n2}^2 - \hat{\omega}_n^2\right)y(t+t_d)\right|. \tag{4.36}$$

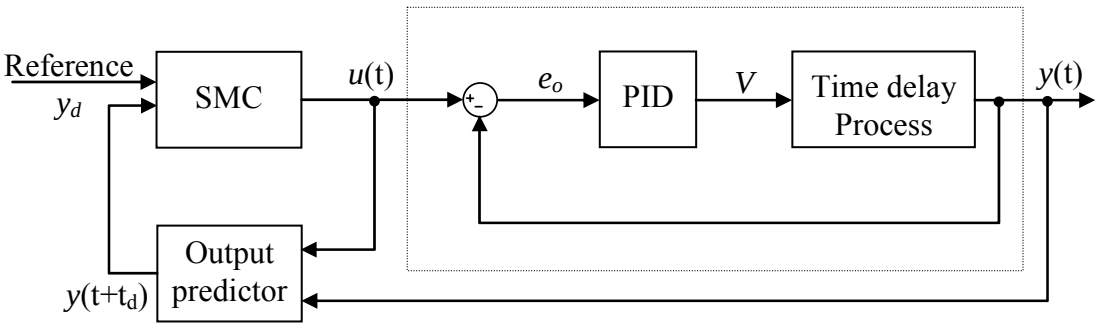

Figure 4.6 Cascade Sliding Mode - PID controller for time-delay systems

Let the control error be defined as

$$e = y(t+t_d) - y_d(t), \tag{4.37}$$

where y_d is the reference input, and the sliding surface be chosen as (4.14).

The control output again consists of an equivalent control for the nominal system (4.32) without uncertainties and a robust control to overcome the uncertainties of the system, as given in (4.15).

From (4.37) and (4.14), one has

$$\dot{S} = \ddot{e} + \lambda\dot{e} = \ddot{y}(t+t_d) - \ddot{y}_d(t) + \lambda\dot{e}. \tag{4.38}$$

Substitution of (4.32) into (4.38) gives

$$\begin{aligned} \dot{S} &= \ddot{e} + \lambda\dot{e} \\ &= f(t+t_d) + \omega_n^2 u(t) - \ddot{y}_d(t) + \lambda\dot{e}. \end{aligned} \tag{4.39}$$

The equivalent control is obtained from $\dot{S} = 0$ for the nominal system, giving

$$u_{eq}(t) = \frac{1}{\hat{\omega}_n^2}\left(-\hat{f}(t+t_d) + \ddot{y}_d(t) - \lambda\dot{e}\right). \tag{4.40}$$

The equivalent control (4.40) will guide the system from the initial state to the sliding surface S=0 if the nominal parameters apply. Now, in order to overcome the uncertainties of the system, the robust control is chosen as

$$u_R(t) = -k.sign(S), \tag{4.41}$$

where the discontinuous gain k must be large enough to overcome the effects of uncertainties.

The attainment of a sliding mode can be guaranteed by selecting first $V_L = \frac{1}{2}S^2$ to be a Lyapunov function. The coefficient k shall be chosen to satisfy the condition (4.22).

Differentiation of V_L gives

$$\dot{V}_L = S\dot{S} = S\left[f(t+t_d) + \omega_n^2 u(t) - \ddot{y}_d(t) + \lambda\dot{e}\right]. \tag{4.42}$$

Substitution of (4.15), (4.40) and (4.41) into (4.42) yields

$$\begin{aligned}\dot{V}_L &= S\left[f(t+t_d) + \frac{\omega_n^2}{\hat{\omega}_n^2}\left(-\hat{f}(t+t_d) + \ddot{y}_d(t) - \lambda\dot{e}\right) - \omega_n^2 k.sign(S) - \ddot{y}_d(t) + \lambda\dot{e}\right] \\ &= \left[\left(f - \hat{f}\right) + \left(\frac{\omega_n^2}{\hat{\omega}_n^2} - 1\right)\left(-\hat{f}(t+t_d) + \ddot{y}_d(t) - \lambda\dot{e}\right)\right]S - \omega_n^2 k.|S|\,.\end{aligned} \tag{4.43}$$

If k is chosen to satisfy

$$k \geq \frac{1}{\omega_{n1}^2}(F+\eta) + \left(1 - \frac{\hat{\omega}_n^2}{\omega_{n1}^2}\right)\left|u_{eq}\right|, \tag{4.44}$$

then the Lyapunov stability condition (4.22) is satisfied.

In the control law (4.40-4.44), the future values of the output and its derivative are required for the realization of the equivalent control and the robust control. An output predictor is therefore employed to estimate these values by casting the prediction as a state estimation process.

Consider a system with delayed input, written in the state space form:

$$\dot{\mathbf{x}}(t) = \mathbf{A}\mathbf{x}(t) + \mathbf{B}u(t - t_d), \tag{4.45}$$

where

$$\mathbf{x}(t) = \begin{bmatrix} x_1(t) \\ x_2(t) \end{bmatrix} = \begin{bmatrix} y(t) \\ \dot{y}(t) \end{bmatrix}, \tag{4.46}$$

$$\mathbf{A} = \begin{bmatrix} 0 & 1 \\ -\hat{\omega}_n^2 & -2\hat{\delta}\hat{\omega}_n \end{bmatrix}, \tag{4.47}$$

$$\mathbf{B} = \begin{bmatrix} 0 \\ \hat{\omega}_n^2 \end{bmatrix}. \tag{4.48}$$

The value of $\mathbf{x}(t+t_d)$ can be extrapolated from (4.45) as

$$\mathbf{x}(t+t_d) = e^{\mathbf{A}t_d}\mathbf{x}(t) + \int_{-t_d}^{0} e^{-\mathbf{A}\theta}\mathbf{B}u(t+\theta)d\theta. \tag{4.49}$$

Using the calculated output and its derivative, the equivalent control (4.40) can be realised with the assumption that the time delay is constant.

It is noted that the SMC control outputs in (4.26), (4.28), and (4.41) have to be switched very rapidly to keep the system trajectory within a small neighbourhood of the sliding surface. A high frequency switching control is, however, very difficult to be achieved in practice due to the limitations of physical actuators. Because real systems cannot respond as rapidly as required, small oscillations around the desired value–chattering– can occur in the responses. To reduce this effect, the signum function in (4.28, 4.41) can be replaced by a saturation function (Hung *et al.*, 1993). However, as a trade-off, the robustness of the controller will be reduced.

4.3 Simulation results

In this section, the above control approaches are tested with a wide range of systems. Firstly, the engine throttle control is simulated as an example of the control design for a linear system. Secondly, for the nonlinear brake control system, a first-order Taylor series approximation is used to linearise the time delay between the input and output. Finally, the control design is verified for the actual brake system with the time-delay.

4.3.1 Linear system: throttle control

System modelling

The actuator for controlling the engine throttle consists of a DC motor and a reduction gear system. It can be modelled as a DC motor with a suitable gain representing the gear ratio. The electrical and mechanical dynamics of a DC motor are described by (Franklin *et al.*, 2002) as

$$J_m\ddot{\theta}_M + B_m\dot{\theta}_M = T_m = K_t I, \tag{4.50}$$

$$L_m\dot{I} + R_m I = V - e_{emf} = V - K_e\dot{\theta}_M, \tag{4.51}$$

where J_m, B_m, L_m, and R_m are respectively the rotor inertia, viscous friction coefficient, armature winding inductance and resistance. V is the applied voltage and I is the armature current. T_m and e_{emf} are the motor torque and back electromotive force. They are related to the current and rotational velocity by constant factors K_t and K_{em}.

From (4.50) and (4.51), the relationship between the motor position and the supplied voltage is obtained as

$$\frac{\theta_M}{V} = \frac{K_t}{s\left[(J_m s + B_m)(L_m s + R_m) + K_t K_{em}\right]}. \tag{4.52}$$

As the motor output is connected to the engine throttle through a gear system, the throttle position can be calculated by

$$\frac{\theta_e}{V} = \frac{\dfrac{K_t K_G}{R_m B_m}}{s\left[\left(\dfrac{J_m}{B_m}s + 1\right)\left(\dfrac{L_m}{R_m}s + 1\right) + \dfrac{K_t K_{em}}{R_m B_m}\right]}, \tag{4.53}$$

where K_G is the gear ratio.

In practice, the electric time constant (L_m/R_m) is very small compared with its mechanical counterpart (J_m/B_m) and may be neglected. In this case, (4.53) becomes

$$\frac{\theta_e}{V} = \frac{K_m}{s[\tau_m s + 1]}, \tag{4.54}$$

with the gain and time constant calculated as

$$K_m = \frac{K_t K_G}{R_m B_m + K_t K_{em}}, \tag{4.55}$$

$$\tau_m = \frac{R_m J_m}{R_m B_m + K_t K_{em}}. \tag{4.56}$$

Control implementation and results

To implement the proposed control approach, a PID controller is first designed for the system and its closed-loop response is obtained. With the actuator parameters chosen as listed in Table 4.1 and $K_P = 5$, $K_I = 100$, $K_D = 0$, the system under PID control exhibits an overshoot around 64% at the peak time of 0.25s. The closed-loop system is then approximated by (4.6) and (4.7) with parameters calculated from (4.3) and (4.4) as

$$\begin{aligned} \omega_n &= 13.54\,\text{rad/s}, \\ \delta &= 0.14. \end{aligned} \tag{4.57}$$

These parameters are constant as long as the system is linear. Therefore, (4.10) becomes,

$$\begin{aligned} \hat{\omega}_n &= \omega_{n1} = \omega_{n2} = \omega_n, \\ \hat{\delta} &= \delta_1 = \delta_2 = \delta. \end{aligned} \tag{4.58}$$

The SMC is implemented with control law (4.28) and condition (4.30). Assuming that the system is perturbed by an external disturbance with amplitude around 20% of the maximum reference (100%), the condition can be chosen as k is 21%.

The control output (%) with $\lambda = 20$ and a comparison in the responses between the PID and the proposed controller are shown in Figures 4.7 and 4.8. It can be seen that, with the PID controller only, a step reference (set-point) (Figure 4.7c) creates an oscillating voltage at the input of the motor (Figure 4.8a) and results in a large overshoot at the engine throttle shaft (Figure 4.8b). In contrast, the SMC modulates the PID input (control output of SMC, u) (Figure 4.7c) and the motor input (Figure 4.8a) to eliminate completely the overshoot while maintaining the desired setting time (Figure 4.8b).

As noticed earlier, chattering can occur at the control outputs. A simple way of reducing this effect is to use a saturation function instead of a signum one. The results with reduced chattering are provided in Figures 4.9 and 4.10. The control output is smooth while the response is still very good as compared with the PID controller.

To test robustness of the controller, an external disturbance is added to the output of the motor shaft. Results are shown in Figure 4.11 for the original control using the sign function and Figure 4.12 for the control with the chattering reduction applied. In both cases, with a disturbance amplitude of around 20% of the reference, the SMC-PID response still follows the reference correctly while the PID response fluctuates over 50%.

TABLE 4.1
THROTTLE SYSTEM PARAMETERS

Parameter	Value
J_m	3.228 x 10^{-6} kg.m^{2}s^{-2}
B_m	3.508 x 10^{-6} Nms
L_m	2.75 x 10^{-6} H
R_m	4 Ω
$K_t = K_{em}$	0.027 Nm/A
K_G	1/30

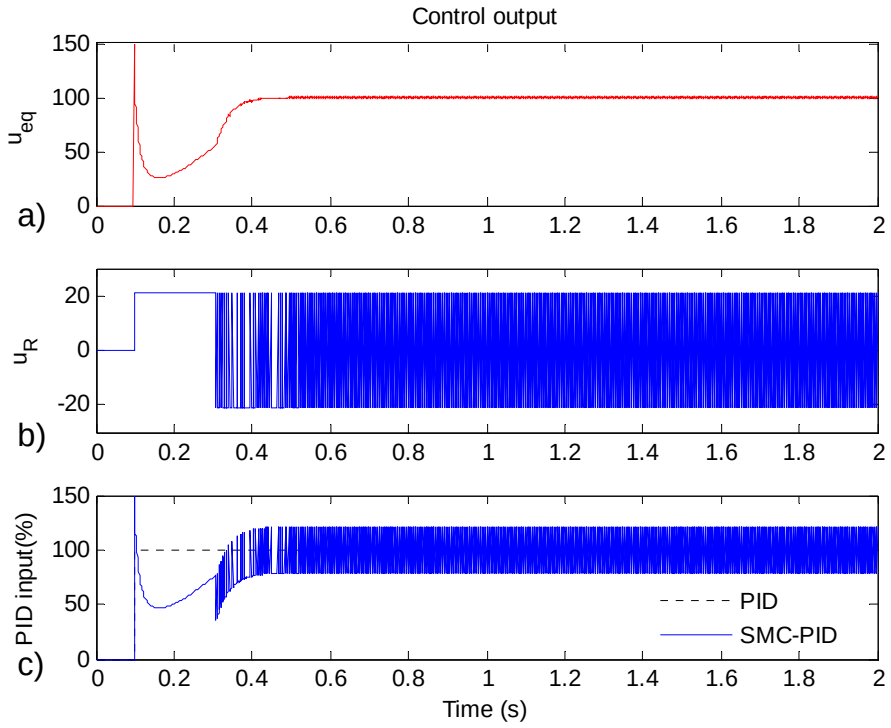

Figure 4.7 Command for throttle control

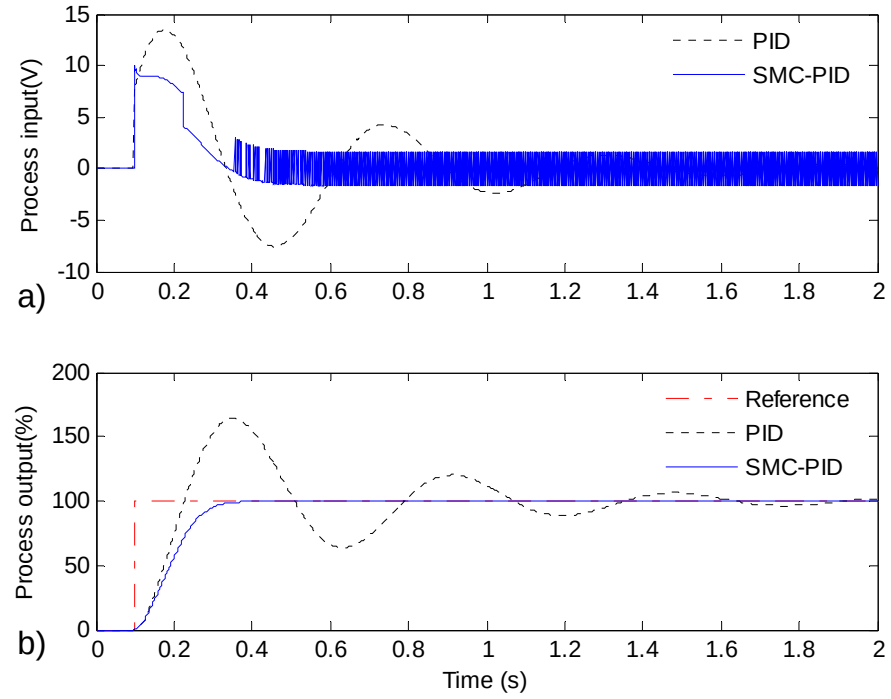

Figure 4.8 Responses of PID controller and SMC-PID for throttle control

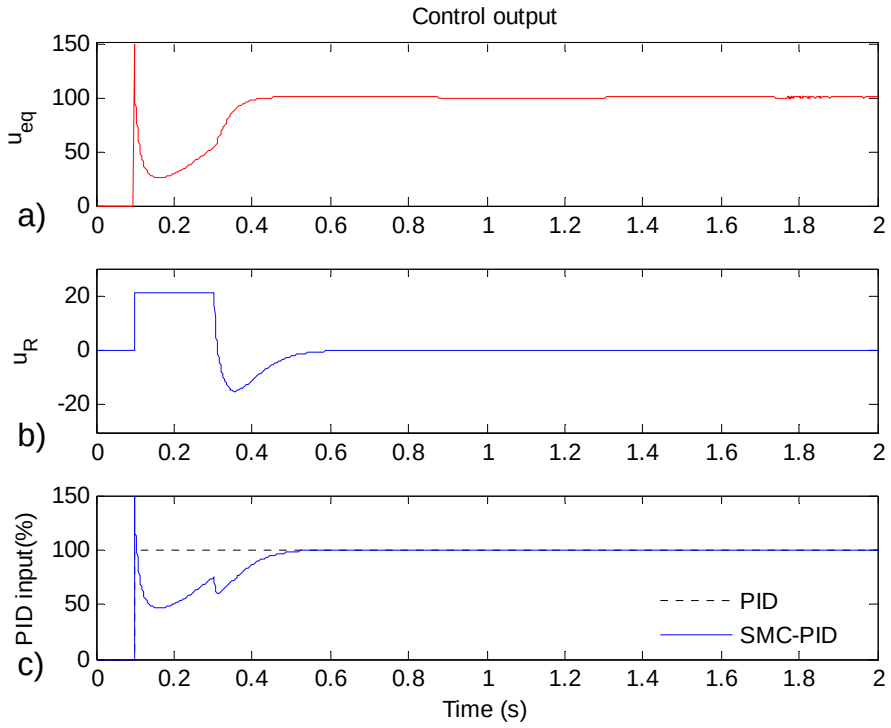

Figure 4.9 Command for throttle control (chattering reduction)

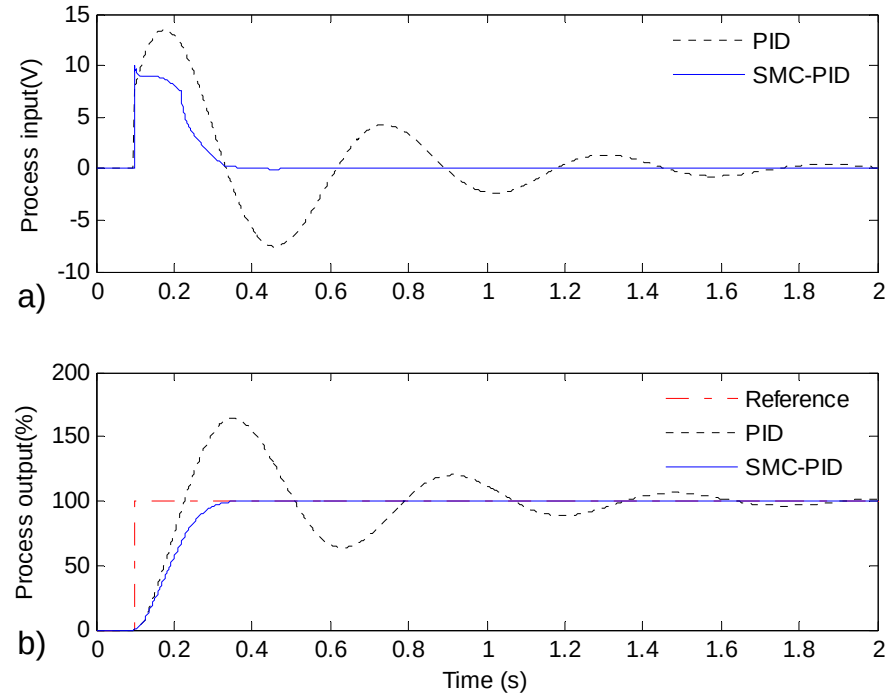

Figure 4.10 Responses of PID controller and SMC-PID for throttle control

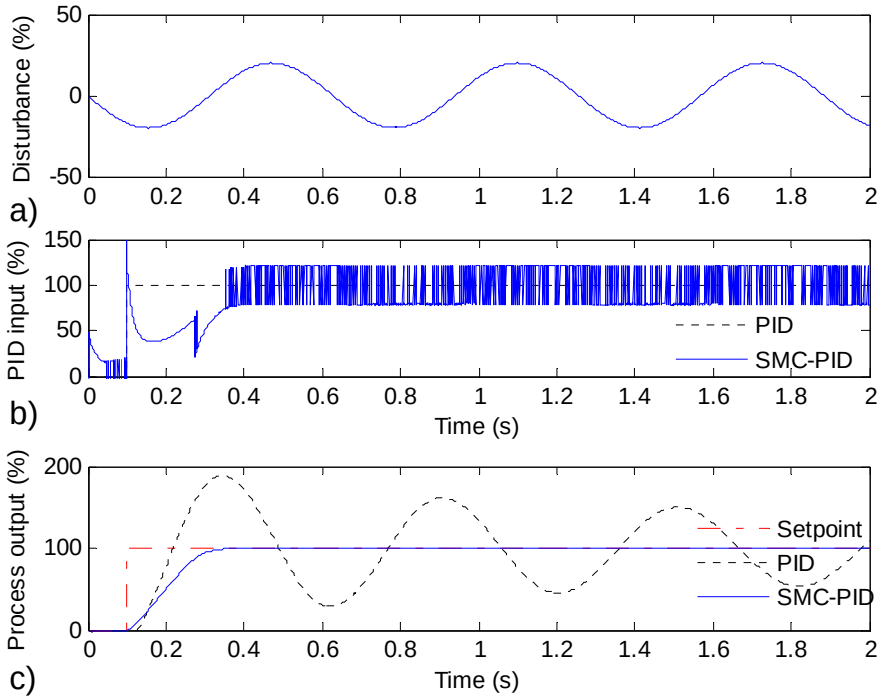

Figure 4.11 Responses with external disturbance (with chattering)

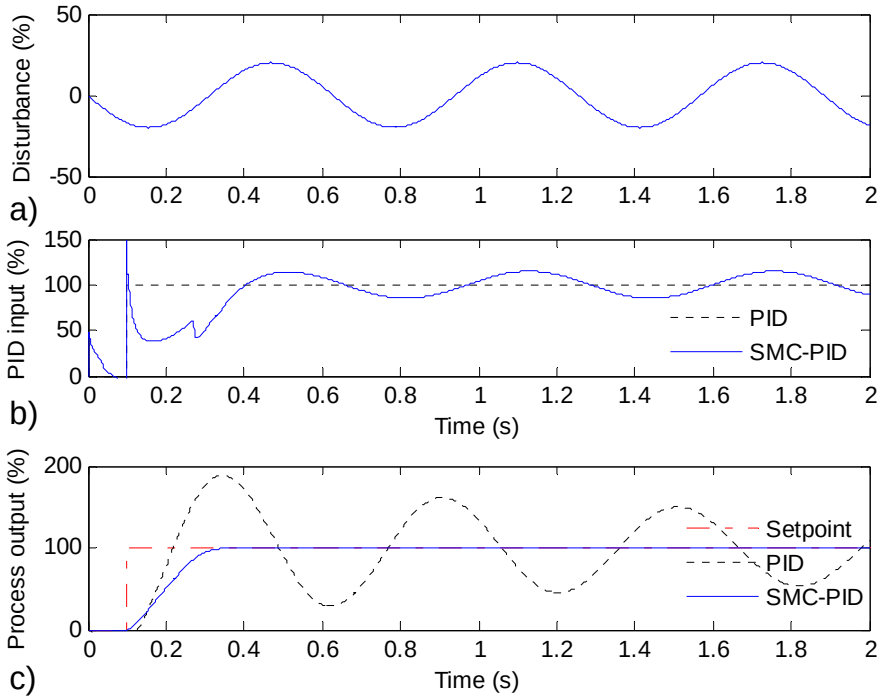

Figure 4.12 Responses with external disturbance (without chattering)

4.3.2 Nonlinear system: brake control with Taylor series approximation for time-delay

System modelling

Figure 4.13 shows the basic block diagram of the brake system, which consists of an amplifier, the linear actuator, and the hydraulic cylinder. The amplifier is used in the torque mode which is equivalent to a current control loop. Assuming that the current control is ideal with very fast rise-time compared with mechanical response, the amplifier can be described by

$$I = K_a.V\,, \tag{4.59}$$

where V and I are the input voltage and the current supplying for the actuator, and K_a is the amplifier's gain.

The force produced at the output of the actuator is proportional to the supplied current:

$$F_m = K_i.I\,. \tag{4.60}$$

The output shaft of the actuator is connected directly to the brake piston. The piston's position can be obtained from the transform function

$$\theta_b = \frac{K_m}{s(J_m s + B_m)}(F_m - F_d), \tag{4.61}$$

where J_m, B_m are the actuator's inertia and viscous damping coefficient. In the above equation, K_m is the equivalent gear ratio inside the actuator, and F_d represents the friction and drag force inside the cylinder which is considered as a disturbance.

The input-output relationship of the hydraulic cylinder is rather complicated and need not be modelled. Here it is estimated from experimental data by using the least squares identification method as

$$y = 1.374\theta_b^2 - 5.138\theta_b + 2.778, \tag{4.62}$$

where both the output brake pressure y and the input piston's position θ_b are normalised within their ranges. This approximation is close to the experimental data, as shown in Figure 4.14.

As mentioned in Section 4.1, a time delay exists between the command input and output pressure response of the brake system. In this section, the time-delay is approximated by a first-order Taylor series approximation which renders the system non-delay,

$$e^{-t_d s} \cong \frac{1}{t_d s + 1}, \tag{4.63}$$

where t_d is the time-delay.

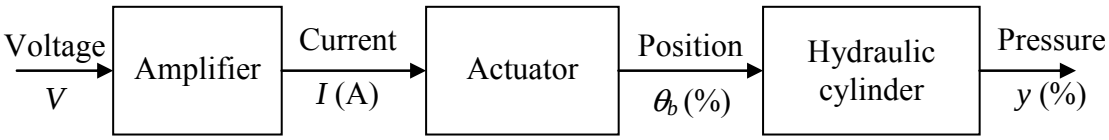

Figure 4.13 Block diagram of the brake system

TABLE 4.2
BRAKING SYSTEM PARAMETERS

Parameter	Value
K_a	2 AV^{-1}
K_i	440 NA^{-1}
K_m	0.1815
B_m	33 Nms
J_m	0.323 $kg.m^2s^{-2}$
t_d	0.2s

TABLE 4.3

PID RESPONSES AND CLOSED-LOOP MODEL PARAMETERS

Step input	Overshoot (%)	Peak time (s)	Damping ratio	Natural frequency (rad/s)
10%	15.1	0.673	0.516	6.71
25%	28.9	0.534	0.368	7.40
50%	38.7	0.443	0.289	8.41
75%	44.7	0.396	0.248	9.15
100%	49.2	0.365	0.220	9.75

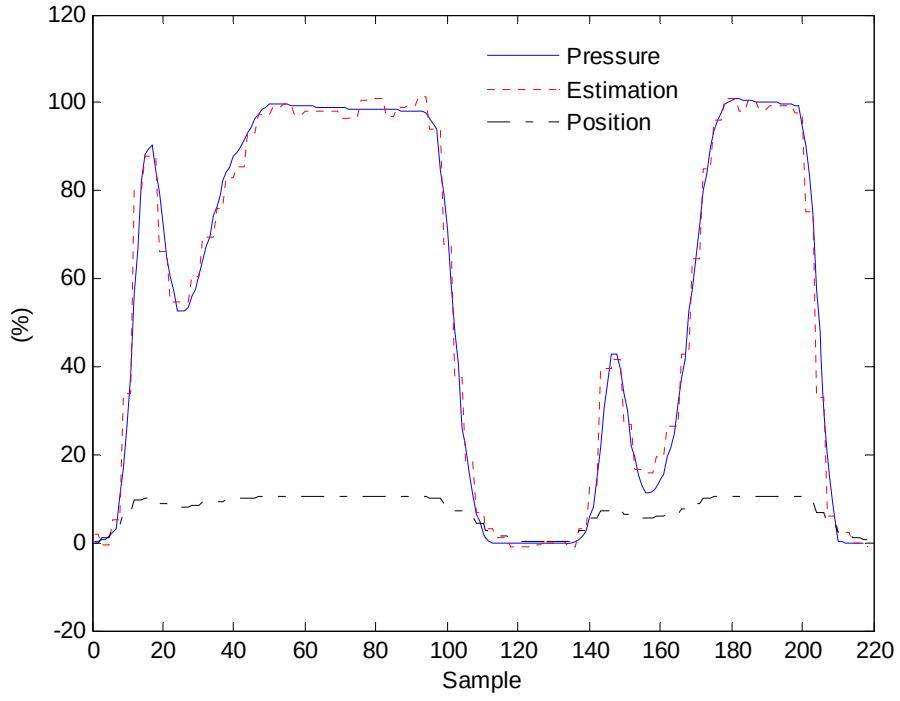

Figure 4.14 Estimated I/O relationship of the hydraulic cylinder

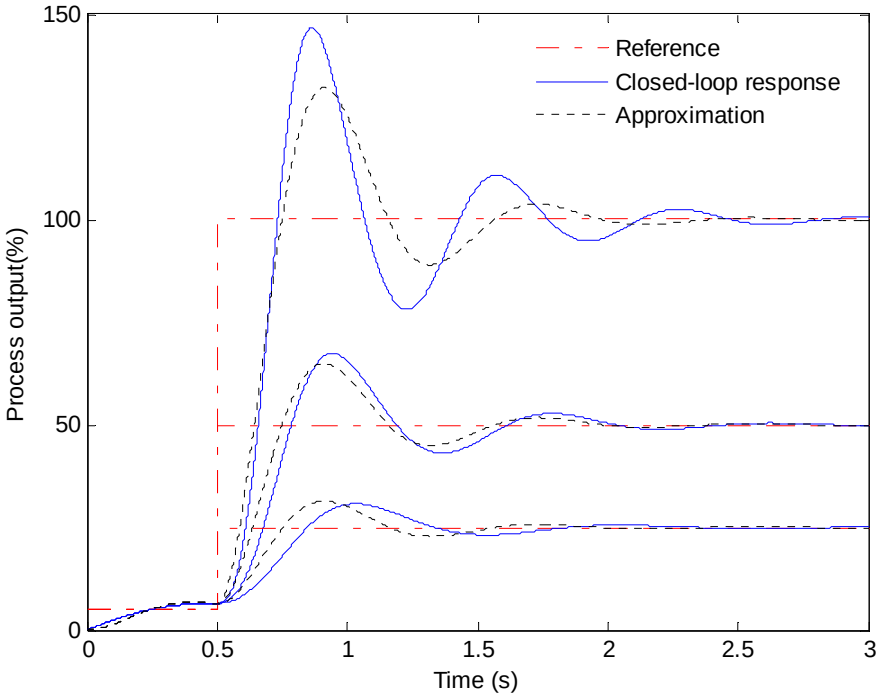

Figure 4.15 Responses of PID closed-loop and approximate model

Control implementation and results

Applying the proposed control approach described in Section 4.2.2, a PID controller is first used to control the brake pressure, where parameters of the system are provided in Table 4.2. The reference is taken from 5% to 100% of the maximum pressure. The PID controller is tuned manually to obtain fast responses. Characterisation of PID responses (overshoot and peak time) and the closed-loop estimations (damping ratio and natural frequency) with the proportional gain of 0.15 and zeros for the other gains is provided in Table 4.3 for different values of the reference. It can be seen that both the overshoot and peak time are influenced by the amplitude of the reference input. As a result, parameters of the estimated closed-loop model (4.6-4.7) vary. The modelling parameters lie in the ranges

$$\begin{aligned} &6.7\,\text{rad/s} \le \omega_n \le 9.8\,\text{rad/s}, \\ &0.2 \le \delta \le 0.52, \end{aligned} \tag{4.64}$$

and have geometric mean values given by (4.10):

$$\hat{\omega}_n = 8.1031\,\text{rad/s}, \qquad \hat{\delta} = 0.3225. \tag{4.65}$$

The SMC is employed for the outer loop with control law (4.26). Due to the system's nonlinearity, there is a discrepancy between the actual responses of the braking system and of the model using mean parameter values (4.65), as shown in Figure 4.15. This mismatch can be overcome by using condition (4.25) with very small value of η. If a disturbance is present, condition (4.29) is used, where D is selected to account for the maximum disturbance.

The SMC control outputs and responses with $\lambda = 20$ and $\eta = 0.1$ are shown in Figures 4.16 and 4.17. With a step reference input, the PID control loop produces a large overshoot in the output pressure while the SMC shapes the PID input (Figure 4.16c) to force the output to become a non-overshoot response (Figure 4.17b). It is interesting to note that the fast rise-time is retained. Compared with the throttle control, the amplitude of the robust control is large (Figure 4.16b) which in turn, leads to a large oscillation in the input voltage (Figure 4.17a). This is necessary to overcome the nonlinearity and the modelling error.

The large oscillation of the input voltage due to the robust control has an adverse effect on the actuator. To reduce this, the robust control is modified by a saturation function. Results are shown in Figures 4.28 and 4.29. It can be seen that the chattering is reduced significantly while the output responses are practically unchanged.

The robustness of the SMC to the system's nonlinearity can be confirmed by setting different values for the reference input. Results with 50% and 10% of the maximum brake pressure are depicted in Figures 4.20 and 4.21. The responses are very good both in terms of no overshoot and fast settling time, compared with those of the PID controller. It is noted that the approximate model is close to the closed-loop system in the middle of the operating range (50%). At the reference of 100% and 10%, the difference between the model and the closed-loop response is rather large, as shown in Figure 4.15. Therefore, good results at 10% and 100% of set-point with a chattering reduction applied can account for the robustness of the controllers but a better treatment for the time delay effect would be worth pursuing.

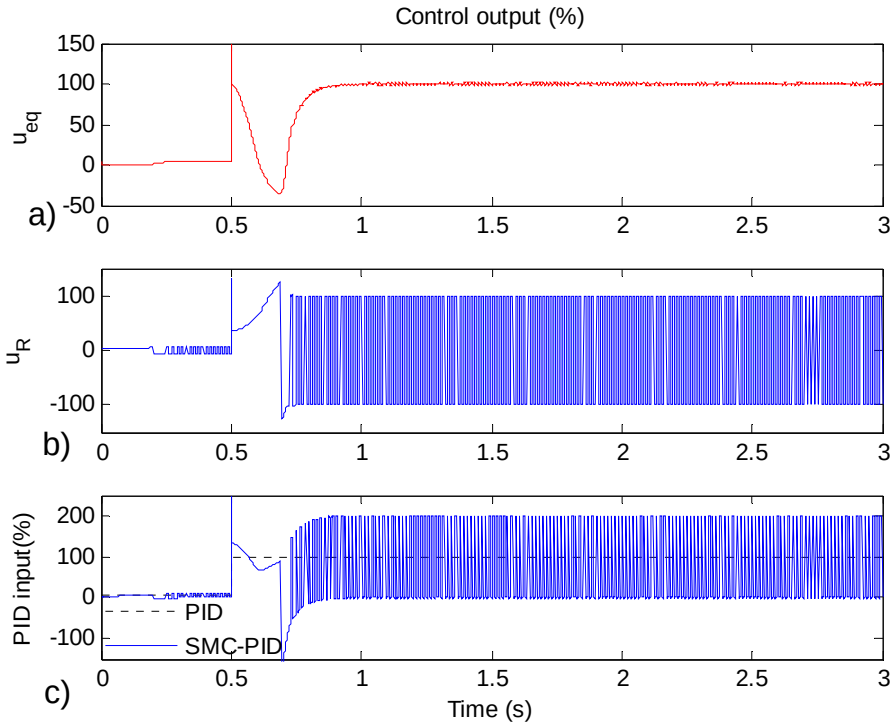

Figure 4.16 Command for brake control

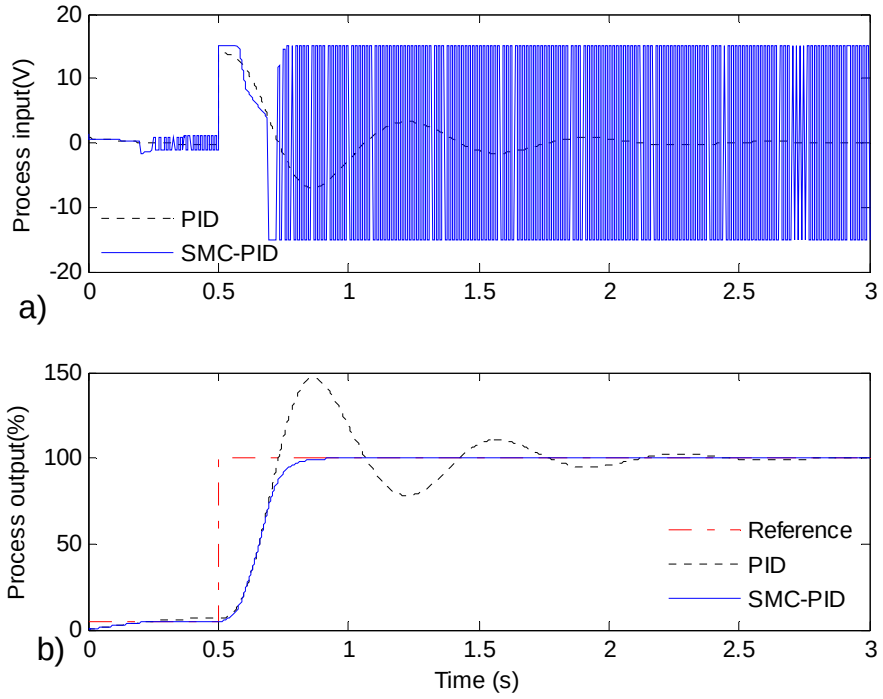

Figure 4.17 Responses of PID controller and SMC-PID for brake control

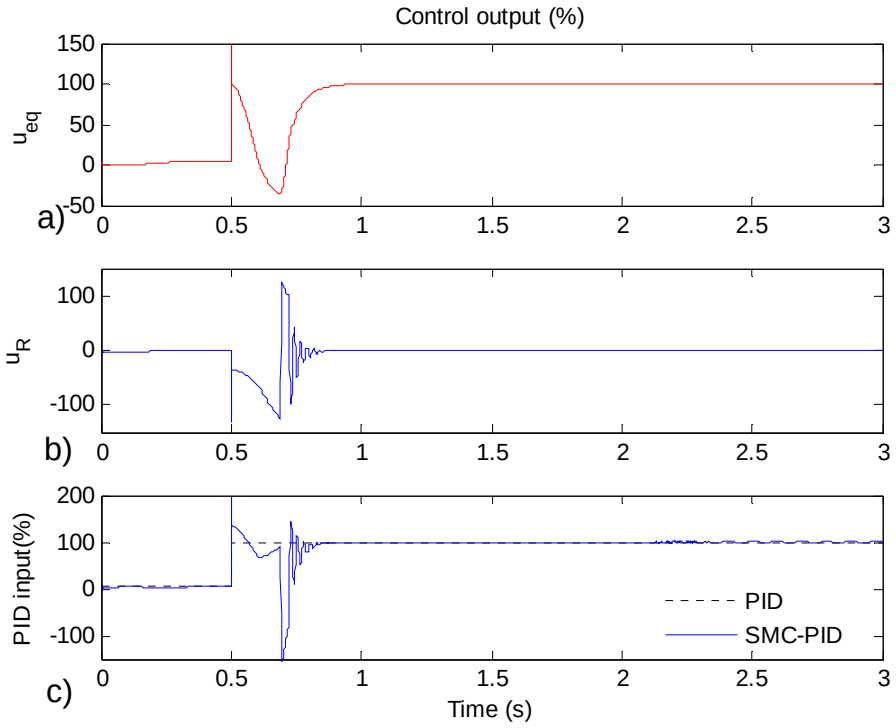

Figure 4.18 Command for brake control (chattering reduction)

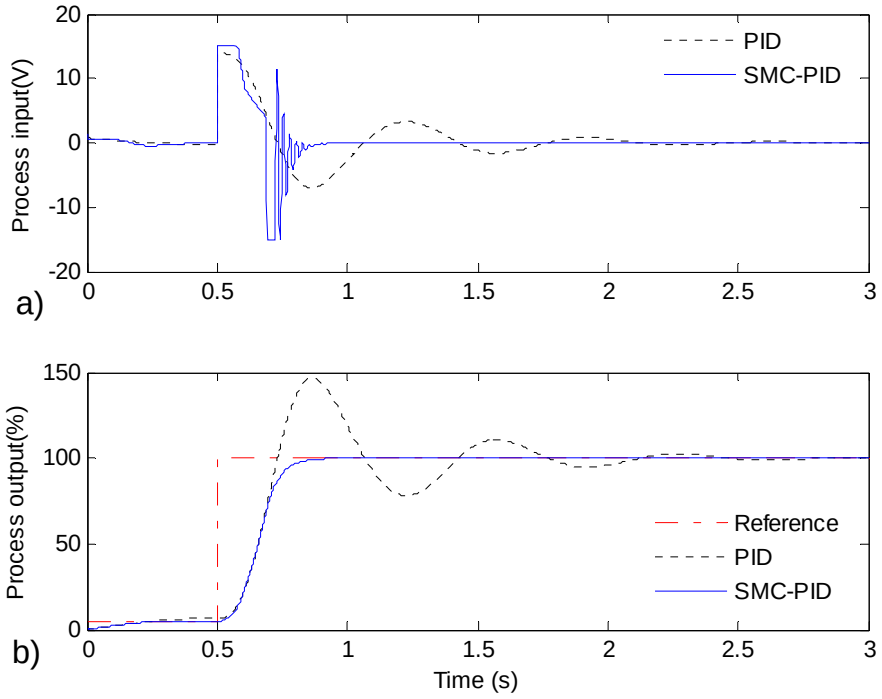

Figure 4.19 Responses of PID controller and SMC-PID for brake control

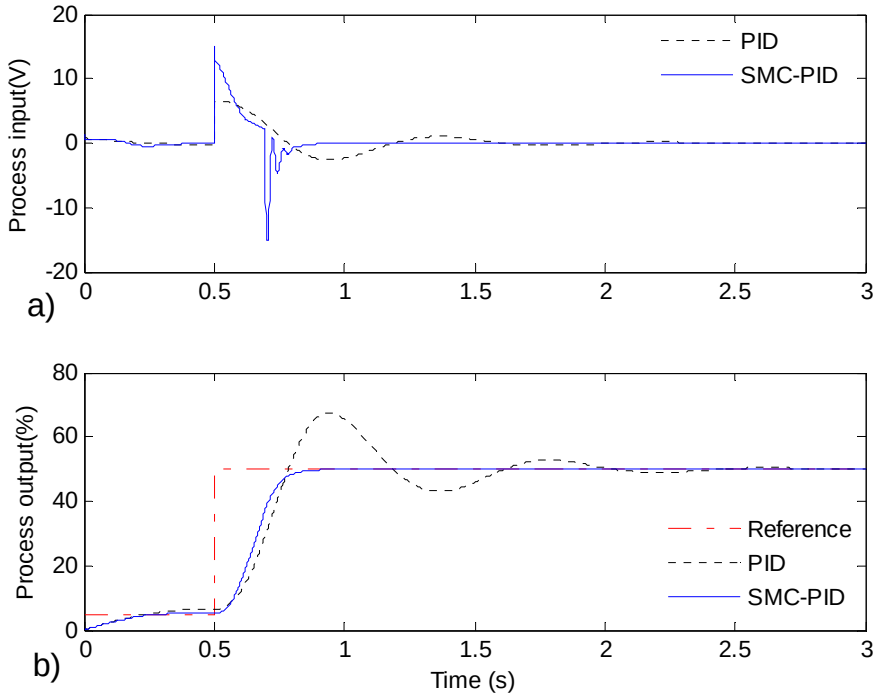

Figure 4.20 Responses with 50% of maximum brake force

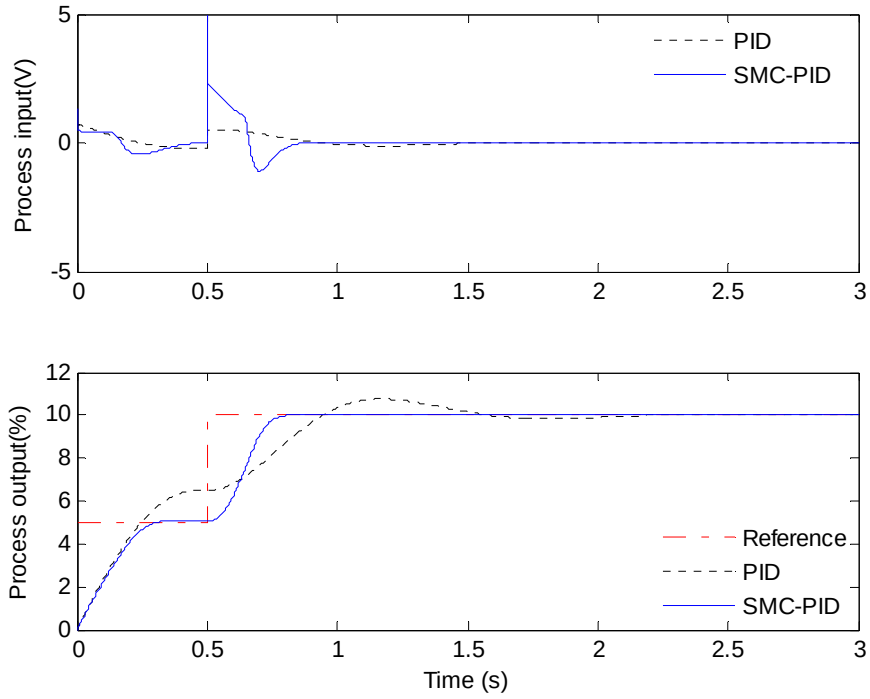

Figure 4.21 Responses with 10% of maximum brake force

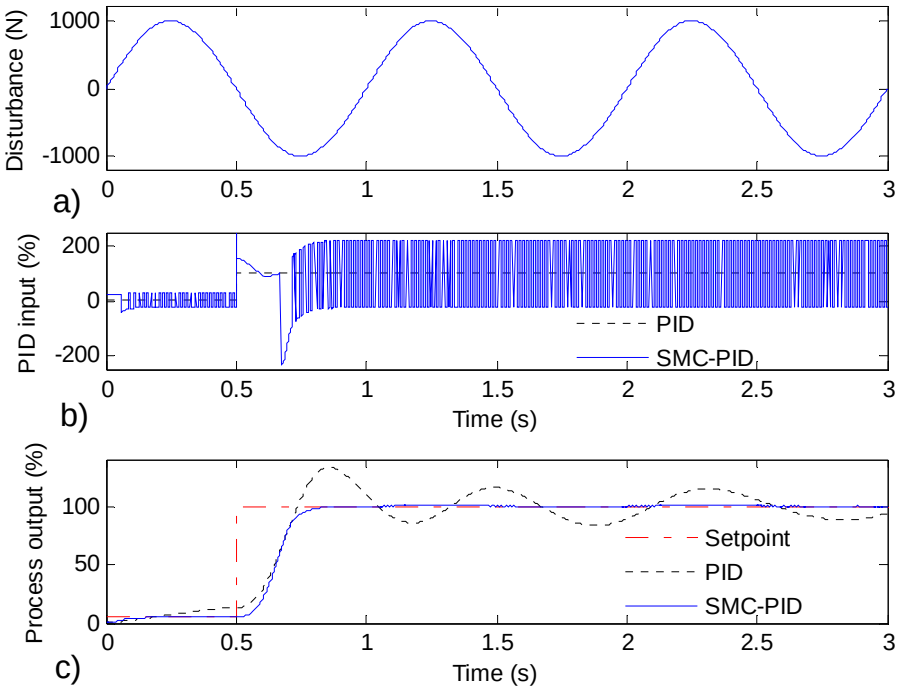

Figure 4.22 Responses with external disturbance (with chattering)

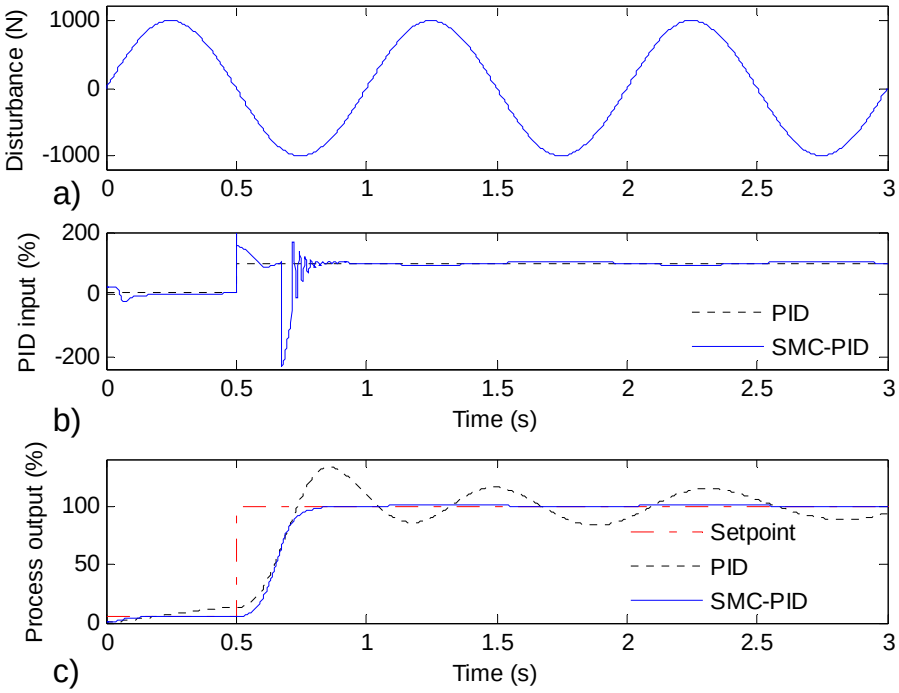

Figure 4.23 Responses with external disturbance (chattering reduction)

In order to test the response of the controller with disturbance, an external force with amplitude around 20% of the maximum actuator's force is applied on the brake piston. Results with D = 1000 are shown in Figure 4.22 for the original controller and Figure 4.23 for the controller with chattering reduction. In both cases, under the disturbance, the SMC controller's responses vary less than 0.05% compared with around 30% for the PID controller.

4.3.3 Nonlinear time-delay system: brake control with time-delay

In this section, the brake system in Section 4.3.2 is considered again with a time delay. The control approach proposed in Section 4.2.3 is used for controlling the brake pressure. A PID controller is present in the inner loop, resulting equivalently in responses of a second-order system. Due to the nonlinearity and time-delay, the model parameters are varied within the ranges

$$\begin{aligned} &6.2\,\text{rad/s} \le \omega_n \le 6.6\,\text{rad/s}\,, \\ &0.2 \le \delta \le 0.7\,, \end{aligned} \tag{4.66}$$

and approximated by geometric mean values in their ranges as

$$\begin{aligned} &\hat{\omega}_n = 0.6369\,\text{rad/s}\,, \\ &\hat{\delta} = 0.3742\,. \end{aligned} \tag{4.67}$$

The SMC is implemented by applying equations (4.40-4.41). Condition (4.44) is used to overcome the mismatching between the closed-loop system and its approximate model, as shown in Figure 4.24. Future values of the output and its derivative are estimated by the predictor (4.49). The predictor is discretised by the following equation,

$$\begin{aligned} \mathbf{x}(t+t_d) &= e^{\mathbf{A}t_d}\mathbf{x}(t) + \sum_{i=-\frac{t_d}{\Delta\theta}}^{0} e^{-\mathbf{A}.i.\Delta\theta}\mathbf{B}u(t+i\Delta\theta)\Delta\theta \\ &= \mathbf{E_1}\mathbf{x}(t) + \mathbf{E_2}\mathbf{U}\,, \end{aligned} \tag{4.68}$$

where $\Delta\theta$ = sample period,

$$\mathbf{E_1} = e^{\mathbf{A}t_d}\,,$$

$$\mathbf{E}_2 = \left[e^{-\mathbf{A}t_d}, \ldots, e^{\mathbf{A}.i.\Delta\theta}, \ldots, \mathbf{I}\right]\mathbf{B},$$

$$\mathbf{U} = \left[u(t-t_d), \ldots, u(t+i\Delta\theta), \ldots, u(t)\right]^T,$$

$$\mathbf{I} = \begin{bmatrix} 1 & 0 \\ 0 & 1 \end{bmatrix},$$

$$i = -\frac{t_d}{\Delta\theta}, -\frac{t_d}{\Delta\theta}+1, \ldots, 0\ .$$

The SMC control output and step responses of the system with $\lambda = 2$ are shown in Figures 4.25 and 4.26. It is observed that the PID controller exhibits a large overshoot in the output (pressure) while the SMC is able to shape the PID input (i.e., the control output of SMC, *u*, shown in Figure 4.25c) and the process input (shown in Figure 4.26a) to result in a non-overshoot step response as shown in Figure 4.26b. For the PID control, the overshoot reaches 50% while the proposed approach gives a very small amount of overshoot. A small chattering around the desired value is encountered as commonly found in SMC.

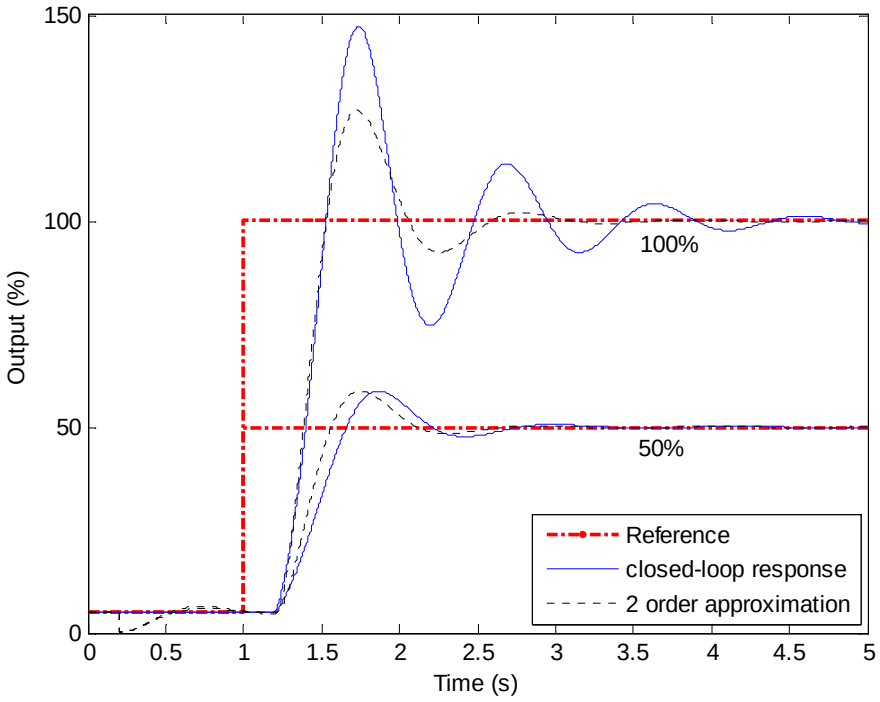

Figure 4.24 PID closed-loop and approximate model responses

To deal with chattering, a saturation function is used instead of the signum function in (4.41). The resulting control outputs and responses depicted in Figures 4.27 and 4.28 show that chattering is alleviated and the overall responses look satisfactory. However, a negligible overshoot may appear due to the trade-off between the SMC robustness and the chattering reduction.

The responses of the output predictor can be compared with the actual outputs as shown in Figure 4.29 in both cases: with and without chattering reduction. With the robust control using a signum function, the predicted output fluctuates around the reference value. Because the SMC by nature involves a high, discontinuous gain, the error in the prediction can result in small ripples in the controlled output, as seen also in Figure 4.26. Using a saturation function, the predictor output signal exhibits a smooth response, as can be seen in Figure 4.29. In overall, the predictor output tends to lead the actual output in time, however, is not exactly a time-shift version of the actual output. The controller has to overcome this mismatching to obtain reasonable responses.

Responses of the system (with a saturation function used) at different operating points, namely 25%, 50% and 75% of the maximal braking effort, are shown in Figure 4.30. All responses indicate a significant reduction of the overshoot while the rise-time remains almost the same for various operating settings. Moreover, the settling time and steady-state accuracy are also preserved. These results serve to demonstrate the expected robustness of the proposed controller at different operating points. This verifies the effectiveness of the proposed approach. It is expected that the approach may be useful for control design for a general uncertain system with input time delay. As a result of the reduction of throttle and brake response overshoot, driving or turning smoothness as an essential component of reliable and controllable UGV operations is therefore guaranteed.

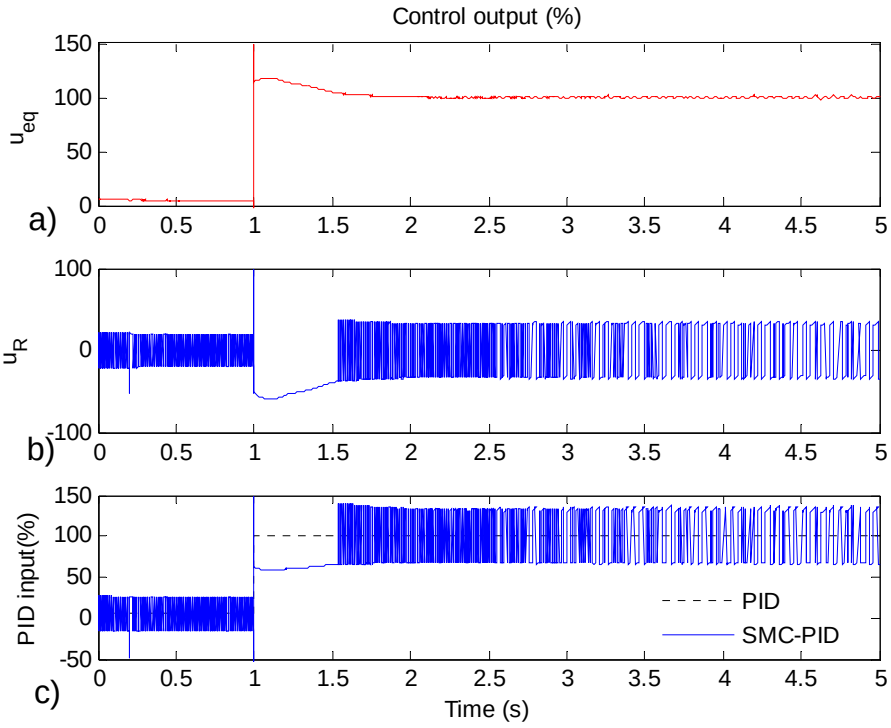

Figure 4.25 Command for brake control with time-delay

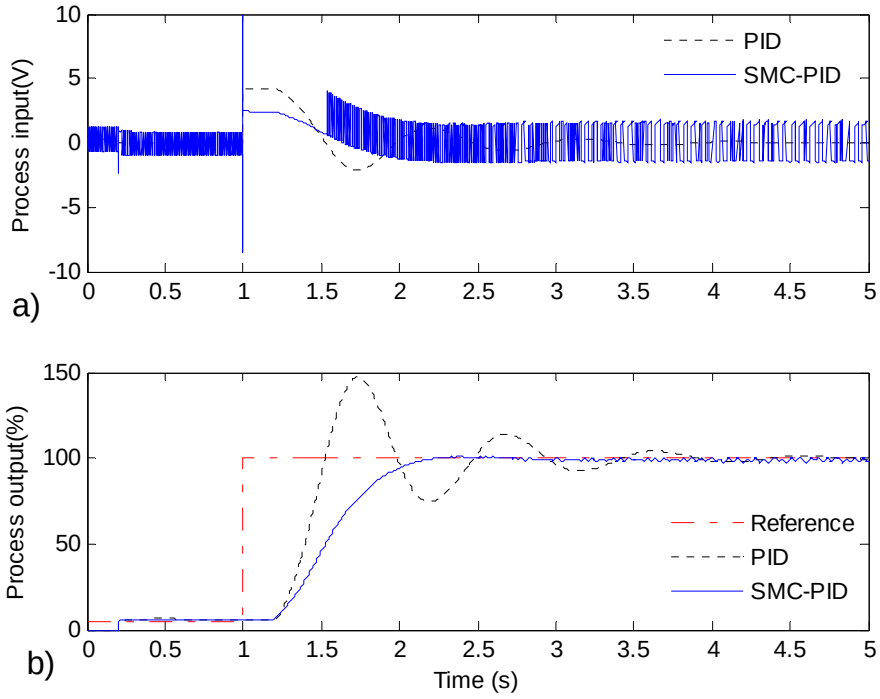

Figure 4.26 Responses of PID controller and SMC-PID for brake control

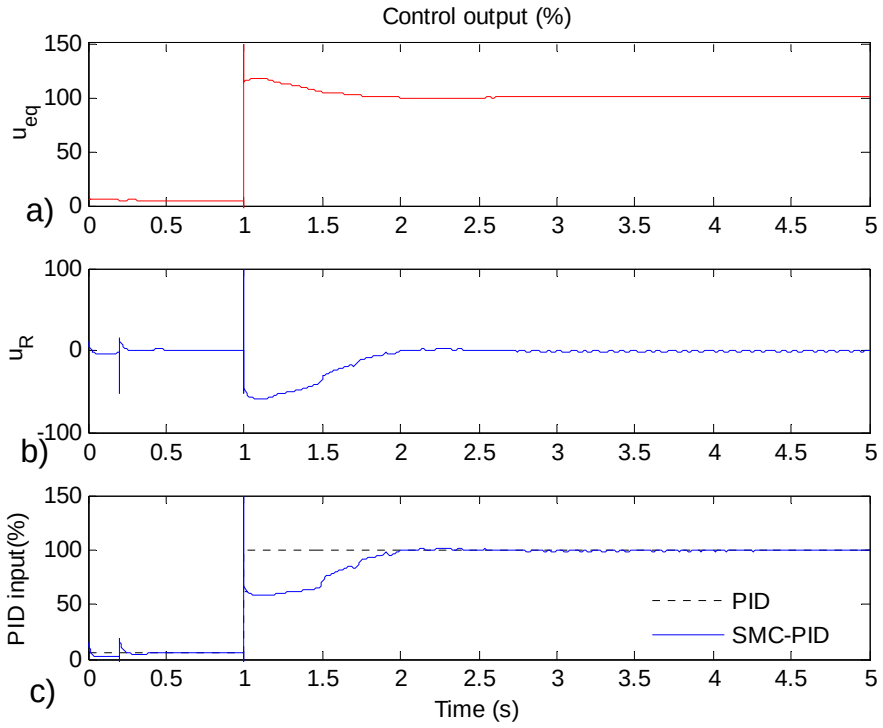

Figure 4.27 Command for brake control with time-delay (chattering reduction)

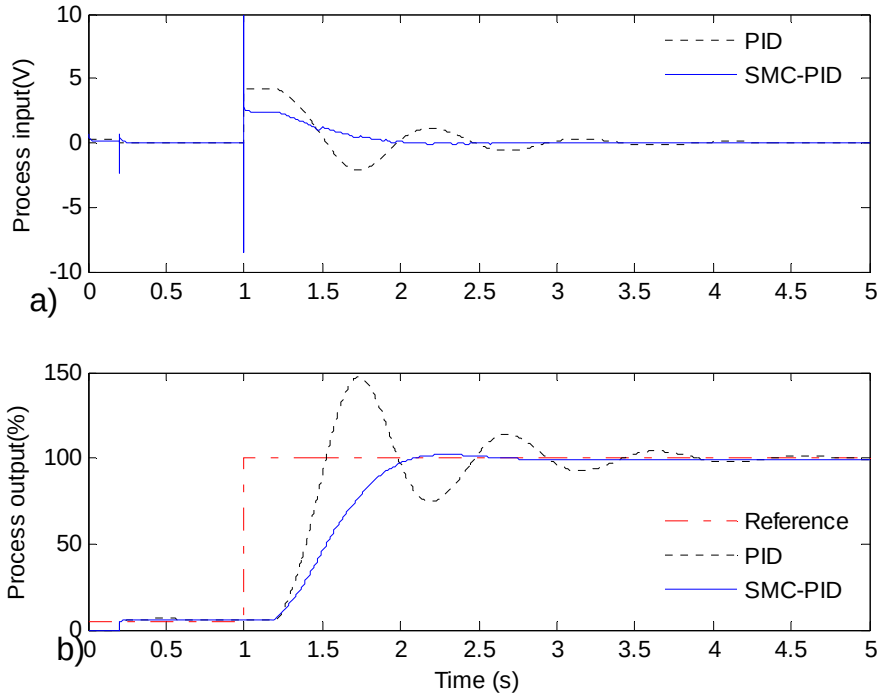

Figure 4.28 Responses of PID controller and SMC-PID for brake control

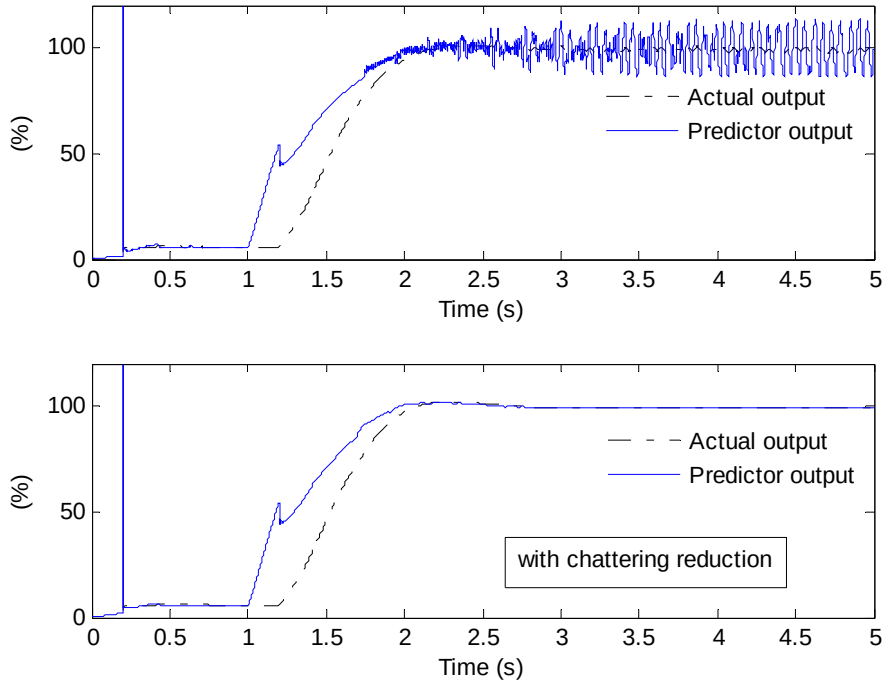

Figure 4.29 Output predictor responses

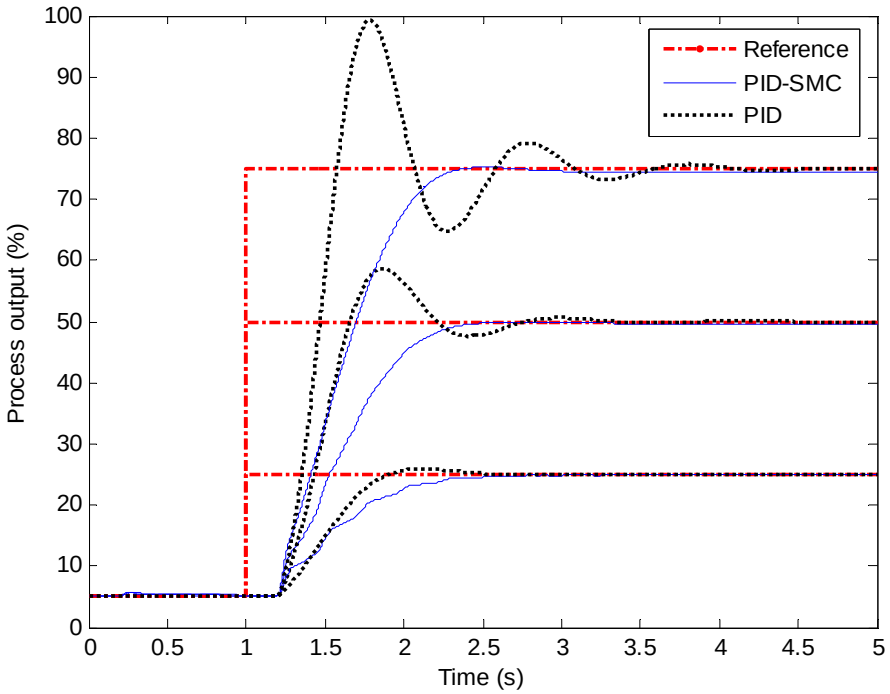

Figure 4.30 Responses of PID and SMC-PID control at different operating points

4.4 Conclusion

This chapter has presented effective methods to suppress overshoot of system responses under PID controllers for a wide range of systems varying from linear to nonlinear with and without time-delay. Based on an equivalent transfer function of the PID inner-loop system, a SMC is designed to shape the input of the PID so that overshoot of its step response is eliminated while robustness of other control performances is preserved. Simulation results for the throttle and the hydraulic brake control systems have indicated that the proposed method is very effective in achieving non-overshoot responses while maintaining the settling time and steady-state error at different operation settings and against large system uncertainties.

The proposed approaches can be applied to control the engine speed, vehicle velocity and turning rate. The engine speed controller can be tested with the driveline model developed in Chapter 3. The velocity and turning rate controllers cannot, however, be verified without considering the interaction between the wheels and terrain because the vehicle behavior depends not only on the driveline and actuator responses but also on the terrain. Effects of different terrain types on the vehicle performances will be considered in the next chapter.

Chapter 5

Vehicle-terrain interaction

In Chapter 3, while considering the driveline model, interaction between the vehicle and terrain was ignored with an assumption that there was no slip between the wheels and terrain. The vehicle is intended for applications in unprepared areas, where the terrain characteristics strongly affect the vehicle performance. Ignoring the vehicle-terrain interaction during navigation can lead the vehicle to dangerous situations such as rolling over. In this chapter, the dynamic processes involved in this interaction are comprehensively analysed and an interaction modelling procedure is proposed for predicting the vehicle behaviour on different types of terrain.

An introduction to vehicle-terrain interaction is given in the first section of this chapter. Section 5.2 presents the fundamental theory that applies to the interaction between a driven wheel and soft terrain. The theoretical development for predicting the performance of the UGV is described in Section 5.3. Simulation results and a validation with experiment data are given in Section 5.4. Finally, conclusions are drawn in the last section.

5.1 Introduction

As mentioned in Chapter 3, the UGV has eight wheels organized in a skid-steering configuration. When the vehicle is turning, the wheels slide on the ground, both in the

longitudinal and lateral directions. The influence of the terrain on the vehicle behaviour is, therefore, very complicated. Attempting to turn or stop when the vehicle is running at high speed or on slopes can result in undesirable or dangerous responses. For safe locomotion it is therefore required to have a good understanding of the interaction between the wheels and terrain.

In analysing vehicle tractive performance, two main approaches have been used. In the first approach, tractive force is assumed to obey the Coulomb friction law, which is proportional to the normal load at the wheel (Creedy, 1985; Weiss, 1971) or the LuGre friction law (Canudas de Wit and C. Horowitz, 1999; Velenis *et al.*, 2005). Different values of friction can be assigned for longitudinal and lateral motion. This approach is widely used for cars and trucks. For off-road vehicles, however, it is not completely applicable (Wong and Chiang, 2001).

The other approach, proposed by Bekker (1969) and later developed as terramechanics, is based on soil mechanics and the measurement of terrain responses under similar conditions happened with vehicles (Wong, 2001). In the work therein, a rectangular plate was used to imitate the loading actions of wheels or tracks on terrain. Data collected in penetration experiments with a rectangular plate was used to derive the relationship between the pressure exerted on the terrain under the plate and the sinkage of the plate. Similarly, shear action of wheels/tracks on a terrain was simulated by a shear plate and the shear stress-shear displacement relation was obtained experimentally from shear tests. By assuming that the terrain interacts on wheels/tracks similarly as it does on a plate, reaction forces of the terrain on the vehicle can be obtained. Recently, many applications of terramechanics in analysing off-road vehicle mobility have been reported (Hutangkabodee *et al.*, 2006; Iagnemma *et al.*, 2004; Ishigami *et al.*, 2007; Legnemma *et al.*, 2004; Ojeda *et al.*, 2006; Shiller, 2007).

Other approaches have been proposed for skid-steering performance analysis, see Creedy, 1985; Weiss, 1971. However, in both approaches, reaction forces are assumed to follow the Coulomb friction which is not realistic for off-road vehicles. In a different approach, Wong and Chiang (2001) developed a comprehensive interpretation incorporating the terramechanics to predict skid-steering behaviours. However, their approach can only be applied to tracked vehicles because the reactions of terrain on the

skid-steering wheeled vehicles are different from and more complex than those on the tracked ones, although their steering principles are similar.

In this chapter, the principles of terramechanics as applied for a rigid driven wheel in two dimensions (longitudinal and vertical) is extended to account for lateral motion and applied to all wheels of the UGV. The reaction forces on the wheels interacting with the ground are then combined with the vehicle kinetics to derive the vehicle dynamics both in straight line running and turning.

5.2 Fundamental of terramechanics

Let us consider a driven rigid wheel running on a deformable ground. Under the action of the vertical load and driving torque, the wheel compresses the soil to a sinkage z, as shown in Figure 5.1 (Iagnemma *et al.*, 2004). The stress acting normal to the wheel-terrain contact point, is derived from the sinkage *z* through the pressure-sinkage relationship (Bekker, 1969):

$$\sigma(\theta) = \left(\frac{k_c}{b} + k_\phi \right) z(\theta)^n, \tag{5.1}$$

$$z(\theta) = r(\cos\theta - \cos\theta_1), \tag{5.2}$$

where n is the sinkage exponent, k_c, k_ϕ are the pressure-sinkage moduli of the terrain, b is the wheel width, r is the wheel radius, θ is the contact angle at a considered point, and θ_1 is the entry angle at which the wheel first makes contact with the terrain.

The maximum normal stress point, θ_m, separates the contact zone into front and rear regions (θ_1-θ_m and θ_m-θ_2), where θ_2 is the wheel angular location at which the wheel loses contact with the terrain. The normal stresses distributed on these regions are calculated by the following equations (Wong and Reece, 1967):

$$\sigma_1(\theta) = \left(\frac{k_c}{b} + k_\phi \right) r^n (\cos\theta - \cos\theta_1)^n, \tag{5.3}$$

$$\sigma_2(\theta)=\left(\frac{k_c}{b}+k_\phi\right)r^n\left(\cos\left(\theta_1-\left(\frac{\theta-\theta_2}{\theta_m-\theta_2}\right)(\theta_1-\theta_m)\right)-\cos\theta_1\right)^n. \tag{5.4}$$

Experiments have shown that θ_2 is very small so that it can be ignored and θ_m is often assumed to lie in the middle of the contact zone (Iagnemma *et al.*, 2004). In this case, equation (5.4) becomes

$$\sigma_2(\theta)=\left(\frac{k_c}{b}+k_\phi\right)r^n(\cos(\theta_1-\theta)-\cos\theta_1)^n. \tag{5.5}$$

For loose sand, saturated clay, sandy loam, and most distributed soils, the shear stress, which is the tangential component of the stress at the wheel-terrain contact point, exhibits an exponential relationship with respect to the shear displacement (Wong, 2001):

$$\tau(\theta)=(c+\sigma(\theta)\tan\phi)\left(1-e^{-j/K}\right), \tag{5.6}$$

where K is the shear deformation modulus, j is the shear displacement, c and ϕ are respectively the cohesion and the internal friction angle of the terrain.

Integrating the vertical and horizontal components of the shear and normal stresses along the contact zone gives the following force balance equations:

$$W=rb\left[\int_{\theta_2}^{\theta_1}\sigma(\theta)\cos\theta d\theta+\int_{\theta_2}^{\theta_1}\tau(\theta)\sin\theta d\theta\right], \tag{5.7}$$

$$DP=rb\left[\int_{\theta_2}^{\theta_1}\tau(\theta)\cos\theta d\theta-\int_{\theta_2}^{\theta_1}\sigma(\theta)\sin\theta d\theta\right], \tag{5.8}$$

and the wheel driving torque:

$$T=r^2b\int_{\theta_2}^{\theta_1}\tau(\theta)d\theta, \tag{5.9}$$

where *W*, *DP* and *T* are the vertical load, horizontal force or drawbar pull, and the torque applied to the wheel axis.

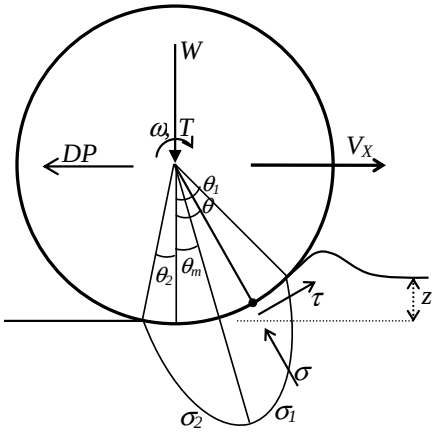

Figure 5.1 Wheel-terrain interaction: free-body diagram

5.3 Wheel-terrain interaction analysis

In this section, a comprehensive analysis for a skid-steering wheeled vehicle is developed by making use of terramechanics theory. In general, shear displacements at a considered point on the wheel and in contact with the ground are obtained from the slip velocity of this point with respect to the ground. Shear stresses are then derived and further integrated over contact zones to give the reaction forces on all wheels. Figure 5.2 shows a free-body diagram of the UGV considered in this thesis where the wheels are in contact with a deformable terrain.

For the sake of enabling the analysis, the following assumptions are made:

1. The ground is firm, flat and homogeneous. The wheel tyres are sufficiently hard relative to the ground to be considered as rigid.
2. The shear stress-shear displacement relationship is uniform in all directions.
3. During turning, the 'bulldozing effect' of the wheels in the lateral direction is small enough to be ignored.
4. The shear stress developed at a wheel-terrain contact point is opposite to the direction of the slip velocity.

5. The vehicle incline angle resulting from wheel sinkage is small enough to be ignored.

Assumption 1 is the necessary condition for applying terramechanics and is reasonable since the UGV wheels are much harder than soft terrains. Assumption 2 is required to derive the terrain lateral reaction, and is a consequence of Assumption 1. Assumption 3 is derived from the fact that wheel sinkage is very small and the lateral load that results from the bulldozing is very small compared to the lateral reaction forces. In addition, Assumption 4 is a fact according to Newton's third law. It is used to derive the reaction forces in longitudinal, lateral, and vertical direction. Finally, Assumption 5 is reasonable as the rear wheel sinkage (z_7 in Figure 5.2) is very small compared with the vehicle's length.

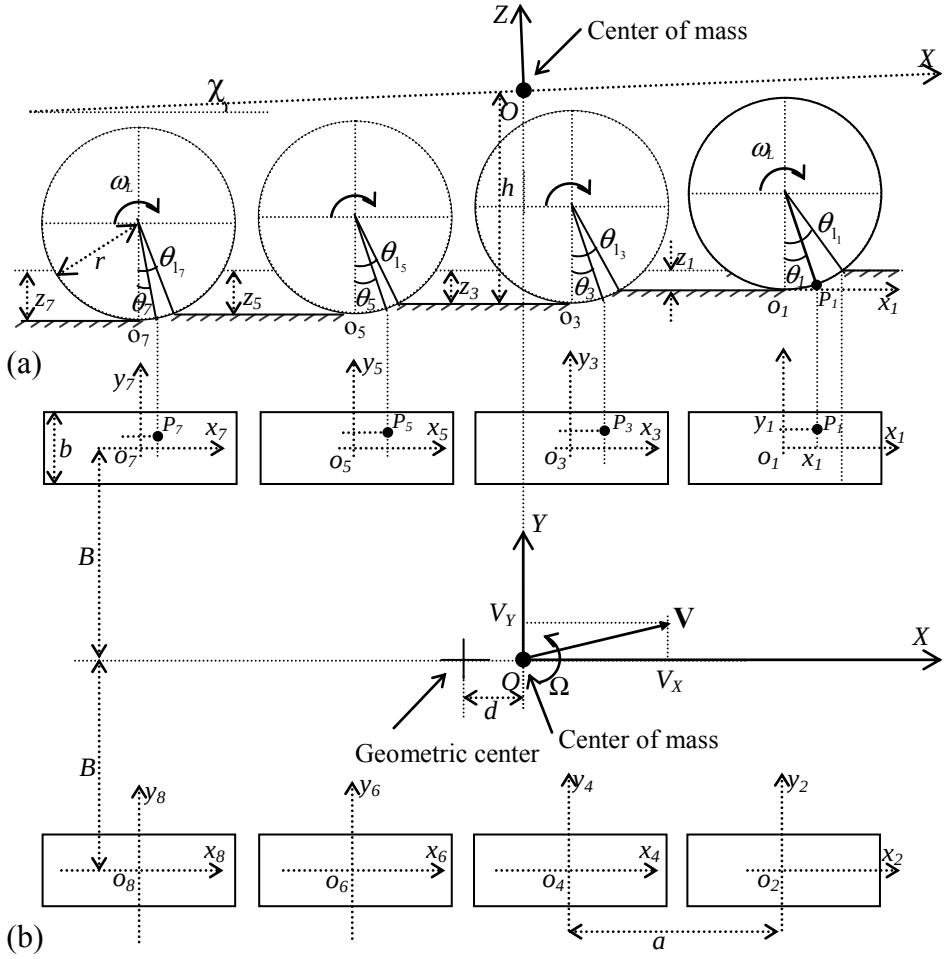

Figure 5.2 Vehicle free-body diagram on deformable terrain

5.3.1 Shear displacement

The vehicle free-body diagram in Figure 5.2 shows a lateral view in part (a) and the projection on a horizontal plane in part (b). Assume that the centre of mass *O* is displaced at a distance *d* along the centreline of the vehicle from the centroid. Let the origin of coordinates system (X, Y, Z), that is fixed to the vehicle, be placed at the centre of mass. The *Z*-axis is pointing vertically upward and the *X*-axis is along the vehicle centreline. Let *h* be the height of the centre of mass above the ground, *a* be the longitudinal distance between successive axles, and 2*B* be the vehicle track width.

Let us consider an arbitrary point $P_i(x_i, y_i)$ on the rim of the i^{th} wheel, $(i = 1,2,...,8)$, which is in contact with the terrain. Positions of these points relative to the vehicle coordinate frame are:

$$\mathbf{P_1}(x_1, y_1) = \left(\frac{3}{2}a - d + x_1\right)\mathbf{i} + (B + y_1)\mathbf{j} - (h - r(1 - \cos\theta_1))\mathbf{k},$$

$$\mathbf{P_2}(x_2, y_2) = \left(\frac{3}{2}a - d + x_2\right)\mathbf{i} + (-B + y_2)\mathbf{j} - (h - r(1 - \cos\theta_2))\mathbf{k},$$

$$\mathbf{P_3}(x_3, y_3) = \left(\frac{1}{2}a - d + x_3\right)\mathbf{i} + (B + y_3)\mathbf{j} - (h - r(1 - \cos\theta_3))\mathbf{k},$$

$$\mathbf{P_4}(x_4, y_4) = \left(\frac{1}{2}a - d + x_4\right)\mathbf{i} + (-B + y_2)\mathbf{j} - (h - r(1 - \cos\theta_4))\mathbf{k},$$

$$\mathbf{P_5}(x_5, y_5) = \left(-\frac{1}{2}a - d + x_5\right)\mathbf{i} + (B + y_5)\mathbf{j} - (h - r(1 - \cos\theta_5))\mathbf{k},$$

$$\mathbf{P_6}(x_6, y_6) = \left(-\frac{1}{2}a - d + x_6\right)\mathbf{i} + (-B + y_2)\mathbf{j} - (h - r(1 - \cos\theta_6))\mathbf{k},$$

$$\mathbf{P_7}(x_7, y_7) = \left(-\frac{3}{2}a - d + x_7\right)\mathbf{i} + (B + y_7)\mathbf{j} - (h - r(1 - \cos\theta_7))\mathbf{k},$$

$$\mathbf{P_8}(x_8, y_8) = \left(-\frac{3}{2}a - d + x_8\right)\mathbf{i} + (-B + y_2)\mathbf{j} - (h - r(1 - \cos\theta_8))\mathbf{k},$$

where $\mathbf{i, j, k}$ are unit vectors on X, Y, Z axis of the vehicle frame, and (x_i, y_i) are the Cartesian coordinates of the point P_i on the i^{th} wheel frame (see Figure 5.2).

Generally,

$$\begin{aligned}
&\mathbf{P_i}(x_i, y_i) = (X_i, Y_i, Z_i) = X_i\mathbf{i} + Y_i\mathbf{j} + Z_i\mathbf{k}\ , \\
&X_i = \left(\frac{3}{2} - E\left[\frac{i-1}{2}\right]\right)a - d + x_i\ , \\
&Y_i = (-1)^{i+1}B + y_i\ , \\
&Z_i = -(h - r(1-\cos\theta_i)),
\end{aligned} \tag{5.10}$$

where (X_i, Y_i, Z_i) are the Cartesian coordinates of the point P_i on the vehicle frame, and $E[i]$ is the largest integer that is less than or equal to i.

Since the value of x_i is

$$x_i = r\sin\theta_i,\ i = 1..8, \tag{5.11}$$

where θ_i is the wheel-terrain contact angle at the point P_i, the coordinates (x_i, y_i) can be equivalently represented by (θ_i, y_i).

Let **V** and **Ω** be the velocity of the centre of mass and the vehicle turning rate with respect to a fixed frame that instantaneously coincides with the vehicle coordinate frame, and $\boldsymbol{\omega}_L$, $\boldsymbol{\omega}_R$ be the angular velocity respectively of the left-side (i=1,3,5,7) and right-side (i=2,4,6,8) wheels. They are defined as:

$$\begin{aligned}
&\mathbf{V} = V_X\mathbf{i} + V_Y\mathbf{j}, \\
&\boldsymbol{\Omega} = \Omega\mathbf{k}, \\
&\boldsymbol{\omega}_\mathbf{L} = \omega_L\mathbf{j}, \\
&\boldsymbol{\omega}_\mathbf{R} = \omega_R\mathbf{j}.
\end{aligned} \tag{5.12}$$

The velocity at the centre of each wheel is given by

$$\begin{aligned}
\mathbf{V_i}(x_i, y_i) &= V_X\mathbf{i} + V_Y\mathbf{j} + \Omega\mathbf{k}\times P_i \\
&= V_X\mathbf{i} + V_Y\mathbf{j} + \Omega\mathbf{k}\times(X_i\mathbf{i} + Y_i\mathbf{j} + Z_i\mathbf{k}) \\
&= (V_X - \Omega Y_i)\mathbf{i} + (V_Y + \Omega X_i)\mathbf{j} = (V_{X_i}, V_{Y_i}),
\end{aligned} \tag{5.13a}$$

where

$$\begin{aligned} V_{X_i} &= V_X - \Omega Y_i, \\ V_{Y_i} &= V_Y + \Omega X_i. \end{aligned} \tag{5.13b}$$

The total velocity at the contact point $P_i(x_i, y_i)$ in the wheel frame of the i^{th} wheel can be decomposed, as illustrated in Figure 5.3, into normal, tangential and lateral components, respectively, as:

$$\begin{aligned} V_{n_i} &= V_{X_i} \sin\theta_i, \\ V_{t_i} &= r\omega_i - V_{X_i} \cos\theta_i, \\ V_{l_i} &= V_{Y_i}, \end{aligned} \tag{5.14}$$

where $\omega_i = \begin{cases} \omega_L, \textbf{ if } i = 1,3,5,7 \\ \omega_R, \textbf{ if } i = 2,4,6,8. \end{cases}$

Among these velocity components, V_{n_i} tends to compact the terrain to sinkage $z(\theta_i)$ while V_{t_i} and V_{l_i} respectively cause the contact point to shear the soil in the tangential and lateral directions. They govern the slip velocity of the considered point with respect to with a coincident point on the ground.

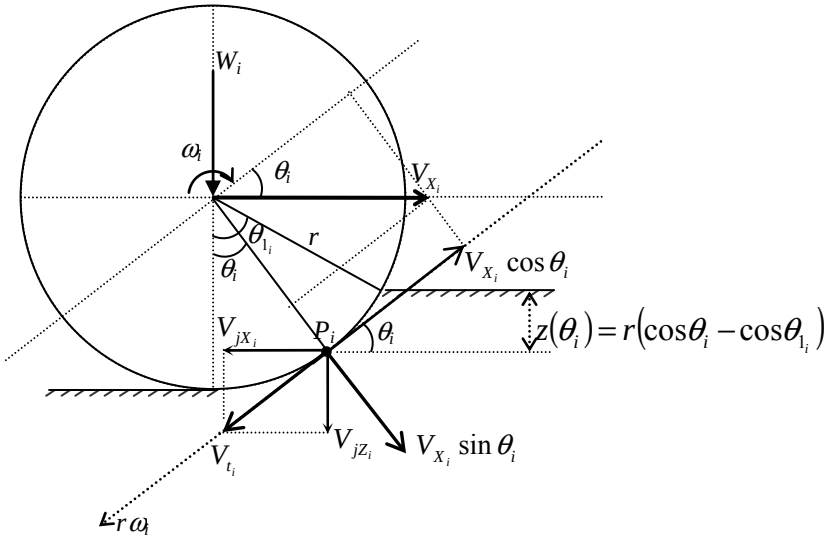

Figure 5.3 Velocity components at a contact point on the i^{th} wheel

Thus, referred to the fixed frame that is instantaneously coincides with the vehicle coordinate frame, the slip velocity of the contact point $P_i(x_i, y_i)$ can be expressed as:

$$\begin{aligned} V_{jX_i} &= -V_{t_i}\cos\theta_i, \\ V_{jY_i} &= V_{l_i}, \\ V_{jZ_i} &= -V_{t_i}\sin\theta_i. \end{aligned} \tag{5.15}$$

Substitution of (5.10)-(5.14) into (5.15) gives

$$\begin{aligned} V_{jX_i} &= \left(V_X - \Omega\left((-1)^{i+1}B + y_i\right)\right)\cos^2\theta_i - r\omega_i\cos\theta_i, \\ V_{jY_i} &= V_Y + \Omega\left(\left(\frac{3}{2} - E\left[\frac{i-1}{2}\right]\right)a - d + r\sin\theta_i\right), \\ V_{jZ_i} &= \left(V_X - \Omega\left((-1)^{i+1}B + y_i\right)\right)\sin\theta_i\cos\theta_i - r\omega_i\sin\theta_i. \end{aligned} \tag{5.16}$$

The longitudinal and lateral slip ratios, relative to the ground, are defined as

$$\begin{aligned} S_{X_i} &= -\frac{V_{jX_i}}{r\omega_i}, \\ S_{Y_i} &= -\frac{V_{jY_i}}{r\omega_i}, \end{aligned} \tag{5.17}$$

for any point in the contact zone. Furthermore, by integrating these shearing rate components from the position where the wheel first makes contact with the ground to the considered point, the shear displacements at the given point in the X, Y and Z directions can be obtained as

$$j_{X_i} = \int_0^t V_{jX_i} dt = \int_{\theta_i}^{\theta_{1_i}} V_{jX_i} \frac{d\theta_i}{\omega_i} = \int_{\theta_i}^{\theta_{1_i}} \left[\left(V_X - \Omega\left((-1)^{i+1} B + y_i \right) \right) \cos^2 \theta_i - r\omega_i \cos\theta_i \right] \frac{d\theta_i}{\omega_i},$$

$$j_{Y_i} = \int_0^t V_{jY_i} dt = \int_{\theta_i}^{\theta_{1_i}} V_{jY_i} \frac{d\theta_i}{\omega_i} = \int_{\theta_i}^{\theta_{1_i}} \left[V_Y + \Omega\left(\left(\frac{3}{2} - E\left[\frac{i-1}{2} \right] \right) a - d + r\sin\theta_i \right) \right] \frac{d\theta_i}{\omega_i}, \qquad (5.18)$$

$$j_{Z_i} = \int_0^t V_{jZ_i} dt = \int_{\theta_i}^{\theta_{1_i}} V_{jZ_i} \frac{d\theta_i}{\omega_i} = \int_{\theta_i}^{\theta_{1_i}} \left[\left(V_X - \Omega\left((-1)^{i+1} B + y_i \right) \right) \sin\theta_i \cos\theta_i - r\omega_i \sin\theta_i \right] \frac{d\theta_i}{\omega_i}.$$

To obtain explicit expressions for these shear displacements one can assume that velocities ω_i, V_X, V_Y, Ω are slowly time-varying and can therefore be considered as constants in the short interval of the integration. Then,

$$j_{X_i} = \frac{1}{\omega_i} \int_{\theta_i}^{\theta_{1_i}} \left[\left(V_X - \Omega\left((-1)^{i+1} B + y_i \right) \right) \left(\frac{1}{2} + \frac{1}{2}\cos 2\theta_i \right) - r\omega_i \cos\theta_i \right] d\theta_i$$

$$= \frac{1}{\omega_i} \left[\left(V_X - \Omega\left((-1)^{i+1} B + y_i \right) \right) \left(\frac{1}{2}\left(\theta_{1_i} - \theta_i\right) + \frac{1}{4}\left(\sin 2\theta_{1_i} - \sin 2\theta_i\right) \right) - r\omega_i \left(\sin\theta_{1_i} - \sin\theta_i\right) \right],$$

$$j_{Y_i} = \frac{1}{\omega_i} \int_{\theta_i}^{\theta_{1_i}} \left[V_Y + \Omega\left(\left(\frac{3}{2} - E\left[\frac{i-1}{2} \right] \right) a - d + r\sin\theta_i \right) \right] d\theta_i$$

$$= \frac{1}{\omega_i} \left[\left(V_Y + \Omega\left(\left(\frac{3}{2} - E\left[\frac{i-1}{2} \right] \right) a - d \right) \right) \left(\theta_{1_i} - \theta_i\right) - r\Omega\left(\cos\theta_{1_i} - \cos\theta_i\right) \right], \qquad (5.19)$$

$$j_{Z_i} = \frac{1}{\omega_i} \int_{\theta_i}^{\theta_{1_i}} \left[\frac{1}{2}\left(V_X - \Omega\left((-1)^{i+1} B + y_i \right) \right) \sin 2\theta_i - r\omega_i \sin\theta_i \right] d\theta_i$$

$$= \frac{1}{\omega_i} \left[-\frac{1}{4}\left(V_X - \Omega\left((-1)^{i+1} B + y_i \right) \right) \left(\cos 2\theta_{1_i} - \cos 2\theta_i\right) + r\omega_i \left(\cos\theta_{1_i} - \cos\theta_i\right) \right].$$

Note that if ω_i is zero, i.e. the wheel is locked, (5.19) is singular and cannot be used. In this case, the shear displacement components can be calculated by

$$j_{X_i} = \int_0^{\Delta t} V_{jX_i} dt,$$

$$j_{Y_i} = \int_0^{\Delta t} V_{jY_i} dt, \tag{5.20}$$

$$j_{Z_i} = \int_0^{\Delta t} V_{jZ_i} dt,$$

where the integral limit, Δt, is the interval from the moment ω_i approaches zero until the current time.

The magnitude of the shear displacement at the wheel-terrain contact point $P_i(x_i, y_i)$ is

$$j_i = \sqrt{j_{X_i}^2 + j_{Y_i}^2 + j_{Z_i}^2}, \; i = 1,2,...,8. \tag{5.21}$$

5.3.2 Shear stress, normal stress and reaction force

Under the normal and the shear pressures at the contact point, the ground reacts with a certain amount of shear stress $\tau_i(\theta_i, y_i)$ determined by (5.6), where the shear displacement is given by (5.21).

Components of the shear stress along X, Y, and Z directions can now be derived using a transformation from standard spherical coordinates to Cartesian coordinates (see Appendix A) as

$$\begin{aligned} \tau_{X_i} &= -\tau_i \cos\alpha_i \sin\beta_i, \\ \tau_{Y_i} &= -\tau_i \sin\alpha_i \sin\beta_i, \\ \tau_{Z_i} &= -\tau_i \cos\beta_i, \end{aligned} \tag{5.22}$$

where the minus sign denotes a stress in the opposite direction to the slip velocity (Assumption 4), which is specified by angles α_i and β_i in spherical coordinates (Appendix A):

$$\begin{aligned} \alpha_i &= \tan^{-1}\left(V_{jY_i} / V_{jX_i}\right), \\ \beta_i &= \tan^{-1}\left(\sqrt{V_{jX_i}^2 + V_{jY_i}^2} / V_{jZ_i}\right). \end{aligned} \tag{5.23}$$

As the normal pressure is distributed in the vertical plane, the components of the normal stress are

$$\begin{aligned} \sigma_{X_i} &= -\sigma_i(\theta_i)\sin\theta_i, \\ \sigma_{Y_i} &= 0, \\ \sigma_{Z_i} &= \sigma_i(\theta_i)\cos\theta_i . \end{aligned} \tag{5.24}$$

The reaction force acting on each wheel is the reaction to the normal stress and shear stress distributed on the wheel. Thus, the total force, acting on a very small contact area around the point $P_i(x_i, y_i)$, expressed in its increment, is determined by:

$$\begin{aligned} dF_{X_i} &= (\tau_{X_i} + \sigma_{X_i})dA_i, \\ dF_{Y_i} &= (\tau_{Y_i} + \sigma_{Y_i})dA_i, \\ dF_{Z_i} &= (\tau_{Z_i} + \sigma_{Z_i})dA_i, \end{aligned} \tag{5.25}$$

where $dA_i = r d\theta_i dy_i$ is an incremental area around the considered contact point.

The total reaction force of the ground on the i^{th} wheel when the considered point on the wheel is about to leave the contact is then obtained by integrating (5.25) over the terrain contact zone:

$$\begin{aligned} F_{X_i} &= \int dF_{X_i} = r\int_{\theta_{2_i}}^{\theta_{1_i}}\int_{-b/2}^{b/2}(\tau_{X_i} + \sigma_{X_i})d\theta_i dy_i, \\ F_{Y_i} &= \int dF_{Y_i} = r\int_{\theta_{2_i}}^{\theta_{1_i}}\int_{-b/2}^{b/2}\tau_{Y_i} d\theta_i dy_i, \\ F_{Z_i} &= \int dF_{Z_i} = r\int_{\theta_{2_i}}^{\theta_{1_i}}\int_{-b/2}^{b/2}(\tau_{Z_i} + \sigma_{Z_i})d\theta_i dy_i . \end{aligned} \tag{5.26}$$

It is interesting to note that if the lateral component of the slip velocity in (5.16) is negligible then the first and third expression of (5.26) becomes the drawbar pull DP_i and vertical weight W_i of each wheel, as given by (5.8) and (5.7) respectively.

5.3.3 Vehicle kinetics

In normal operation, the total reaction forces on the wheels determine the vehicle acceleration, support the vehicle mass, and overcome the turning resistance to turn the vehicle. The following force and moment balance equations can be obtained ($\theta_{2i} \cong 0$ at the end of the contact) for the vehicle as a whole by summing over the eight wheels.

- **Acceleration:**

$$\sum_{i=1}^{8} F_{X_i} = r\sum_{i=1}^{8}\int_{0}^{\theta_{1i}}\int_{-b/2}^{b/2}\tau_{X_i}\,d\theta_i dy_i - r\sum_{i=1}^{8}\int_{0}^{\theta_{1i}}\int_{-b/2}^{b/2}\sigma_i(\theta_i)\sin\theta_i d\theta_i dy_i = ma_X\,, \tag{5.27}$$

$$\sum_{i=1}^{8} F_{Y_i} = r\sum_{i=1}^{8}\int_{0}^{\theta_{1i}}\int_{-b/2}^{b/2}\tau_{Y_i}\,d\theta_i dy_i = ma_Y\,, \tag{5.28}$$

where m=W/g, W is the vehicle weight, g is the gravitational acceleration, and a_X and a_Y are the vehicle accelerations along longitudinal and lateral directions respectively.

- **Rolling resistance:**

The second term in (5.27) involving the normal stress indicates a resistive component against the tractive effort. Since the component of gravitational force is zero on flat ground, if the aerodynamic resistance and longitudinal drawbar load are negligible, the total rolling resistance is

$$F_R = r\sum_{i=1}^{8}\int_{0}^{\theta_{1i}}\int_{-b/2}^{b/2}\sigma_i(\theta_i)\sin\theta_i d\theta_i dy_i\,. \tag{5.29}$$

- **Weight balance:**

The vertical load supported by the i^{th} wheel is

$$F_{Z_i} = r\int_{0}^{\theta_{1i}}\int_{-b/2}^{b/2}(-\tau_i\cos\beta_i + \sigma_i(\theta_i)\cos\theta_i)d\theta_i dy_i = W_i\,, \tag{5.30a}$$

where W_i is the vertical load distributed on the i^{th} wheel.

Total vertical load supported by the vehicle is

$$\sum_{i=1}^{8} F_{Z_i} = \sum_{i=1}^{8} W_i = W = mg\,. \tag{5.30b}$$

- **Rolling and turning moment:**

The rolling and pitching moments around the X and Y axis can be derived as

$$\begin{aligned} M_X &= \sum_{i=1,2}^{8} \int Y_i dF_{Z_i} - \sum_{i=1}^{8} \int Z_i dF_{Y_i} \\ &= r \sum_{i=1,2}^{8} \int_0^{\theta_{l_i}} \int_{-b/2}^{b/2} \left((-1)^{i+1} B + y_i\right)\left(\tau_{Z_i} + \sigma_{Z_i}(\theta_i)\right) d\theta_i dy_i \\ &\quad + r \sum_{i=1}^{8} \int_0^{\theta_{l_i}} \int_{-b/2}^{b/2} \left(h - r\left(1 - \cos\theta_i\right)\right) \tau_{Y_i} d\theta_i dy_i\,, \end{aligned} \tag{5.31a}$$

$$\begin{aligned} M_Y &= \sum_{i=1}^{8} \int Z_i dF_{X_i} - \sum_{i=1}^{8} \int X_i dF_{Z_i} \\ &= -r \sum_{i=1}^{8} \int_0^{\theta_{l_i}} \int_{-b/2}^{b/2} \left(h - r\left(1 - \cos\theta_i\right)\right)\left(\tau_{X_i} + \sigma_{X_i}\right) d\theta_i dy_i \\ &\quad - r \sum_{i=1}^{8} \int_0^{\theta_{l_i}} \int_{-b/2}^{b/2} \left(\left(\frac{3}{2} - E\left[\frac{i-1}{2}\right]\right) a - d + r\sin\theta_i\right)\left(\tau_{Z_i} + \sigma_{Z_i}\right) d\theta_i dy_i\,, \end{aligned} \tag{5.31b}$$

and similarly for the turning moment:

$$\begin{aligned} M_Z &= -\sum_{i=1}^{8} \int Y_i dF_{X_i} + \sum_{i=1}^{8} \int X_i dF_{Y_i} \\ &= -r \sum_{i=1}^{8} \int_0^{\theta_{l_i}} \int_{-b/2}^{b/2} \left((-1)^{i+1} B + y_i\right)\left(\tau_{X_i} + \sigma_{X_i}\right) d\theta_i dy_i \\ &\quad + r \sum_{i=1}^{8} \int_0^{\theta_{l_i}} \int_{-b/2}^{b/2} \left(\left(\frac{3}{2} - E\left[\frac{i-1}{2}\right]\right) a - d + r\sin\theta_i\right) \tau_{Y_i} d\theta_i dy_i = I_Z \dot{\Omega}\,, \end{aligned} \tag{5.32}$$

where in normal conditions of the vehicle on a flat ground, rolling and pitching moments (5.31a, 5.31b) are zero, and I_Z is the vehicle moment of inertia around Z axis.

- **Moment of turning resistance:**

It is noted that while the first term in (5.32) denotes the total thrust required at the vehicle track width in skid steering to create a turning moment, the second term in (5.32) represents the moment of turning resistance due to the lateral components of the shear stresses acting on the wheels:

$$M_R = -r\sum_{i=1}^{8}\int_{0}^{\theta_{1_i}}\int_{-b/2}^{b/2}\left(\left(\frac{3}{2}-E\left[\frac{i-1}{2}\right]\right)a-d+r\sin\theta_i\right)\tau_{Y_i}\,d\theta_i\,dy_i\,. \tag{5.33}$$

5.3.4 Vertical load distribution

The vehicle weight is in general distributed on each wheel according to its position and the vehicle acceleration. For simplicity, it is assumed that all stresses can be concentrated on the origin of each wheel frame ($x_i = y_i = 0$). The rolling and pitching moments (5.31) of the vehicle on flat terrain then become

$$M_X = B\sum_{i=1}^{4}\left(F_{Z_{2i-1}}-F_{Z_{2i}}\right)+h\sum_{i=1}^{8}F_{Y_i}=0, \tag{5.34a}$$

$$\begin{aligned} M_Y = &-h\sum_{i=1}^{8}F_{X_i}-\left(\frac{3}{2}a-d\right)\left(F_{Z_1}+F_{Z_2}\right)-\left(\frac{1}{2}a-d\right)\left(F_{Z_3}+F_{Z_4}\right)\\ &+\left(\frac{1}{2}a+d\right)\left(F_{Z_5}+F_{Z_6}\right)+\left(\frac{3}{2}a+d\right)\left(F_{Z_7}+F_{Z_8}\right)=0. \end{aligned} \tag{5.34b}$$

While at the end of the wheel-terrain contact θ_{2_i} is approximately zero (Iagnemma *et al.*, 2004), the entry angle θ_{1_i} at the beginning of the contact is of particular interest when interpreting the wheel-terrain interaction. To determine this angle, one would make use of the vehicle weight balance (5.30) to solve a set of independent equations. One way to do this is to assume that the reaction force on Z direction on each wheel is linearly related to its position (X_i, Y_i) on the vehicle frame by (Waldron, 2004):

$$F_{Z_i} = q + vX_i + wY_i\,, \tag{5.35}$$

where q, v, and w are variables to be determined. Substitution of (5.35) into (5.30b), (5.34a) and (5.34b) with the accelerations in (5.27) and (5.28) taken into account leads to a set of three independent equations, from which one can obtain

$$\begin{aligned} q &= \frac{m}{40a^2}\left(g\left(4d^2+5a^2\right)-4hda_X\right), \\ v &= \frac{m\left(gd-ha_X\right)}{10a^2}, \\ w &= -\frac{hma_Y}{8B^2}. \end{aligned} \tag{5.36}$$

Then, the vertical loads acting on each wheel can be determined from (5.35) as

$$\begin{aligned} W_1 &= \frac{m}{40aB}\left((5a+6d)Bg-6Bha_X-5aha_Y\right), \\ W_2 &= \frac{m}{40aB}\left((5a+6d)Bg-6Bha_X+5aha_Y\right), \\ W_3 &= \frac{m}{40aB}\left((5a+2d)Bg-2Bha_X-5aha_Y\right), \\ W_4 &= \frac{m}{40aB}\left((5a+2d)Bg-2Bha_X+5aha_Y\right), \\ W_5 &= \frac{m}{40aB}\left((5a-2d)Bg+2Bha_X-5aha_Y\right), \\ W_6 &= \frac{m}{40aB}\left((5a-2d)Bg+2Bha_X+5aha_Y\right), \\ W_7 &= \frac{m}{40aB}\left((5a-6d)Bg+6Bha_X-5aha_Y\right), \\ W_8 &= \frac{m}{40aB}\left((5a-6d)Bg+6Bha_X+5aha_Y\right). \end{aligned} \tag{5.37}$$

These loads, in turn, are distributed over the wheel-terrain contact zones in terms of the normal stress as given in (5.1) or (5.3)-(5.5), and compress the ground to wheel sinkages z_i, $i = 1,2,...,8$. Angle θ_{1_i}, at which each wheel first enters in contact with the terrain, can be determined by solving (5.30a) and the right hand side is the weight distributions given in (5.37), e.g. by using some search algorithm. For this, a simple algorithm is proposed, as shown in the flow chart of Figure 5.4. A binary search algorithm can be applied for a fast solution.

When the vehicle moves in a straight line, following wheels will run in the rut of all preceding wheels, which gives rise to repetitive loadings on the soil. Taking this phenomenon into account, the normal stress distributions (5.3) and (5.5) for $i \geq 2$ (i=3,4,..,8) are rewritten as

$$\sigma_i(\theta_i) = \begin{cases} \sigma_{1_i} = \left(\dfrac{k_c}{b} + k_\phi\right)\left[z_{i-2} + r\left(\cos\theta_i - \cos\theta_{1_i}\right)\right]^n, & 0 \leq \theta_i \leq \theta_{m_i} \\ \sigma_{2_i} = \left(\dfrac{k_c}{b} + k_\phi\right)\left[z_{i-2} + r\left(\cos\left(\theta_{1_i} - \theta_i\right) - \cos\theta_{1_i}\right)\right]^n, & \theta_{m_i} \leq \theta_i \leq \theta_{1_i}, \end{cases} \tag{5.38}$$

where z_{i-2} (i=3,4,..,8) are the residual sinkages that remain in the ruts after all preceding wheels have passed.

Depending on the degree of elastic rebound of the terrain, the remaining sinkage may change from zero (fully elastic) to $z_{i-2}\left(\theta_{m_i}\right)$ (fully plastic). It should be noted that in turning, a follower wheel may run partially in a previous rut or even in a different path. In any case the remaining sinkage when turning still lies between these extremes.

5.3.5 Interaction modelling procedure

The above analysis provides a general framework for characterising the wheel-terrain interaction. The proposed model can be incorporated in a computer algorithm to predict velocity profiles and interaction characteristics of the vehicle, given its geometry and terrain parameters. The inputs to the algorithm are the left and right wheel speeds, measured from the wheel encoders or from the outputs of the vehicle driveline model. Initial conditions at time step k = 1 are obtained either from experimental data (e.g. from

GPS position measurements) or from calculations of the vehicle velocities for the no-slip case. The following procedure is suggested for stepping from discrete time step *k* to time step (*k*+1).

(i) Data collection and update:

Read $\omega_L(k)$, $\omega_R(k)$ at time step *k*. Assign current values for vehicle positions, velocities and accelerations.

(ii) Wheel vertical load computation:

From previous acceleration values, compute the wheel vertical loads given in (5.37). Search for entry angle θ_{1_i} using a binary search to satisfy (5.30a) (Figure 5.4).

(iii) Slip velocity and displacement computation:

Compute slip velocity components (5.16), and shear displacements (5.21).

(iv) Normal and shear stress computation:

Compute normal stresses (5.38), shear stresses (5.6) and their X, Y, and Z components (5.22).

(v) Next state computation:

Compute the accelerations $a_X(k+1)$, $a_Y(k+1)$ according to (5.27) and (5.28) and the turning acceleration $\dot{\Omega}(k+1)$ according to (5.32), then calculate the next values of velocities $V_X(k+1)$, $V_Y(k+1)$ and turning rate $\Omega(k+1)$. Obtain the vehicle position at (*k*+1) in the fixed coordinate frame (Appendix B).

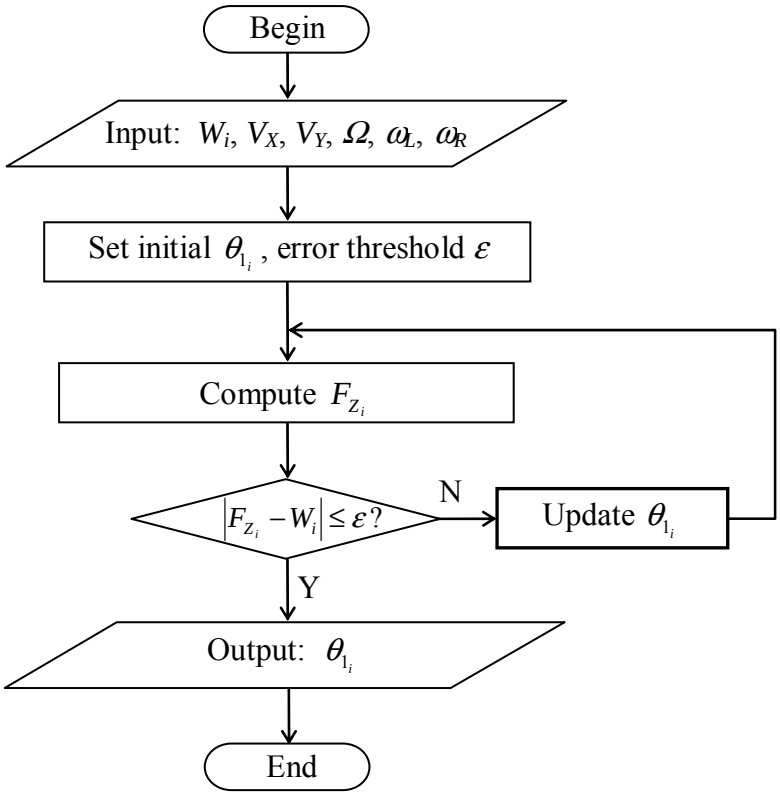

Figure 5.4 General flow chart for entry angle search

5.4 Simulation results and experimental verification

In this section, the main results from the vehicle-terrain interaction analysis are verified in simulation and compared with experimental data obtained from a field test. Terrain parameters used in the simulation are provided in (Wong, 2001) as listed in Table 5.1. All terrains are assumed to behave as plastic media. Geometrical parameters of the UGV are given in Table 5.2. Given initial conditions of the vehicle and readings of the left and right wheel angular speeds, the objectives are:

- To use the proposed dynamic model of the interaction to predict all future velocity profiles;
- To obtain the vehicle running path, particularly its performance during skid-steering turning; and
- To validate the simulation with field test results.

TABLE 5.1

TERRAIN PARAMETERS

Terrain	c (kPa)	ϕ (^{o})	k_c (kN/m^{n+1})	k_ϕ (kN/m^{n+2})	n	K (m)
Dry sand	1.04	28	0.99	1528	1.10	0.010
Sandy loam	1.72	29	5.27	1515	0.70	0.025
Clayed soil	4.14	13	13.19	692	0.50	0.006
Dry clay	68.95	34	12.70	1556	0.13	0.006

TABLE 5.2

VEHICLE PARAMETERS

m (kg)	Iz (kg.m^2)	r (m)	b (m)	a (m)	B (m)	d (m)	h (m)
490	309.43	0.25	0.246	0.61	0.61	0.17	0.35

5.4.1 Simulation results

The simulation presents a scenario when the vehicle is controlled to accelerate from zero in a straight line (during the interval 0-3s) and then make a skid-steered right turn (3-6s). The set of angular velocity data of the left-side and right-side wheels, as shown in Figure 5.5, obtained to steer the vehicle in the desired pattern is applied to the above vehicle-terrain interaction modelling procedure to predict the vehicle performance when operating on four different terrain types. The resulting vehicle trajectories are shown in Figure 5.6. The wheel slip ratio, vehicle velocity, rolling resistance and moment of the turning resistance can also be obtained from (5.17), (5.29) and (5.33) respectively, and they are shown in Figures 5.7, 5.8, 5.19 and 5.10. The results indicate that running paths of the vehicle on various terrains appear to be different under the same steering commands. The running path lengths are much less than the theoretical value, calculated

when no slip occurs, and decrease from dry sand, dry clay, clayed soil to sandy loam (see Figure 5.6). This is because the wheels slip on the ground (Figure 5.7) and vehicle therefore runs at smaller velocities than the theoretical value (Figure 5.8).

On all terrains, wheel slip ratios are very large during acceleration. When the vehicle makes a turn the inner wheels slow down and their longitudinal slips are reduced in magnitude and change in direction. Meanwhile, the outer wheels tend to slide faster longitudinally (Figure 5.7). On dry sand, the slip ratio of the outer wheels significantly increases as compared with the other terrain types.

Figure 5.9 shows that rolling resistance slightly increases when turning. The effect is smallest on dry clay, with clayed soil coming next, then sandy loam, and finally, dry sand. Likewise, the turning resistance moment of dry clay is smallest, next is sandy loam, then clayed soil, and dry sand coming last (Figure 5.10). This indicates that the vehicle manoeuvrability on dry clay is much better than on dry sand.

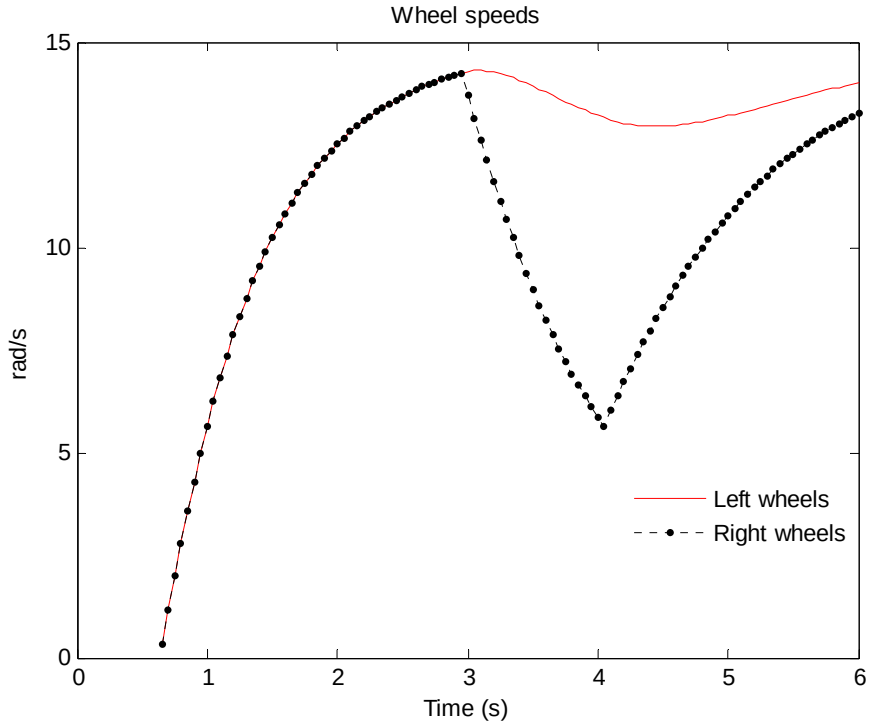

Figure 5.5 Wheel angular velocities used for the simulation

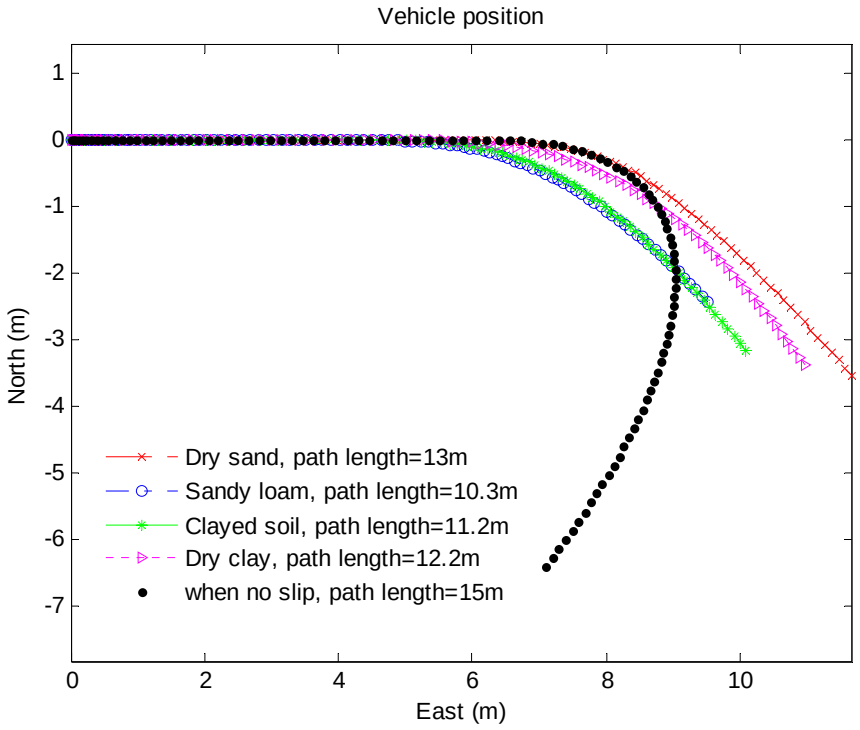

Figure 5.6 Vehicle trajectories predicted on different terrains

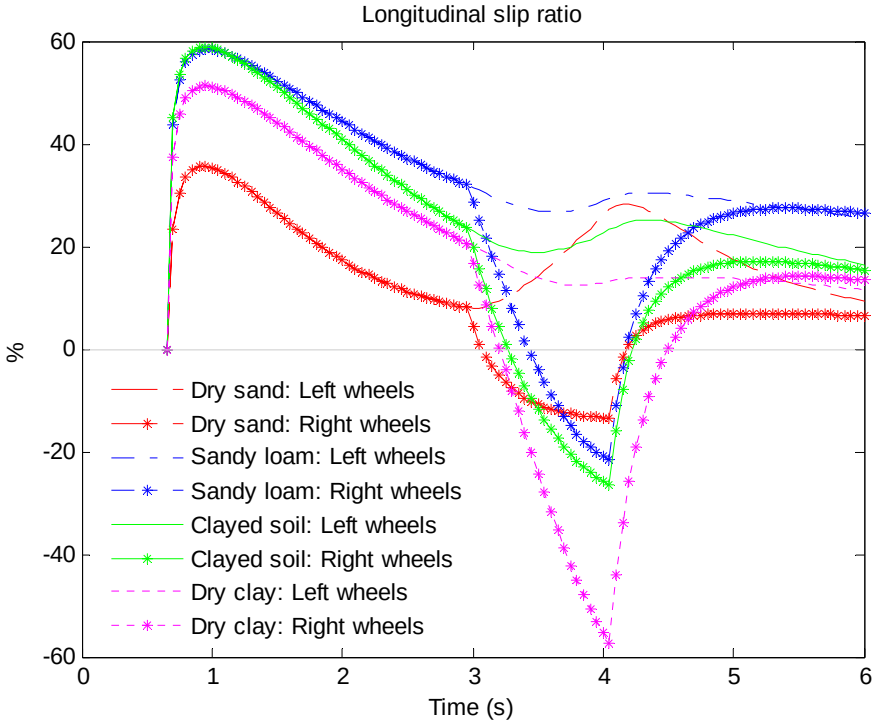

Figure 5.7 Wheel slip ratios on different terrains

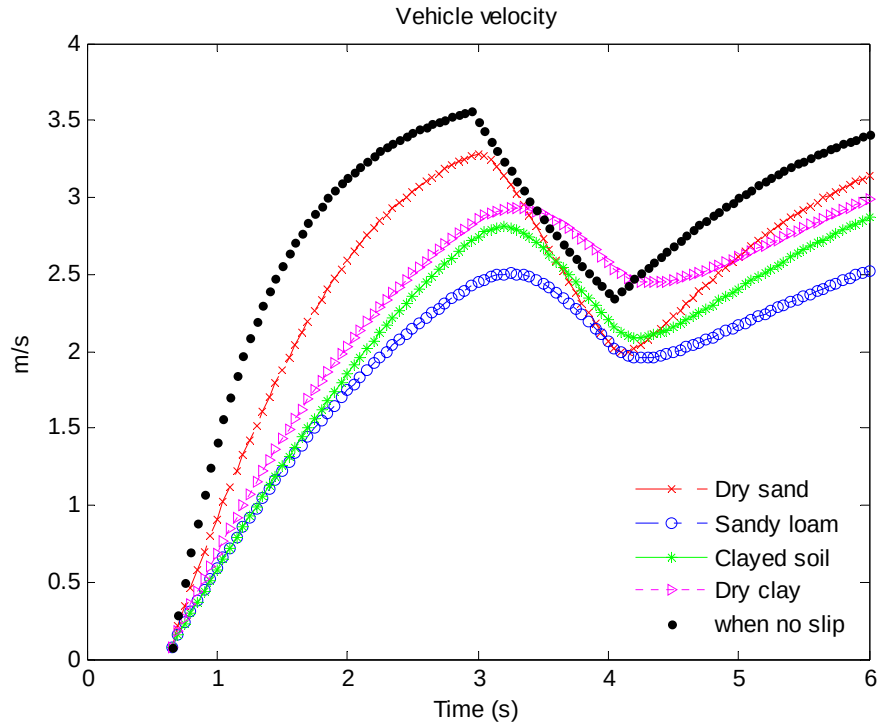

Figure 5.8 Vehicle velocities on different terrains

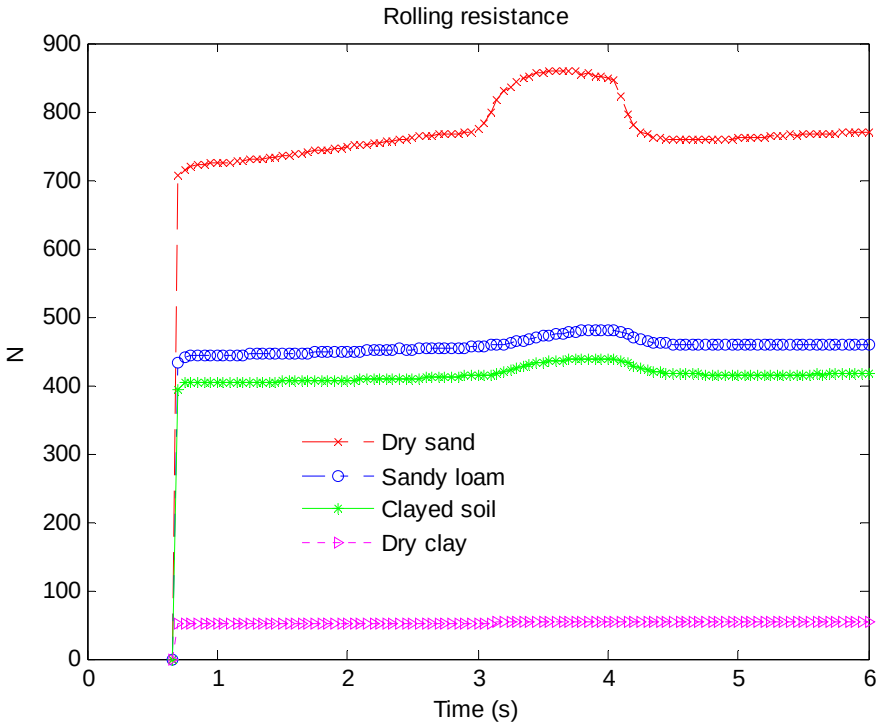

Figure 5.9 Rolling resistances on different terrains

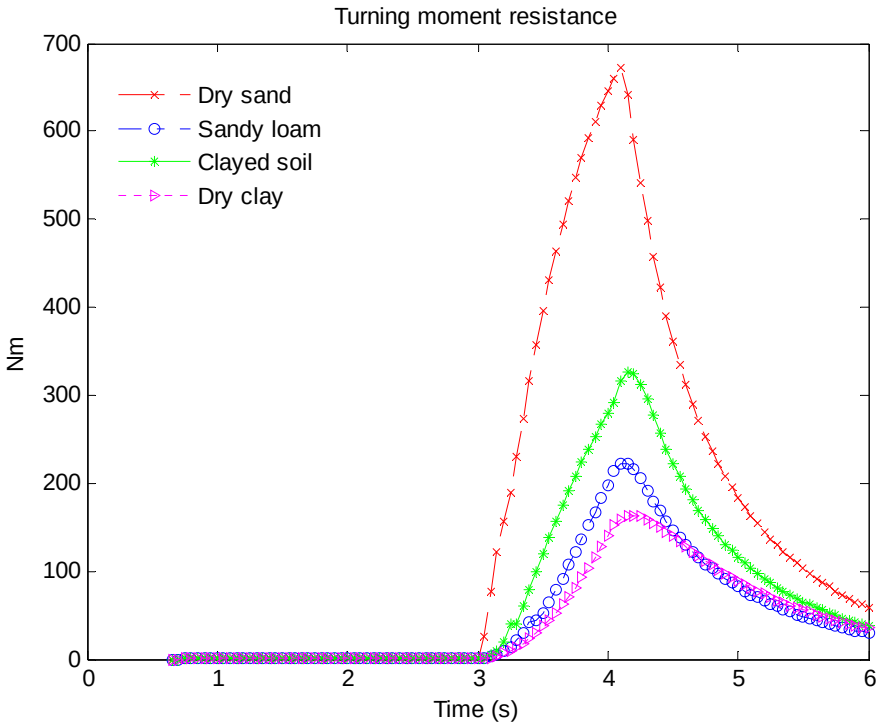

Figure 5.10 Turning moment resistances on different terrains

5.4.2 Comparison with experimental data

Several experiments were conducted on a farm near Marulan in the Southern Tablelands region of New South Wales on the 150 meridian. Position data were logged from differential GPS and used to validate the proposed interaction model.

A segment of wheel speed data, including a turn, recorded during the UGV operation on the dry, brown land in Marulan is input to the interaction model with initial conditions calculated from GPS data. Future states of the vehicle on different terrains are estimated over a five second period and compared with GPS data recorded during the experiment. Results are shown in Figure 5.11. It can be seen that with the same pattern of wheel speeds (Figure 5.12), the predicted trajectory of the vehicle is rather coincident with the experimental running path, and the terrain is most like the clayed soil type. It is noted that here the origin of the earth coordinate system is placed at the initial position of the vehicle.

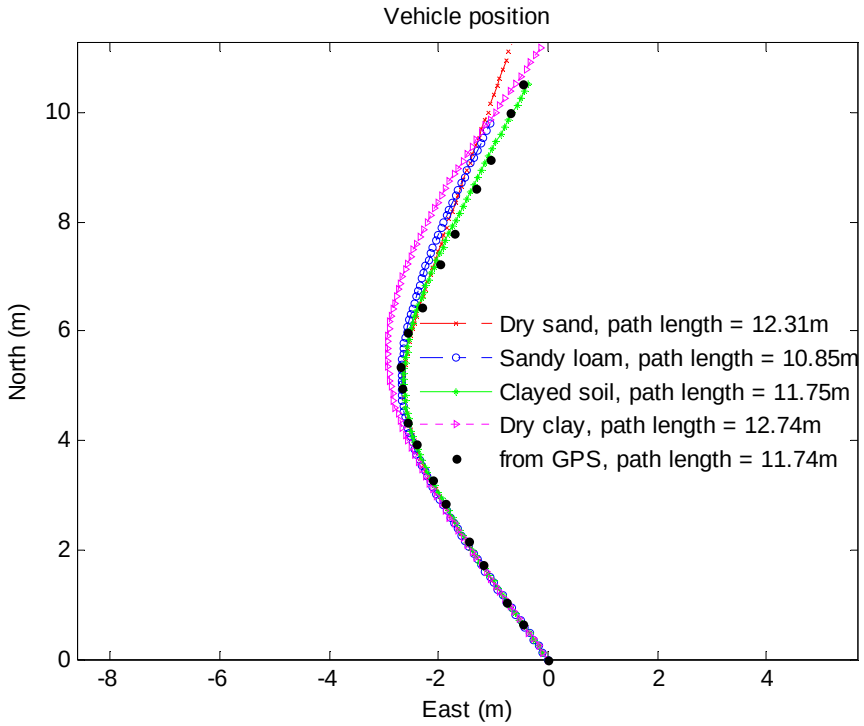

Figure 5.11 Vehicle trajectories: compared with experimental data

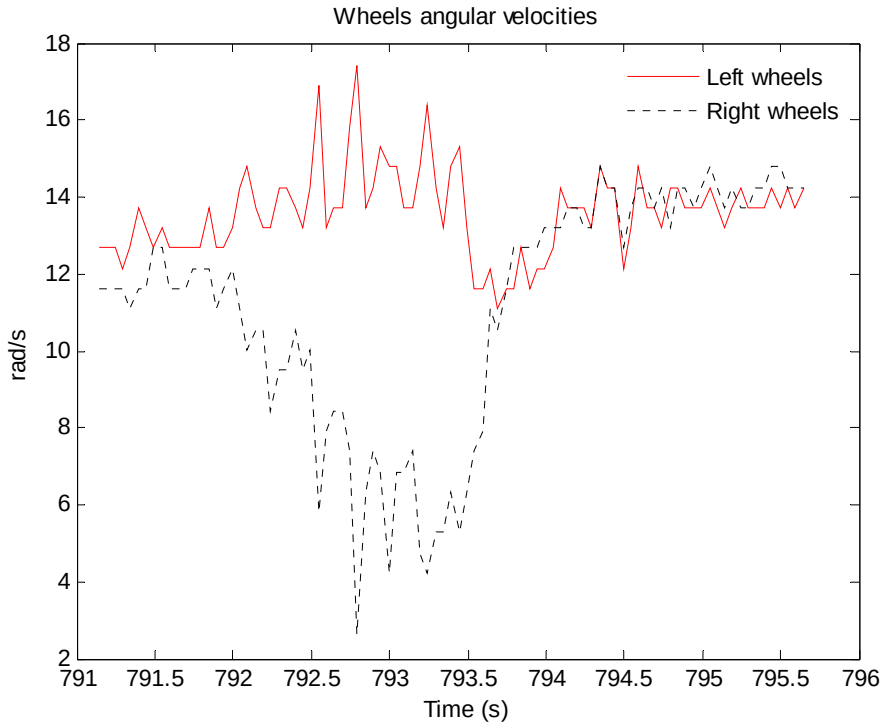

Figure 5.12 Wheel angular velocities: experimental data using for the comparison

5.5 Conclusion

This chapter has presented a comprehensive analysis for the wheel-terrain interaction of the skid-steering UGV. The novel interaction model takes into account the vehicle kinetics and the relationship between shear stress and shear displacement in deformable ground to characterize analytically the performance of the vehicle during contact with the terrain. Reaction forces, slip ratios, rolling and turning moments can be calculated. A procedure is proposed for computing these interaction parameters. The model was tested in simulation with four types of typical terrains and compared with field test data. Future positions of the vehicle predicted by the model from the current state are close to the experimental trajectory, which indirectly verifies its validity. In the next chapter, a fast algorithm will be developed for one-line applications of the vehicle-terrain interaction analysis.

Chapter 6

Fast algorithm for terrain interaction analysis

In Chapter 5, a comprehensive analysis for the vehicle-terrain interaction had been developed. Using the proposed procedure, the vehicle behaviours on different terrains can be predicted. Solving the integral equations in the procedure is, however, time-consuming. The developed theory is therefore not suitable for on-line applications which require rapid solutions. In this chapter, a fast algorithm is developed to speed up the computation process.

The problem of concern is introduced in the first section. The proposed algorithm is developed in Sections 6.2, 6.3, and 6.4. Comparisons with the original procedure are provided in Section 6.5 and a conclusion is drawn in the last section.

6.1 Introduction

In the vehicle-terrain interaction analysis developed in Chapter 5, the behaviour of the vehicle on soft terrain is predicted from the reaction forces of the terrain acting on the wheels. The reaction force is derived by integrating the normal stress and shear stress over the contact patch. The normal stress itself is an exponential function of the wheel sinkage (5.1) which is in turn related to the contact angle address by equation (5.2).

Meanwhile, the shear stress is also an exponential function of the shear displacement, with the amplitude determined by the normal stress. The distribution of normal stress along the contact zone depends on the terrain properties and the vertical load on the wheel. As shown in Figure 6.1, this distribution is nonlinear, especially for clayed soil and dry clay. The situation for the shear stress is more complex as it also depends on the shear displacement which can change from time to time. Consequently, there are no direct approaches available for solving the integral equations given in Chapter 5. Instead, they are usually approximated by recursive algorithms such as adaptive Simpson quadrature or adaptive Lobatto quadrature. As a result, the terrain interaction modelling procedure runs quite slowly, limiting the application of the proposed analysis. A faster method is highly desirable.

With regard to this particular problem, there has been little research effort reported in the literature. In (Shibly *et al.*, 2005), based on an observation that the normal and shear stresses under a rigid driven wheel are nearly linear, a new version of the basic wheel-terrain interaction equations (5.1-5.9) is developed. By approximating the normal stress and shear stress by straight lines going through their start and end points, as shown in Figure 6.2, the integral equations (5.7-5.9) can be solved directly, and solutions quickly found. Figure 6.1 indicates, however, that the distribution of normal and shear stresses is near-linear only for dry sand. For other terrain types, they are highly nonlinear and Shibly's method can lead to large errors. In addition, this approach can be applied only if lateral forces on the wheels are ignored.

In this chapter, Shibly's idea is refined to yield an efficient algorithm without losing accuracy. The stress is also approximated by a straight line going through its maximum stress point. The other point of intersection between the actual stress and its linearised approximation is chosen so that effects of the approximation error on the vehicle performance are minimised (Figure 6.2). The modified method is applied for all components of normal stress and shear stress in the longitudinal, lateral, and vertical directions and new equations for the reaction forces are obtained from that linearisation. A new version of the vehicle-terrain interaction analysis that does not involve involving integral equations is then developed, thus alleviating the computational demands. The

new development is verified by comparison with the original version given in Chapter 5 and with Shibly's method, both in terms of computation speed and accuracy.

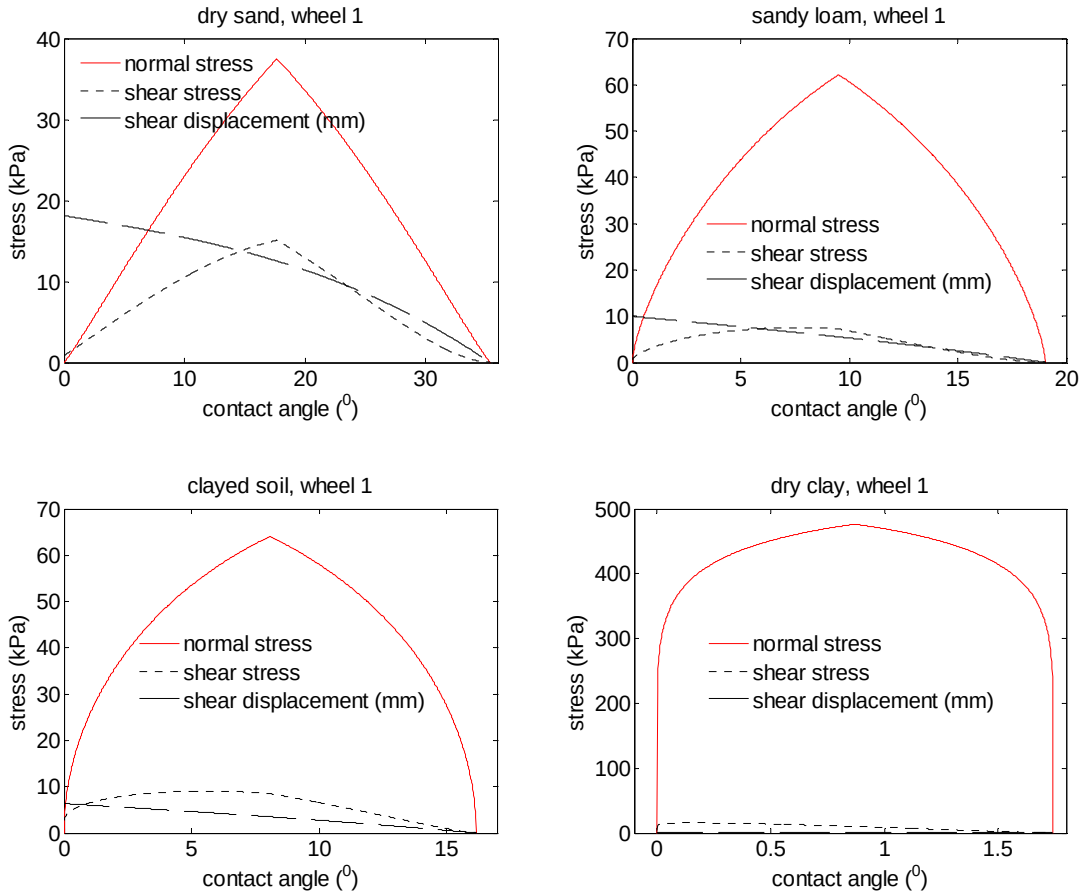

Figure 6.1 Distribution of normal stress, shear stress, and shear displacement under the first wheel on different terrain types

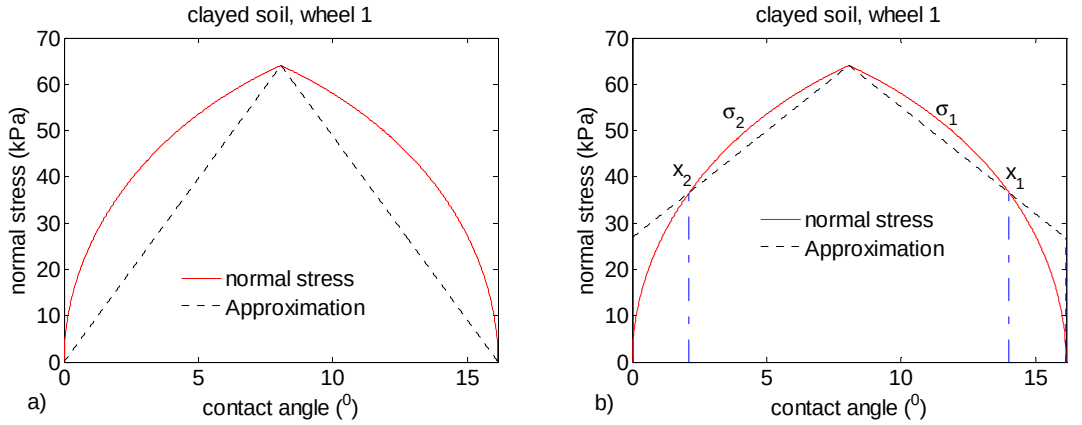

Figure 6.2 Linearisation of normal stress: (a) Shibly's method, (b) modified method

6.2 Linearisation of normal stress

In this section, normal stress beneath a wheel is linearised so that its integral can be obtained in closed form. Criteria are first chosen to minimize the approximation error, and then two methods for normal stress approximation are developed.

6.2.1 Approximation criteria

Let us consider the normal stress under the i^{th} wheel of the UGV, as shown in the diagram of Figure 5.2. The distribution of the stress is divided into front and rear regions by the maximum stress point θ_{m_i} (5.38):

$$\sigma_i(\theta_i)=\begin{cases}\sigma_{1_i}=\left(\dfrac{k_c}{b}+k_\phi\right)\left[z_{i-2}+r\left(\cos\theta_i-\cos\theta_{1_i}\right)\right]^n, & 0\le\theta_i\le\theta_{m_i},\\ \sigma_{2_i}=\left(\dfrac{k_c}{b}+k_\phi\right)\left[z_{i-2}+r\left(\cos\left(\theta_{1_i}-\theta_i\right)-\cos\theta_{1_i}\right)\right]^n, & \theta_{m_i}\le\theta_i\le\theta_{1_i}.\end{cases} \tag{6.1}$$

As mentioned in Chapter 5, depending on the degree of elastic rebound of the terrain, the remaining sinkage z_{i-2} may change from zero (fully elastic) to $z_{i-2}(\theta_{m_i})$ (fully plastic). For the front wheels, z_{i-2} are zero. Let us first consider the case when z_{i-2} is zero, which applied to the first and second wheels or to all wheels on fully elastic terrain, as shown in Figure 6.1.

As the stress is normal to the wheel rim, its components in the X and Z directions are (5.24),

$$\begin{aligned}\sigma_{X_i}&=-\sigma_i(\theta_i)\sin\theta_i,\\ \sigma_{Z_i}&=\sigma_i(\theta_i)\cos\theta_i.\end{aligned} \tag{6.2}$$

In most cases, the contact angle θ_i is small, and as a result, σ_{X_i} is very small compared with σ_{Z_i}. The largest influence of the normal stress is on the reaction force in the Z direction, as (5.26)

$$F_{Z_i} = \int dF_{Z_i} = r \int_{\theta_{2i}}^{\theta_{1i}} \int_{-b/2}^{b/2} \left(\tau_{Z_i} + \sigma_{Z_i}\right) d\theta_i dy_i \,. \tag{6.3}$$

If the normal stress is approximated so that its effect on the component F_{Z_i} is not changed, then the error due to the approximation will be minimised. This is the criterion applied for the proposed method, described in the following.

6.2.2 Method 1

As mentioned in the first section, the normal stress is approximated by a straight line passing through the maximum stress point and a point on the stress curve, as shown in Figure 6.2. The position of this point will be determined so that the approximation criterion is satisfied.

In general, the linear approximation of the normal stresses in the front and rear regions can be described by

$$\begin{aligned} \hat{\sigma}_{1_i} &= k_{1_i}\theta_i + c_{1_i}, \\ \hat{\sigma}_{2_i} &= k_{2_i}\theta_i + c_{2_i}, \end{aligned} \tag{6.4}$$

where $k_{1_i}, k_{2_i}, c_{1_i}$, and c_{2_i} are constants to be determined.

As the stress and its approximating lines intersect at the maximum stress point, (6.4) becomes

$$\begin{aligned} \hat{\sigma}_{1_i} &= k_{1_i}\left(\theta_i - \theta_{m_i}\right) + \sigma_{1_i}\left(\theta_{m_i}\right) = k_{1_i}\theta_i - k_{1_i}\theta_{m_i} + \sigma_{1_i}\left(\theta_{m_i}\right) = k_{1_i}\theta_i + c_{1_i}, \\ \hat{\sigma}_{2_i} &= k_{2_i}\left(\theta_i - \theta_{m_i}\right) + \sigma_{2_i}\left(\theta_{m_i}\right) = k_{2_i}\theta_i - k_{2_i}\theta_{m_i} + \sigma_{2_i}\left(\theta_{m_i}\right) = k_{2_i}\theta_i + c_{2_i}, \end{aligned} \tag{6.5}$$

where

$$\begin{aligned} c_{1_i} &= -k_{1_i}\theta_{m_i} + \sigma_{1_i}\left(\theta_{m_i}\right), \\ c_{2_i} &= -k_{2_i}\theta_{m_i} + \sigma_{2_i}\left(\theta_{m_i}\right). \end{aligned} \tag{6.6}$$

The angular coefficients of the approximations are chosen so that

$$\int_{\theta_{m_i}}^{\theta_{1_i}} \hat{\sigma}_{1_i}(\theta_i)\cos\theta_i d\theta_i = \int_{\theta_{m_i}}^{\theta_{1_i}} \sigma_{1_i}(\theta_i)\cos\theta_i d\theta_i = A_{1_i},$$
$$\int_{\theta_{2_i}}^{\theta_{m_i}} \hat{\sigma}_{2_i}(\theta_i)\cos\theta_i d\theta_i = \int_{\theta_{2_i}}^{\theta_{m_i}} \sigma_{2_i}(\theta_i)\cos\theta_i d\theta_i = A_{2_i}, \tag{6.7}$$

where A_{1_i} and A_{2_i} are constants assigned for the expressions in the right hand side of (6.7).

Substitution of (6.5) into (6.7) gives

$$\begin{aligned}
\int_{\theta_{m_i}}^{\theta_{1_i}} \hat{\sigma}_{1_i}(\theta_i)\cos\theta_i d\theta_i &= \int_{\theta_{m_i}}^{\theta_{1_i}} \left[k_{1_i}(\theta_i - \theta_{m_i}) + \sigma_{1_i}(\theta_{m_i})\right]\cos\theta_i d\theta_i \\
&= \left[k_{1_i}(\theta_{1_i} - \theta_{m_i})\sin\theta_{1_i} + k_{1_i}(\cos\theta_{1_i} - \cos\theta_{m_i}) + \sigma_{1_i}(\theta_{m_i})(\sin\theta_{1_i} - \sin\theta_{m_i})\right] \\
&= A_{1_i}, \\
\int_{\theta_{2_i}}^{\theta_{m_i}} \hat{\sigma}_{2_i}(\theta_i)\cos\theta_i d\theta_i &= \int_{\theta_{2_i}}^{\theta_{m_i}} \left[k_{2_i}(\theta_i - \theta_{m_i}) + \sigma_{2_i}(\theta_{m_i})\right]\cos\theta_i d\theta_i \\
&= \left[k_{2_i}(\theta_{m_i} - \theta_{2_i})\sin\theta_{2_i} + k_{2_i}(\cos\theta_{m_i} - \cos\theta_{2_i}) + \sigma_{2_i}(\theta_{m_i})(\sin\theta_{m_i} - \sin\theta_{2_i})\right] \\
&= A_{2_i}.
\end{aligned} \tag{6.8}$$

The angular coefficients can then be derived from (6.8a) and (6.8b) as

$$k_{1_i} = \frac{A_{1_i} - \sigma_{1_i}(\theta_{m_i})(\sin\theta_{1_i} - \sin\theta_{m_i})}{(\theta_{1_i} - \theta_{m_i})\sin\theta_{1_i} + \cos\theta_{1_i} - \cos\theta_{m_i}},$$
$$k_{2_i} = \frac{A_{2_i} - \sigma_{2_i}(\theta_{m_i})(\sin\theta_{m_i} - \sin\theta_{2_i})}{(\theta_{m_i} - \theta_{2_i})\sin\theta_{2_i} + \cos\theta_{m_i} - \cos\theta_{2_i}}. \tag{6.9}$$

6.2.3 Method 2

The difference between the normal stress and its component in the Z direction is insignificant, as seen in Figure 6.5. The angular coefficients of the approximations can therefore be chosen so that

$$\int_{\theta_{m_i}}^{\theta_{1_i}} \hat{\sigma}_{1_i}(\theta_i)d\theta_i = \int_{\theta_{m_i}}^{\theta_{1_i}} \sigma_{1_i}(\theta_i)d\theta_i = A'_{1_i},$$
$$\int_{\theta_{2_i}}^{\theta_{m_i}} \hat{\sigma}_{2_i}(\theta_i)d\theta_i = \int_{\theta_{2_i}}^{\theta_{m_i}} \sigma_{2_i}(\theta_i)d\theta_i = A'_{2_i}. \tag{6.10}$$

Substitution of (6.5) into (6.7) gives

$$\int_{\theta_{m_i}}^{\theta_{1_i}} \hat{\sigma}_{1_i}(\theta_i)d\theta_i = \int_{\theta_{m_i}}^{\theta_{1_i}} \left[k_{1_i}(\theta_i - \theta_{m_i}) + \sigma_{1_i}(\theta_{m_i})\right]d\theta_i$$
$$= \frac{k_{1_i}}{2}(\theta_{1_i} - \theta_{m_i})^2 + (\theta_{1_i} - \theta_{m_i})\sigma_{1_i}(\theta_{m_i}) = A'_{1_i},$$
$$\int_{\theta_{2_i}}^{\theta_{m_i}} \hat{\sigma}_{2_i}(\theta_i)d\theta_i = \int_{\theta_{2_i}}^{\theta_{m_i}} \left[k_{2_i}(\theta_i - \theta_{m_i}) + \sigma_{2_i}(\theta_{m_i})\right]d\theta_i \tag{6.11}$$
$$= -\frac{k_{2_i}}{2}(\theta_{m_i} - \theta_{2_i})^2 + (\theta_{m_i} - \theta_{2_i})\sigma_{2_i}(\theta_{m_i}) = A'_{2_i}.$$

This yields

$$k_{1_i} = \frac{2\left(A'_{1_i} - (\theta_{1_i} - \theta_{m_i})\sigma_{1_i}(\theta_{m_i})\right)}{(\theta_{1_i} - \theta_{m_i})^2},$$
$$k_{2_i} = \frac{2\left(-A'_{2_i} - (\theta_{m_i} - \theta_{2_i})\sigma_{2_i}(\theta_{m_i})\right)}{(\theta_{m_i} - \theta_{2_i})^2}. \tag{6.12}$$

The other coefficients of the approximation are the same as in Method 1 (6.6). Simulation shows that the results using Method 2 are nearly the same as those that result from using Method 1. The difference is less than 0.17% of the angular coefficient.

It should be noted that if $\theta_{2_i} = 0$, and $\theta_{m_i} = \theta_{1_i}/2$ (as assumed in Chapter 5), the stress is symmetric and therefore $k_{2_i} = -k_{1_i}$. In this case, the computation for the approximation of the shear stress in the rear region is not necessary owing to symmetry.

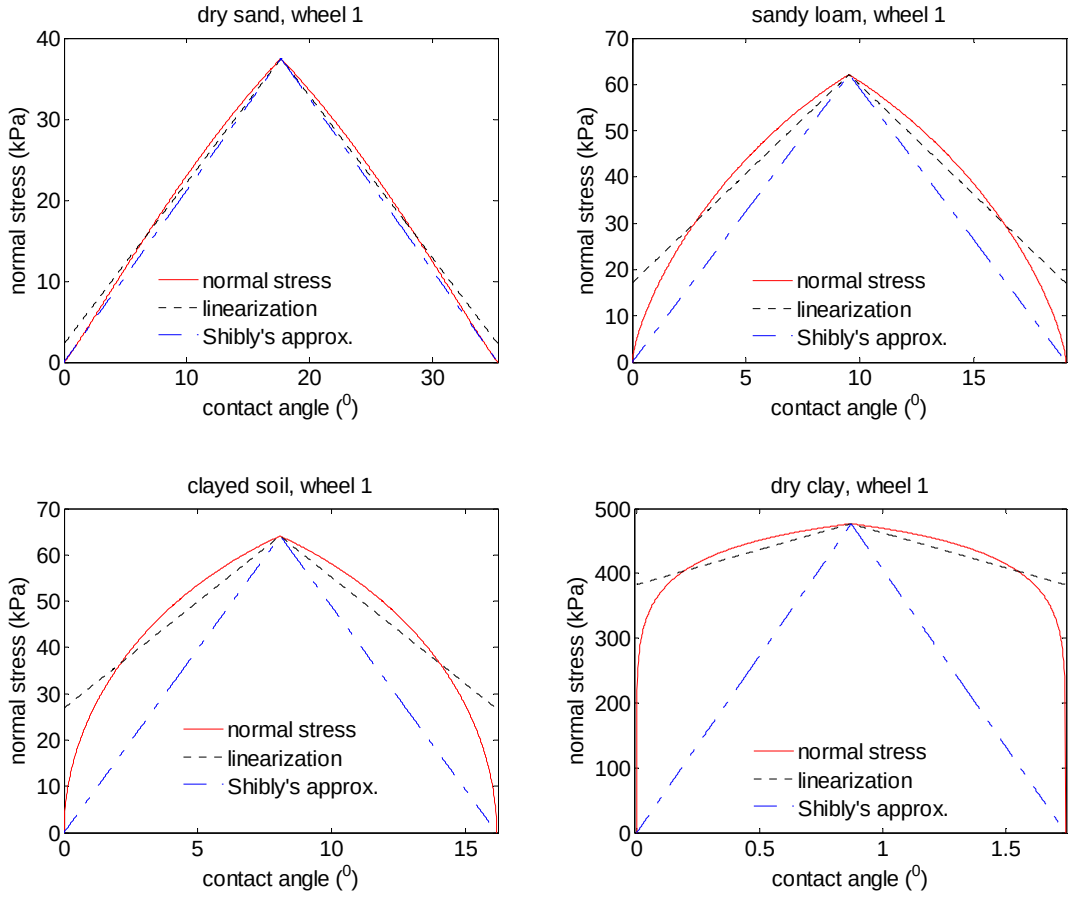

Figure 6.3 Linearisation of normal stress

6.2.4 Results

Results of the proposed linearisation methods are shown in Figure 6.3 in comparison with those of Shibly's method. It can be seen that the approximation in Shibly's method is only close to the actual normal stress on dry sand. For other terrains, the difference is very large. In contrast, using the modified approach gives a linearised stress that is less than the actual stress in a range of the contact angle, but larger outside of the range. Over the contact zone, however, the largest effect of the stress on the vehicle performance is retained, and as a result, the error of the approximation is smallest.

Let θ_{x1_i} and θ_{x2_i} be the contact angles at which the normal stress intersects its approximations in the front and rear regions respectively. Simulations using the proposed methods with experimental wheel data collected from a field test, as presented in Figure 5.12, show that on a given terrain, the ratios $\theta_{x1_i}/\theta_{1_i}$ and $\theta_{x2_i}/\theta_{1_i}$ are almost

constant with different values of θ_{1_i}, as shown in Figure 6.4. This is a great advantage because it is not necessary to recalculate angles θ_{x1_i} and θ_{x2_i} each time when the entry angle changes. Instead, the average values of these ratios can be used:

$$\frac{\theta_{x1_i}}{\theta_{1_i}} = \begin{cases} 0.8124, \text{ for dry sand}, \\ 0.8566, \text{ for sandy loam}, \\ 0.8687, \text{ for clayed soil}, \\ 0.8900, \text{ for dry clay}, \end{cases} \tag{6.13}$$

and

$$\frac{\theta_{x2_i}}{\theta_{1_i}} = \begin{cases} 0.1399, \text{ for dry sand}, \\ 0.1398, \text{ for sandy loam}, \\ 0.1302, \text{ for clayed soil}, \\ 0.1098, \text{ for dry clay}. \end{cases} \tag{6.14}$$

As the intersections of the normal stress and its approximations can be derived from (6.13) and (6.14), the approximating lines can now be simply described as

$$\begin{aligned} \hat{\sigma}_{1_i} &= k_{1_i}\theta_i + c_{1_i}, \\ k_{1_i} &= \frac{\sigma_{1_i}(\theta_{x1_i}) - \sigma_{1_i}(\theta_{m_i})}{\theta_{x1_i} - \theta_{m_i}}, \\ c_{1_i} &= -k_{1_i}\theta_{m_i} + \sigma_{1_i}(\theta_{m_i}), \end{aligned} \tag{6.15}$$

$$\begin{aligned} \hat{\sigma}_{2_i} &= k_{2_i}\theta_i + c_{2_i}, \\ k_{2_i} &= \frac{\sigma_{2_i}(\theta_{x2_i}) - \sigma_{2_i}(\theta_{m_i})}{\theta_{x2_i} - \theta_{m_i}}, \\ c_{2_i} &= -k_{2_i}\theta_{m_i} + \sigma_{2_i}(\theta_{m_i}). \end{aligned} \tag{6.16}$$

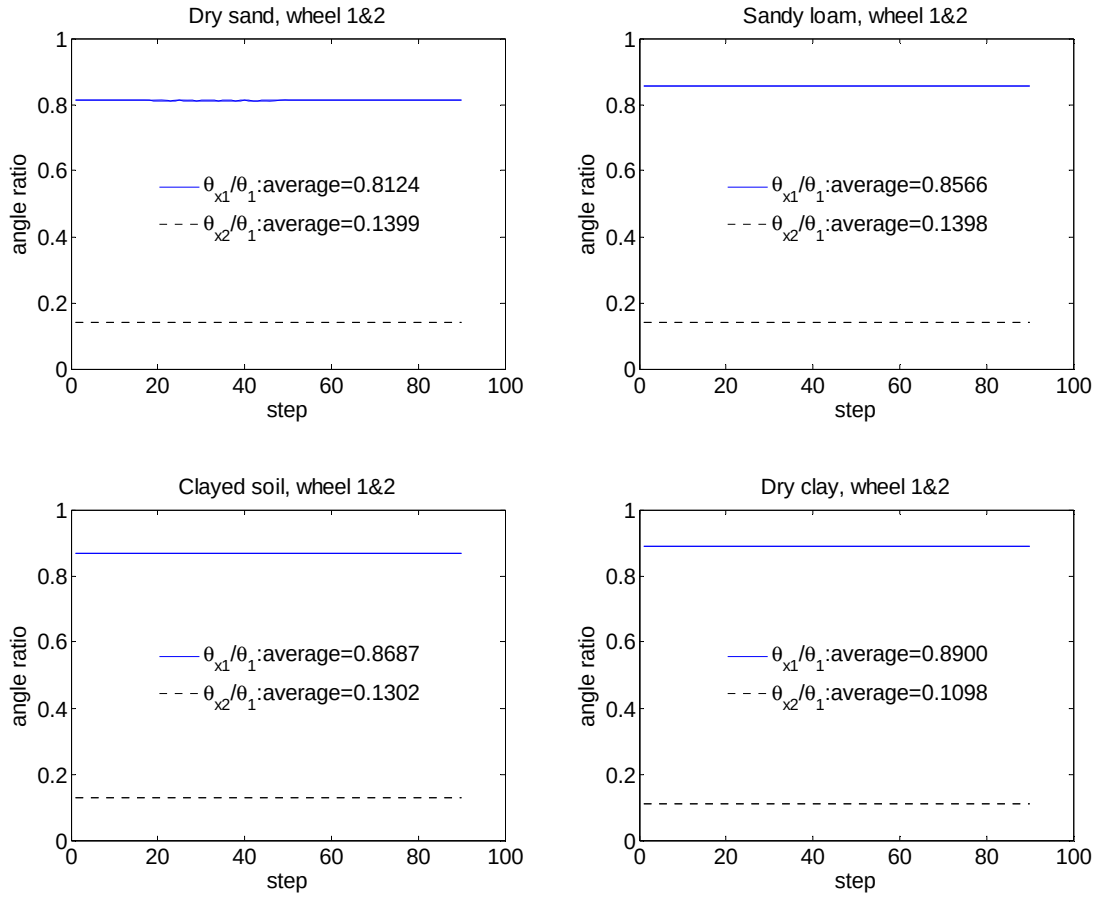

Figure 6.4 Distribution of the angle ratios for the normal stress approximation

From (6.12), (6.13), and (6.2), components of the normal stress in the X and Z directions can be derived and substituted in the vehicle-terrain integral equations. If the stress components are also linearised, the fast version of vehicle-terrain analysis can be further simplified. From the observation that the shapes of normal stress and its components in the X and Z directions are near-identical (Figure 6.5), the same intersection points in (6.12) and (6.13) can be used to approximate the stress components as follows

$$\begin{aligned} \hat{\sigma}_{1X_i} &= k_{1X_i}\theta_i + c_{1X_i}, \\ k_{1X_i} &= \frac{\sigma_{1X_i}(\theta_{x1_i}) - \sigma_{1X_i}(\theta_{m_i})}{\theta_{x1_i} - \theta_{m_i}}, \\ c_{1X_i} &= -k_{1X_i}\theta_{m_i} + \sigma_{1X_i}(\theta_{m_i}), \end{aligned} \tag{6.17}$$

$$\hat{\sigma}_{2X_i} = k_{2X_i}\theta_i + c_{2X_i},$$

$$k_{2X_i} = \frac{\sigma_{2X_i}(\theta_{x2_i}) - \sigma_{2X_i}(\theta_{m_i})}{\theta_{x2_i} - \theta_{m_i}}, \tag{6.18}$$

$$c_{2X_i} = -k_{2X_i}\theta_{m_i} + \sigma_{2X_i}(\theta_{m_i}),$$

$$\hat{\sigma}_{1Z_i} = k_{1Z_i}\theta_i + c_{1Z_i},$$

$$k_{1Z_i} = \frac{\sigma_{1Z_i}(\theta_{x1_i}) - \sigma_{1Z_i}(\theta_{m_i})}{\theta_{x1_i} - \theta_{m_i}}, \tag{6.19}$$

$$c_{1Z_i} = -k_{1Z_i}\theta_{m_i} + \sigma_{1Z_i}(\theta_{m_i}),$$

$$\hat{\sigma}_{2Z_i} = k_{2Z_i}\theta_i + c_{2Z_i},$$

$$k_{2Z_i} = \frac{\sigma_{2Z_i}(\theta_{x2_i}) - \sigma_{2Z_i}(\theta_{m_i})}{\theta_{x2_i} - \theta_{m_i}}, \tag{6.20}$$

$$c_{2Z_i} = -k_{2Z_i}\theta_{m_i} + \sigma_{2Z_i}(\theta_{m_i}).$$

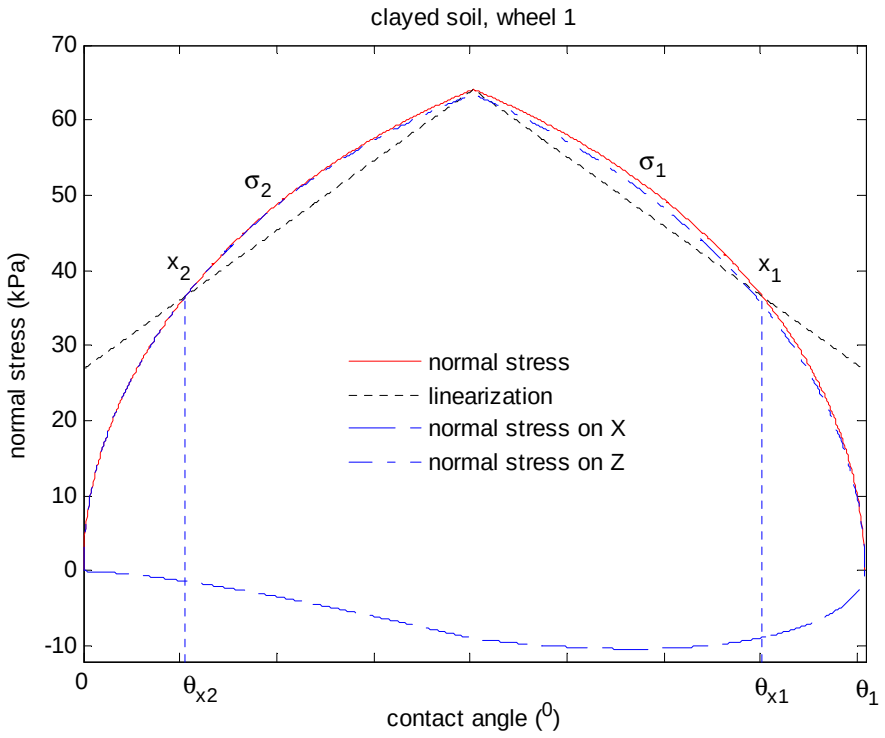

Figure 6.5 Normal stress and its components

It should be noted that if Shibly's method is applied to the normal stress components, the variables θ_{x1_i} and θ_{x2_i} in (6.17-6.20) will be replaced by θ_{1_i} and θ_{2_i}, respectively. Both Shibly's and the above methods can be applied for all wheels.

6.3 Linearisation of shear stress

In this section, the shear stress acting on a wheel is expressed in a new spherical coordinate system to derive criteria for minimizing the approximation error. Two methods are then developed for approximating the shear stress.

6.3.1 Approximation criteria

Let us consider the shear stress under the i^{th} wheel with sliding velocity components in the X-Z plane, as shown in Figure 6.6a, in the horizontal plane (Figure 6.6b), and in a new spherical coordinate system, as shown in Figure 6.6c. In this spherical coordinates, θ_i becomes the azimuth. The other angle, φ_i, is the elevation and measure the angle between the shear stress and its projection on the X-Z plane. In the new spherical coordinates, components of the shear stress are given by

$$\begin{aligned}
\tau_{X_i} &= \tau_i \cos\varphi_i \cos\theta_i = \tau_i \cos\gamma_i \cos\theta_i, \\
\tau_{Y_i} &= \tau_i \sin\varphi_i = -\tau_i \sin\gamma_i, \\
\tau_{Z_i} &= \tau_i \cos\varphi_i \sin\theta_i = \tau_i \cos\gamma_i \sin\theta_i,
\end{aligned} \tag{6.21}$$

where the elevation angle, φ_i, can be calculated from the angle between the sliding velocity and its projection on X-Z plane as

$$\varphi_i = -\gamma_i = -\tan^{-1}\left(\frac{V_{jY_i}}{V_{t_i}}\right), \tag{6.22}$$

and the components of the sliding velocity are determined from the vehicle velocity (V_X, V_Y), turning rate (Ω) and wheel speed (ω_i) (5.13-5.15) as

$$V_{jY_i} = V_{l_i} = V_Y + \Omega X_i ,$$
$$V_{t_i} = r\omega_i - (V_X - \Omega Y_i)\cos\theta_i . \tag{6.23}$$

As noted above, the contact angle θ_i is small so that τ_{Z_i} is very small compared with τ_{X_i}. When the vehicle runs in a straight line, the elevation angle φ_i is zero and so is τ_{Y_i}. In most cases, therefore, the largest effect of the shear stress is on its component along the X direction τ_{X_i}. This component, in turn, is the main contribution to the longitudinal reaction force, or drawbar pull, expressed in (5.26) as

$$F_{X_i} = \int dF_{X_i} = r\int_{\theta_{2_i}}^{\theta_{1_i}}\int_{-b/2}^{b/2}(\tau_{X_i} + \sigma_{X_i})d\theta_i dy_i , \tag{6.24}$$

If the shear stress is approximated so that its effect on F_{X_i} is unchanged, then the error of the approximation is smallest. This is the criterion applied in the following proposed methods.

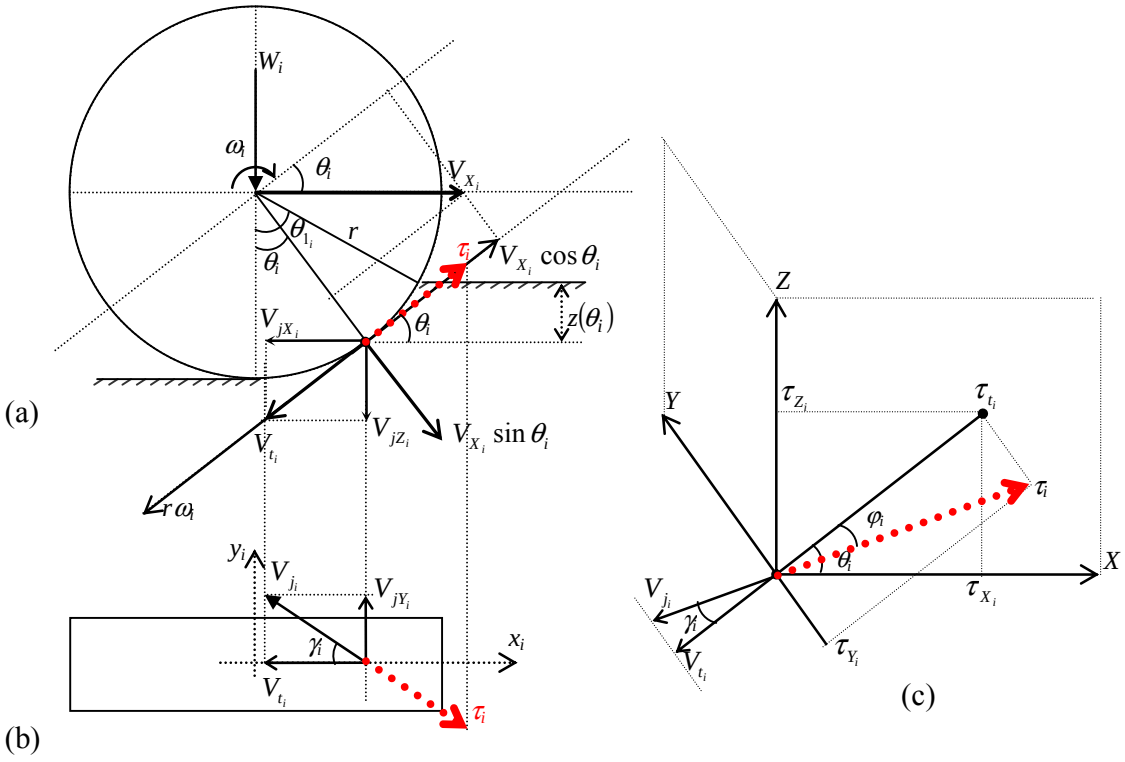

Figure 6.6 New representation of shear stress

6.3.2 Method 3

Like the normal stress, the shear stress in each region is approximated by a straight line through the maximum stress point and a point on the stress curve. The position of this point will be determined so that the approximation criterion is satisfied.

In general, the linearisation can be described by

$$\begin{aligned} \hat{\tau}_{1_i} &= k_{3_i}\theta_i + c_{3_i}, \\ \hat{\tau}_{2_i} &= k_{4_i}\theta_i + c_{4_i}, \end{aligned} \tag{6.25}$$

where $k_{3_i}, k_{4_i}, c_{3_i}$, and c_{4_i} are constants to be calculated.

Because the stress and its approximating lines intersect at the maximum stress point, (6.25) becomes,

$$\begin{aligned} \hat{\tau}_{1_i} &= k_{3_i}\left(\theta_i - \theta_{m_i}\right) + \tau_{1_i}\left(\theta_{m_i}\right) = k_{3_i}\theta_i - k_{3_i}\theta_{m_i} + \tau_{1_i}\left(\theta_{m_i}\right) = k_{3_i}\theta_i + c_{3_i}, \\ \hat{\tau}_{2_i} &= k_{4_i}\left(\theta_i - \theta_{m_i}\right) + \tau_{2_i}\left(\theta_{m_i}\right) = k_{4_i}\theta_i - k_{4_i}\theta_{m_i} + \tau_{2_i}\left(\theta_{m_i}\right) = k_{4_i}\theta_i + c_{4_i}, \end{aligned} \tag{6.26}$$

where

$$\begin{aligned} c_{3_i} &= -k_{3_i}\theta_{m_i} + \tau_{1_i}\left(\theta_{m_i}\right), \\ c_{4_i} &= -k_{4_i}\theta_{m_i} + \tau_{2_i}\left(\theta_{m_i}\right). \end{aligned} \tag{6.27}$$

To satisfy the approximation criteria, the angular coefficients of the approximations are chosen so that

$$\begin{aligned} \int_{\theta_{m_i}}^{\theta_{1_i}} \hat{\tau}_{1_i}(\theta_i)\cos\theta_i d\theta_i &= \int_{\theta_{m_i}}^{\theta_{1_i}} \tau_{1_i}(\theta_i)\cos\theta_i d\theta_i = A_{3_i}, \\ \int_{\theta_{2_i}}^{\theta_{m_i}} \hat{\tau}_{2_i}(\theta_i)\cos\theta_i d\theta_i &= \int_{\theta_{2_i}}^{\theta_{m_i}} \tau_{2_i}(\theta_i)\cos\theta_i d\theta_i = A_{4_i}. \end{aligned} \tag{6.28}$$

Substitution of (6.26) into (6.28) gives,

$$\begin{aligned}
\int_{\theta_{m_i}}^{\theta_{1_i}} \hat{\tau}_{1_i}(\theta_i)\cos\theta_i d\theta_i &= \int_{\theta_{m_i}}^{\theta_{1_i}} \left[k_{3_i}\left(\theta_i - \theta_{m_i}\right) + \tau_{1_i}\left(\theta_{m_i}\right)\right]\cos\theta_i d\theta_i \\
&= \left[k_{3_i}\left(\theta_{1_i} - \theta_{m_i}\right)\sin\theta_{1_i} + k_{3_i}\left(\cos\theta_{1_i} - \cos\theta_{m_i}\right) + \tau_{1_i}\left(\theta_{m_i}\right)\left(\sin\theta_{1_i} - \sin\theta_{m_i}\right)\right] \\
&= A_{3_i}, \\
\int_{\theta_{2_i}}^{\theta_{m_i}} \hat{\tau}_{2_i}(\theta_i)\cos\theta_i d\theta_i &= \int_{\theta_{2_i}}^{\theta_{m_i}} \left[k_{4_i}\left(\theta_i - \theta_{m_i}\right) + \tau_{2_i}\left(\theta_{m_i}\right)\right]\cos\theta_i d\theta_i \\
&= \left[k_{4_i}\left(\theta_{m_i} - \theta_{2_i}\right)\sin\theta_{2_i} + k_{4_i}\left(\cos\theta_{m_i} - \cos\theta_{2_i}\right) + \tau_{2_i}\left(\theta_{m_i}\right)\left(\sin\theta_{m_i} - \sin\theta_{2_i}\right)\right] \\
&= A_{4_i}.
\end{aligned} \tag{6.29}$$

The angular coefficients are then determined as

$$\begin{aligned}
k_{3_i} &= \frac{A_{3_i} - \tau_{1_i}\left(\theta_{m_i}\right)\left(\sin\theta_{1_i} - \sin\theta_{m_i}\right)}{\left(\theta_{1_i} - \theta_{m_i}\right)\sin\theta_{1_i} + \left(\cos\theta_{1_i} - \cos\theta_{m_i}\right)}, \\
k_{4_i} &= \frac{A_{4_i} - \tau_{2_i}\left(\theta_{m_i}\right)\left(\sin\theta_{m_i} - \sin\theta_{2_i}\right)}{\left(\theta_{m_i} - \theta_{2_i}\right)\sin\theta_{2_i} + \left(\cos\theta_{m_i} - \cos\theta_{2_i}\right)}.
\end{aligned} \tag{6.30}$$

6.3.3 Method 4

If the inner wheels are locked during turning, the elevation angle φ_i can reach 45^0, as determined from (6.22) and (6.23). In that case, the component of shear stress in the X direction τ_{X_i} is considered nearly the same that in the Y direction τ_{Y_i}. Taking this observation into account, the angular coefficients of the approximations can be chosen so that

$$\begin{aligned}
\int_{\theta_{m_i}}^{\theta_{1_i}} \hat{\tau}_{1_i}(\theta_i)d\theta_i &= \int_{\theta_{m_i}}^{\theta_{1_i}} \tau_{1_i}(\theta_i)d\theta_i = A'_{3_i}, \\
\int_{\theta_{2_i}}^{\theta_{m_i}} \hat{\tau}_{2_i}(\theta_i)d\theta_i &= \int_{\theta_{2_i}}^{\theta_{m_i}} \tau_{2_i}(\theta_i)\theta_i d\theta_i = A'_{4_i}.
\end{aligned} \tag{6.31}$$

Substitution of (6.26) into (6.31) gives,

$$\begin{aligned}
\int_{\theta_{m_i}}^{\theta_{1_i}} \hat{\tau}_{1_i}(\theta_i)d\theta_i &= \int_{\theta_{m_i}}^{\theta_{1_i}} \left[k_{3_i}\left(\theta_i - \theta_{m_i}\right) + \tau_{1_i}\left(\theta_{m_i}\right)\right]d\theta_i \\
&= \left[\frac{k_{3_i}}{2}\left(\theta_{1_i} - \theta_{m_i}\right)^2 + \left(\theta_{1_i} - \theta_{m_i}\right)\tau_{1_i}\left(\theta_{m_i}\right)\right] \\
&= A'_{3_i}, \\
\int_{\theta_{2i}}^{\theta_{m_i}} \hat{\tau}_{2_i}(\theta_i)d\theta_i &= \int_{\theta_{2i}}^{\theta_{m_i}} \left[k_{4_i}\left(\theta_i - \theta_{m_i}\right) + \tau_{2_i}\left(\theta_{m_i}\right)\right]d\theta_i \\
&= \left[-\frac{k_{4_i}}{2}\left(\theta_{m_i} - \theta_{2_i}\right)^2 + \left(\theta_{m_i} - \theta_{2_i}\right)\tau_{2_i}\left(\theta_{m_i}\right)\right] \\
&= A'_{4_i}.
\end{aligned} \tag{6.33}$$

The angular coefficients can now be obtained as

$$\begin{aligned}
k_{3_i} &= \frac{2\left(A'_{3_i} - \left(\theta_{1_i} - \theta_{m_i}\right)\tau_{1_i}\left(\theta_{m_i}\right)\right)}{\left(\theta_{1_i} - \theta_{m_i}\right)^2}, \\
k_{4_i} &= \frac{2\left(-A'_{4_i} + \left(\theta_{m_i} - \theta_{2_i}\right)\tau_{2_i}\left(\theta_{m_i}\right)\right)}{\left(\theta_{m_i} - \theta_{2_i}\right)^2}.
\end{aligned} \tag{6.32}$$

Other approximation coefficients, c_{3_i} and c_{4_i}, are the same as in Method 3 (6.27). Simulation shows that results from Method 4 are nearly the same with Method 3. The difference is less than 0.16% of the angular coefficient.

6.3.4 Results

Results of the proposed approaches are shown in Figure 6.7 in comparison with Shibly's method. It can be seen that in the front region, the stress is nearly linear; as a result, the differences among the approximations and the actual stress are small. In the rear region, however, the linearisation result from Shibly's method is far away from the stress, especially for sandy loam, clayed soil, and dry clay. In contrast, in the proposed methods, the 'area' under the approximating line is maintained the same with that of the actual stress which can minimise the approximation error.

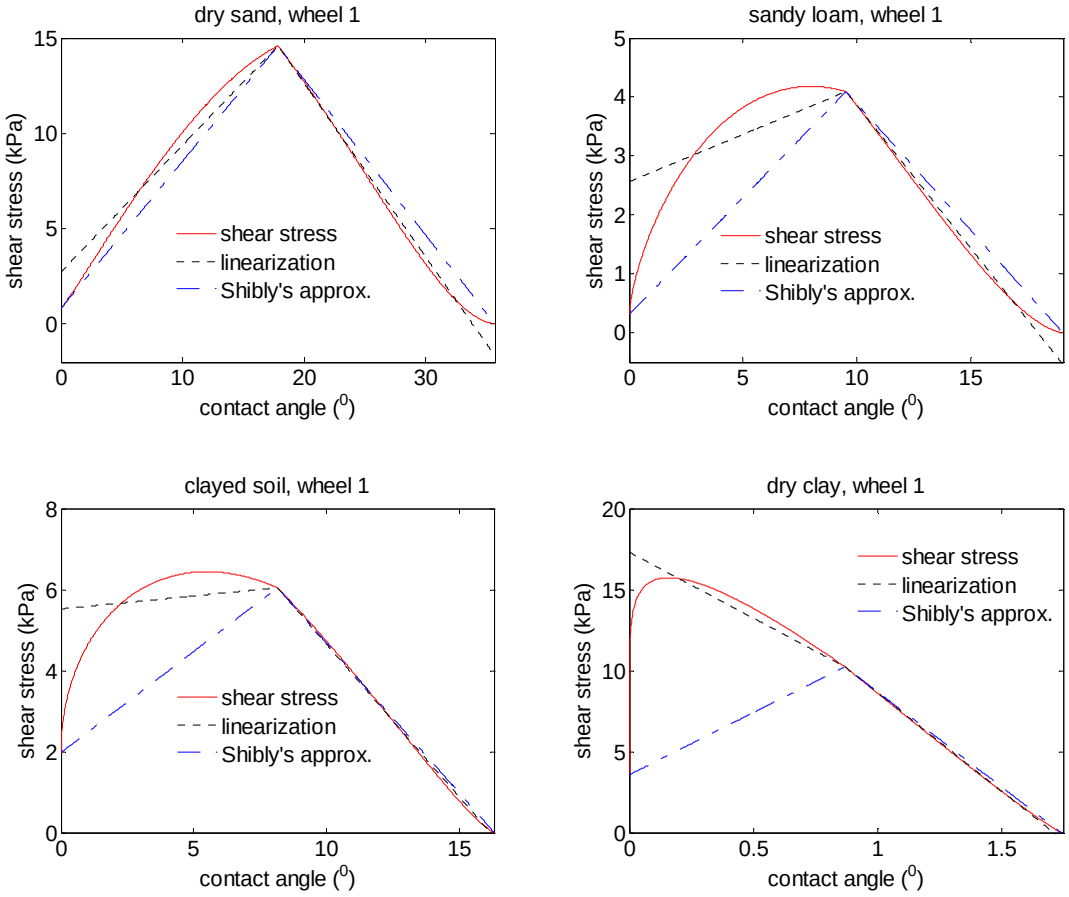

Figure 6.7 Linearisation of shear stress

Let θ_{c1_i} and θ_{c2_i} be the contact angles at which the shear stress intersects its approximations in the front and rear regions respectively. Simulations with experimental data, as presented in Figure 5.12, show that on a given terrain, the ratios $\theta_{c1_i}/\theta_{1_i}$ and $\theta_{c2_i}/\theta_{1_i}$ do not vary much when θ_{1_i} or wheel slip changes, as shown in Figure 6.8. The average values of these ratios, calculated with different values of θ_{1_i} and slip ratio, can therefore be used to derive θ_{c1_i} and θ_{c2_i} instead calculating θ_{c1_i} and θ_{c2_i} each time θ_{1_i} or slip ratio changes.

$$\frac{\theta_{c1_i}}{\theta_{1_i}} = \begin{cases} 0.8665, & \text{for dry sand} \\ 0.8767, & \text{for sandy loam} \\ 0.8001, & \text{for clayed soil} \\ 0.8638, & \text{for dry clay}, \end{cases} \tag{6.34}$$

and

$$\frac{\theta_{c2_i}}{\theta_{1_i}} = \begin{cases} 0.1815, & \text{for dry sand} \\ 0.1490, & \text{for sandy loam} \\ 0.1420, & \text{for clayed soil} \\ 0.1178, & \text{for dry clay.} \end{cases} \tag{6.35}$$

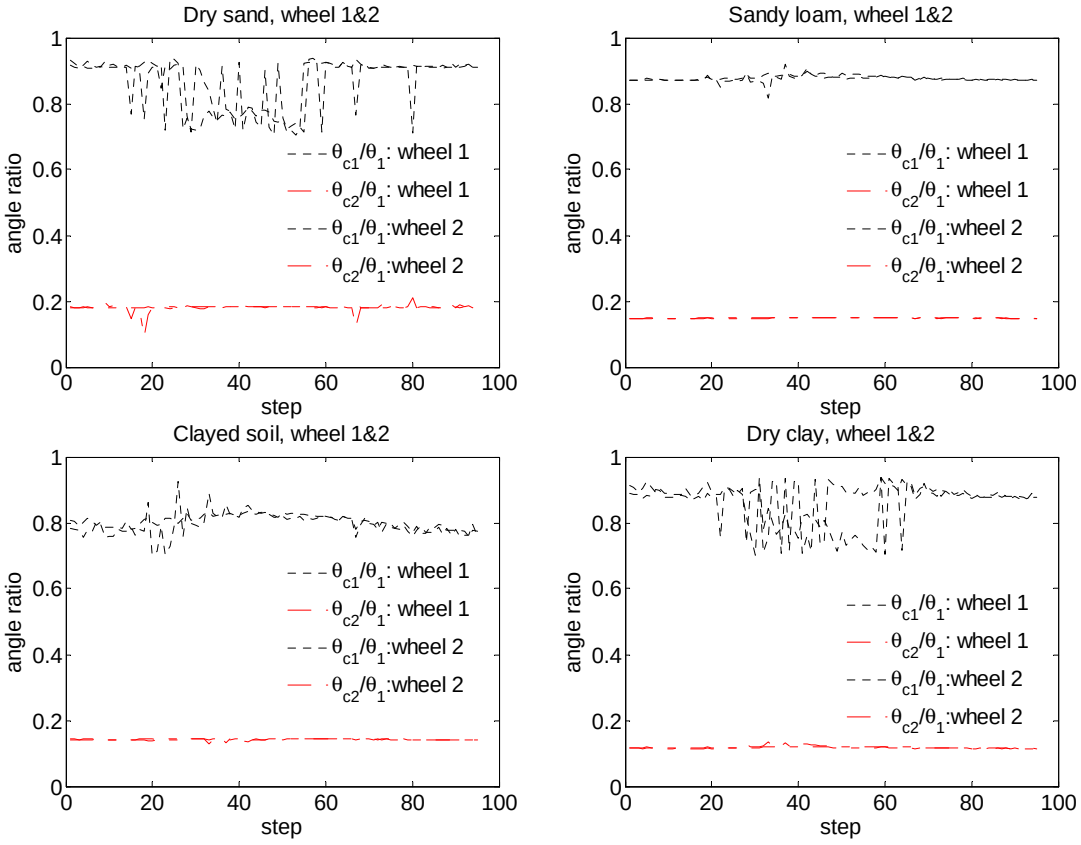

Figure 6.8 Distribution of the angle ratios for shear stress approximation

As the intersections of the normal stress and its approximations are derived from (6.34) and (6.35), the straight lines for approximation can now be expressed by

$$\begin{aligned}
\hat{\tau}_{1_i} &= k_{3_i}\theta_i + c_{3_i}, \\
k_{3_i} &= \frac{\tau_{1_i}\left(\theta_{c1_i}\right) - \tau_{1_i}\left(\theta_{m_i}\right)}{\theta_{c1_i} - \theta_{m_i}}, \\
c_{3_i} &= -k_{3_i}\theta_{m_i} + \tau_{1_i}\left(\theta_{m_i}\right),
\end{aligned} \tag{6.36}$$

$$\begin{aligned}
\hat{\tau}_{2_i} &= k_{4_i}\theta_i + c_{4_i}, \\
k_{4_i} &= \frac{\tau_{2_i}\left(\theta_{c2_i}\right) - \tau_{2_i}\left(\theta_{m_i}\right)}{\theta_{c2_i} - \theta_{m_i}}, \\
c_{4_i} &= -k_{4_i}\theta_{m_i} + \tau_{2_i}\left(\theta_{m_i}\right),
\end{aligned} \tag{6.37}$$

From the observation that the shapes of shear stress and its components in the X, Y and Z directions are nearly similar, as shown in Figure 6.9, the same intersection points in (6.36) and (6.37) can be used in approximating the shear stress components as follows

$$\begin{aligned}
\hat{\tau}_{1X_i} &= k_{3X_i}\theta_i + c_{3X_i}, \\
k_{3X_i} &= \frac{\tau_{1X_i}\left(\theta_{c1_i}\right) - \tau_{1X_i}\left(\theta_{m_i}\right)}{\theta_{c1_i} - \theta_{m_i}}, \\
c_{3X_i} &= -k_{3X_i}\theta_{m_i} + \tau_{1X_i}\left(\theta_{m_i}\right),
\end{aligned} \tag{6.38}$$

$$\begin{aligned}
\hat{\tau}_{1Y_i} &= k_{3Y_i}\theta_i + c_{3Y_i}, \\
k_{3Y_i} &= \frac{\tau_{1Y_i}\left(\theta_{c1_i}\right) - \tau_{1Y_i}\left(\theta_{m_i}\right)}{\theta_{c1_i} - \theta_{m_i}}, \\
c_{3Y_i} &= -k_{3Y_i}\theta_{m_i} + \tau_{1Y_i}\left(\theta_{m_i}\right),
\end{aligned} \tag{6.39}$$

$$\begin{aligned}
\hat{\tau}_{1Z_i} &= k_{3Z_i}\theta_i + c_{3Z_i}, \\
k_{3Z_i} &= \frac{\tau_{1Z_i}\left(\theta_{c1_i}\right) - \tau_{1Z_i}\left(\theta_{m_i}\right)}{\theta_{c1_i} - \theta_{m_i}}, \\
c_{3Z_i} &= -k_{3Z_i}\theta_{m_i} + \tau_{1Z_i}\left(\theta_{m_i}\right),
\end{aligned} \tag{6.40}$$

$$\hat{\tau}_{2X_i} = k_{4X_i}\theta_i + c_{4X_i},$$
$$k_{4X_i} = \frac{\tau_{2X_i}(\theta_{c2_i}) - \tau_{2X_i}(\theta_{m_i})}{\theta_{c2_i} - \theta_{m_i}}, \tag{6.41}$$
$$c_{4X_i} = -k_{4X_i}\theta_{m_i} + \tau_{2X_i}(\theta_{m_i}),$$

$$\hat{\tau}_{2Y_i} = k_{4Y_i}\theta_i + c_{4Y_i},$$
$$k_{4Y_i} = \frac{\tau_{2Y_i}(\theta_{c2_i}) - \tau_{2Y_i}(\theta_{m_i})}{\theta_{c2_i} - \theta_{m_i}}, \tag{6.42}$$
$$c_{4Y_i} = -k_{4Y_i}\theta_{m_i} + \tau_{2Y_i}(\theta_{m_i}),$$

$$\hat{\tau}_{2Z_i} = k_{4Z_i}\theta_i + c_{4Z_i},$$
$$k_{4Z_i} = \frac{\tau_{2Z_i}(\theta_{c2_i}) - \tau_{2Z_i}(\theta_{m_i})}{\theta_{c2_i} - \theta_{m_i}}, \tag{6.43}$$
$$c_{4Z_i} = -k_{4Z_i}\theta_{m_i} + \tau_{2Z_i}(\theta_{m_i}).$$

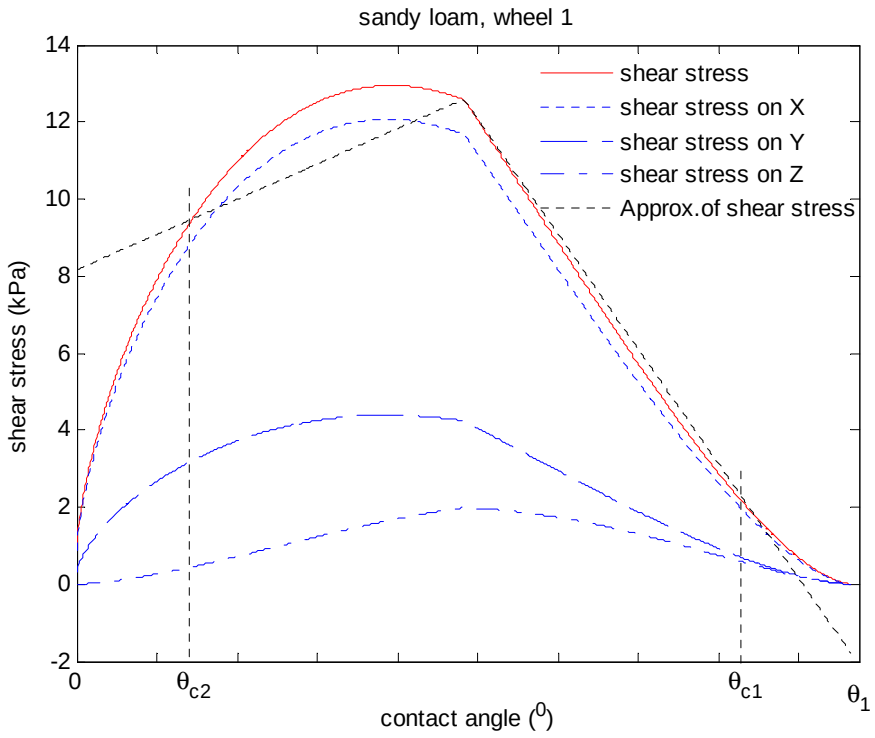

Figure 6.9 Shear stress and its components in a moderate turn

It is noted that if Shibly's method is applied to the approximation of the shear stress components, then angles θ_{c1_i} and θ_{c2_i} in (6.38-6.43) will be replaced by θ_{1_i} and θ_{2_i}, respectively. Both Shibly's and the proposed methods can be applied for all wheels. If the ground behaves as a plastic medium, due to the remaining sinkage, z_{i-2} in (6.1), the normal and shear stresses of the follower wheels (i=3,4,…,8) are nearly linear. In that case, the differences between the actual stresses and their linearisations are not significant, even for Shibly's method.

6.4 Vehicle-terrain interaction analysis algorithm

In the terrain interaction analysis developed in Chapter 5, the behaviour of the vehicle on a given terrain is predicted from the turning moment and reaction forces of the terrain on the vehicle. These variables are obtained from the integrals of components of normal and shear stresses. In this section, the above approximations of the stresses are employed to derive explicit equations for the terrain interaction model, and thus result in a fast algorithm for the analysis.

6.4.1 Reaction forces

The total reaction forces of the ground on the i^{th} wheel is determined by (5.26),

$$F_{X_i} = \int dF_{X_i} = r\int_{\theta_{2_i}}^{\theta_{1_i}}\int_{-b/2}^{b/2}\left(\tau_{X_i}+\sigma_{X_i}\right)d\theta_i dy_i \,,$$

$$F_{Y_i} = \int dF_{Y_i} = r\int_{\theta_{2_i}}^{\theta_{1_i}}\int_{-b/2}^{b/2}\tau_{Y_i}d\theta_i dy_i \,, \qquad (6.44)$$

$$F_{Z_i} = \int dF_{Z_i} = r\int_{\theta_{2_i}}^{\theta_{1_i}}\int_{-b/2}^{b/2}\left(\tau_{Z_i}+\sigma_{Z_i}\right)d\theta_i dy_i \,.$$

All integrals in the analysis of the terrain interaction are of a double type. Integrals along θ_i of the above approximation can easily be computed. Normal stress is independent of y_i and its integral along y_i can therefore be obtained directly. Shear stress is also independent of y_i if the turning rate is zero. During turning, the shear stress may

change along the y_i axis as the shear displacement is varying. However, as shown in Figure 6.10, the differences among shear stresses at the both sides (y_i=± b/2) and in the middle (y_i =0) of a wheel in a moderate turn are very small. It can therefore be assumed that shear stress at any point (θ_i, y_i) in the contact zone is the same as that at the point (θ_i, 0) on the centre line of the wheel. In that case, (6.44) becomes

$$
\begin{aligned}
F_{X_i} &= rb\left[\int_{\theta_{2_i}}^{\theta_{m_i}}\left(\tau_{2X_i}+\sigma_{2Xi}\right)d\theta_i+\int_{\theta_{m_i}}^{\theta_{1_i}}\left(\tau_{1X_i}+\sigma_{1X_i}\right)d\theta_i\right],\\
F_{Y_i} &= rb\left[\int_{\theta_{2_i}}^{\theta_{m_i}}\tau_{2Y_i}d\theta_i+\int_{\theta_{m_i}}^{\theta_{1_i}}\tau_{1Y_i}d\theta_i\right],\\
F_{Z_i} &= rb\left[\int_{\theta_{2_i}}^{\theta_{m_i}}\left(\tau_{2Z_i}+\sigma_{2Z_i}\right)d\theta_i+\int_{\theta_{m_i}}^{\theta_{1_i}}\left(\tau_{1Z_i}+\sigma_{1Z_i}\right)d\theta_i\right].
\end{aligned}
\tag{6.45}
$$

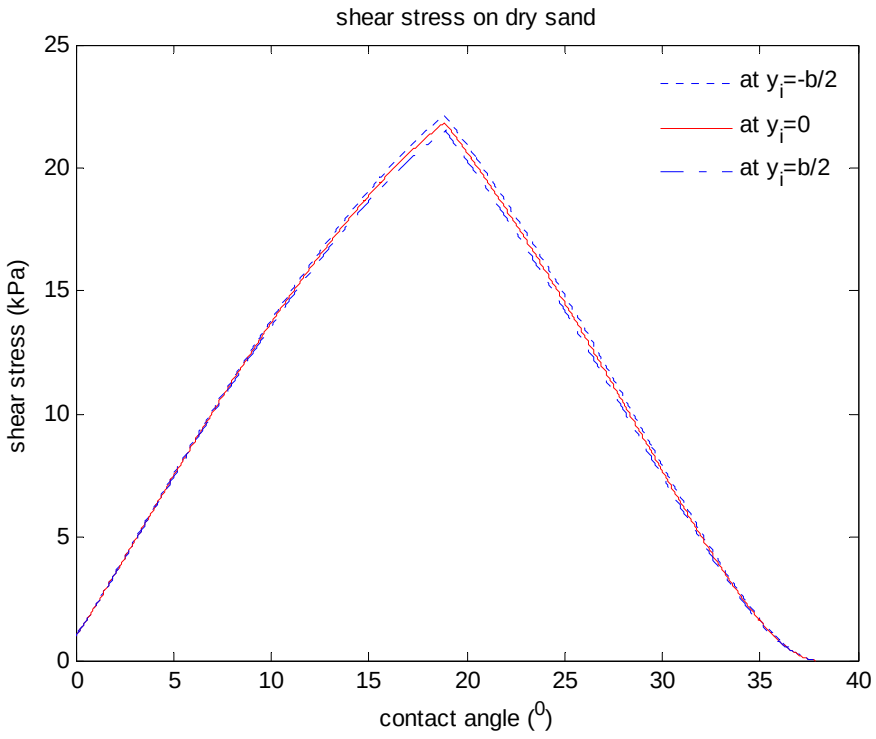

Figure 6.10 Distribution of shear stress along y_i at a turning rate of -0.39 rad/s

Substituting the approximations of stress components (6.17-6.20, 6.38-6.43) into (6.45) gives

$$\hat{F}_{X_i} = rb\left[\int_{\theta_{2_i}}^{\theta_{m_i}}\left[\left(k_{2X_i}+k_{4X_i}\right)\theta_i+\left(c_{2X_i}+c_{4X_i}\right)\right]d\theta_i+\int_{\theta_{m_i}}^{\theta_{1_i}}\left[\left(k_{1X_i}+k_{3X_i}\right)\theta_i+\left(c_{1X_i}+c_{3X_i}\right)\right]d\theta_i\right],$$

$$\hat{F}_{Y_i} = rb\left[\int_{\theta_{2_i}}^{\theta_{m_i}}\left[k_{4Y_i}\theta_i+c_{4Y_i}\right]d\theta_i+\int_{\theta_{m_i}}^{\theta_{1_i}}\left[k_{3Y_i}\theta_i+c_{3Y_i}\right]d\theta_i\right], \tag{6.46}$$

$$\hat{F}_{Z_i} = rb\left[\int_{\theta_{2_i}}^{\theta_{m_i}}\left[\left(k_{2Z_i}+k_{4Z_i}\right)\theta_i+\left(c_{2Z_i}+c_{4Z_i}\right)\right]d\theta_i+\int_{\theta_{m_i}}^{\theta_{1_i}}\left[\left(k_{1Z_i}+k_{3Z_i}\right)\theta_i+\left(c_{1Z_i}+c_{3Z_i}\right)\right]d\theta_i\right].$$

Solving (6.46) leads to

$$\hat{F}_{X_i} = rb\left[\begin{array}{l}\left(\frac{\left(k_{2X_i}+k_{4X_i}\right)}{2}\left(\theta_{m_i}^2-\theta_{2_i}^2\right)+\left(c_{2X_i}+c_{4X_i}\right)\left(\theta_{m_i}-\theta_{2_i}\right)\right)\\+\left(\frac{\left(k_{1X_i}+k_{3X_i}\right)}{2}\left(\theta_{1_i}^2-\theta_{m_i}^2\right)+\left(c_{1X_i}+c_{3X_i}\right)\left(\theta_{1_i}-\theta_{m_i}\right)\right)\end{array}\right],$$

$$\hat{F}_{Y_i} = rb\left[\left(\frac{k_{4Y_i}}{2}\left(\theta_{m_i}^2-\theta_{2_i}^2\right)+c_{4Y_i}\left(\theta_{m_i}-\theta_{2_i}\right)\right)+\left(\frac{k_{3Y_i}}{2}\left(\theta_{1_i}^2-\theta_{m_i}^2\right)+c_{3Y_i}\left(\theta_{1_i}-\theta_{m_i}\right)\right)\right], \tag{6.47}$$

$$\hat{F}_{Z_i} = rb\left[\begin{array}{l}\left(\frac{\left(k_{2Z_i}+k_{4Z_i}\right)}{2}\left(\theta_{m_i}^2-\theta_{2_i}^2\right)+\left(c_{2Z_i}+c_{4Z_i}\right)\left(\theta_{m_i}-\theta_{2_i}\right)\right)\\+\left(\frac{\left(k_{1Z_i}+k_{3Z_i}\right)}{2}\left(\theta_{1_i}^2-\theta_{m_i}^2\right)+\left(c_{1Z_i}+c_{3Z_i}\right)\left(\theta_{1_i}-\theta_{m_i}\right)\right)\end{array}\right].$$

With the assumption that $\theta_{2_i}=0$ and the maximum stress occurs in the middle of the contact zone, i.e. $\theta_{m_i}=\frac{1}{2}\theta_{1_i}$, (6.47) becomes

$$\hat{F}_{X_i} = rb\left(\frac{\left(3k_{1X_i} + k_{2X_i} + 3k_{3X_i} + k_{4X_i}\right)}{8}\theta_{l_i}^2 + \frac{\left(c_{1X_i} + c_{2X_i} + c_{3X_i} + c_{4X_i}\right)}{2}\theta_{l_i}\right),$$

$$\hat{F}_{Y_i} = rb\left(\frac{3k_{3Y_i} + k_{4Y_i}}{8}\theta_{l_i}^2 + \frac{c_{3Y_i} + c_{4Y_i}}{2}\theta_{l_i}\right), \tag{6.48}$$

$$\hat{F}_{Z_i} = rb\left(\frac{\left(3k_{1Z_i} + k_{2Z_i} + 3k_{3Z_i} + k_{4Z_i}\right)}{8}\theta_{l_i}^2 + \frac{\left(c_{1Z_i} + c_{2Z_i} + c_{3Z_i} + c_{4Z_i}\right)}{2}\theta_{l_i}\right).$$

6.4.2 Vehicle kinetics

- **Acceleration and weight balance:**

Substitution of (6.48) into equations (5.27, 5.28, and 5.30) gives the total reaction forces in the X, Y, and Z directions as

$$\hat{F}_X = \sum_{i=1}^{8}\hat{F}_{X_i} = rb\sum_{i=1}^{8}\left(\frac{\left(3k_{1X_i} + k_{2X_i} + 3k_{3X_i} + k_{4X_i}\right)}{8}\theta_{l_i}^2 + \frac{\left(c_{1X_i} + c_{2X_i} + c_{3X_i} + c_{4X_i}\right)}{2}\theta_{l_i}\right) = ma_X,$$

(6.49)

$$\hat{F}_Y = \sum_{i=1}^{8}\hat{F}_{Y_i} = rb\sum_{i=1}^{8}\left(\frac{3k_{3Y_i} + k_{4Y_i}}{8}\theta_{l_i}^2 + \frac{c_{3Y_i} + c_{4Y_i}}{2}\theta_{l_i}\right) = ma_Y, \tag{6.50}$$

$$\hat{F}_Z = \sum_{i=1}^{8}\hat{F}_{Z_i} = rb\sum_{i=1}^{8}\left(\frac{\left(k_{1Z_i} + k_{2Z_i} + k_{3Z_i} + k_{4Z_i}\right)}{8}\theta_{l_i}^2 + \frac{\left(c_{1Z_i} + c_{2Z_i} + c_{3Z_i} + c_{4Z_i}\right)}{2}\theta_{l_i}\right) = mg, \tag{6.51}$$

$$\hat{F}_{Zi} = \left(\frac{\left(3k_{1Z_i} + k_{2Z_i} + 3k_{3Z_i} + k_{4Z_i}\right)}{8}\theta_{l_i}^2 + \frac{\left(c_{1Z_i} + c_{2Z_i} + c_{3Z_i} + c_{4Z_i}\right)}{2}\theta_{l_i}\right) = W_i,\ i = 1,2,...,8. \tag{6.52}$$

- **Turning moment:**

The turning moment is determined from (5.32) as

$$\hat{M}_Z = \underbrace{-\sum_{i=1}^{8}\int Y_i d\hat{F}_{X_i}}_{C_1} + \underbrace{\sum_{i=1}^{8}\int X_i d\hat{F}_{Y_i}}_{C_2} = I_Z\dot{\Omega}. \tag{6.53}$$

With the assumption that the approximations of stresses are independent of y_i, the first term, C_1, in (6.53) is calculated as

$$\begin{aligned} C_1 &= -r\sum_{i=1}^{8}\int_0^{\theta_{1_i}}\left(\hat{\tau}_{X_i}+\hat{\sigma}_{X_i}\right)d\theta_i\int_{-b/2}^{b/2}\left((-1)^{i+1}B+y_i\right)dy_i \\ &= -B\sum_{i=1}^{8}(-1)^{i+1}\underbrace{rb\int_0^{\theta_{1_i}}\left(\hat{\tau}_{X_i}+\hat{\sigma}_{X_i}\right)d\theta_i}_{\hat{F}_{X_i}} = -B\sum_{i=1}^{8}(-1)^{i+1}\hat{F}_{X_i}. \end{aligned} \tag{6.54}$$

The second term, C_2, in (6.53) can be expanded as

$$\begin{aligned} C_2 &= rb\sum_{i=1}^{8}\int_0^{\theta_{1_i}}\left(a\left(\frac{3}{2}-E\left[\frac{i-1}{2}\right]\right)-d+r\sin\theta_i\right)\hat{\tau}_{Y_i}d\theta_i \\ &= \sum_{i=1}^{8}\left[a\left(\frac{3}{2}-E\left[\frac{i-1}{2}\right]\right)-d\right]\underbrace{rb\int_0^{\theta_{1_i}}\hat{\tau}_{Y_i}d\theta_i}_{\hat{F}_{Y_i}}+\sum_{i=1}^{8}r^2b\int_0^{\theta_{1_i}}\sin\theta_i\hat{\tau}_{Y_i}d\theta_i \\ &= \sum_{i=1}^{8}\left[a\left(\frac{3}{2}-E\left[\frac{i-1}{2}\right]\right)-d\right]\hat{F}_{Y_i}+\underbrace{\sum_{i=1}^{8}r^2b\int_0^{\theta_{1_i}}\sin\theta_i\hat{\tau}_{Y_i}d\theta_i}_{C_3}. \end{aligned} \tag{6.55}$$

Substitution of (6.39) into the third term, C_3, gives

$$\begin{aligned} C_3 &= r^2b\sum_{i=1}^{8}\left[\int_0^{\theta_{m_i}}\left(k_{4Y_i}\theta_i+c_{4Y_i}\right)\sin\theta_i d\theta_i+\int_{\theta_{m_i}}^{\theta_{1_i}}\left(k_{3Y_i}\theta_i+c_{3Y_i}\right)\sin\theta_i d\theta_i\right] \\ &= r^2b\sum_{i=1}^{8}\begin{bmatrix}k_{4Y_i}\left(\sin\theta_{m_i}-\theta_{m_i}\cos\theta_{m_i}\right)-c_{4Y_i}\cos\theta_{m_i}+c_{4Y_i}+k_{3Y_i}\left(\sin\theta_{1_i}-\theta_{1_i}\cos\theta_{1_i}\right)\\ -k_{3Y_i}\left(\sin\theta_{m_i}-\theta_{m_i}\cos\theta_{m_i}\right)-c_{3Y_i}\cos\theta_{1_i}+c_{3Y_i}\cos\theta_{m_i}\end{bmatrix} \\ &= r^2b\sum_{i=1}^{8}\begin{bmatrix}k_{3Y_i}\left(\sin\theta_{1_i}-\theta_{1_i}\cos\theta_{1_i}\right)-c_{3Y_i}\cos\theta_{1_i}\\ +\left(k_{4Y_i}-k_{3Y_i}\right)\left(\sin\theta_{m_i}-\theta_{m_i}\cos\theta_{m_i}\right)-\left(c_{4Y_i}-c_{3Y_i}\right)\cos\theta_{m_i}+c_{4Y_i}\end{bmatrix}. \end{aligned} \tag{6.56}$$

From (6.53-6.56), the turning moment now becomes

$$\hat{M}_Z = -B\sum_{i=1}^{8}(-1)^{i+1}\hat{F}_{X_i} + \sum_{i=1}^{8}\left[a\left(\frac{3}{2} - E\left[\frac{i-1}{2}\right]\right) - d\right]\hat{F}_{Y_i} + C_3 = I_Z\dot{\Omega}. \qquad (6.57)$$

6.4.3 Terrain interaction modelling procedure using fast algorithm

The modelling procedure of the vehicle-terrain interaction analysis presented in Chapter 5 is now combined with the proposed fast algorithm as described below:

(i) Data update:

Read $\omega_L(k)$, $\omega_R(k)$ at time step *k*. Assign current values for vehicle position, velocities and accelerations.

(ii) Wheel vertical load computation:

From previous acceleration values, compute the wheel vertical loads given in (5.37). Solve equation (6.52) to obtain the entry angle of each wheel, θ_{1_i}, so that the reaction force acting on the wheel in the Z direction $\hat{F}_{Zi}$ balances the vertical load.

(iii) Linearisation of normal and shear stress:

Compute shear displacements (5.21), normal stresses (6.1-6.2), and then shear stresses (6.21) in the X, Y, and Z directions at $\theta_{2_i}(0)$, θ_{m_i}, and θ_{1_i} of the contact angle with $y_i = 0$.

Compute the coefficients of the linear approximations of normal and shear stresses (6.15-6.20, 6.36-6.43).

(iv) Next state computation:

Compute the accelerations $a_X(k+1)$, $a_Y(k+1)$ according to (6.49), (6.50), turning acceleration $\dot{\Omega}(k+1)$ according to (6.57), then the next values of $V_X(k+1)$, $V_Y(k+1)$ and turning rate $\Omega(k+1)$. Obtain the vehicle position at $(k+1)$ in the fixed coordinate frame (Appendix B).

6.5 Comparison of results

In this section, the main results from the proposed algorithm are compared with those of the original version of the vehicle-terrain interaction analysis in Chapter 5 in terms of accuracy and computation speed. The effectiveness of the proposed methods is also verified through comparison with Shibly's approach. Terrain parameters and geometrical parameters of the UGV used in this section are the same as were given in Table 5.1 and Table 5.2.

The vehicle trajectories predicted from the original version and this algorithm with the same pattern of wheel angular velocities used in Chapter 5 (see Figure 5.11) are shown here in Figure 6.11. It can be seen that on clayed soil, the result from the proposed approach coincides with that from the benchmark, which is the solution of the original terramechanics equations described in Chapter 5. In turn, the proposed approach produces results very close to the experimental position data obtained from DGPS. Similar results are also encountered on other terrains. In reference to the benchmark, on average the closed-form version of the terrain analysis runs 74.11 times faster.

For the purpose of comparison with Shibly's method in terms of accuracy, the terrains are assumed to behave like those elastic media in which the error of linearisation is largest. Results on clayed soil are shown in Figures 6.12 and 6.13 for the vehicle drawbar pull and turning moment respectively. It can be seen that results from the approach proposed in this chapter are almost identical to those of the terramechanics benchmark while results from Shibly's method are less accurate. On average, the proposed fast algorithm leads to an error of 0.53% in the drawbar pull and 0.64% in the turning moment compared with 23.7% and 22.8% from Shibly's method. The errors are calculated by

$$\frac{\left|\hat{F}_X\right|-\left|F_X\right|}{\left|F_X\right|}\times 100\%, \text{ and } \frac{\left|\hat{M}_X\right|-\left|M_X\right|}{\left|M_X\right|}\times 100\%. \tag{6.58}$$

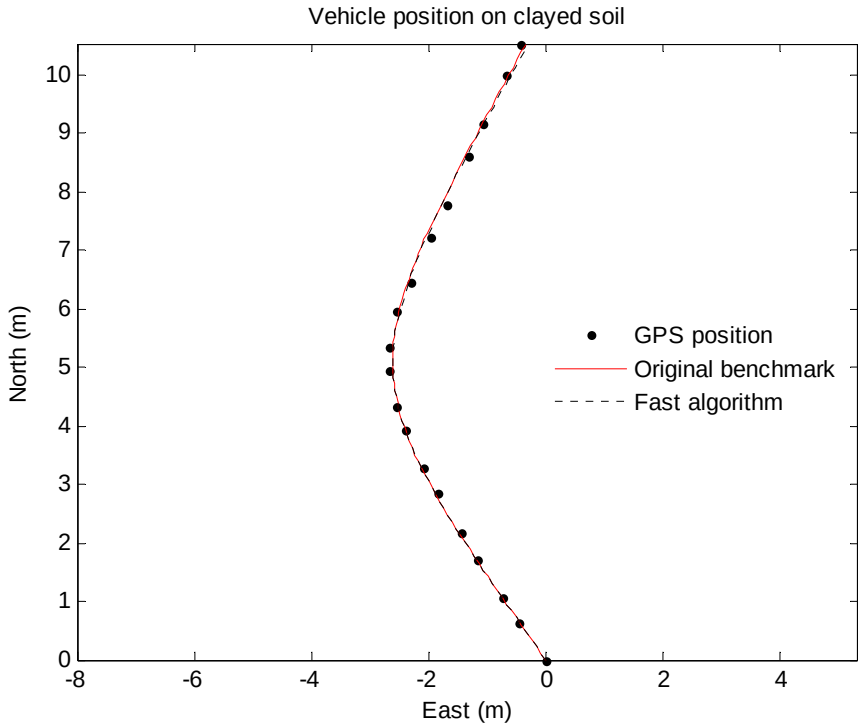

Figure 6.11 Vehicle trajectory: compared between the original and fast algorithms

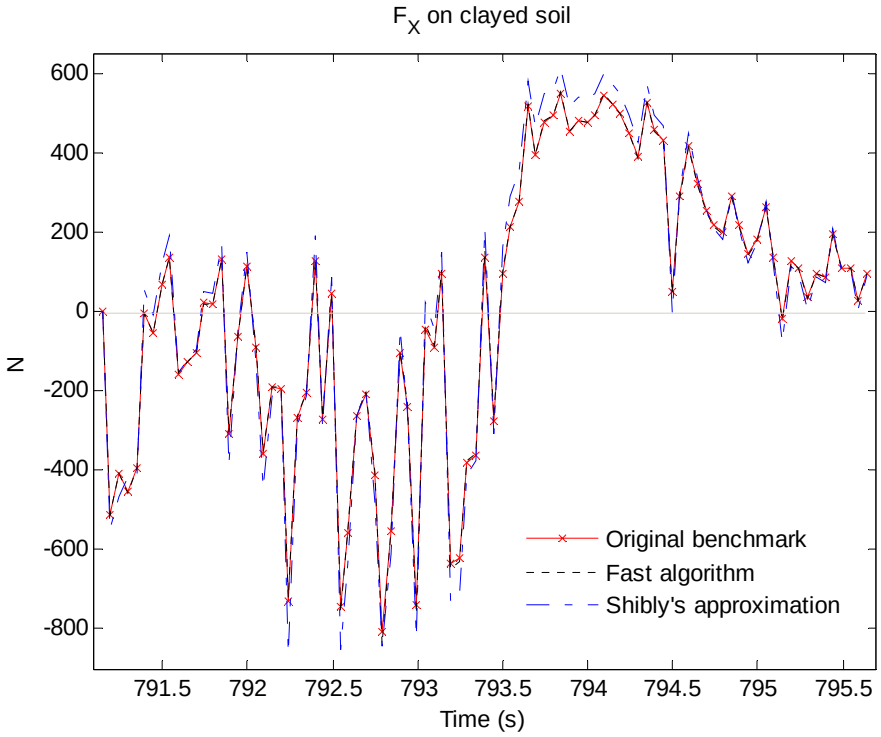

Figure 6.12 Vehicle drawbar pull on clayed soil

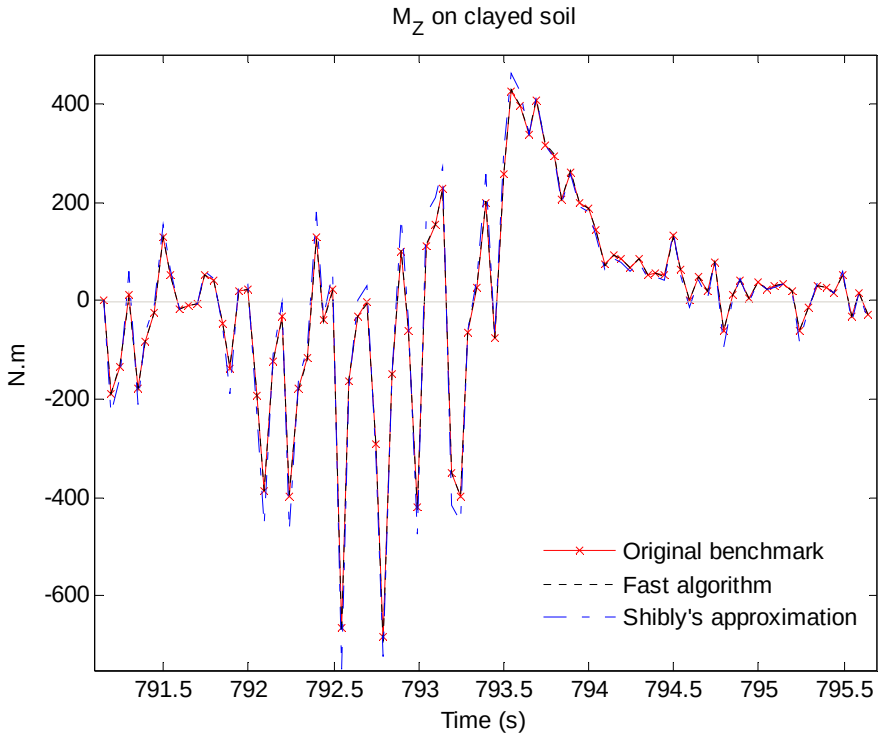

Figure 6.13 Vehicle turning moment on clayed soil

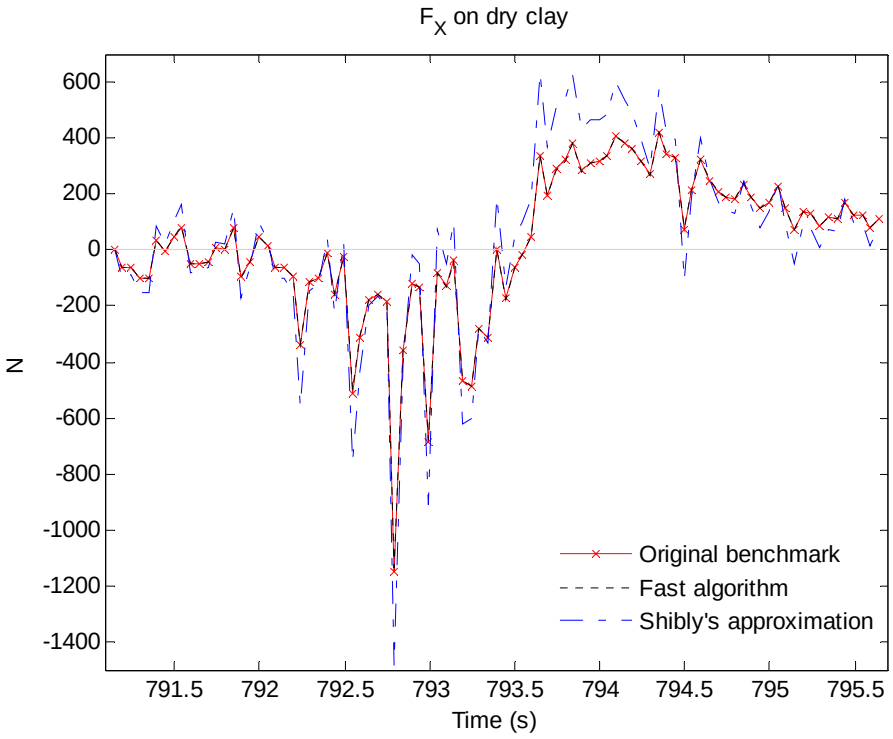

Figure 6.14 Vehicle drawbar pull on dry clay

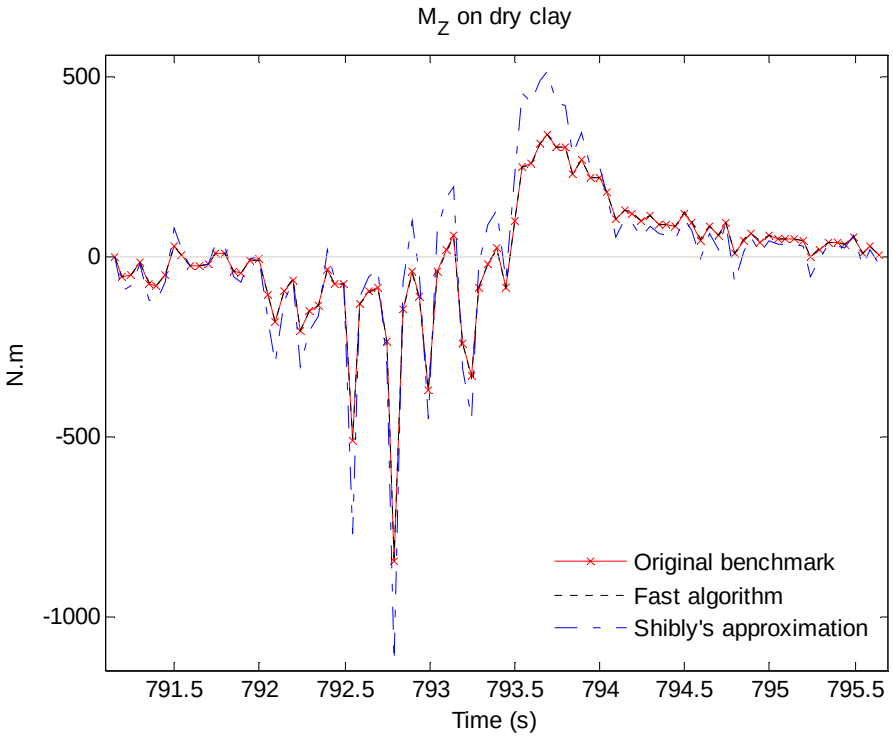

Figure 6.15 Vehicle turning moment on dry clay

It should be noted that the error in Shibly's method different in dry sand and dry clay, tends to exacerbate in dry clay, and always remain larger than the error in the proposed method, as compared with the benchmark results obtained from the terramechanics equations. This can be seen in Figures 6.14 and 6.15. On dry sand, there is a large difference between the drawbar pull and turning moment calculated from Shibly's method and those from the original benchmark. The averaged errors are 126% and 95% for drawbar pull and turning moment respectively. Meanwhile, results from the proposed approach are still close to the original. The errors are very small as the averaged differences are just 0.36% in the drawbar pull and 0.29% in the turning moment, although the normal and shear stresses are highly nonlinear.

6.6 Conclusion

In this chapter a highly efficient algorithm has been developed for implementation of the UGV-terrain interaction analysis. From the linearisation of normal stress, shear stress, and their components, a new version of terrain analysis is obtained that does not

involve integral equations. As a result, the new algorithm can run much faster than the original benchmark. Simulation results and experimental validation have shown that the proposed method is highly accurate as compared with the other method. In the next chapter, the fast algorithm will be integrated into a UGV simulator, in conjunction with the driveline model and motion control described in previous chapters.

Chapter 7

Vehicle simulator

A model of the UGV driveline has been developed in Chapter 3. Robust low-level controllers have been designed as reported in Chapter 4. In Chapter 5, dynamic processes involved in the UGV-terrain interaction have been analysed to predict vehicle performance on different terrains. In this chapter, the driveline model is augmented with the fast algorithm presented in Chapter 6 to take into account the reaction of terrain on the vehicle. All developments so far are integrated in a unique simulator for the UGV.

An introduction to the UGV simulator is given in the first section. In Section 7.2, the driveline model is combined with the terrain interaction analysis. The basic vehicle motion control is described in Section 7.3. A conclusion is drawn in the last section.

7.1 Introduction

In Chapter 3, the driveline model was developed based on the assumption that the vehicle rolling resistance is a proportional of the vehicle weight and velocity (Kiencke and Nielsen, 2000). This assumption is widely used for predicting vehicle performance on hard ground where it is satisfactory. Vehicle behaviour on soft terrain is, however, significantly dissimilar to the results from this empirical method (Wong, 2001). The driveline model therefore needs to incorporate terrain interaction to yield better results.

In the driveline models developed in Chapter 3, the traction torque at the wheels is calculated from the vehicle rolling resistance, acceleration, and component of gravitational force along a slope. In the physical analysis of the interaction between the vehicle and terrain presented in Chapter 5, the traction torque can be derived from the shear stresses developed at the wheels in contact with the terrain. This means that if the traction torque resulting from the terrain interaction analysis is fed back to the driveline model, then the vehicle modelling will be more realistic and accurate.

In this chapter, all proposed approaches so far are implemented on a UGV simulator as configured in Figure 7.1. The driveline model is used to derive the left and right wheel speeds from the throttle, left and right brake inputs. Using the wheel speeds as inputs, the terrain interaction model calculates the vehicle behaviours such as velocity, turning rate, and traction torque. The outputs from the terrain interaction model are fed back to the driveline model to determine new values of wheel speeds, and to the motion control process to update the pattern of throttle and brakes. The fast algorithm described in Chapter 6 is used to implement the terrain interaction modelling procedure and the development proposed approach in Chapter 4 is applied for vehicle motion control.

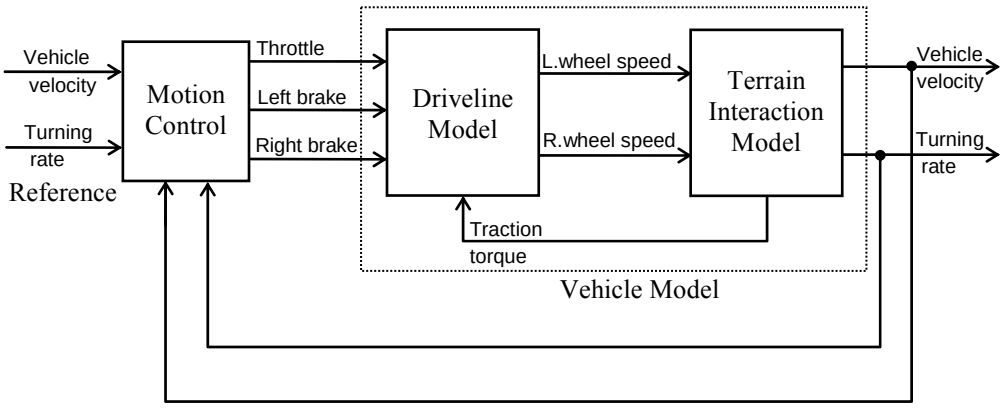

Figure 7.1 Basic structure of the UGV simulator

7.2 Vehicle modelling

In this section, the vehicle model is developed by combining the driveline model and the vehicle-terrain analysis. Let us first consider the traction torque developed on the UGV wheels as they interact with the terrain.

7.2.1 Traction torque

As stated in the terramechanics theory, the total traction torque of a driving wheel is determined by integrating the shear stress over the contact zone (see (5.9)):

$$T = r^2 b \int_{\theta_2}^{\theta_1} \tau(\theta) d\theta, \tag{7.1}$$

where *r* and *b* are the wheel radius and width.

For the UGV, the shear stress is vector quantity, as shown in Figure 6.6. Only the shear stress component that is tangential to the wheel rim (the projection of the shear stress on X-Z plane) contributes to the traction torque. Therefore, the total traction torque developed on the i^{th} wheel is

$$T_i = r^2 \int_{\theta_{2_i}}^{\theta_{1_i}} \int_{-b/2}^{b/2} \tau_{t_i} d\theta_i dy_i, \tag{7.2}$$

where τ_{t_i} is the tangential component of the shear stress derived from the shear stress τ_i and the elevation angle (6.22), φ_i, as

$$\tau_{t_i} = \tau_i \cos\varphi_i. \tag{7.3}$$

Equations (7.2-7.3) can be inserted in the computation procedure given in Chapter 5 to predict the traction torque. However, computing this integral is time-consuming. As mentioned in Chapter 6, in most cases the shapes of the shear stress and its projection on the X-Z plane are nearly equivalent. In fact, in straight-line running, φ_i is zero; and as a result, τ_{t_i} coincides with τ_i. The linearisation method described in Chapter 6 (6.34-

6.43) can therefore be applied to approximate the tangential shear stress component in the front and rear regions as

$$\begin{aligned}
&\hat{\tau}_{1t_i} = k_{3t_i}\theta_i + c_{3t_i},\\
&k_{3t_i} = \frac{\tau_{1t_i}(\theta_{c1_i}) - \tau_{1t_i}(\theta_{m_i})}{\theta_{c1_i} - \theta_{m_i}},\\
&c_{3t_i} = -k_{3t_i}\theta_{m_i} + \tau_{1t_i}(\theta_{m_i}),
\end{aligned} \tag{7.4}$$

$$\begin{aligned}
&\hat{\tau}_{2t_i} = k_{4t_i}\theta_i + c_{4t_i},\\
&k_{4t_i} = \frac{\tau_{2t_i}(\theta_{c2_i}) - \tau_{2t_i}(\theta_{m_i})}{\theta_{c2_i} - \theta_{m_i}},\\
&c_{4t_i} = -k_{4t_i}\theta_{m_i} + \tau_{2t_i}(\theta_{m_i}),
\end{aligned} \tag{7.5}$$

where θ_{c1_i} and θ_{c2_i} are the contact angles at which the shear stress intersects its approximation and can be derived from (6.34-6.35).

From the above linearisation and also from the observation that the shear stress is nearly independent of y_i as shown in Figure 6.10, the traction torque (7.2) can now be approximated by

$$\begin{aligned}
\hat{T}_i &= r^2 b\left[\int_{\theta_{2_i}}^{\theta_{m_i}} \hat{\tau}_{2t_i} d\theta_i + \int_{\theta_{m_i}}^{\theta_{1_i}} \hat{\tau}_{1t_i} d\theta_i\right] = r^2 b\left[\int_{\theta_{2_i}}^{\theta_{m_i}} (k_{4t_i}\theta_i + c_{4t_i}) d\theta_i + \int_{\theta_{m_i}}^{\theta_{1_i}} (k_{3t_i}\theta_i + c_{3t_i}) d\theta_i\right]\\
&= r^2 b\left[\frac{k_{4t_i}}{2}(\theta_{m_i}^2 - \theta_{2_i}^2) + c_{4t_i}(\theta_{m_i} - \theta_{2_i}) + \frac{k_{3t_i}}{2}(\theta_{1_i}^2 - \theta_{m_i}^2) + c_{3t_i}(\theta_{1_i} - \theta_{m_i})\right].
\end{aligned} \tag{7.6}$$

In the case where $\theta_{2_i} = 0$ and $\theta_{m_i} = \theta_{1_i}/2$, equation (7.6) becomes

$$\hat{T}_i = r^2 b\left[\frac{3k_{3t_i} + k_{4t_i}}{8}\theta_{1_i}^2 + \frac{c_{3t_i} + c_{4t_i}}{2}\theta_{1_i}\right]. \tag{7.7}$$

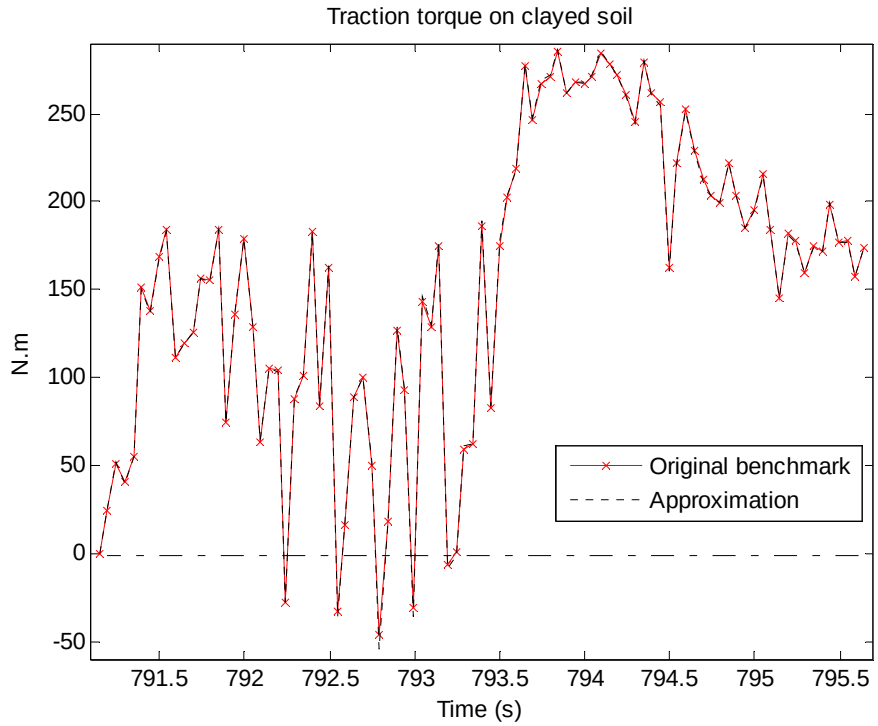

Figure 7.2 Traction torque on clayed soil

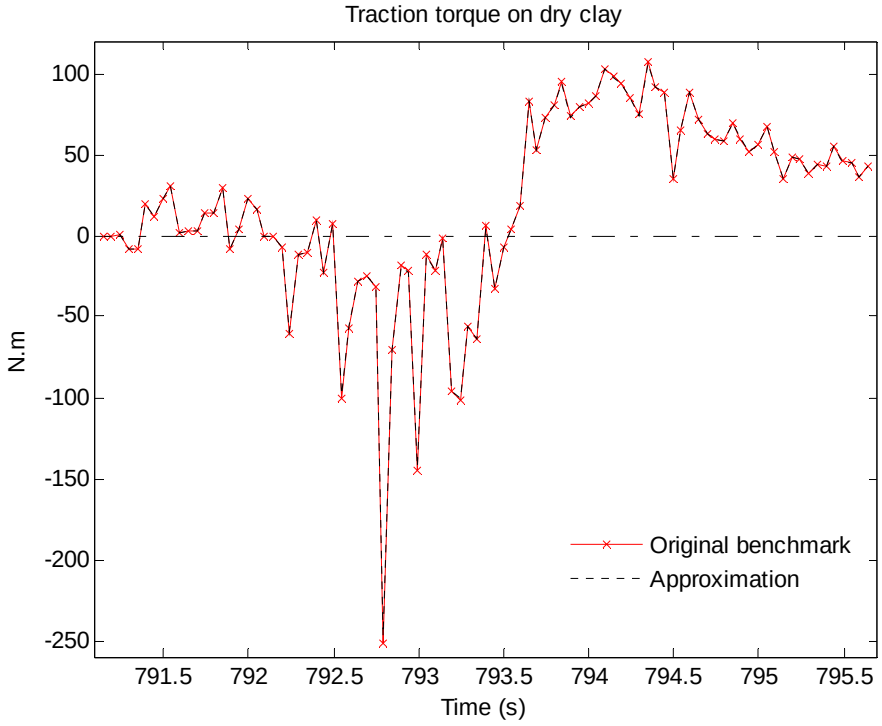

Figure 7.3 Traction torque on dry clay

Equation (7.7) is inserted in the fast computation procedure presented in Chapter 6. The total traction torques of all wheels on clayed soil and dry clay, as predicted from the same pattern of wheel speeds in Chapter 5 (Figure 5.12), are shown in Figures 7.2 and 7.3 in comparison with the original benchmarks. On average, the approximation error is less than 1%. This is sufficiently accurate to be used in the vehicle simulator.

7.2.2 Modified driveline model

Let us first consider the driveline model in straight-line running. As mentioned in Chapter 3, the total load torque acting on the wheel shafts consists of the torques required for traction, $rF_{t,w}$, for wheel acceleration, $J_w\dot{\omega}_w$, and for overcoming the wheel internal friction, $b_w\omega_w$, as (3.12)

$$T_w = J_w\dot{\omega}_w + b_w\omega_w + rF_{t,w}, \tag{7.8}$$

where J_w and b_w are the apparent composite moment of inertia and internal friction coefficient of all eight wheels of the vehicle.

To take into account the vehicle-terrain interaction, the traction torque is derived from the reaction of terrain on the wheels, giving

$$T_w = J_w\dot{\omega}_w + b_w\omega_w + \sum_{i=1}^{8} T_i . \tag{7.9}$$

Similarly, the total loads acting on left and right wheel shafts during turning are modified from (3.32) to obtain

$$\begin{aligned} T_{wL} &= \frac{1}{2}J_w\dot{\omega}_{wL} + \frac{1}{2}b_w\omega_{wL} + \sum_{i=1}^{4} T_{2i-1}, \\ T_{wR} &= \frac{1}{2}J_w\dot{\omega}_{wR} + \frac{1}{2}b_w\omega_{wR} + \sum_{i=1}^{4} T_{2i}. \end{aligned} \tag{7.10}$$

The loads from the wheel acting on the left and right outputs of the differential (3.33) then become

$$T_{dL} = \frac{1}{2} J_w K_3^2 \dot{\omega}_{dL} + \frac{1}{2} b_w K_3^2 \omega_{dL} + K_3 \sum_{i=1}^{4} T_{2i-1},$$
$$T_{dR} = \frac{1}{2} J_w K_3^2 \dot{\omega}_{dR} + \frac{1}{2} b_w K_3^2 \omega_{dR} + K_3 \sum_{i=1}^{4} T_{2i}, \quad (7.11)$$

where ω_{dL} and ω_{dR} are the rotational speeds at the left and right outputs of the differential (3.19), and K_3 is the gear ratio of the chain system (3.7).

At the differential, these torques are combined with the left and right brake forces, T_{bL} and T_{bR}, given in (3.34-35), to yield the total load on the differential

$$T_d = \frac{1}{2} J_w K_3^2 (\dot{\omega}_{dL} + \dot{\omega}_{dR}) + \frac{1}{2} b_w K_3^2 (\omega_{dL} + \omega_{dR}) + K_3 \sum_{i=1}^{8} T_i + T_{bL} + T_{bR}$$
$$= J_w K_3^2 \dot{\omega}_d + b_w K_3^2 \omega_d + K_3 \sum_{i=1}^{8} T_i + T_{bL} + T_{bR}, \quad (7.12)$$

where ω_d is the rotational speed of the differential case.

The total load torque and friction from the differential referred to the CVT through the gearbox (3.36) is now given by

$$T_c = J_w K_3^2 K_2^2 \dot{\omega}_c + (b_w K_3^2 K_2^2 + b_d K_2^2 + b_G) \omega_c + K_3 K_2 \sum_{i=1}^{8} T_i + (T_{bL} + T_{bR}) K_2, \quad (7.13)$$

where b_d and b_G are the viscous friction coefficients of the differential and gearbox, ω_c is the output speed of the CVT, and K_2 is the gear ratio of the gearbox.

During turning, the difference in rotational speed between the differential's case and its outputs (3.19) is determined as (3.37)

$$x = \frac{(T_{dR} - T_{dL}) + (T_{bR} - T_{bL})}{b_{D,in}}, \quad (7.14)$$

where $b_{D,in}$ is the friction coefficient inside the differential's case.

Substitution of (7.11) and (3.19) into (7.14) gives

$$J_w K_3^2 \dot{x} + \left(b_w K_3^2 + b_{D,in}\right)x = K_3 \sum_{i=1}^{4} \left(T_{2i} - T_{2i-1}\right) + \left(T_{bR} - T_{bL}\right). \tag{7.15}$$

From (7.15), the speed difference (3.39a) is expressed as a first-order transfer function of the differences between the right and left wheel traction efforts and the brake forces,

$$x = \frac{K_3 \sum_{i=1}^{4} \left(T_{2i} - T_{2i-1}\right) + \left(T_{bR} - T_{bL}\right)}{J_w K_3^2 s + \left(b_w K_3^2 + b_{D,in}\right)}. \tag{7.16}$$

The left and right wheel speeds can therefore be derived from (3.41) as

$$\begin{aligned} \omega_{wL} &= \omega_c K_2 K_3 + x K_3 , \\ \omega_{wR} &= \omega_c K_2 K_3 - x K_3 . \end{aligned} \tag{7.17}$$

The rest of the driveline model remains the same as in the original equations (3.1-3.4). It is noted that the vehicle dynamics are apparently absent in the modified model because it has been absorbed within the vehicle-terrain interaction analysis. In the terrain interaction model, the reaction forces calculated from the wheel speeds are combined with the vehicle dynamics and kinetics to derive the vehicle velocity, turning rate, and traction torque.

7.2.3 Results

To validate the modified driveline model, the same pattern of experimental data as given in Chapter 3, as shown in Figures 3.20 and 3.21, is used. The performance of the new driveline as it interact with clayed soil (the most likely type of the terrain where the vehicle is running) is shown in Figure 7.4 and Figure 7.5 for the engine, gearbox, and wheel speeds in comparison with those using the original model (with 60% wheel slip assumed) and from experiments. Notably, there is a close agreement in the results between the new model and experiments. During acceleration (in the 596-601s interval), the responses of the gearbox and wheels are much closer to the experimental ones than those using the original model. As mentioned in Chapter 3, however, in the experimental results gearbox and wheel speeds increase at a slower rate than in the simulation, perhaps due to the slip in the CVT during periods of acceleration.

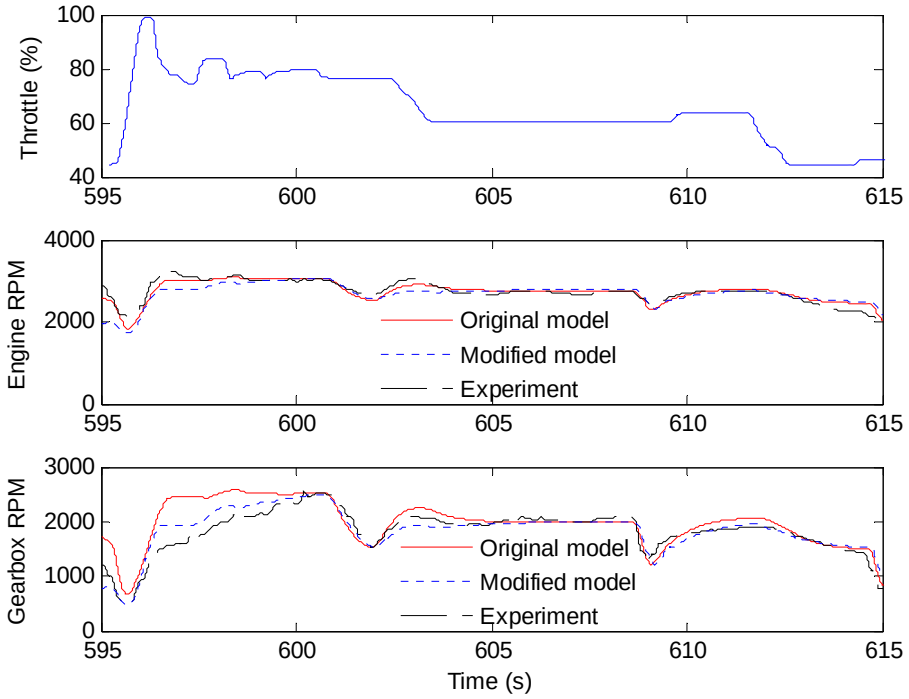

Figure 7.4 Engine and gearbox responses on clayed soil

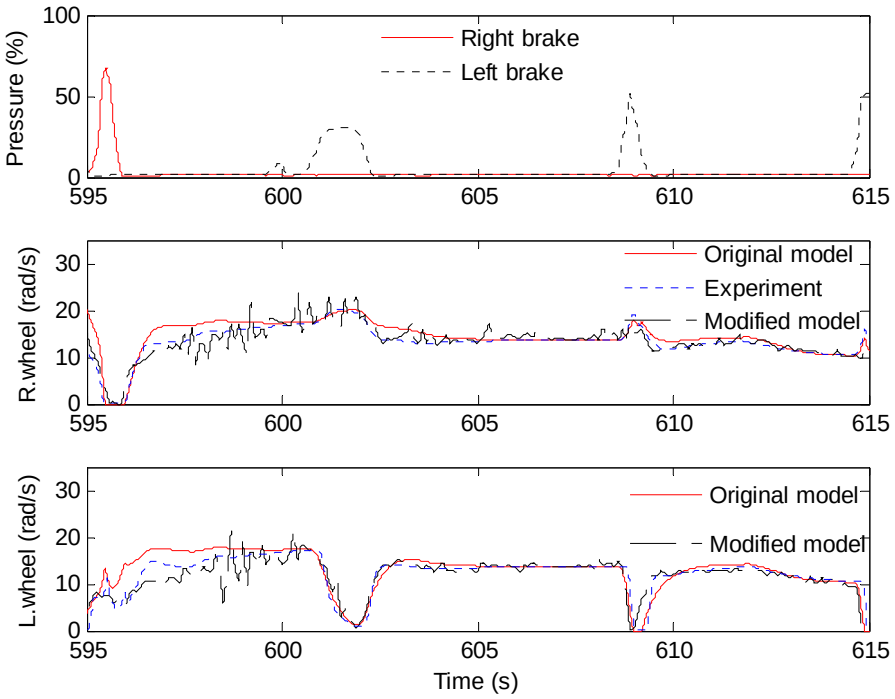

Figure 7.5 Wheel responses on clayed soil

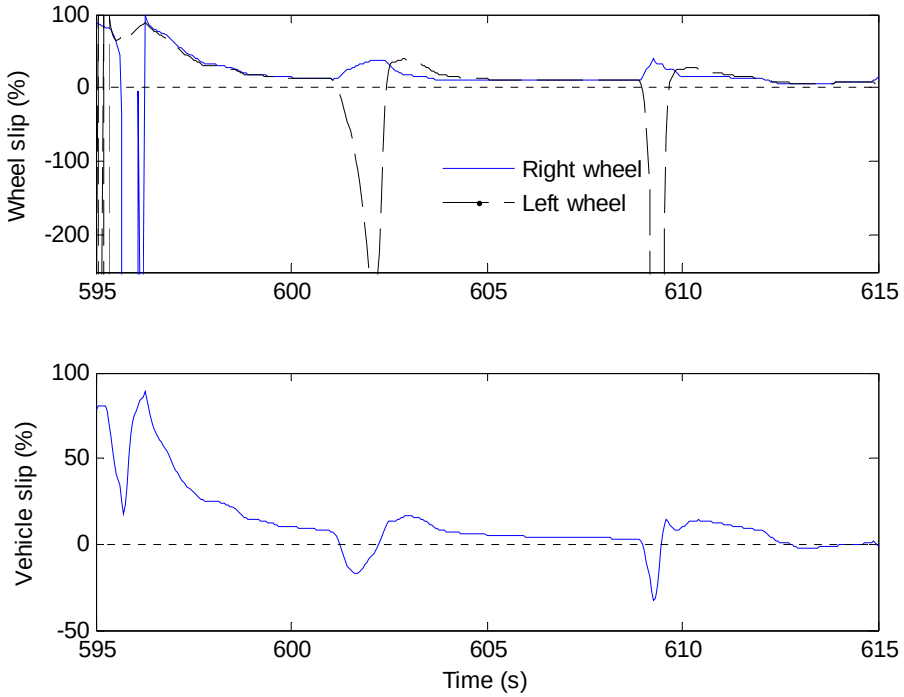

Figure 7.6 Wheel slip ratios on clayed soil

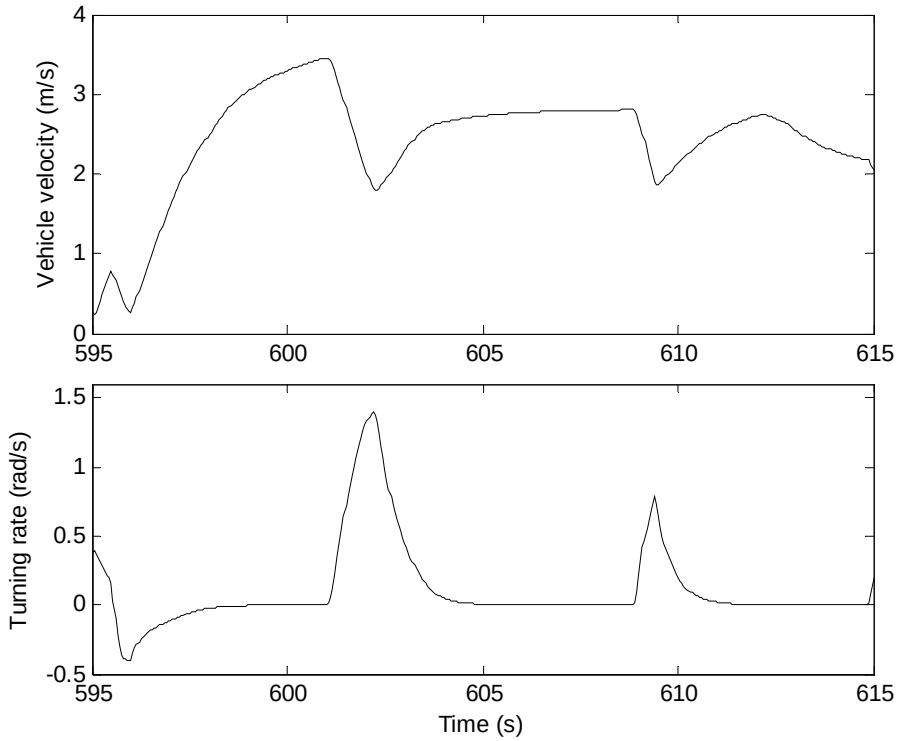

Figure 7.7 Vehicle velocity and turning rate on clayed soil

Responses of the vehicle in the interaction with clayed soil are shown in Figure 7.6 for wheel slip ratios and in Figure 7.7 for the vehicle velocity and turning rate. The longitudinal wheel slips are calculated separately for left and right sides as per (5.17). The 'average' wheel slip (or vehicle slip) is derived from Wong's definition as given in (3.43) with the average value of left and right wheel speeds. In the original model, the wheel slip is ignored or assumed as constant; the results shown in Figure 7.6 however indicate that it is strongly time varying. During acceleration, the wheel slip is very large. Meanwhile, in turning, the outer wheels have a higher tendency to slide while the inner wheel slip changes direction and can become theoretically negative infinite if the wheels are locked.

Responses of the vehicle on different terrains can be better compared with the input pattern shown in Figure 7.8, whereby the vehicle is first accelerated for 10 seconds (from t=5s to t=15s), then turned right with the brake force of 15% for 5 seconds (from t=15s to t=20s), and finally turned left at 25% of the full brake effort (from t=25s to t=30s). The total traction torque acting on the vehicle and the wheel responses are depicted in Figures 7.9 and 7.10 for different terrains. It can be seen that the traction is largest on dry sand, very small on dry clay while those on sandy loam and clayed soil are nearly the same. As a result, the wheel speeds on dry sand are around 26% less than those on dry clay. On sandy loam and clayed soil they are nearly coincident, as shown in Figure 7.10. It is noted that the wheels respond to the throttle and brake inputs at almost at the same rate for all terrains.

Other results in the interaction with terrains are shown in Figures 7.11, 7.12, and 7.13 for the wheel slips, the vehicle velocity, turning rate, and trajectory. In the steady state, the wheel slips on dry sand and dry clay are very small (around 5%) while on clayed soil and sandy loam, they are around 10% and 19% (see Figure 7.11, t=14s-15s). During acceleration, however, the wheel slip on dry clay is much larger than on dry sand while those on sandy loam and clay soil are nearly the same (t=5s-7s). In turning (t=25s-30s) on dry sand, the slip of the outer wheels increases much more than on the other terrains. Due to the wheel slips and rotational speeds, the vehicle velocity and turning rate are largest on dry clay, and decrease gradually for clayed soil, dry sand and sandy loam (Figure 7.12). As a result, the running path on dry clay is longest (see Figure 7.13). This

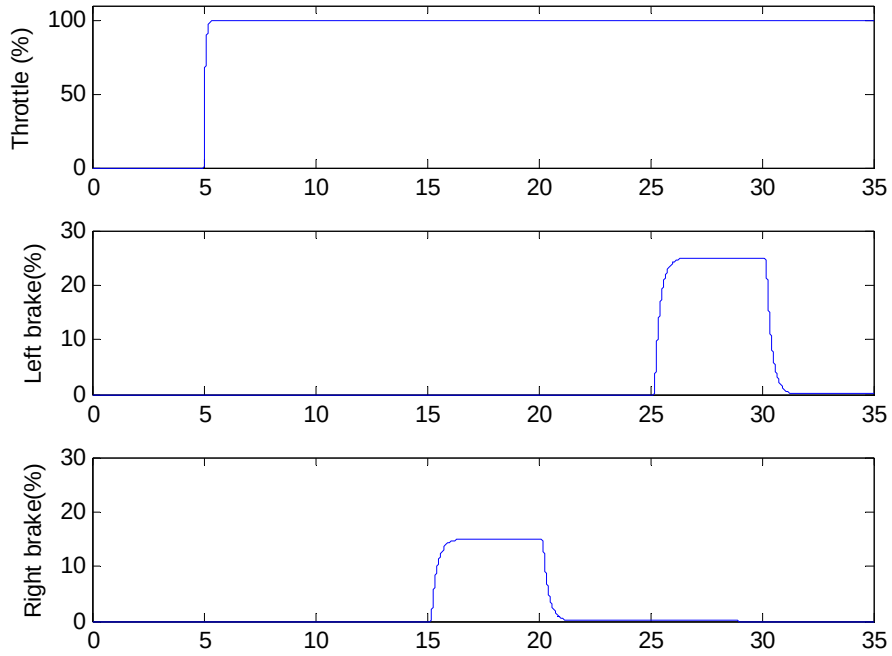

Figure 7.8 Vehicle inputs used for the simulation

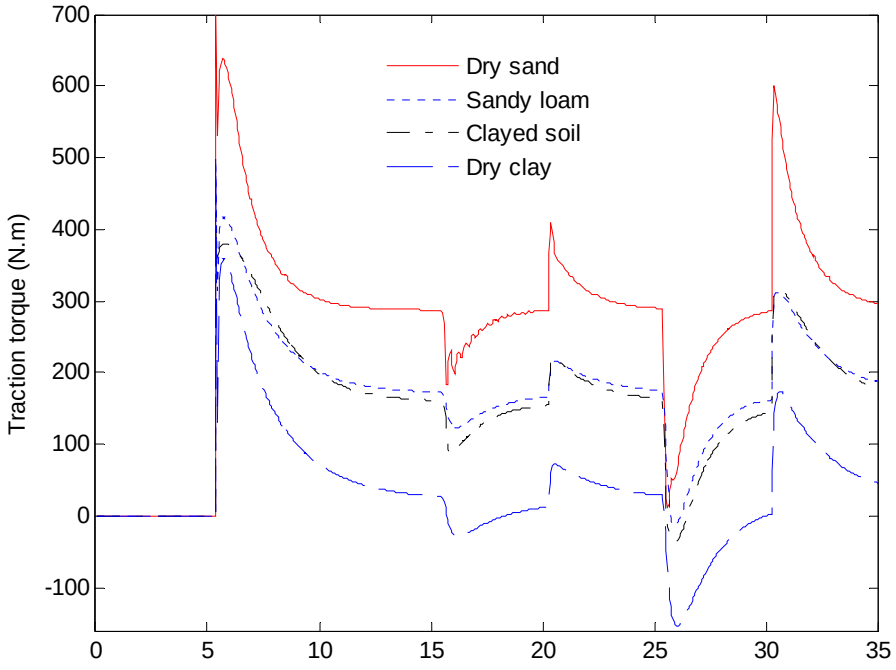

Figure 7.9 Vehicle traction torque on different terrains

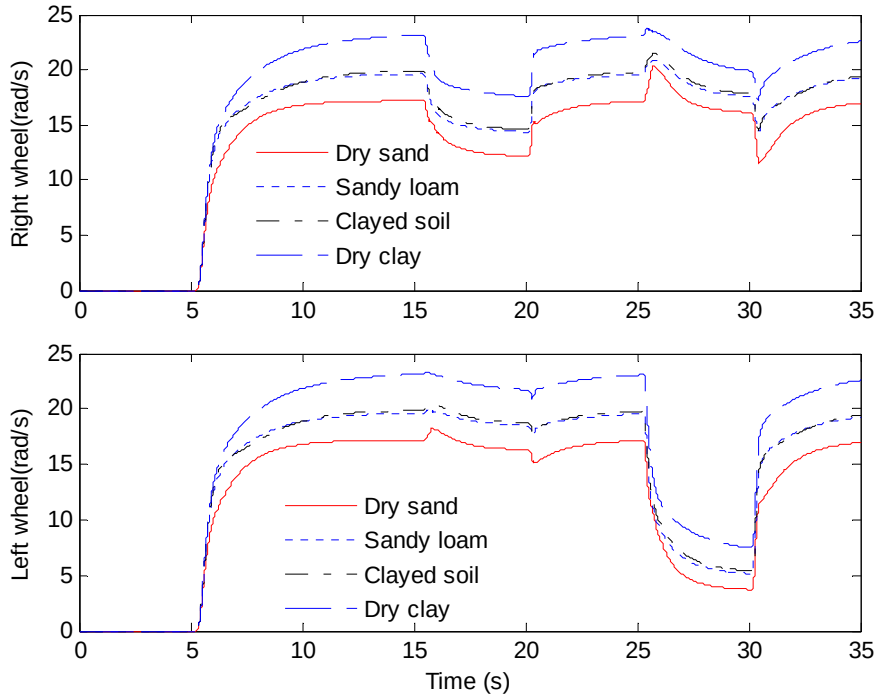

Figure 7.10 Wheel responses on different terrains

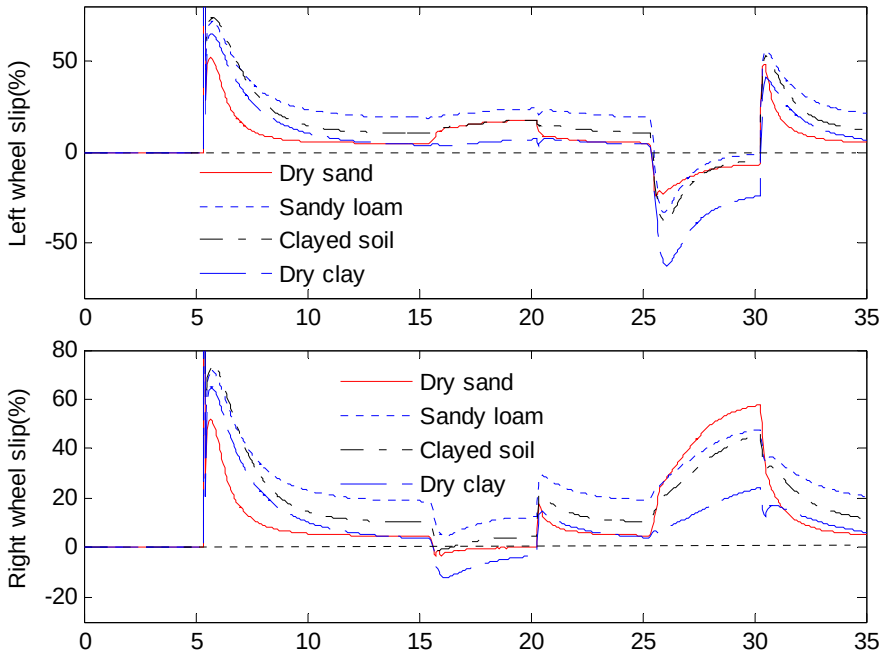

Figure 7.11 Slip ratios on different terrains

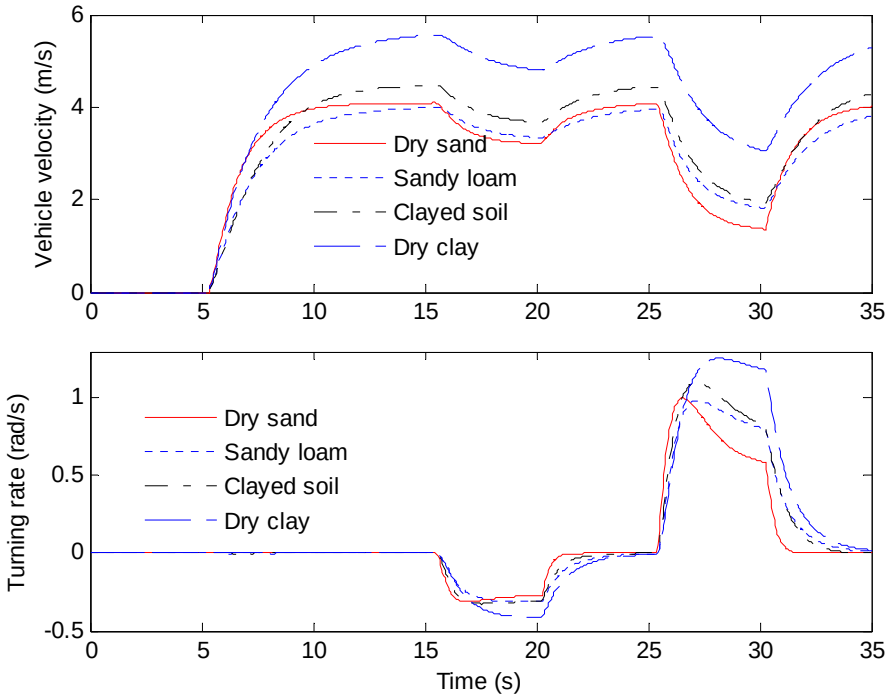

Figure 7.12 Vehicle velocity and turning rate on different terrains

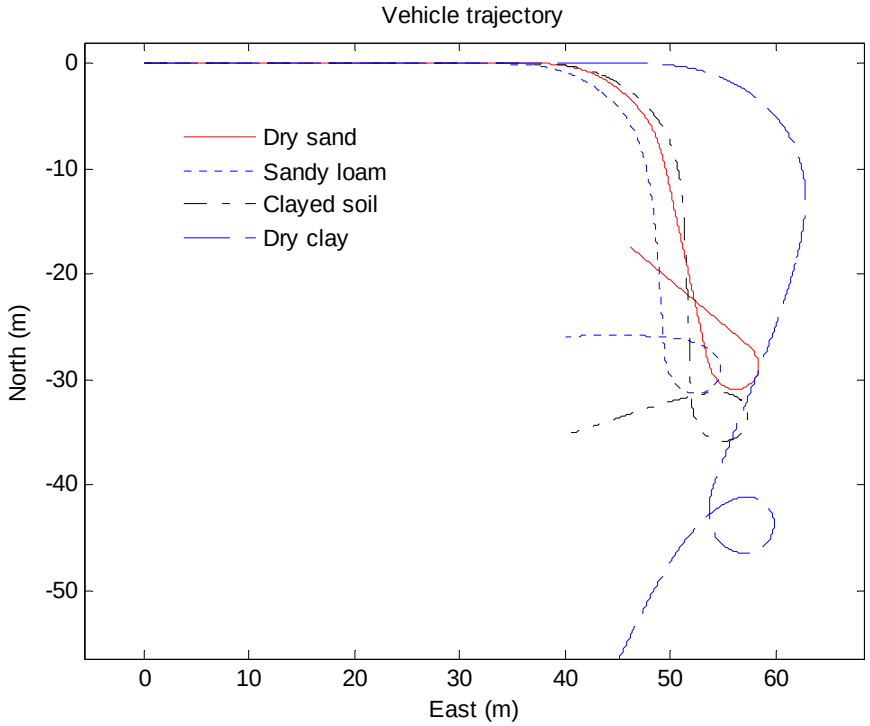

Figure 7.13 Vehicle trajectory on different terrains

indicates that the vehicle mobility on dry clay is much better than on dry sand and sandy loam. It is interesting to note that the vehicle can accelerate faster on dry sand and dry clay than on sandy loam and clayed soil (see slopes of the vehicle velocity profiles on Figure 7.12, t=5-7s). Responses to the turn command appear to be fastest on dry sand.

7.3 Motion control

In this section, the proposed approach described in Chapter 4 is employed to control the vehicle velocity and turning rate. These variables are coupled with each other, as shown in Figure 7.12. For simplicity and acceptable performance, however, the controllers are implemented separately for velocity and turning rate. To reduce the computational load, the throttle and brake control loops (in Chapter 4) are replaced by first-order functions (3.26).

7.3.1 Velocity control

The vehicle velocity is first regulated by a PID controller with $K_P = 20$, $K_I = 20$, and $K_D = 0$. Results are shown in Figure 7.14 for different terrains. A time-delay of 0.45s is observed between the reference and the output. It can be seen that with the same controller, the vehicle responds differently: fast on dry sand and dry clay, slower on clayed soil and sandy loam. Overshoot is very large, except on dry sand. This indicates that there is no fixed controller tuning that is best for navigation on all terrains.

From the results, the closed-loop system is equivalently modelled using equations (4.2-4.4) for all terrains. Characteristics of the responses and model parameters are provided in Table 7.1. It is noted that these parameters vary across a large range due to the different effects of the terrains in interaction with the vehicle. For implementation of the proposed control approach, the modelling parameters are chosen in the intervals

$$\begin{aligned} 1.0\,\text{rad/s} \le \omega_n \le 1.8\,\text{rad/s}, \\ 0.4 \le \delta \le 0.7, \end{aligned} \tag{7.18}$$

and estimated by (4.10) giving

$$\hat{\omega}_n = 1.3416 \text{ rad/s}, \qquad \hat{\delta} = 0.5292. \tag{7.19}$$

From the resulting closed-loop model of the system, the SMC is employed by using the control laws (4.40-4.41) subject to the condition (4.44). Future values of the output and its derivative are estimated from the predictor (4.46-4.49, 4.68). The control system and driveline model are implemented on *Matlab/Simulink*. The predictor and terrain interaction model are realized via *SFunctions* and executed at the sampling rates of 1 kHz and 20 Hz respectively. It should be noted that due to the engine inertia in the throttle control loop, the vehicle cannot respond as quickly as required by the SMC. As a result, chattering can occur at the velocity output. To suppress this chattering, a saturation function is applied in the control law instead of the signum function. In addition, the system uncertainty is very large as the modelling parameters vary widely. The value of η (4.22) must be selected sufficient large to overcome the uncertainty.

Results with η = 1 in the case of reduced chattering are shown in Figure 7.15 for different terrains. The control design parameter λ is chosen as 1 on dry sand and 0.5 for other terrains. It can be seen that the overshoot decreases significantly as its maximum is just 1.7% on dry clay compared with 24% of the system response under PID controller. The rise time is shortest on dry sand and gradually increases on dry clay, clayed soil, and sandy loam. The settling time still remains fast as compared with that of the PID-controlled responses.

TABLE 7.1

PID RESPONSES AND CLOSED-LOOP MODEL PARAMETERS FOR VELOCITY

Terrain	Overshoot (%)	Peak time (s)	Damping ratio	Natural frequency (rad/s)
Dry sand	4.7	3.20	0.698	1.787
Sandy loam	14.7	4.35	0.519	1.041
Clayed soil	21.4	3.95	0.440	1.064
Dry clay	24.2	3.35	0.412	1.223

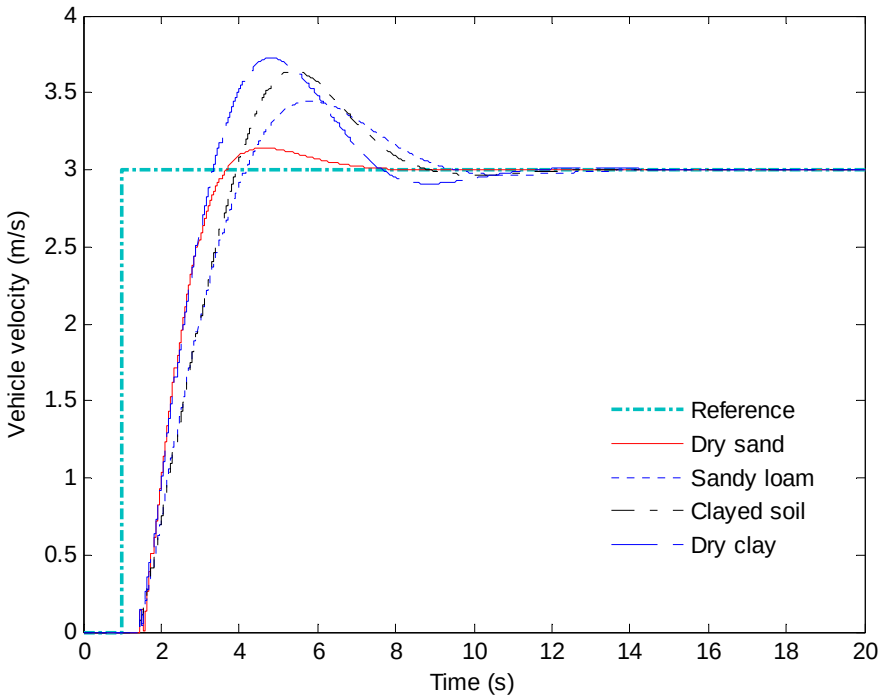

Figure 7.14 Velocity responses under PID controller

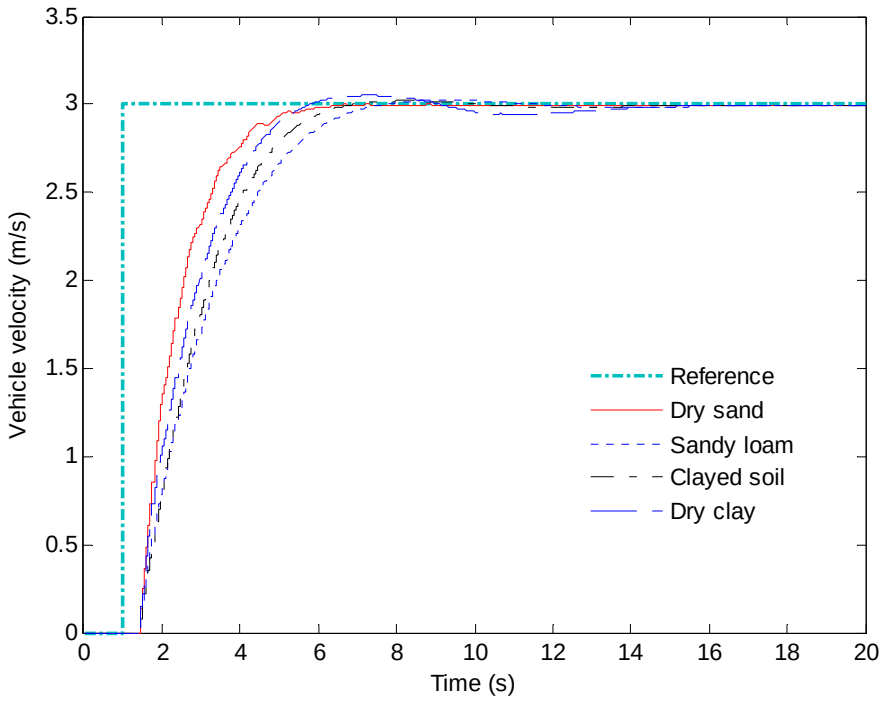

Figure 7.15 Velocity responses with SMC-PID controller

7.3.2 Turning control

To derive the closed-loop model for the turning rate variable, a PID controller is first used on the inner loop to shape the system response to that of a second-order transfer function. As seen in Figure 7.12, however, during turning the vehicle velocity is reduced significantly. This, in turn, affects the turning rate itself. To compensate for this effect, a proportion of the turning rate controller's output is fed forward to the velocity controller as a simple form of decentralized control (Vázquez and Morilla, 2002). The results with $K_P = 15$, $K_I = 25$, and $K_D = 0$ are depicted in Figure 7.16, and characteristics of the responses and the model parameters are listed in Table 7.2. The turning results are taken when the vehicle is running at a velocity of 3m/s. The responses are fast, but overshoots are very large. A time-delay of 0.45s occurs between the reference input command and the start of output response.

From Table 7.2, the modelling parameters are chosen in the intervals

$$\begin{aligned} &2.1\,\text{rad/s} \le \omega_n \le 3.3\,\text{rad/s}, \\ &0.16 \le \delta \le 0.45, \end{aligned} \tag{7.20}$$

and estimated by (4.10), giving

$$\begin{aligned} &\hat{\omega}_n = 2.6325\,\text{rad/s}, \\ &\hat{\delta} = 0.26833. \end{aligned} \tag{7.21}$$

The SMC (4.39, 4.44) and the output predictor (4.46-4.449, 4.68) are implemented for the resulting closed-loop model. Reponses with η = 0.2 and reduced chattering are shown in Figure 7.17 for different terrain types. The design parameter λ is chosen as 5 for dry sand and 0.7 for other terrains. It can be seen that the overshoot is suppressed significantly as its maximum is less than 2.7% on dry clay compared with around 60% of the system response under PID control. The settling time is still fast compared with that of the PID responses. However, due to a high discontinuous gain a small chattering in the turning rate still occurs on dry sand. It should be noted that owing to power constraints the vehicle cannot keep running at large velocity during turning. The harder it turns, the slower it can run.

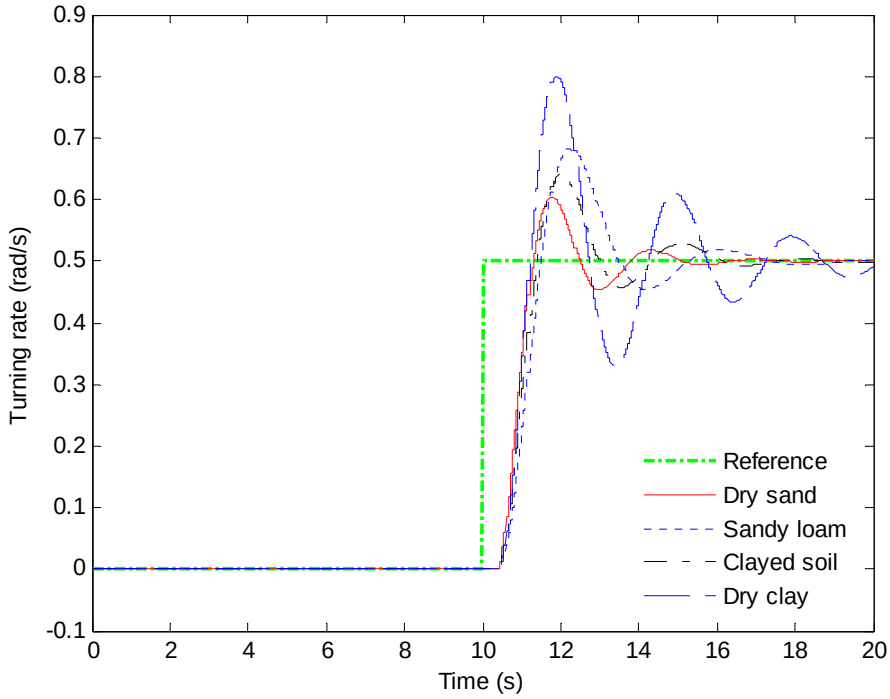

Figure 7.16 Turning responses under PID controller

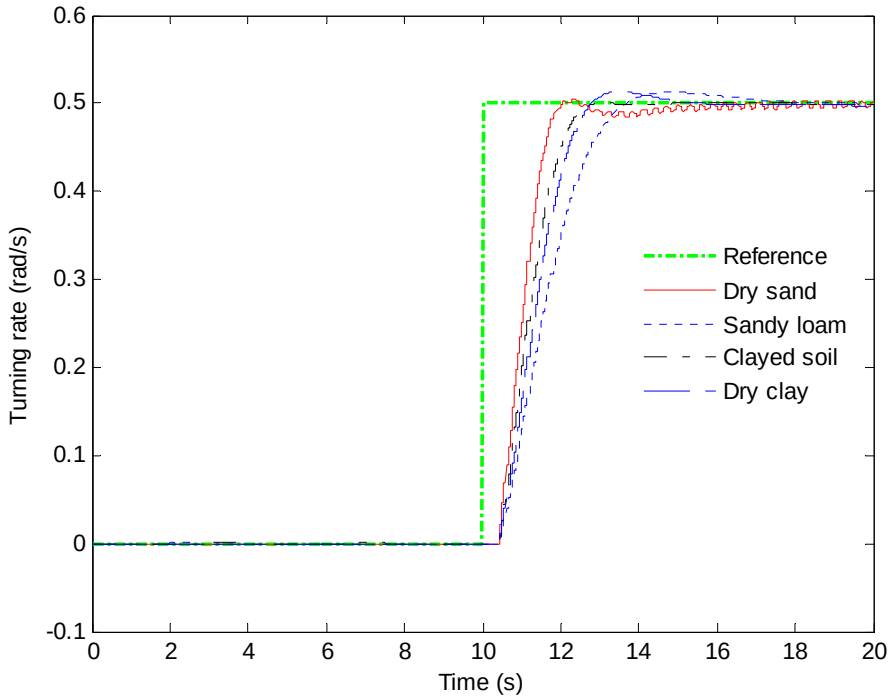

Figure 7.17 Turning responses with SMC-PID controller

TABLE 7.2

PID RESPONSES AND CLOSED-LOOP MODEL PARAMETERS FOR TURNING RATE

Terrain	Overshoot (%)	Peak time (s)	Damping ratio	Natural frequency (rad/s)
Dry sand	21	1.30	0.449	3.257
Sandy loam	36	1.75	0.306	2.155
Clayed soil	28	1.55	0.374	2.562
Dry clay	60	1.45	0.160	2.364

7.4 Conclusion

In this chapter, all developments in this thesis have been integrated into a unique simulator for the UGV. The driveline model developed in Chapter 3 is modified to take into account the interaction between wheels and terrain. Simulations have shown that the results obtained by using the new driveline model are closer to those obtained from experiments, than those obtained by using the original model described in Chapter 3. The combination of the driveline and the terrain interaction models (Chapters 5 and 6) gives a powerful tool to examine all issues related to mobility of the vehicle which are critical for persistent autonomy of the UGV on all terrain types. The control approach proposed in Chapter 4 has been applied successfully to eliminate overshoots in the velocity and turning responses of the vehicle under PID controllers. This is very important for the vehicle to better follow a defined trajectory.

Chapter 8

Summary and conclusion

8.1 Introduction

This thesis has presented the modelling and control of a skid-steering unmanned ground vehicle (UGV). In particular, the vehicle driveline has been analysed and a model was developed to predict the behaviours of its components. In addition, the complex processes involved in the interaction between the wheels and terrain have been analysed and an interaction modelling procedure was proposed. Combined with the driveline model and realised by a fast algorithm in a UGV simulator, every significant dynamic process involved in the vehicle mobility, from the driveline to the terrain interaction, was examined. Furthermore, a new control approach was proposed to eliminate overshoot for PID controlled-loops with input time-delay, and to achieve robustness against nonlinearities and uncertainties. Applied for controlling the vehicle throttle, brakes, velocity, and turning rate, the proposed approach has given better vehicle dynamic performance than can be achieved using PID control.

The next section gives a summary of each chapter in the thesis. Main contributions of the research are described in Section 8.3. Lastly, Section 8.4 suggests some future research directions.

8.2 Chapter summary

Chapter 1 gave an introduction of the research. It commenced with the definitions and a short survey of UGVs. An overview of the research areas required for an UGV as a whole system and the thesis's focus were presented. The main contributions of the thesis as well as publications were listed. The thesis structure was also provided.

In Chapter 2, each area of the research was covered with the relevant literature survey and accompanied by the suitable proposed approaches. Firstly, works in driveline modelling were reviewed and the proposed UGV driveline model was briefly introduced. Then techniques for tuning PID controllers and coping with time-delay and uncertainties were described, followed by the proposed control approach for cases with and without time-delay. Furthermore, the literature on mobility performance analysis for skid-steering vehicles was reviewed and the approach proposed for analysing the interaction between the UGV and terrain was introduced. Finally, the fast algorithm for terrain interaction analysis and relevant work were presented.

Chapter 3 described the development of the vehicle driveline model. Starting with an introduction to the UGV driveline, it described the dynamics of all components in the driveline and developed a model for the whole driveline. Differing from the approach for modelling of a normal car/truck driveline, in this work the rotational speed of the engine was transferred through the CVT, gearbox, differential, and chain systems to the wheels. Total loads on the wheels and other components were referred back to the engine shaft for updating the engine speed, based on the Newton's second law and viscous frictions. Giving a pattern of throttle and brake forces at the inputs, the model could predict the responses of all components. Through simulation, a problem with the computation has been encountered due to a large number of algebraic loops in the driveline model. The problem was solved by combining the gearbox, differential, chain, and wheels together to reduce the number of algebraic loops.

The low level control development was presented in Chapter 4. Overshoot at the brake output was revealed as a typical problem of the PID controllers implemented on the UGV which could severely affect on the overall performances of the vehicle. Based on

an assumption that the closed-loop system under PID control could be equivalently modelled by a second-order function, a sliding mode controller (SMC) was designed for the outer loop conforming to cascade control principle. The order reduction property of the SMC can ensure overshoot is suppressed while its robustness property can overcome the difficulties due to modelling error, nonlinearity, and disturbances. For the time-delay case, an output predictor was employed to compensate for the effect of time-delay. The approach was applied for controlling the vehicle throttle and brakes.

Issues related to the interaction between the wheels and the terrain were examined in Chapter 5. The basis of terramechanics theory applied to a rigid driving wheel on deformable terrain was extended to account for the interaction in the lateral direction and applied to all wheels of the UGV. By integrating the normal and shear stresses acting on a contact patch between a wheel and terrain, the reaction forces of the terrain on the wheel could be obtained on three dimensions. Combined with the vehicle kinetics, the dynamic responses of the vehicle interacting with the terrain were obtained. The development was summarised in an interaction modelling procedure. Using the wheel rotational speeds and terrain parameters as inputs, the model is able to predict the behaviour of the vehicle on different terrains.

A fast algorithm for online implementation of the terrain interaction analysis was presented in Chapter 6. It was developed from an idea that uses linear approximations of normal and shear stresses to obtain an explicit formulation for the terrain interaction forces with a certain error. Based on the criteria, chosen so that error of the approximation was smallest, the normal stress and shear stress were equivalently linearised. By doing that, all integrals involved in the terrain interaction analysis became explicit and could be evaluated in closed form. As a result, the computational process is substantially faster when compared with the original model, and accurate compared with other relevant work. The development was also summarised in a new interaction modelling procedure which was ready for online implementation.

In Chapter 7, the vehicle driveline model developed in Chapter 3 was modified to take into account the interaction with terrain. The new driveline model was obtained by replacing the empirical traction load in the original model by one obtained from the terrain reaction. As a result, the model was more realistic and accurate. The combination

of the driveline model and terrain interaction model also enabled examination of the vehicle responses on different terrains with the same pattern of inputs (throttle and brake forces). The proposed approach in Chapter 4 was employed to control the vehicle velocity and turning rate in the UGV simulator.

8.3 Thesis contribution

8.3.1 The vehicle driveline model

There are three contributions in the vehicle driveline developments. First is the model of CVT. Although simplified and linearised from experiment data, it is able to describe the complex relationship between the input and output. Second is the model of the vehicle differential during turning. In driveline modelling for cars or trucks, the turning mechanics are usually ignored. In contrast, in this model, the difference in rotational speeds between the differential outputs are analysed and expressed explicitly in terms of a first order transfer function of the difference in loads between the outputs. An overall time constant for the differential derived to relate to the weight of the vehicle, wheels, with viscous friction coefficients of the wheels and the differential. The most important contribution is the incorporation of terrain interaction in the driveline model. Most driveline models ignore this interaction or assume that it obeys the Coulomb friction law which is not exactly valid for UGV navigation over deformable terrain. Meanwhile, the complex processes involved in the wheel-terrain interaction are integrated into the vehicle model, resulting in more accurate prediction.

8.3.2 Robust low-level control for the vehicle nonlinear dynamics

The contribution in the proposed control approach is that it can exploit the advantages of both SMC and PID controllers to compensate for their drawbacks. In fact, the PID scheme is used to derive the equivalent closed-loop model for the SMC design. As a result, the approach can be applied for a class of systems without prior knowledge of their structure. This model-free feature is not available for the SMC alone. In contrast, the order reduction property of the SMC is employed to suppress overshoots in the responses, whereas this is intractable when using only a PID controller. In addition the

robustness of the SMC enables it to compensate for nonlinearities, disturbances and modelling uncertainties. The proposed approach can therefore efficiently suppress overshoots for this kind of system subject to nonlinearities and input time delay.

8.3.3 Dynamic modelling of the vehicle-terrain interaction

It is well known that knowledge of vehicle-terrain interaction plays an important role in increasing the autonomy of a UGV and securing its safe mobility. In this work, the current theory applied for a driving wheel on soft terrain is extended to account for the lateral reaction of the terrain. This is very important because the performance of a skid-steering vehicle in turning depends on the turning moment resistance which is mainly derived from the reaction forces acting on the wheels in the lateral direction. The development is applied to all wheels of the UGV to obtain the reaction forces from the terrain acting on the wheels, the turning moment and turning movement resistance. Combined with the vehicle kinetics, all characteristics related to the UGV-terrain interaction such as the vehicle velocity, turning rate, slip ratios, traction, drawbar pull, and resistances have been comprehensively formulated provided that the terrain parameters are known.

8.3.4 Fast algorithm for terrain interaction analysis

A significant contribution in this work is that it improves the accuracy of the approximation method, applied for the normal and shear stresses, to speed up the computation process for the terrain interaction analysis. Thus, the analysis is able to be performed with a high computational efficiency while it is also accurate enough as compared with the relevant method reported in the literature. Using this approach, a new terrain interaction model is developed for online prediction of vehicle behaviour.

8.3.5 UGV simulator

The simulator for the whole vehicle, incorporating the driveline model, terrain interaction model, and the basic motion controllers, is helpful for further developments on the UGV mobility characteristics. Alternatively, it can be used to predict the response of the vehicle on a certain terrain with a pattern of inputs.

8.4 Future work

Based on the research presented in this thesis, the following directions are suggested for further investigation:

- Slip in the CVT: Responses of the driveline model are close to the experimental data. During periods of acceleration, however, there were mismatches between the simulation results and those from experiments. This was likely because of the slip occurred between the CVT clutches and the V-belt which was ignored in the model. If this slip is analysed and inserted in the model, the results will be improved.

- Adaptive scheme for time-delay estimation: The proposed control approach gave good results for time-delay systems. It is, however, sensitive to the magnitude of time-delay. Changes to the time-delay can lead to unsatisfactory responses. For time-varying delay systems, values of the delay therefore need to be updated online in order to obtain better results with the proposed method.

- Auto-tuning method for SMC parameters: The rise time of the SMC-PID controller depends on the value of λ. The lager it is, the faster the response is. As a trade-off, however, large value of λ can lead to overshoot, especially for time-delay systems. In this thesis, this value is currently chosen by trial-error, depending on the current rise time and the desired one. An automatic adjustment of this parameter is therefore desirable.

- Terrain parameters estimation and classification: In this thesis, the proposed terrain interaction analysis is verified with the four typical terrains whose parameters are known. As mentioned in Chapter 7, there will be no motion controller that is suitable for all terrains. If parameters of the terrain over which the vehicle is running are known, or, at least the type of the terrain is available, the vehicle can be controlled more effectively. This is also very important for safe and autonomous mobility of the UGV.

Bibliography

Artstein, Z. (1982). "Linear systems with delayed control: A reduction." *IEEE Transaction on Automatic Control*, **27**(4), 869 - 879.

Aström, K. J., and Hagglund, T. (1995). *PID Controllers: Theory, Design, and Tuning*, Instrument Society of America.

Aström, K. J., and Hagglund, T. (2004). "Revisiting the Ziegler-Nichols step response method for PID control." *Journal of process control*, **14**(6), 635-650.

Balluchi, A., Benvenuti, L., Lemma, C., Murrieri, P., and Sangiovanni Vincentelli, A. L. (2005).
"Hybrid models of an automotive driveline." *Internal Technical Report,* PARADES, Rome.

Bekker, M. G. (1956). *Theory of Land Locomotion*, University of Michigan Press, Ann Arbor.

Bekker, M. G. (1969). *Introduction to Terrain-Vehicle System*, University of Michigan Press, Ann Arbor.

Besharati Rad, A., Lo, W. L., and Tsang, K. M. (1997). "Self-tuning PID controller using Newton-Raphson search method." *IEEE Transactions on Industrial Electronics*, **44**(5), 717-725.

Camacho, O., Rojas, R., and García, W. (1999). "Variable structure control applied to chemical processes with inverse response." *ISA Transaction*, **38**(1), 55-72.

Canudas de Wit, and C. Horowitz, R. (1999) "Observers for tire/road contact friction using only wheel angularvelocity information." *Proc. of the 38th IEEE Conference on Decision and Control*, Phoenix, AZ, USA, 3932-3937, 7-10 December 1999.

Cho, J., Sung, S., and Lee, I. (2002). "Cascade control strategy for external carbon dosage in predenitrifying process." *Water Science and Technology*, **45**(4-5), 53-60.

Cominos, P., and Munro, N. (2002). "PID controllers: Recent tuning methods and design to specification." *Control Theory and Applications, IEE Proceedings*, **149**, 46-53.

Creedy, A. P. (1985). "Skid steering of wheeled and tracked vehicles: Analysis with Coulomb friction assumptions." *Report of the Engineering Development Establishment, Australian Army,* Maribyrnong, Victoria, Australia.

Crossley, P. R., and Cook, J. A. (1991). "A nonlinear engine model for drivetrain system development." *Proc. of the IEE International Conference 'Control 91'*, Edinburgh, UK, **2**, 921-925, 25-28 March, 1991.

Deur, J., Hrovat, D., and Asgari, J. (2003) "Analysis of mean value engine model with emphasis on intake manifold thermal effects." *Proc. of the 2003 IEEE Conference on Control Applications*, 161- 166, 23-25 June 2003

Deur, J., Pavkovic, D., Peric, N., and Jansz, M. (2002) "Analysis and optimization of an electronic throttle for linear operating modes." *Proc. of the 10th International Power Electronics and Motion Control Conference*, Dubrovnik-Cavtat, Croatia, (CD-ROM).

Deur, J., Pavkovic, D., Peric, N., Jansz, M., and Hrovat, D. (2004). "An electronic throttle control strategy including compensation of friction and limp-home effects." *IEEE Transactions on Industry Applications*, **40**(3), 821 - 834.

Deur, J., Petric, J., Asgari, J., and Hrovat, D. (2005) "Recent advances in control-oriented modeling of automotive power train dynamics." *Proc. of the IEEE International Symposium on Industrial Electronics*, 269- 278, 20-23 June, 2005

Douglass, R. J. (1998). "The DARPA autonomous land vehicle: A phase I retrospective and a prospective for the future." *Proc. of the Conference on Space and Military Applications of Automation and Robotics*, Huntsville AL, 249, 21-22 June, 1988.

Durrant-Whyte, H. (2001). "A critical review of the state-of-the-art in autonomous land vehicle systems and technology." *Sandia Report SAND2001-3685,* Sandia National Laboratories, Albuquerque, New Mexico.

Everett, H. R. (1995). *Sensors for Mobile Robot Systems: Theory and Application*, Wellesley, MA.

Fiagbedzi, Y., and Pearson, A. (1986). "Feedback stabilization of linear autonomous time lag systems." *IEEE Transactions on Automatic Control*, **31**(9), 847- 855.

Franklin, G. F., Powell, J. D., and Emami-Naeini, A. (2002). *Feedback Control of Dynamic Systems*, Prentice Hall, Upper Saddle River, NJ.

Fredriksson, J. (2006). "Improved driveability of a hybrid electric vehicle using powertrain control." *International Journal of Alternative Propulsion*, **1**(1), 97 - 111.

Gage, D. W. (1995). "UGV history 101: A brief history of unmanned ground vehicle (UGV) development efforts." *Unmanned Systems Magazine*, **13**(3), 9-16.

Gaing, Z.-L. (2004). "A particle swarm optimization approach for optimum design of PID controller in AVR system." *IEEE Transaction on Energy Conversion*, **19**(2), 384-391.

Grotjahn, M., Quernheim, L., and Zemke, S. (2006) "Modelling and identification of car driveline dynamics for anti-jerk controller design." *Proc. of the 2006 IEEE International Conference on Mechatronics*, 131-136, July 2006.

Hang, C. C., Aström, K. J., and Ho, W. K. (1991) "Refinements of the Ziegler-Nichols tuning formula." *Control Theory and Applications, IEE Proceedings D*, 111-118,

Hang, C. C., Lee, T. H., and Tay, T. T. (1984). "The use of recursive parameter estimation as an auto-tuning aid." *Proc. ISA Annual Conference*, USA, 387-396, 1994.

Hang, C. C., and Sin, K. K. (1991). "On-line auto tuning of PID controllers based on the cross-correlation technique." *IEEE Transactions on Industrial Electronics*, **38**(6), 428 - 437.

Hendricks, E. (1997). "Engine modelling for control applications: A critical survey." *Meccanica*, **32**, 387-396.

Hendricks, E., and Sorenson, S. C. (1990). "Mean value modelling of spark ignition engines." *Engines, SAE Technical Paper No. 900616*.

Hogg, R. W., Rankin, A. L., Roumeliotis, S. I., McHenry, M. C., Helmick, D. M., Bergh, C. F., and Matthies, L. (2002) "Algorithms and sensors for small robot path following." *Proc. of the 2002 IEEE International Conference on Robotics and Automation*, Washington, DC, 3850-3857, 2002.

Hung, J. Y., Gao, W., and Hung, J. C. (1993). "Variable structure control: A survey." *IEEE Transactions on Industrial Electronics*, **40**(1), 2 - 22.

Hutangkabodee, S., Zweiri, Y. H., Seneviratne, L. D., and Althoefer, K. (2006). "Performance prediction of a wheeled vehicle on unknown terrain using identified soil parameters." *Proc. of the 2006 IEEE International Conference on Robotics and Automation*, Orlando, Florida, 3356-3361, May 2006.

Iagnemma, K., Kang, S., Shibly, H., and Dubowsky, S. (2004). "Online terrain parameter estimation for wheeled mobile robots with application to planetary rovers." *IEEE Transactions on Robotics*, **20,** (5), 921-927.

Ioannou, P., and Xu, Z. (1994). "Throttle and brake control systems for automatic vehicle following." *Journal of Intelligent Transportation Systems*, **1**(4), 345-377.

Ishigami, G., Miwa, A., Nagatani, K., and Yoshida, K. (2007). "Terramechanics-based model for steering maneuver of planetary exploration rovers on loose soil." *Journal of Field Robotics*, **24**(3), 233-250.

Karimi, A., Garcia, D., and Longchamp, R. (2003). "PID controller tuning using Bode's integrals." *IEEE Transactions on Control Systems Technology*, **11**(6), 812-821.

Kawasaki. (2004). "4 cycles engines: FD620D."
URL: http://www.kawpowr.com/4cycle/horiz_fd620d.asp, accessed May 2004.

Kaya, I. (2001). "Improving performance using cascade control and a smith predictor." *ISA Transaction*, **40**(3), 223-234.

Kaya, I., and Atherton, D. P. (2005) "Improved cascade control structure for controlling unstable and integrating processes." *Proc. of the 44th IEEE Conference on Decision and Control, and the European Control Conference 2005*, 7133-7138, 12-15 Dec. 2005.

Kelly, A. (1994). "A feedforward control approach to the local navigation problem for autonomous vehicles." Technical Report CMU-RI-TR-94-17, Carnegie Mellon University.

Kiencke, U., and Nielsen, L. (2000). *Automotive Control Systems*, Springer, Berlin.

Kuang, M. L., Fodor, M., and Hrovat, D. (1999) "Hydraulic brake system modeling and control for active control of vehicle dynamics." *Proc. of the American Control Conference*, San Diego, California, 4538-4542, June 1999.

Kurtz, J. (1998) "DEMO III experimental unmaned vehicle autonomous mobility system overview." *Proc. of the 1998 IEEE International Symposium on Intelligent Control (ISIC), IEEE International Symposium on Computational Intelligence in Robotics and Automation (CIRA), Intelligent Systems and Semiotics (ISAS) Joint Conference*, Gaithersburg, MD, USA, 640-643, 14-17 September 1998.

Lee, Y., and Oh, S. (2002). "Enhanced control with a general cascade control structure." *Ind. Eng. Chem. Res.*, **41**(11), 2679 -2688.

Legnemma, K., Brooks, C., and Dubowsky, S. (2004). "Visual, tactile, and vibration-based terrain analysis for planetary rovers." *Proceedings of 2004 IEEE Aerospace Conference*, **2**, 841 - 848.

Lowrie, J. W., Thomas, M., Gremban, K., and Turk, M. (1985). "Autonomous land vehicle (ALV) preliminary road-following demonstration." *Intelligent Robots And Computer Vision*, **579**, 336-350.

Lu, X.-Y., and Hedrick, J. K. (2005). "Heavy-duty vehicle modelling and longitudinal control." *Vehicle System Dynamics*, **43**(9), 653 - 669.

Lucente, G., Montanari, M., and Rossi, C. (2005) "Hybrid modelling of a car driveline for servo-actuated gear shift." *Proc. of the IEEE International Symposium on Industrial Electronics*, 223- 228, June 20-23, 2005.

Maciuca, D. B., and Hedrick, J. K. (1995) "Advanced nonlinear brake system control for vehicle platooning." *Proc. of European Control Conference*, Rome, Italy, 2402-2407, 5-8 September, 1995.

Makila, P. M., and Partington, J. R. (1999). "Laguerre and Kautz shift approximations of delay systems." *International Journal of Control*, **72**(10), 932-946.

Matthies, L., Litwin, T., Owens, K., Rankin, A., Murphy, K., Coombs, D., Gilsinn, J., Hong, T., Legowik, S., Nashman, M., and Yoshimi, B. (1998) "Performance evaluation of UGV obstacle detection with CCD/FLIR stereo vision and LADAR." *Proc. of the 1998 IEEE International Symposium on Intelligent Control (ISIC), IEEE International Symposium on Computational Intelligence in Robotics and Automation (CIRA), Intelligent Systems and Semiotics (ISAS) Joint Conference*, Santa Barbara, CA, 658-670, June 1998.

Moravec, H. P. (1980). "Obstacle avoidance and navigation in the real world by a seeing robot rover." Technical Report, Carnegie-Mellon Robotics Institute, Pittsburgh, PA.

Moravec, H. P. (1983). "The Stanford cart and CMU rover." *Proc. of the IEEE*, **7**(7), 872-894, July 1983.

Murphy, K. N. (1992) "Navigation and retro-traverse on a remotely operated vehicle." *Proc. of the Singapore International Conference on Intelligent Control and Instrumentation*, 323-328, 17-21 Feb 1992.

Murphy, K. N. (1994) "Analysis of robotic vehicle steering and controller delay." *Proc. of the Fifth Intemational Symposium on Robotics and Manufacturing*, Maui, Hawai, 631-636, August, 1994.

Nilsson, N. J. (1969). "A mobile automaton: An application of artificial intelligence." *Proc. of the First International Joint Conference on Artificial Intelligence*, 509-520, 1969.

Nilsson, N. J. (1984). "Shakey the robot." Technical Report, AI Center, SRI International, Menlo Park, CA.

Ontario Drive & Gear (2007). "Argo operators manual."
URL: http://www.argovehicles.com/pages/manuals.html, accessed May 2007.

Ojeda, L., Borenstein, J., Witus, G., and Karlsen, R. (2006). "Terrain characterization and classification with a mobile robot." *Journal of Field Robotics*, **23**(2), 103-122.

Partington, J. R. (1991). "Approximation of delay systems by fourier-laguerre series." *Automatica*, **27**, 569-572.

Richard, J.-P. (2003). "Time-delay systems: An overview of some recent advances and open problems." *Automatica*, **39**(10), 1667-1694.

Rossi, C., Tilli, A., and Tonielli, A. (2000). "Robust control of a throttle body for drive by wire operation of automotive engines." *IEEE Transactions on Control Systems Technology*, **8**(6), 993 - 1002.

Setlur, P., Wagner, J. R., Dawson, D. M., and Samuels, B. (2003). "Nonlinear control of a continuously variable transmission (cvt)." *IEEE Transactions on Control Systems Technology*, **11**(1), 101 - 108.

Shen, J.-C. (2001). "Fuzzy neural networks for tuning PID controller for plants with underdamped responses." *IEEE Transactions on Fuzzy Systems*, **9**(2), 333-342.

Shibly, H., Iagnemma, K., and Doubowsky, S. (2005). "An equivalent soil mechanics formulation for rigid wheels in deformable terrain with application to planetary exploration rovers." *Journal of Terramechanics*, **42**, 1-13.

Shiller, Z. M., M.P.; Rubinstein, D. (2007) "Dynamic stability of off-road vehicles considering a longitudinal terramechanics model." *Proc. of the 2007 IEEE International Conference on Robotics and Automation*, 1170-1175, 10-14 April 2007.

Shoemaker, C. M., and Bomstein, J. A. (1998). "The DEMO III UGV program: A testbed for autonomous navigation research." *Proc. of the 1998 IEEE International Symposium on Intelligent Control (ISIC), IEEE International Symposium on Computational Intelligence in Robotics and Automation (CIRA), Intelligent Systems and Semiotics (ISAS) Joint Conference*, Gaithersburg, MD, USA, 644-651, 14-17 Sep 1998.

Slotine, J. J., and Li, W. (1991). *Applied Nonlinear Control*, Prentice-Hall, Englewood Cliffs, NJ.

Spiegel, M. R. (1968). *Mathematical Handbook of Formulas and Tables*, McGraw-Hill, New York.

Spofford, J. R., Rimey, R. D., and Munkeby, S. H. (1997). "Overview of the UGV / DEMO II program." In reconnaissance, surveillance, and target acquisition for the unmanned ground vehicle: Providing surveillance 'eyes' for an autonomous vehicle, edited by O. Firschein and T.M. Strat, Morgan Kaufman, Defense Advanced Research Projects Agency. Information Systems Office., 21-40.

Tan, K. K., Zhao, S., and Xu, J. X. (2007). "Online automatic tuning of a proportional integral derivative controller based on an iterative learning control approach." *IET Control Theory & Applications*, **1**(1), 90-96.

Tan, W., Liu, J., Chen, T., and Marquez, H. J. (2005). "Robust analysis and PID tuning of cascade control systems." *Chemical Engineering Communications*, **192**, 1204 - 1220.

Tanelli, M., Astolfi, A., and Savaresi, S. M. (2006) "Robust nonlinear proportional-integral control for active braking control systems." *Proc. of the 45th IEEE Conference on Decision and Control*, San Diego, CA, 1745 - 1750, 13-15 December 2006.

Thomson. (2007). "Industrial linear actuators."
URL: http://www.danahermotion.com/documents/, accessed May 2007.

Utkin, V. I. (1993). "Sliding mode control design principles and applications to electric drives." *IEEE Transactions on Industrial Electronics*, **40**(1), 23-36.

Vázquez, F., and Morilla, F. (2002) "Tuning decentralized PID controllers for MIMO systems with decouplers." *Proc. of the 15th IFAC World Congress*, Barcelona, Spain, 2002.

Velenis, E., Tsiotras, P., Canudas de Wit, C., and Sorine, M. (2005). "Dynamic tyre friction models for combined longitudinal and lateral vehicle motion." *Vehicle System Dynamics*, **43**(1), 3-29.

Visioli, A. (2001). "Tuning of PID controllers with fuzzy logic." *IEE Proc. - Control Theory and Applications*, **148**(1), 1-8, Jan 2001.

Waldron, K. (2004). "Argo ground interaction equations." Internal document, unpublished.

Wang, Q.-G., Lee, T.-H., Fung, H.-W., Bi, Q., and Zhang, Y. (1999). "PID tuning for improve performance." *IEEE Transactions on Control Systems Technology*, **7**(4), 457-465.

Wang, Z., and Hu, H. (1999). "Robust stability test for dynamic systems with short delays by using Padé approximation." *Nonlinear Dynamics*, **18**(3), 275-287.

Weiss, K. R. (1971). "Skid-steering." *Automobile Engineer*, 22-25.

Wikipedia. (2007). "Unmanned ground vehicle."
URL: http://en.wikipedia.org/wiki/UGV, accessed May 2007.

Wilber, B. M. (1972). "A Shakey primer." Technical Report, Stanford Research Institute, Menlo Park, CA.

Wong, J.-Y., and Reece, A. R. (1967). "Prediction of rigid wheel performance based on analysis of soil-wheel stresses, Part 1: performance of driven rigid wheels." *Journal of Terramechanics*, **4**(1), 81-98.

Wong, J. Y. (2001). *Theory of Ground Vehicle*, Wiley, New York, 3rd edition.

Wong, J. Y., and Chiang, C. F. (2001). "A general theory for skid steering of tracked vehicles on firm ground." *Proceedings of the Institution of Mechanical Engineers, Part D: Journal of Automobile Engineering*, **215**(D3), 343-355.

Yanakiev, D., and Kanellakopoulos, I. (1996). "Speed tracking and vehicle follower control design for heavy-duty vehicles." *Vehicle System Dynamics*, **25**(4), 251 - 276.

Yoerger, D. R., and Slotine, J.-J. E. (1987). "Task resolved motion control of vehicle-manipulator systems." *International Journal of Robotics and Automation*, **2**(3), 144-151.

Yokoyama, M., Shimizu, K., and Okamoto, N. (1998) "Application of sliding-mode servo controllers to electronic throttle control." *Proc. of the 37th IEEE Conference on Decision and Control*, Tampa, FL, USA, 1541 - 1545, 16-18 December 1998.

Young-Hoon, R., and Jun-Ho, O. (2000). "Sliding mode control with uncertainty adaptation for uncertain input-delay systems." *International Journal of Control*, **73**, 1255 - 1260.

Yu, C.-C. (1999). *Autotuning of PID Controllers: Relay Feedback Approach*, Springer, London, New York.

Zanasi, R., Visconti, A., Sandoni, G., and Morselli, R. (2001). "Dynamic modeling and control of a car transmission system." *Proc. of the 2001 IEEE/ASME International Conference on Advanced Intelligent Mechatronics*, Como, Italy, **1**, 416 - 421, 8-12 July 2001.

Zhang, W., Xu, X., and Sun, Y. (1999). "Quantitative performance design for integrating processes with time delay." *Automatica*, **35**(4), 719-723.

Zhuang, M., and Atherton, D. P. (1994). "Optimum cascade PID controller design for siso systems." *International Conference on Control*, **1**, 606 - 611.

Ziegler, J. G., and Nichols, N. B. (1942). "Optimum setting for automatic controllers." *ASME transaction*, **64**, 759-768.

Appendix A

Transformation between spherical coordinates and Cartesian coordinates

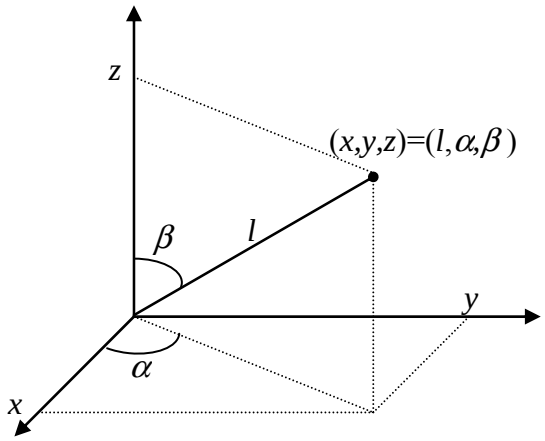

Figure A.1 Spherical coordinates

Transfromation from spherical coordinates into Cartesian coordinates (Spiegel, 1968):

$$x = l\cos\alpha\sin\beta,$$

$$y = l\sin\alpha\sin\beta,$$

$$z = l\cos\beta.$$

Transfromation from Cartesian coordinates into spherical coordinates:

$$l = \sqrt{x^2 + y^2 + z^2},$$

$$\alpha = \tan^{-1}\left(\frac{y}{x}\right),$$

$$\beta = \cos^{-1}\left(\frac{z}{l}\right) = \tan^{-1}\left(\frac{\sqrt{x^2 + y^2}}{z}\right).$$

Appendix B

Transformation from vehicle coordinates to earth coordinates

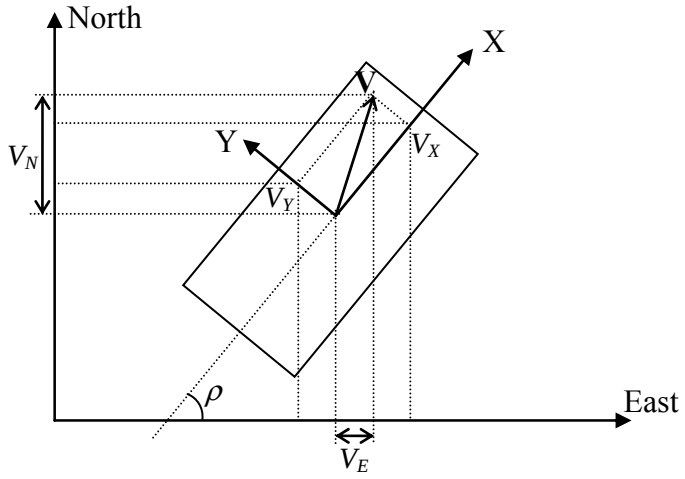

Figure B.1 Vehicle coordinates versus earth coordinates

Components of the vehicle velocity in the earth coordinates are (Spiegel, 1968):

$$V_E = V_X \cos\rho - V_Y \sin\rho,$$

$$V_N = V_X \sin\rho + V_Y \cos\rho.$$

Position of the vehicle in the earth coordinates is calculated by:

$$E = \int_0^t V_E dt = \int_0^t (V_X \cos\rho - V_Y \sin\rho) dt,$$

$$N = \int_0^t V_N dt = \int_0^t (V_X \sin\rho + V_Y \cos\rho) dt.$$